Hydrodynamics inside a laboratory-scale semi-dry flue gas desulphurisation riser

C Prinsloo

orcid.org/0000-0003-0785-1265

Dissertation accepted in fulfilment of the requirements for the degree *Master of Engineering Chemical Engineering* at the North-West University

Supervisor:	Mr AF van der Merwe
Co-supervisor:	Mr LA le Grange
Co-supervisor:	Mr FH Conradie

Graduation:	August 2023
Student number:	27084523

ABSTRACT

Since power plants were initially designed without SO_2 emission control in mind, power generating facilities are struggling to comply with the increasingly stringent emissions legislation. One possible approach to address this problem is using sulphur capturing technology. From the available methods, the characteristics of semi-dry flue gas desulphurisation (FGD) technology makes it a promising avenue to explore. Accordingly, a laboratory scale circulating fluidised bed (CFB) riser was designed with the intention of performing FGD research. Although much research was performed on fast fluidisation and the role of CFB's in FGD, little is known about the influence of varying riser heights on the hydrodynamics. Given the novelty that was associated with the new system, the aim of this study was to describe the hydrodynamics of hydrated lime inside the riser. This aim was achieved by discussing the influence of design and operating conditions on the two-phase flow inside the system using both experimental findings and CFD modelling.

Similarity parameters were applied to literature data to determine a suitable range of operating conditions and the desired particle size for this study. This ensured that the fast fluidisation regime was obtained inside the riser such that the results remained relevant for future work. The hydrodynamics were quantified through a few measured or calculated responses, including the local and average solids volume fraction at several sampling ports, the radial non-uniformity index and the pressure differentials associated with the riser. To discuss the influence of the varying design and operating conditions on each response, extensive experimental work was required. Therefore, the required time and resources were minimised by making use of a 2^3 full factorial as well as a central composite design approach. This enabled the construction of linear and quadratic regression models which supplemented the discussion regarding the hydrodynamics inside the riser.

The inlet air velocity, solids feed rate and riser height settings were the three varying factors and among these, the solids feed rate exhibited the weakest correlation with the responses mentioned before. The experimental results indicated that preferential particle flow occurred near the riser wall on the opposite side of the air inlet. This non-uniformity could be reduced by increasing the inlet air velocity, decreasing the solids feed rate or decreasing the riser height.

Throughout literature, prominent exit effects were reported on risers with T-shaped outlets. In this study, however, it was found that such an effect was only present inside the medium and tall risers if the gas velocity was smaller than 6.5 m/s. Above 6.5 m/s, an exit effect was only present in the medium sized riser. In addition, the pressure differential across the cylindrical riser sections with respect to the overall pressure differential could be reduced by increasing the inlet air velocity. It was further found that the exit assembly at the top of the medium height riser provided the least resistance to flow given that the particles had to travel a shorter distance to the downstream cyclone.

Apart from the experimental work, two-phase CFD models were created to supplement the discussions regarding the riser hydrodynamics. The riser geometries were constructed in Siemens NX-12™ and the simulations were performed in STAR-CCM+™. An Eulerian-Lagrangian approach with two-way coupling was selected based on the fluidisation regime inside the riser. In addition, the homogeneous Schiller-Neumann drag model was employed and the D[4,3] of the sorbent was chosen as the average particle size. The models successfully described the trends that were observed in the experimental work, despite the inability thereof to capture exact values. In addition, the CFD data revealed flow swirling at the top of the riser and confirmed that lower riser aspect ratios (or height-to-diameter – H/D) ratios were associated with more uniform particle distributions. The latter finding contradicts literature and should be explored in future work. It was found that several experimental observations regarding the riser hydrodynamics could be explained with the assistance of the CFD models which was the desired outcome for this study.

Key terms:

Hydrodynamics, H/D ratio, CFD, FGD, CFB

ACKNOWLEDGEMENTS

I would like to acknowledge my primary supervisor Mr. Frikkie van der Merwe for the vast amount of time, energy and patience that he dedicated to this work. I also wish to express my appreciation to my co-supervisor Dr. Frikkie Conradie, for his meticulous guidance and experienced advice along the journey. Their contributions to every aspect of this study were invaluable. I further wish to acknowledge Mr Louis Le Grange, who enthusiastically assisted me with any CFD related obstacles. Due to his expertise, the modelling endeavours were less overwhelming. This study would also not have been possible without the funding received from OMV and EPPEI. Their financial assistance was deeply appreciated.

I had the pleasure of working with final year students Zander Maritz, Keagan Velde and Khotso Moletsane who always showed up with a positive attitude during my experimental work. A special thanks to my peers who selflessly assisted me and also to the workshop staff, who helped to overcome many technical obstacles. I further wish to extend my deepest gratitude to my friends, my dad and my stepmom for believing in me and making this experience meaningful. In this regard, I would like to recognise the support from Mr. Marcus Keulder and Marco De Sousa during an especially challenging stretch of this study. And lastly, I would like to express my deepest gratitude towards Mr. Winroe Meyer for his continuous encouragement during the writing of this dissertation.

I hereby also give praise to the Father, Son and Holy Spirit who has shown me endless mercy and has blessed me with this opportunity.

TABLE OF CONTENTS

LIST OF FIGURES

LIST OF TABLES

NOMENCLATURE

LIST OF ABBREVIATIONS

CAD	Computer aided design
CCD	Central composite design
CFB	Circulating fluidised bed
CFB-FGD	Circulating fluidised bed flue gas desulphurisation
CFD	Computational fluid dynamics
CFL	Courant–Friedrichs–Lewy
CSTR	Continuously stirred tank reactor
DEM	Discrete element method
DOE	Design of experiments
D[4,3]	Volume moment mean diameter (De Brouckere mean)
D[3,2]	Surface volume mean diameter (Sauter mean)
E-E	Eulerian-Eulerian
E-L	Eulerian-Lagrangian
EMMS	Energy minimization multi-scale
ESP	Electrostatic precipitator
FCC	Face centred
FDM	Finite difference method
FEM	Finite element method
FGD	Flue gas desulphurization
FVM	Finite volume method
ICFB	Internally circulating fluidized bed
KTGF	Kinetic theory of granular flow
LES	Large eddy simulation
LOI	Loss of ignition
MSE	Mean square error
O-S	Syamlal & O'Brien
PDE	Partial differential equation
PEPT	Positron emission particle tracking
PSD	Particle size distribution
P&ID	Process and instrumentation diagram
RANS	Reynolds Averaged Navier-Stokes

RKE	Realizable k-ε
RMS	Root mean square
RR	Recirculation ratio
RTD	Resistance temperature detector
R^2	Coefficient of determination
SGS-TKE	Sub grid scale turbulent kinetic energy
SIMPLE	Semi-implicit method for pressure linked equations
SKE	Standard k-ε
SS	Sum of squares
SSE	Sum of squares of the error
SST	Total sum of squares
t-Statistic	Test statistic
URANS	Unsteady Reynolds Averaged Navier Stokes
XRF	X-ray fluorescent

LIST OF COMPOUNDS

Formula	Name	Common name
Ca	Calcium	-
$CaCO_3$	Calcium Carbonate	Limestone
CaO	Calcium oxide	Quicklime
$Ca(OH)_2$	Calcium Hydroxide	Hydrated lime
$CaSO_3$	Calcium Sulphite	-
$CaSO_4$	Calcium Sulphate	-
$CaSO_4 \cdot 2H_2O$	Calcium Sulphate dihydrate	Gypsum
$CaSO_4 \cdot ½H_2O$	Calcium Sulphate hemihydrate	Plaster of Paris
$CaSO_3 \cdot ½H_2O$	Calcium Sulphite hemihydrate	-
H_2O	Dihydrogen monoxide	Water
O_2	Oxygen	-
S	Sulphur	-
SO_2	Sulphur dioxide	-
ZnO	Zinc oxide	-

LIST OF CONSTANTS

Constant	Value	Unit	Definition
c	394	m/s	Speed of sound in air (120°C)
g	9.81	m/s^2	Gravitational constant
π	3.14	-	-

LIST OF SYMBOLS

Roman letters		Greek letters	
A	Area (m^2)	β	Momentum exchange coefficient (Ns/m^4)
A_{cell}	Area of a cell face (m^2)	β	Regression coefficient
Ar	Archimedes number	γ	Material density ratio
C	Radial region in the riser	ε_d	Turbulent dissipation rate (m^2/s^3)
CI	Confidence interval	ε_f	Void fraction
C_D	Drag coefficient	ε_s	Local solid volume fraction
Co	Courant number	$\bar{\varepsilon}_s$	Apparent/average solid volume fraction
C_μ	Turbulent eddy viscosity constant	ϵ	Particulate loading parameter
D_r	Riser inner diameter (m)	κ	Turbulent kinetic energy (J)
D	Hydraulic riser diameter (m)	μ	Dynamic viscosity ($N{\cdot}s/m^2$)
d_d	Mean particle diameter: dispersed phase (m)	μ_t	Turbulent eddy viscosity (m^2/s)
d_i	Particle size i (μm)	ν	Kinematic viscosity (m^2/s)
d_p	Particle diameter (m)	ρ	Density (kg/m^3)
d_{32}	Sauter mean diameter (m)	ρ_{H_2O}	Water density (kg/m^3)
e	Wall roughness (m)	σ	Stress tensor (kg/ms^2)
$\bar{e}$	Mean kinetic energy (J)	$\hat{\sigma}$	Standard deviation
E	Energy per unit mass (m^2/s^2)	$\hat{\sigma}^2$	Mean square error
f_f	Friction factor	τ_{ij}	Reynolds stress (m^2/s^2)
F	Normalisation factor	ϕ	Sphericity

F_B	Body forces per unit volume (kg/m^{2}s^2)
F_D	Drag force (kg·m/s^2)
F_M	Momentum source term (kg·m/s)
F_P	Particle mass flow (kg/s)
Fr_D	Froude number
G	Mass flux (kg/m^{2}s)
G_s	External circulating flux (kg/m^{2}s)
H	Installed cylindrical riser sections
h	Riser height (m)
k	Number of factor levels
L_k	Characteristic length (m)
L^*	Dimensionless diameter ratio
M	Mach number
$\dot{m}$	Mass flow rate (kg/s)
$\dot{m}_{down}$	Mass flow rate of downward flowing solids (kg/s)
n	Number of observations
$\dot{n}$	Molar flow rate (mole/s)
p	Number of regression coefficients (excl. constant)
P	Pressure (Pa)
ΔP_{riser}	Pressure drop across the riser (Pa)
$\Delta P_{sections}$	Pressure drop across the installed cylindrical sections (Pa)
q	Heat flux (kg/s^3)
Q	Volumetric flow rate (m^3/s)
$r\ or\ R$	Residual
R^2	Coefficient of determination
Re	Reynolds number
S	Strain rate (s^{-1})
S_E	Energy source per unit volume (kg/ms^3)
S_ε	Source term in ε equation (kg/ms^4)
S_{ij}	Strain rate tensor (s^{-1})

SS	Sum of squares
St	Stokes number
t_0	Test statistic
$t_{\alpha/2,n-1}$	Upper $100\left(\frac{\alpha}{2}\right)$ percentage point in t-distribution
t_{CFD}	Time step (s)
t_p	Particle relaxation time (s)
$Test_{ff}$	The influence of roughness on the friction factor
U	Velocity (m/s)
U_{cell}	Velocity across a cell face (m/s)
U_{ch}	Choking velocity (m/s)
U_k	Characteristic velocity (m/s)
U_{mf}	Minimum fluidisation velocity (m/s)
U_p	Particle velocity (m/s)
U_0	Superficial gas velocity (m/s)
U_t	Terminal velocity (m/s)
U_{TR}	Transport velocity (m/s)
V	Volume percentage in the size range (%)
V_{cell}	Cell volume (m^3)
X	Design matrix in coded units
y	Measured response
$\hat{y}$	Predicted response
y_i	Measured response in row i
$\bar{y}$	Mean of measured response
z	liquid head (m)

CHAPTER 1 – INTRODUCTION

1.1 BACKGROUND

Sangeetha and Sivakumar (2019) performed a temporal and spatial sulphur dioxide (SO_2) analysis throughout South-Africa making use of data collected between 2004 and 2013[1]. The so-called SO_2 hotspot in South-Africa, illustrated in Figure 1.1, is attributed to the proximity of coal-fired power plants in Gauteng and Mpumalanga[1]. The sulphur-bearing impurities in the coal that is used to generate electricity forms SO_2 during the combustion process which is released into the environment if not removed. Apart from the emission source, meteorological conditions (such as relative humidity and wind speed) also affect the distribution of SO_2 throughout the atmosphere[1].

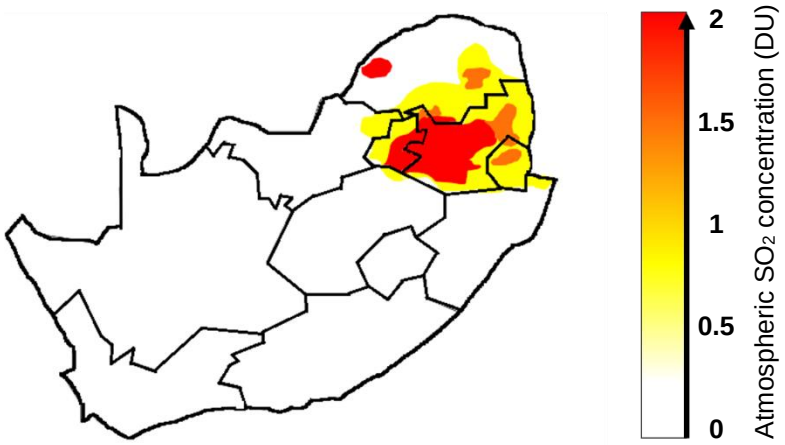

***Figure 1.1**: SO_2 variation throughout the planetary boundary layer height over South Africa in autumn (Adapted from Sangeetha & Sivakumar, 2019)[1]*

SO_2 reacts with atmospheric water to produce sulphurous acid (H_2SO_3), which in turn leads to a phenomenon called acid rain. Acid rain is harmful to forests, agriculture, lakes, sensitive aquatic ecosystems, buildings and monuments[2,3]. The impact of SO_2 on human health has also been widely investigated. The two most common diseases related to chronic ambient SO_2 exposure are cardiovascular and respiratory diseases[3,4,5]. The casual relationship of SO_2 to cerebrovascular and chronic obstructive pulmonary diseases is also mentioned in research[6]. Furthermore, elevated exposure to SO_2 is known to increase the occurrence of asthma and bronchitis, and aggravates existing respiratory problems in asthmatic patients [7,8].

Apart from the respiratory and cardiovascular problems, no definitive evidence exists to suggest that sulphur dioxide plays a role in the formation of lung cancer [5,9]. It is however known that SO_2 prevents the production of a pro-inflammatory cytocine in human lung cells[9,10] and when combined with arsenic it promotes cell migration which may be relevant for future liver cancer research[10]. To avoid causing harm to humans and to mitigate damage to the environment, global and national environmental legislation has become stricter regarding the maximum allowable SO_2 emissions from power plants. According to South-African environmental legislation the maximum permissible emission of SO_2 from electricity generating activities, was planned to decrease from 3500 mg/Nm^3 to 500 mg/Nm^3 in 2020 but instead reduced to 1000 mg/Nm^3 according to recent legislation[11,12]. Since power plants were initially designed with minimum consideration for SO_2 emissions, most of the existing power generating facilities are struggling to comply with the strict legislation[13]. Short-term solutions such as changing fuel sources (to cleaner fuels), pre-treating raw materials or blending fuel sources have been implemented, however, the current solutions do not prove sufficient to reach the new SO_2 targets [1,13]. For this reason, flue gas desulphurisation (FGD) processes are being implemented to achieve the legislative emission requirements[1].

During FGD processes an absorbent with a high specific area (usually hydrated lime or limestone) is brought into contact with flue gas to reduce the amount of SO_2 before it is released[14,13,15]. A FGD process can be classified as wet, dry or semi-dry and the calcium based wet-FGD technology is the most popular of the three[3,16]. During a wet-FGD process, an aqueous solution containing the absorbent is mixed with the flue gas and up to 98% of the SO_2 is removed[17]. Wet-FGD processes exhibit a high reagent utilisation efficiency and more stable operating conditions when compared to dry and semi-dry processes[16,18]. The impressive removal efficiency and sorbent utilisation is however achieved at the cost of large volumes of fresh water and a lot of waste is produced. Additional drawbacks of wet-FGD processes include the large equipment footprint, equipment corrosion, high energy consumption and high installation cost[16,19,20].

Alternatively, a dry FGD process entails the introduction of a dry solid sorbent. This eliminates the need for large quantities of water as is required for wet processes, and the dry waste originating from dry FGD processes is more easily disposed of due to the absence of water[17]. Unfortunately, dry processes exhibit low sulphur removal efficiencies and less effectively utilises the desulphurisation reagent[16]. Due to the low sorbent utilisation, dry processes typically require 3-4 times the theoretical amount of sorbent to remove significant amounts of SO_2, which limits its applications[15]. In order to combine the advantages of both wet and dry FGD technologies, semi-dry processes have been developed.

Such processes require less water and produce less pollution than wet-processes, while having faster reaction rates and higher sulphur removal efficiencies than dry-processes. In order for FGD technology to qualify as a semi-dry process, the dry alkaline sorbent will either be humidified, or will come into contact with water at some point in the FGD system[17]. A popular semi-dry FGD method is termed a spray drying process which requires a large amount of space and particle residence times of around 15s. The second, simpler alternative, is the circulating fluidised bed (CFB) process which is trademarked by a moderate SO_2 removal efficiency of approximately 50% which can be increased to over 97% if operated optimally[3,16,21,22,23]. Low sorbent utilisation, deposit formation and the choking/particle settling within the CFB equipment can be expected, if the most suitable operating parameters are not identified[16,21]. This can be done by studying the hydrodynamics and flow patterns of the powdered sorbent particles within the CFB.

Hydrodynamics refers to the study of the forces acting on solid particles submerged in a fluid and the relative motion between the solids and fluids. These forces include, but are not limited to, frictional, drag, pressure and viscous forces. The macroscopic flow behaviour inside CFB risers is governed by these forces and is generally quantified through measurable parameters. Such parameters include the (i) solids hold-up, (ii) gas and solids mixing and (iii) velocity profiles[24]. Changes in the forces acting on the particles, and hence the macroscopic flow behaviour, can be brought about by varying the operating conditions, particle characteristics or the riser geometry. Throughout literature, computational fluid dynamics (CFD) software is often used to find the most optimal operating conditions through investigation of the following variables[16,18,20,25,26]:

- The sorbent recirculation rate,
- reagent feed rate,
- water feed rate and injection point,
- flue gas flowrate,
- feed temperatures and
- Lime adsorbent to sulphur (Ca/S) molar ratio (which in most literature studies are set to a value between 1.2 - 2)[21,23].

CFD software numerically solves equations that govern the flow of fluids, solids or a mixture of phases throughout a domain[27]. When the model has converged/is converging, a graphical illustration of the solution is provided by such software, further enhancing the user's understanding of the hydrodynamics within the geometry.

Since a variety of configurations can be simulated using CFD modelling, it has become a time saving and cost-effective design and optimisation tool that eliminates the need to build numerous prototypes. Furthermore, a CFD model reveals the transport and thermodynamic behaviour of fluids and particles within regions that may be experimentally inaccessible[28]. Therefore, CFD models are effective tools for troubleshooting and design purposes and can determine the best recirculation rates and local and global particle residence times[29,30]. Furthermore, information about the hydrodynamics of the sorbent allows for the proper upscaling of CFB reactors[31].

1.2 Problem Statement, Aim and Objectives

1.2.1 Problem statement

Despite large amounts of available research in the use of circulating fluidised beds for semi-dry flue gas desulphurisation, little is known and understood about the interaction between the gas and solid particles as well as the influence of the aspect (height to diameter) ratio of the riser on the hydrodynamics therein.

1.2.2 Aim

The aim of this study is to describe the hydrodynamics of hydrated lime in the CFB riser using an experimental and a two-phase CFD model approach.

1.2.3 Objectives

- To experimentally quantify the influence of the riser aspect ratio, gas velocity and solids feed rate on the hydrodynamics inside the CFB riser.
- To numerically quantify the influence of the riser aspect ratio, gas velocity and solids feed rate on the hydrodynamics inside the CFB riser.

1.3 Dissertation outline

Chapter 1 - Introduction:

In this chapter, the value of FGD technology is highlighted by discussing the current national atmospheric SO_2 emission status. Furthermore, the available categories of FGD technologies are briefly covered to support the reasoning behind semi-dry FGD research. Next, the definition of a hydrodynamic study and the benefits of CFD modelling for such an investigation is provided. The chapter is finalised with the problem statement, aim and objectives to be addressed in this work.

Chapter 2 - Literature review:

This chapter starts with a description of a general CFB-FGD process. Thereafter, the hydrodynamics inside CFB's are discussed, including the type of fluidisation required for FGD-CFB applications. Furthermore, scaling laws are supplied with which the operating conditions of laboratory, pilot and industrial scale systems may be compared. Afterwards, literature findings regarding determining and analysing the solids holdup in CFB risers are summarised. Finally, the influence of design and operating parameters on hydrodynamics is discussed in terms of the information from the previous subsections. A summary of literature findings on the use of CFD modelling for small and large-scale CFB applications is also included. In addition, the work that was done on the CFD modelling of FGD CFB's is discussed.

Chapter 3 - Experimental method:

Details of the experimental setup, its operation and the sorbent characterisation are provided in the chapter. The procedure that was followed for the statistical design of the experiments is discussed and the resulting experimental program is provided. Furthermore, the iso-kinetic sampling system together with the other measurement equipment and techniques are described.

Chapter 4 – CFD model construction:

In this chapter, the CFD modelling procedure is explained. The model development includes a description of the Eulerian-Lagrangian fluid mechanics, discretisation, solution algorithm and residuals. The reasoning behind each selection during the construction of the simulation is included within this discussion. Next the construction of the various geometries in NX-12^{TM} as well as the pre- and post-processing in the STAR-CCM+^{TM} simulation software is described. The simulation conditions are then outlined and critically evaluated. This chapter is concluded with the construction of the mesh together with the grid and time-step independence analysis.

Chapter 5 - Results and discussion:

In this chapter, the objectives of this study are revisited when results obtained to substantiate the objectives are being discussed. The hydrodynamics are discussed from an experimental point of

view in the first subsection by considering the influence of the varying factors on the solids holdup and pressure differentials. The second subsection supplements the experimental findings from a CFD-modelling perspective, and additional information that could not be gathered experimentally is considered. The third subsection contains the results from the regression analysis, which further highlights the correlation strength between the varying factors and specific hydrodynamic indicators. The final subsection addresses the differences and similarities between the CFD and experimental results.

Chapter 6 - Conclusions and recommendations

The conclusions regarding the effect of operating and design parameters on the hydrodynamics inside the CFB riser are provided in this chapter. This chapter highlights the overall agreement of the findings to the literature, and the shortcomings of the CFD models and experimental procedures are listed. From the conclusions, recommendations for future work are provided.

CHAPTER 2 - LITERATURE REVIEW

2.1 CIRCULATING FLUIDISED BEDS AND FLUE GAS DESULPHURISATION TECHNOLOGY

Circulating fluidised beds (CFB's) are also referred to as fast fluidised beds, riser reactors or pneumatic transport reactors[24]. The first CFB reactors were developed in the 1940's and replaced the use of fixed beds in hydrocarbon cracking processes[24,32,33,34]. These systems were termed fluid catalytic cracking (FCC) units and underwent further improvement throughout the years. However, the use of a riser in conjunction with CFB technology and the study of its hydrodynamics first started in the 1960's and by the 1970's CFB systems were installed in Germany for the removal of acidic gasses[23,32,33]. CFB technology has proven to be well suited for flue gas desulphurisation (FGD) processes which have high selectivity requirements, fast reaction rates and solids as primary reactants[24]. CFB's further provide excellent contact between the multiple phases being processed and easily tolerate SO_2 fluctuations, which resulted in the use thereof for FGD since the 1980's[22,23,35].

Many different sorbents are available for FGD-CFB processes. Sodium-based sorbents are used in wet FGD applications. For semi-dry FGD processes, commonly selected sorbents include fly ash, activated carbon, coal char and zeolites[3,363,37]. A novel sodium-zinc-based sorbent for semi-dry FGD was proposed by Zhang *et al.* (2015) since the reaction product could be regenerated to provide useful ZnO and relatively pure SO_2[38]. They went on to explain that calcium based FGD products often oxidise to produce gypsum ($CaSO_4$), which is usually discarded as waste. Koralegadra *et al.,* (2019) supported this claim by stating that 43% of FGD gypsum ends up in landfills[13]. However, they also noted that the remainder had been successfully repurposed for applications such as drywalling, asphalt production and agriculture[13].

Despite the gypsum by-product, hydrated lime ($Ca(OH)_2$) remains the most popular sorbent used for CFB-FGD processes, although limestone and pre-treated lime are also commonly used[5,18,23,25,29,30,39]. Unslaked lime requires hydration, during which the solids are submerged in an excess amount of water for multiple hours, after which it is dried at temperatures that will not reverse the process (< 580°C)[40]. The sorbents used for medium to large-scale FGD processes contain between 30% - 90% $Ca(OH)_2$[18,41] or 20% - 60% calcium oxide (CaO) depending on the application[18,26,42]. During a semi-dry FGD process, the hydrated lime is injected into a stream of preheated air and flue gas upon entering the riser reactor[21]. Downstream of the CFB reactor, a fabric filter and/or an electrostatic precipitator (ESP) is often installed to collect the solid products that are formed by the neutralisation reaction inside the riser[21,23,25].

This installation increases the time available for the flue gas to react with the sorbent; up to 5% of the removal has been found to take place inside an ESP[15,23]. In the absence of oxygen, $CaSO_3$ is produced according to the primary overall reaction provided in Reaction 2-1[18]. However, even with a limited oxygen supply, a small quantity of the more desirable and valuable hemihydrate of calcium sulphate (plaster of Paris) can be produced according to the overall reaction provided by Reaction 2-2[43,21].

$$Ca(OH)_{2\,(s)} + SO_{2\,(g)} \rightarrow CaSO_3 \cdot \frac{1}{2}H_2O_{(s)} + \frac{1}{2}H_2O_{(g)} \qquad \textbf{2-1}$$

$$Ca(OH)_{2\,(s)} + SO_{2\,(g)} + \frac{1}{2}O_{2\,(g)} \rightarrow CaSO_4 \cdot \frac{1}{2}H_2O_{(s)} + \frac{1}{2}H_2O_{(g)} \qquad \textbf{2-2}$$

The underlying mechanisms behind the reactions presented by Reactions 2-1 & 2-2 include (i) the diffusion of SO_2 in water, (ii) the consequent dissolution of SO_2 to form H_2SO_3, (iii) the decomposition of H_2SO_3 to hydrogen and sulphite ions, (iv) the dissolution of hydrated lime to calcium and hydroxide ions and (v) the reaction between calcium and sulphite ions. In wet and semi-dry processes, absorption is the dominant mechanism for a successful reaction, while adsorption is the determining factor during dry processes[15]. Water is a crucial component during wet and semi-dry processes since diffusion and dissolution, as discussed previously, cannot occur without it. Humidification inside an FGD unit is achieved by spraying water into the CFB, and in some cases, the relative humidity exponentially increases the removal efficiency[21,25,39,44].

In industrial semi-dry FGD-CFB processes, up to 98% of the solid sorbent material is returned to the riser, and the recirculation rate is controlled using either mechanical or non-mechanical valves[21,23]. At low process temperatures (<650°C), a mechanical valve is preferred since it controls the recirculation rate more efficiently when compared to a non-mechanical valve[24]. However, non-mechanical valves are affordable, simpler and more suitable for high-temperature processes. An example is a standpipe that accumulates a solids inventory from the cyclone and controls the solids feed rate to the riser using aeration[24]. The recycling of sorbent through the system leads to a higher sorbent utilisation when compared to dry processes, further supporting its use in the industry[21,23].

2.2 THE HYDRODYNAMICS OF A CIRCULATING FLUIDISED BED RISER

2.2.1 Fluidisation in circulating fluidised beds

According to Geldart (1973), a particle can be classified into one of four categories based on its physical properties[45]. The four categories are indicated in Figure 2.1, and the majority of the FGD sorbents reported in the literature are either group A or C particles[15,25,26,23,46,47]. Since Geldart's publication, much work has been done to elaborate on which particles belong to groups A – D based on different observations at elevated temperatures and pressures[48]. It was found that particles that fall into one category may still exhibit characteristics belonging to another, depending on the vast amount of variables that play a role during fluidisation[48]. It is especially difficult to discern between group A's and group C's behaviour at the boundary of transition conditions between the two groups[48]. Nonetheless, the Geldart classification gives an initial indication of the conditions required for particles to transition from one fluidisation regime to another in a fluidised bed. Apart from its Geldart classification, the type of fluidisation a particle will undergo depends largely on the solids flux and superficial gas velocity[49].

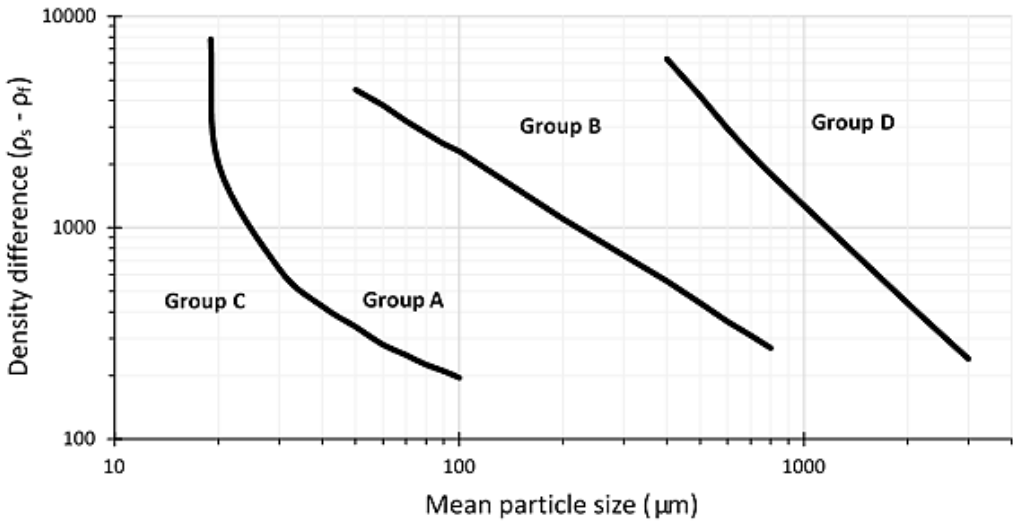

***Figure 2.1**: Geldart's powder classification diagram with air as carrier phase at atmospheric conditions (Adapted from* Geldart, 1973)[45]

Six general fluidisation regimes include the fixed bed, bubbling, slugging, turbulent, fast fluidisation and pneumatic transport regimes, as illustrated by Figure 2.2. However, Zhang *et al.,* (2015) identified four operating regimes that are specifically used for CFB's[49].

These included dilute and dense riser upwards flow, core annular flow and a turbulent fluidised bottom bed with a core annulus particle distribution[49]. From these four regimes, the dilute riser upwards flow should be regarded as pneumatic transport in Figure *2.2*, while the three remaining regimes represent different stages of the fast fluidisation regime.

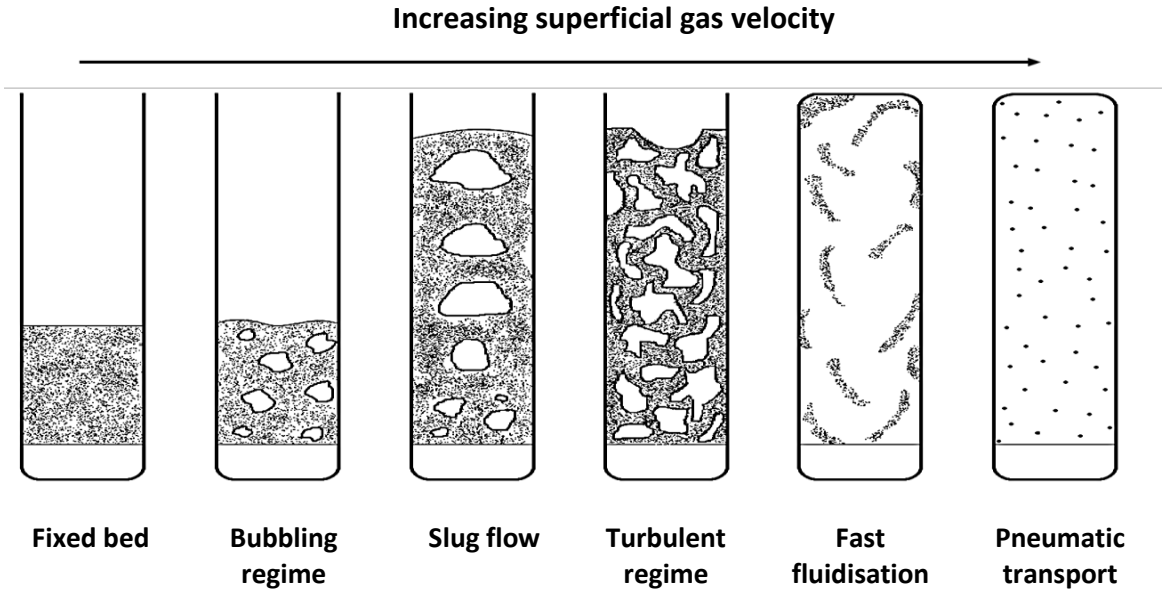

Figure 2.2: *Flow regimes for upward gas flow through solid material with the use of a gas distributor (Adapted from Grace, 1986)*[48]

The minimum fluidisation, slip, choking and transport velocities of a given particle-riser system form a framework within which fluidisation may be described. The minimum fluidisation velocity (U_{mf}) can be determined experimentally by incrementally increasing the superficial gas velocity through a particle bed until the maximum value of the bed pressure drop is obtained. The maximum pressure drop indicates that the minimum fluidisation velocity has been reached[50]. Furthermore, the minimum fluidisation velocity depends on the particle size, particle size distribution (PSD), density and sphericity of the sorbent particles[51]. In a mixture containing two different sizes of the same particle, the average U_{mf} of each of the two-particle groups is used[51]. Thus, the minimum fluidisation velocity decreases as the fraction of small particles in the mixture increases[51]. This illustrates how the choice of sorbent size affects not only the reaction rate but also the fluidisation regime inside a riser reactor. Apart from the minimum fluidisation velocity, the slip velocity is also of importance during CFB operation and is defined as the difference between the interstitial gas and particle velocities.

Most CFB's are operated at high slip velocities, which exceed the single particle terminal velocities[24,49]. A CFB riser reactor is always operated well above the minimum fluidisation velocity, with the slowest fluidisation regime being dense riser up-flow (in the lower bounds of the fast fluidisation regime in Figure 2.2). During dense riser up-flow, a decrease in gas velocity or an increase in the solids flux (G_s) will lead to an increase in axial pressure losses experienced inside the riser. This results in type C choking, which is characterised by severe slugging, instable flow and large pressure fluctuations[52,49]. Choking occurs when the saturation carrying capacity of the gas has been exceeded. The saturation carrying capacity is defined as the maximum solids circulation rate that can be maintained at a specific velocity. The specific velocity below which stable riser operation cannot be maintained is termed the choking velocity (U_{ch}), and it increases as the solid feed rate to the riser is increased[49,53]. Nonetheless, FGD-CFB's throughout literature are operated well within the fast fluidisation regime rather than at its lower boundary, resulting in solids flowing out through the top of the riser and a continuous sorbent feed at the bottom[54]. Furthermore, the solids are in a dispersed phase, while the gas is in a continuous phase[24]. The onset of the fast fluidisation regime occurs at velocities much higher than the particle terminal velocities for Geldart A particles, and literature further suggests that the fast fluidisation regime is subject to one or a combination of the following criteria[24,49,54,55,56,57]:

- The CFB is operated at velocities (U) exceeding the transport velocity (U_{TR}). Commercial CFB's are commonly operated at $U - U_{TR}$ of between 0.5 – 5 m/s.
- The axial particle concentration profile exhibits a bottom dense, middle transition and top dilute phase (S-shaped profile). This phenomenon may be accompanied by solid refluxing at the riser walls.
- The presence of the S-shaped density profile commonly reported in hydrodynamic studies of CFB risers depends on the solids circulation rate being in excess of the saturation carrying capacity and the design of the recycle loop.

The transport velocity (U_{TR}) mentioned previously, lies beyond the choking velocity (U_{ch}) such that $U_{mf} < U_{ch} < U_{TR,}$ and it should be regarded as a lower operating limit for CFB risers. In order to calculate the transport velocity of a given fluid-particle system, the Archimedes number provided in Equation 2-1 should be determined[58,59]. Once the Archimedes number has been calculated, the particle Reynolds number, given in Equation 2-2, may be used together with a suitable empirical correlation to calculate the transport velocity[60]. These correlations have been found to be 90% accurate[49]. Kim *et al.,* (2018) summarised the most popular empirical correlations that are available throughout literature[61].

However, only the correlations that are applicable at low (<10) Archimedes numbers have been provided in Table 2-1 accordance with the result.

$$Ar = \frac{\boldsymbol{g} {d_p}^3 \rho_f (\rho_p - \rho_f)}{{\mu_f}^2} \quad \textbf{2-1}$$

$$Re_d = \frac{\boldsymbol{U_f} d_p \rho_f}{\mu_f} \quad \textbf{2-2}$$

In these expressions, g represents the gravitational acceleration, d_p the mean particle diameter and ρ_f, ρ_p, μ_f and U_f refer to the particle. Once the transport velocity has been determined, the operating gas velocity may be chosen in density, fluid density, fluid viscosity and fluid velocity, respectively.

Table 2-1: *Summary of correlations developed to determine the transport velocity in fluid-particle systems*

Authors	Correlation	Applicable range of Archimedes numbers
Bi and Grace[59]	$Re_{TR} = 1.53Ar^{0.5}$	$2.00 < Ar < (4.00 \times 10^6)$
Smolders and Bayens[62]	$Re_{TR} = 1.75Ar^{0.468}$	$1.00 < Ar < (2.00 \times 10^5)$
Khurram *et al.*[63]	$Re_{TR} = 0.458Ar^{0.482}\left(\frac{h}{D}\right)^{0.357}$	$0.81 < Ar < (1.21 \times 10^5)$ $8 < \left(\frac{h}{D}\right) < 112$

In Annexure A, the ratio between the operating superficial gas velocity and the transport velocity (U_0/U_{TR}) of industrial and pilot scale CFB-FGD units were calculated[25,26,46,64]. All three correlations from Table 2-1 were used, and the ratio varied between 2.5 – 3.1, depending on the application. This shows that most of the commercial CFB-FGD units operate at a superficial gas velocity that is at least double the calculated transport velocity.

2.2.2 Similarity parameters

Given the difficulty associated with basic measurements inside an industrial-scale CFB riser, the use of smaller-scale facilities is necessary for hydrodynamic studies. However, it is important that the results obtained through the analysis of laboratory or pilot-scale CFB risers can also be achieved on an industrial scale. To this end, van der Meer *et al.* (1999) listed eight parameters that govern the hydrodynamics in a CFB riser. These included the (i) superficial gas velocity, (ii) external solids circulation flux, (iii) mean particle diameter, (iv) particle density, (v) riser hydraulic diameter, (vi) gas density, (vii) gas viscosity and (viii) gravitational acceleration[65]. In turn, these parameters influence the riser pressure drop, solids hold-up, slip velocity, local solid volume fraction, and the local solids mass flux (and velocity)[65]. Van der Meer *et al.* (1999) further identified five dimensionless groups that describe these eight governing parameters, summarised by Equations 2-3 - 2-7[65]. By ensuring that these dimensionless groups for both small- and large-scale applications are equal, dynamic similarity will be achieved.

$$Fr_D = \frac{\boldsymbol{U_0}^2}{\boldsymbol{g}D} \quad \textbf{2-3}$$

$$\frac{\rho_p}{\rho_f} \quad \textbf{2-4}$$

$$\frac{d_p}{D} \quad \textbf{2-5}$$

$$Re_d \quad \textbf{2-6}$$

$$\frac{G_s}{\rho_p \boldsymbol{U_0}} \quad \textbf{2-7}$$

$$\frac{\boldsymbol{U_0}}{\boldsymbol{U_t}} \quad \textbf{2-8}$$

In most cases, it is impractical to ensure complete similarity between two units[37]. For this reason, scaling is performed with the use of three instead of five dimensionless groups. These are represented by Equations 2-3, 2-7 and 2-8. By applying these scaling laws, the fluidisation regime, solids holdup by volume fraction and the macroscopic moment of the solids remain reasonably similar between two CFB applications[65].

The validity of these three dimensionless groups have been verified at particle Reynolds numbers below 4, but acceptable results could also be obtained at particle Reynolds numbers between 5 – 15[66]. Van der Meer *et al.* (1999) further stated that dynamic similarity at particle Reynolds numbers exceeding 15 could not be maintained[65]. Hence, the use of the similarity parameters is restricted to low particle Reynolds numbers. By applying the similarity parameters to current industrial-scale CFB's, the operating conditions of a laboratory-scale experiment can be specified. This would ensure that the results are comparable to current applications and that the correct fluidisation regime is used. However, limited details regarding the operation of large-scale FGD-CFB units are reported throughout literature. The wide range of operating conditions that are associated with general CFB's is provided in Table 2-2. Furthermore, the operating parameters of CFB's that were specifically designed for FGD purposes have been listed in the third column of Table 2-2 for comparison. These were obtained from studies that were performed on two industrial-scale FGD units[47,64], the reaction between SO_2 and commercially available hydrated lime[39] and a pilot scale unit with an 18 m tall riser[23].

Zhou *et al.* (2011) tabulated several operating parameters of an industrial-scale FGD-CFB unit that was used for the desulphurisation of a municipal solid waste incinerator, which is provided in the fourth column of Table 2-2. They applied the three most important dimensionless groups to the data in column four in order to design an experimental plan. Hence, their results were comparable to other related literature findings. The final two columns of Table 2-2 contain operating conditions of circulating fluidised bed combustion (CFBC) and fluid catalytic cracking (FCC) processes, respectively. When comparing the data, it becomes apparent that the solids flux of an FGD process is significantly less than that of CFBC or FCC processes. This can be attributed to the rapid by-product formation and frequent catalyst regeneration that is required for those two processes[24,33].

Although the similarity parameters serve as a guide for up or down-scaling process units, care should be taken to eliminate the influence of external factors on the results. One such factor is electrostatic build-up which increases the pressure losses experienced along the riser – especially in cases where research was based on the use of plastic particles. Usually, this factor is eliminated by humidifying the carrier air to 40% – 60% or adding a powder additive[35,67]. Another factor is particle roughness; however, most industrial CFB's use rough particles and the slight differences in the particle friction coefficient does not influence the riser hydrodynamics[35].

***Table 2-2**: Design parameters for various types of large-scale CFB units*

Parameter	General CFB's [54,48]	CFB-FGD units [23,39,47,64,68]	Zhou *et al.*, (2011) [64]	CFBC Units [24,49,35,65]	FCC Units [24]
U_0	2 – 12	> 3	4.43	$5 - 9$	6 – 28
G_s	10 – 1000	$1 - 10$	1.60	$10 - 100$	400 – 1200
d_p (µm)	$50 - 500$	$10 - 125$	48	$100 - 300$	40 – 80
ρ_p	–	$2200 - 2600$	2250	$1800 - 2600$	1100 – 1700
D	0.5 – 9	$1 - 8$	4.30	1 – 3	0.7 – 1.5
ρ_f	–	–	0.78	–	–
μ_f	–	–	2.30×10^{-5}	–	–

**All parameters are in SI-units except for particle size.*

Chang and Louge (1992) have adapted the five known similarity parameters to account for non-spherical particles; their proposed parameters are provided in Annexure B[35]. They further stated that the hydrodynamics inside a CFB riser does not depend on the equipment placed before or after the reactor provided that the solids flux inside the riser is controlled. In conclusion, the operating conditions from industrial CFB's can be adapted for laboratory-scale units to design experiments that are suitable for an intended application. For this purpose, known operating conditions, such as those reported in Table 2-2, should be used. Although a good approximation of the operating conditions may be obtained through this process, the hydrodynamic behaviour inside the laboratory scale unit may still deviate from that of the industrial scale unit.

2.2.3 The solid volume fraction in FGD-CFB's

The reaction rate, conversion and selectivity of the chemical reactions occurring inside an FGD-CFB are dependent on the solid volume fraction inside the riser. This is attributed to the influence of the solid volume fraction on the contact efficiency between the various phases and the heat and mass transfer[24,31,32,69,70]. The solid volume fraction also influences the residence time which is normally between 3 – 6 seconds in a large-scale unit[21,23]. Furthermore, an increased residence time has been found to increase the desulphurisation efficiency in FGD-CFB's[20]. For this reason, one of the objectives of a hydrodynamic study of a CFB is to discuss the solids holdup. For CFB's operating at or above the fast fluidisation regime, this is achieved by discussing the solid volume fraction in both the radial and axial directions with respect to the centreline of the riser reactor.

2.2.3.1 Local and average solid volume fractions

In order to discuss the radial or axial solids distribution throughout a riser reactor, the local (ε_s) and average ($\bar{\varepsilon}_s$) solid volume fractions have to be measured or calculated. To this end, various intrusive (I) and non-intrusive (NI) measurement methods were summarised by Silva *et al.,* (2012) and Van Ommen *et al.,* (2007) and are summarised as follows[71,72]:

- Laser Doppler anemometry (NI)
- Tomography (NI)
- Radioactive particle tracking (NI)
- Particle image velocimetry (NI)
- Differential pressure measurement using pitot tubes (I)
- Fibre optic probes (I)
- Capacitance probes (I)

Non-intrusive techniques do not influence the flow behaviour in the riser and should be used whenever possible[71]. However, intrusive fibre optic and capacitance probes are often used together with accompanying software which reduces human errors and lowers the analysis effort[31,73,74]. Another intrusive measurement technique that was not included in the list is a sampling probe. Non-isokinetic and isokinetic probes have been used for solids sampling throughout literature and are more readily available than other equipment[71,72]. Non-isokinetic samplers have been able to determine the solid volume fraction with an accuracy of above 90% and require less auxiliary equipment when compared to iso-kinetic samplers[32,38,64]. Although the added auxiliary equipment of an isokinetic sampler is a drawback, its benefit lies in the lessened flow disturbance when compared to non-isokinetic sampling[75,76]. This can be ascribed to its working principle, which requires that the superficial gas velocity at the sampling point must be equal to the suction velocity of the probe. From solids sampling, the local solid volume fraction is determined using Equation 2-9.

$$\varepsilon_s = \frac{Q_p}{Q_{mix}} = \frac{\dot{m}_p/\rho_p}{U_{suction} \times A_{probe}} \qquad \textbf{2-9}$$

In the previous expression ε_s is the local solid volume fraction, Q_p and Q_{mix} are the volumetric flow rate of the particles and total mixture, respectively and $\dot{m}_p$ is the mass flow rate of the particles. The particle mass flow rate, $\dot{m}_p$, can be determined by dividing the mass of the material sampled at a point by the sample collection duration[77]. To determine the volumetric flow rate of the mixture, Q_{mix}, the suction velocity of the probe is used to represent the velocity of the particle-gas mixture. The particulars of iso-kinetic sampling are further discussed in Section 3.3.4.3. In addition to the various measurement methods, the local solid volume fraction is approximated using a suitable empirical correlation such as those summarised by Li *et al,* (2019)[31].

Such correlations make use of the radial position from the riser centre line (r), the riser radius (R) and an approximated average local volume fraction ($\bar{\varepsilon}_s$) as input variables[31]. Hence, an empirical correlation together with either an intrusive or a non-intrusive measurement technique is used to determine the local average solid volume fraction. Once the local solid volume fraction at various positions along the riser radius has been determined, an average solid volume fraction can be calculated using Equation 2-10[78].

$$\bar{\varepsilon}_s = \frac{2}{R^2}\int_0^R \varepsilon_s r\, dr \qquad \textbf{2-10}$$

In the above equation $\bar{\varepsilon}_s$ represents the average solid volume fraction, ε_s the local solid volume fraction, R the riser radius and r the measurement distance from the riser centre.Alternatively, various researchers determined the value of the average solid volume fraction without knowledge of the local solid volume fraction through Equation 2-11[51,57,64,79,80,81]. In this case, the only required measurement is the pressure difference between two points along the riser height. This is a popular method for studies that are focussed on the axial solids holdup in a system as opposed to the radial distribution of particles. Although this approach is convenient, it neglects the effect of wall friction and gas-particle interaction on the measured pressure differential[69,82]. This leads to estimation errors in the development region of the riser, where such effects are enhanced[69].

$$(1-\varepsilon) = \bar{\varepsilon}_s = \frac{\Delta P}{\rho_p \boldsymbol{g} \Delta h} \qquad \textbf{2-11}$$

In the previous equation, ΔP is the measured pressure difference, ρ_p the particle density, g the gravitational constant and Δh the distance between the two pressure measurement points.

Similar to local solid volume fractions, empirical correlations have also been developed to predict the average solid volume fraction. Such correlations rely on information regarding the riser diameter, particle properties and operating conditions as input variables and are summarised in Li *et al.,* (2019)[31]. To conclude, throughout literature the $\bar{\varepsilon}_s$ has been determined from various intrusive and non-intrusive techniques which include averaging local ε_s values using pressure measurements and applying researched and published correlations.

2.2.3.2 Radial solids holdup profiles in CFB's

Throughout the literature, the radial solids distribution at various riser heights has been studied by plotting the local solid volume fractions (ε_s) across the diameter of a riser. Each value is plotted against the distance of its sampling point from the centre of the riser (r) divided by the magnitude of the riser radius (R). By dividing the distance of the sampling point by the radius, a normalised distance is obtained with an r/R of 0 and 1, indicating the riser's centre and the risers' wall, respectively, as illustrated in Figure 2.3 a). The most frequently reported radial solids distribution is the core-annulus flow profile which is a typical characteristic of the fast fluidisation regime[30,31,32,54,64,69,78]. This type of flow occurs when the solids concentration is high at the walls of the riser and low at the centre, where the majority of the gas passes through the riser. The resulting radial solids distribution profile is flat at the centre and increased near the wall region, which is defined at an r/R of above 0.75-0.9. This results in a concave parabolic shape as illustrated in Figure 2.3 b)[33,69,78].

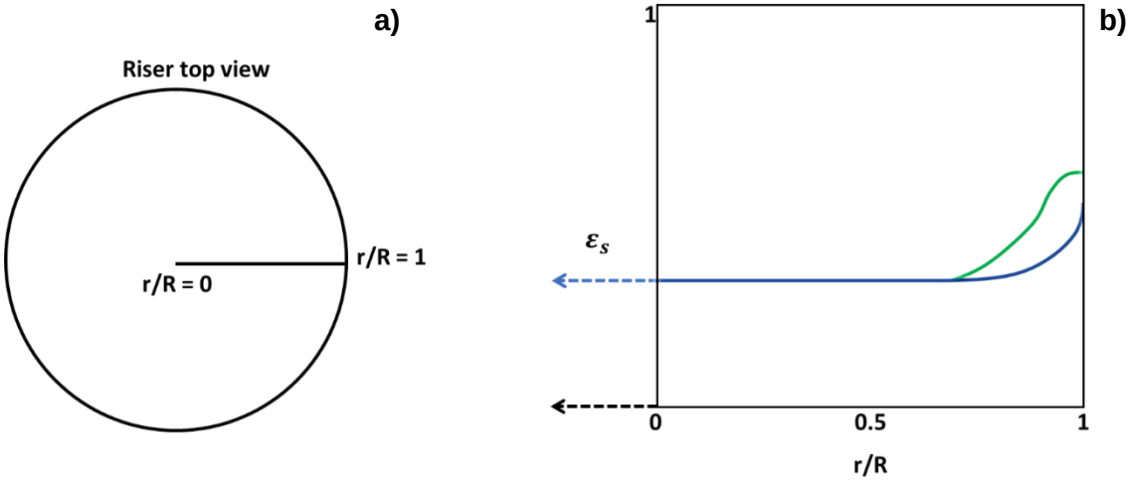

***Figure 2.3**: **a)** r/R normalisation and **b)** green and blue guides representing two different core-annulus solids distributions forming half of a parabolic curve (Adapted from Yan & Zhu (2004) and Wang et al., (2014))*[69,78]

During core annulus flow, downward flowing particles in the wall region are frequently reported, provided that the operating mass flux is sufficiently high[30,32,37]. Although such a non-uniform particle distribution increases the particle residence time, inhomogeneous flow in both the axial and radial direction has been found to decrease the desulphurisation efficiency in CFB riser reactors[20]. This is attributed to the weakened particle-flue gas interactions resulting from the high solids concentration near the wall of the riser, which prevents sufficient gas flow across the particles[26,46]. When the concave parabolic solids distribution curve is observed, it is usually predominant near the bottom of the riser, where the flow is not yet fully developed.

As the flow develops, the curve flattens along the height of the riser until the solids are more uniformly distributed over its cross-sectional area[31]. Consequently, the second most common radial solids distribution has a flat profile. To quantify the deviation of the particles from a flat radial profile, the radial non-uniformity index ($\mathrm{RNI}(\varepsilon_s)$) provided in Equation 2-12 is commonly used[20,83,84]. The $\mathrm{RNI}(\varepsilon_s)$ value ranges between zero and one, with a smaller value indicating a more uniform radial solids distribution or less of a parabolic shape.

$$RNI(\varepsilon_s) = \frac{\sigma(\varepsilon_s)}{\sqrt{\bar{\varepsilon}_s \times \left(\varepsilon_{s,max} - \bar{\varepsilon}_s\right)}} \qquad \textbf{2-12}$$

Here, $\sigma(\varepsilon_s)$, $\bar{\varepsilon}_s$ and $\varepsilon_{s,max}$ represent the standard deviation, average and maximum value of the local solid volume fraction measurements, respectively.

2.2.3.3 Axial solids holdup profiles in CFB's

To discuss the axial distribution of solids in a CFB riser, the average solid volume fraction ($\bar{\varepsilon}_s$) is plotted against the riser height[24]. A wide variety of axial solids density profiles within CFB risers have been reported in literature, and typical profiles include the S-shaped, exponentially decaying, C-shaped and linear profiles as Illustrated in Figure 2.4 a) – d)[31,69]. However, these profiles depend on the operating conditions, particle properties and the riser geometry and can exhibit novel profiles in some instances. An example of this can be found in a study by Wu et al., (2020) in which a W-shaped axial solids distribution was observed due to the chosen riser design[20].

Upon entry, particles are accelerated from an initial to a finite velocity and are said to create a development/acceleration region[67]. The flow in the riser becomes fully developed once the pressure drop becomes invariant with riser height, corresponding to a constant average solids holdup[24,79]. An S-shaped (or sigmoidal) profile, as illustrated in Figure 2.4 a), is common in systems operating under medium solids loadings (typically exceeding 100 kg/m^{2}s) and high gas velocities, as is the case in FCC-CFB applications[69]. As mentioned previously, one of the requirements to achieve this profile is a solids flux close to or in excess of the saturation carrying capacity, which can be seen in a study by Yan and Zhu (2004)[69]. A bottom dense phase trademarks this sigmoidal axial solids holdup profile, a top dilute phase and a distinct inflexion point between the two[24]. Therefore, the solids holdup remains reasonably constant at the bottom and decays throughout the freeboard region, which extends across the length of the acceleration region[24]. It was already mentioned in Section 2.2.1 that the S-shaped profile is often a measure of the onset of fast fluidisation[69].

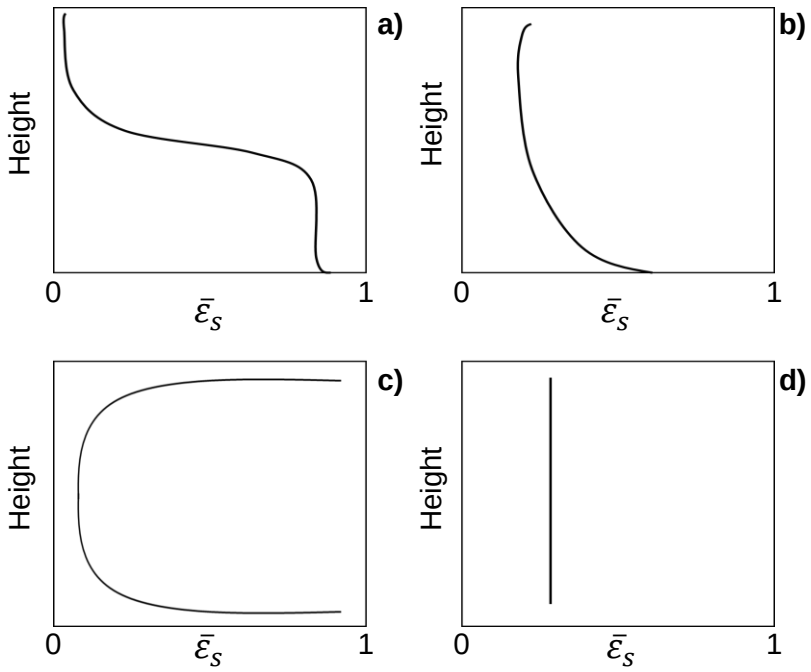

Figure 2.4: *Various axial suspension density profiles: a) S-shaped; b) exponentially decaying; c) C-shaped & d) Linear (Adapted from Berruti et al., (1995) and Monazam et al., (2016))*[24,79]

As for FGD-CFB studies or studies utilising similar particles and operating conditions, exponentially decaying profiles, as illustrated in Figure 2.4 b), are often reported. However, the solids load in the riser reactor has to be well below the saturation carrying capacity to avoid achieving an S-shaped profile[24,31,67,69,70].

The exponentially decaying axial profile is trademarked by a higher solids holdup at the bottom of the riser (i.e. the acceleration region) than at the top. Furthermore, a gradual transition from the bottom dense to the top dilute phase can be identified[24,31,49,64]. A C-shaped axial suspension density profile has been obtained for a range of particle densities and sizes in CFB risers that were operated at medium solids fluxes (6 - 280 kg/m^{2}s) and comparatively high superficial gas velocities (5 - 7 m/s)[67,79,85]. An abrupt T-shaped or strongly restricted riser exit geometry paired with operating conditions that were well below the saturation carrying capacity was present in all of the studies that reported the C-shaped axial profile, which is further discussed when addressing the riser geometry considerations in section 2.2.4.1[79]. Finally, linear axial profiles of the solids holdup are characteristic of dilute pneumatic transport, in which case all of the solids are evenly distributed throughout the riser reactor. This occurs when a sufficiently low amount of solids are injected into the gas phase, and the solids flux is only slightly increased[86].

2.2.3.4 Clustering

Clustering is the phenomenon by which particles temporarily group together during the operation of a CFB to form ellipsoidal shapes with a higher solids volume fraction when compared to their surroundings[81]. In a review article by Cahyadi *et al.,* (2017), the process of cluster formation is explained as follows[87]:

- Inelastic interparticle collisions create a local decrease in particle velocity and gas pressure (due to the dissipation of kinetic energy).
- The local decrease in pressure causes gas and particles to flow towards the region to form a cluster or a mesoscale structure, which is associated with a larger slip velocity than a single particle[24].
- The cluster has a higher density than a single particle, and collisions involving clusters decrease the local granular temperature (particle velocity fluctuations) even further. This leads to the additional growth of the cluster.
- Increasingly forceful interparticle collisions involving the clusters eventually lead to the deformation thereof into smaller clusters or a dispersed particle phase.

The ongoing formation and deformation of clusters influence the drag force, pressure drop, slip velocity, local voidage, mixing, heat and mass transfer within risers[87]. Clustering further leads to inhomogeneous solids distributions in the radial and axial directions of the riser and has been found to decrease the desulphurisation efficiency in FGD applications[26].

2.2.4 The influence of operating and design parameters on CFB hydrodynamics

2.2.4.1 CFB riser geometry

The assembly through which particles exit a riser reactor has a significant influence on the hydrodynamics. A T-shaped (or abrupt) exit structure is the most popular choice throughout literature, although L-shaped and C-shaped (or smooth) exit structures, illustrated in Figure 2.5, are also common[88,89]. Although smooth exit geometries provide the least resistance to the flow of solids, a large area of the bend undergoes erosion and corrosion[85].

Dwivedi *et al.,* (2021), however, stated that although a T-shaped outlet undergoes erosion across a smaller area it occurs at a much faster rate when compared to smooth exit geometries[90]. Hence, an exit geometry cannot solely be chosen based on its hydrodynamic influence. Regardless of the mentioned issue, T-shaped exits are widely used for CFB's and due to the abrupt change in geometry, a C-shaped axial solids holdup profile is often reported. The C-shaped profile is caused by the enhanced back mixing and internal recirculation that occurs when a portion of the particles collide with the walls above and around the exit. These collisions cause particles to travel downwards along the walls of the riser until they become suspended again[24,79,85]. Furthermore, inertia allows several particles to become dislodged from the gas phase to travel up into the cavity, illustrated in Figure 2.5 a). If the cavity is sufficiently high, such particles eventually lose momentum and fall back down into the riser. Consequently, the solids holdup at the top of the riser is increased, contributing to a phenomenon termed an exit effect[79,85,89]. Research has shown that more substantial exit effects are observed when installing outlets with larger cavity heights. However, after a certain point, the suspension density becomes independent from further changes to the cavity height and this limit is reached sooner during low solids flux operation[85,88].

The exit effect caused by T-shaped outlets has also been reported to improve the heat transfer at the top of the riser, which could improve the reaction rates [79,85,88]. However, the exit effect from a T-shaped outlet is not only influenced by the structure itself. Monazam *et al.,* (2016) observed that the operating conditions and the type of particle feeder could prevent particle accumulation at the top of the riser, despite the presence of a restricted exit geometry[79]. They also observed that the exit effect was more pronounced during increased solids mass flux operation[79].

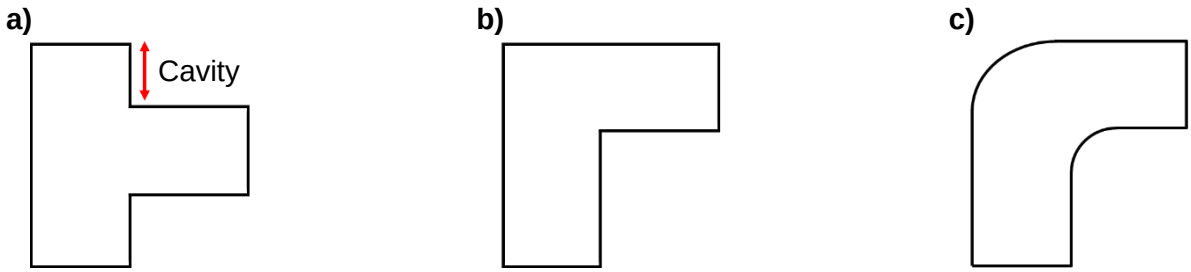

Figure 2.5: *Exit geometries for CFB risers that are frequently used throughout literature: a) T-shaped; b) L-shaped and c) C-shaped (Adapted from Zhang et al., (2013))*[88]

The combined influence of various factors on hydrodynamics was also considered in a study by Pugsley *et al.,* (1997). The authors investigated the exit effects in both a thin and a wide riser, each with the same height-to-diameter (H/D) ratio[89]. They reported that in both risers, the exit effects were limited to the top of the riser for Geldart A particles, whereas the increased solids holdup extended all the way to the base of the wider riser for Geldart B particles. Breault *et al.,* (2017) found that a higher gas velocity or a lower solids flux further increased the solids concentration at the top of the riser resulting from a T-shaped exit[85]. These authors illustrated that the effect of the exit structure on the hydrodynamics could be altered by the riser geometry, particle properties and operating conditions.

Throughout literature, H/D ratios between 3 – 28 have been used specifically for laboratory and pilot scale FGD-CFB research purposes[18,23,25,26,46,64,91]. In FGD applications, the height of a riser is chosen such that a sufficient volume of particles can be contained. The required volume of particles will vary based on the reactive surface area. Furthermore, the desired residence time of the sorbent depends on the sulphur removal efficiency that was intended for the process and this is also a design specification for the vessel[21,24,68]. Studies have shown that lowering the H/D ratio leads to one of two cases:

- Case 1: The overall average solids holdup ($\bar{\varepsilon}_s$) decreases.
- Case 2: The overall average solids holdup ($\bar{\varepsilon}_s$) increases.

Xu *et al.,* (2000) operated within or close to the bubbling fluidisation regime and reported that the first case could be applied to Geldart A particles while the second case applies to Geldart B particles[92].

Conversely, Yan *et al.,* (2004) operated in the fast fluidisation regime and reported that the second case held for both Geldart A and B particles[69]. They argued that the contrast between their study and that of Xu *et al.* (2000) was due to the difference in the fluidisation regimes[69]. Various other authors confirmed that Case 2 was applicable to both Geldart A and B particles when operating in the fast fluidisation regime, which applies to FGD-CFB's as discussed in Section 2.2.1[69,70,82].

Case 1 was explained by the lessened contribution of wall effects (such as friction) to the gas-particle flow in wide diameter risers, which allowed particles to travel through the riser with more ease[33,69,92]. However, Yan *et al.,* (2004) explained Case 2 by stating that the gas still experienced an increased flow resistance near the walls of the riser as opposed to the centre. This created a velocity gradient across the riser radius, and a wider riser could facilitate a greater gas velocity gradient. In turn, the greater gas velocity gradient leads to greater particle accumulation near the riser walls. This explained the higher overall solids concentration that was observed in larger-diameter risers[69].

A supplementary explanation for the second case was provided by Pugsley *et al.,* (1997), who stated that near-wall particle accumulation is limited in thinner risers since the area available for the gas to flow independently from the particles is less[89]. Thus, wider risers facilitate a thicker annulus (near wall particle accumulation). This explanation was also supported by the findings from Noymer *et al.,* (2000)[70]. Since the non-uniformity in the radial solids holdup profiles increase as the riser's diameter increases, the flow development within the fast fluidisation regime is slower[32,69]. This could explain why Chang and Louge (1992) found and increased tendency of choking in wider risers[35]. Despite the influence of the riser diameter on the radial and overall solids holdup, it has not been found to transform an S-shaped axial solids holdup profile to an exponential, linear or C-shaped profile or vice versa[69]. Furthermore, the choice of exit geometries and H/D ratios are not the only geometrical factors that influence the riser hydrodynamics.

In one study, particles were fed to a CFB with a loop seal instead of a valve which decelerated the flow development and enhanced the non-uniformity of the solids distribution throughout the unit[79]. The loop seal included a particle collection chamber below the cyclone in which fluidising air was used to reintroduce particles to the riser. Another study found that by introducing the gas through nozzles, the uniformity of the solids distribution at the bottom of the riser increased[24]. Furthermore, by adding both gas nozzles and a distributor plate, the saturation carrying capacity of the system could be increased, which allowed for higher solid flux operation[82].

On the other hand, the influence of structural changes to the riser, such as the addition of baffles, mechanical rakes, rings, dispersion plates or enlarged riser sections, has also received some attention. Such inserts not only improved the phase mixing, flow development and particle residence times but also increased the desulphurisation efficiency in FGD related studies[16,20,29,91,]. The improved FGD efficiency was thought to arise from the increased attrition between the particles themselves and the wall due to the inserts. As the layer of accumulated reaction product on the unreacted sorbent was removed via attrition, more active sites became available, and the sulphur removal efficiency was enhanced[20,29]. Unfortunately, internal structures also increase the drag force that the particle-laden flow experiences and less economical operating conditions are required for continued operation. Furthermore, more frequent equipment maintenance is to be expected due to the increased structural abrasion[20].

2.2.4.2 Superficial gas velocity and solids flux

Most hydrodynamic studies found that i) an increase in the superficial gas velocity (U_0) or ii) a decrease in the solids flux (G_s) inside the riser reduces the overall solids holdup as well as the particle residence times in CFB reactors[93]. These observations hold true for a wide variety of applications, including laboratory and pilot scale CFB systems that are operated at solid mass fluxes of between 1 – 200 kg/m^{2}s and with Geldart A or B particles[20,31,69,81,82,85]. As discussed in Section 2.2.3.2, a radial parabolic solids holdup profile in a CFB riser is produced by the increased particle accumulation at the walls of the riser (r/R > 0.75)[69,78]. Research indicates that the near-wall particles, rather than the particles at the riser's centre, respond the most to changes in the superficial gas velocity or the solids flux[31,69,78]. This means that while an increased superficial gas velocity or a decreased solids flux decreases the solids concentration near the walls, the behaviour of the solids in the centre will remain more or less constant. Wang *et al.,* (2014) found, on the other hand, that at high solids flux operation (G_s > 700 kg/m^{2}s) the particles in the middle region of the riser (0.5 < r/R < 0.75) as opposed to those at the wall were the most sensitive to changes in operating conditions[78]. In addition, the dilute region in the centre of the riser increased significantly as the velocity was increased or the solids flux was decreased. This is in contrast with low solids flux operation where the area of the dilute region remained unchanged.

At a constant solids flux, the radial uniformity of the particle distribution improves as the gas velocity is increased, which results in a lower $\mathrm{RNI}(\varepsilon_s)$ value at every riser height[31,78]. A decreased solids flux at a constant gas velocity has been shown to have the same effect[20,64].

This relationship can be illustrated using an operating diagram such as the one provided in Figure 2.6[32]. An increase in superficial gas velocity or a decrease in solids flux will result in a transition from a less uniform (parabolic) to a more uniform (flat) radial particle distribution. Furthermore, particle downflow near the riser walls has been found to increase as the $\mathrm{RNI}(\varepsilon_s)$ increases. This was illustrated by Van de Velden *et al.* (2007) using the diagram provided in Figure 2.7, in which the enhanced particle downflow at lower gas velocities is apparent[33]. In their study, they observed that the downward particle velocity was approximately equal to the single particle terminal velocity[33]. This agrees with the findings from Yang *et al.,* (2021) who reported high solids velocities in the centre of the riser but low solids velocities near the riser walls[93]. Although consistent with other work[32], the findings from Van de Velden *et al.* (2007) is in contrast with that of Zhou *et al.,* (2011) who reported that a higher gas velocity enhanced the downward flow of particles but only at the lower sections of the riser[64]. This could be attributed to the venturi that was used in their reactor which induced a large velocity at the bottom of the riser that forced solids to scatter towards the walls and recirculate.

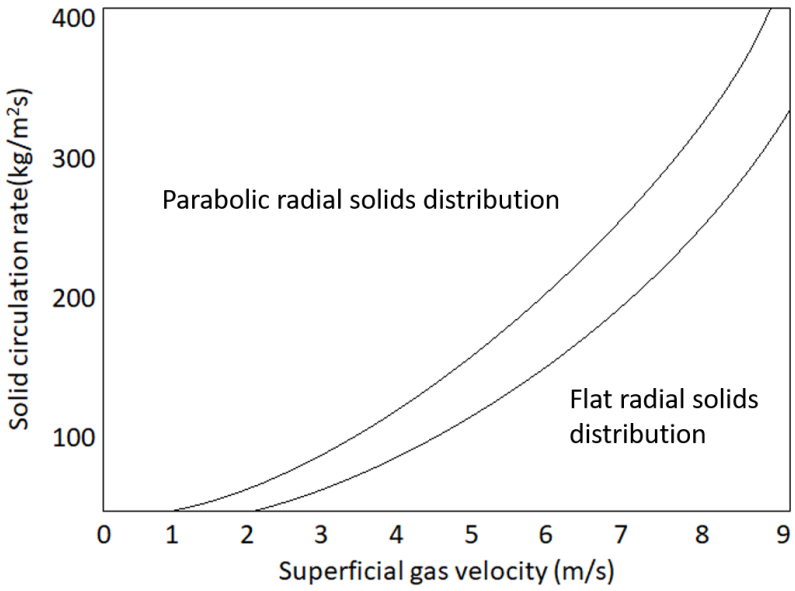

Figure 2.6: *Operating conditions corresponding to parabolic and flat radial solids profiles (adapted from Yan et al., (2005))*[32]

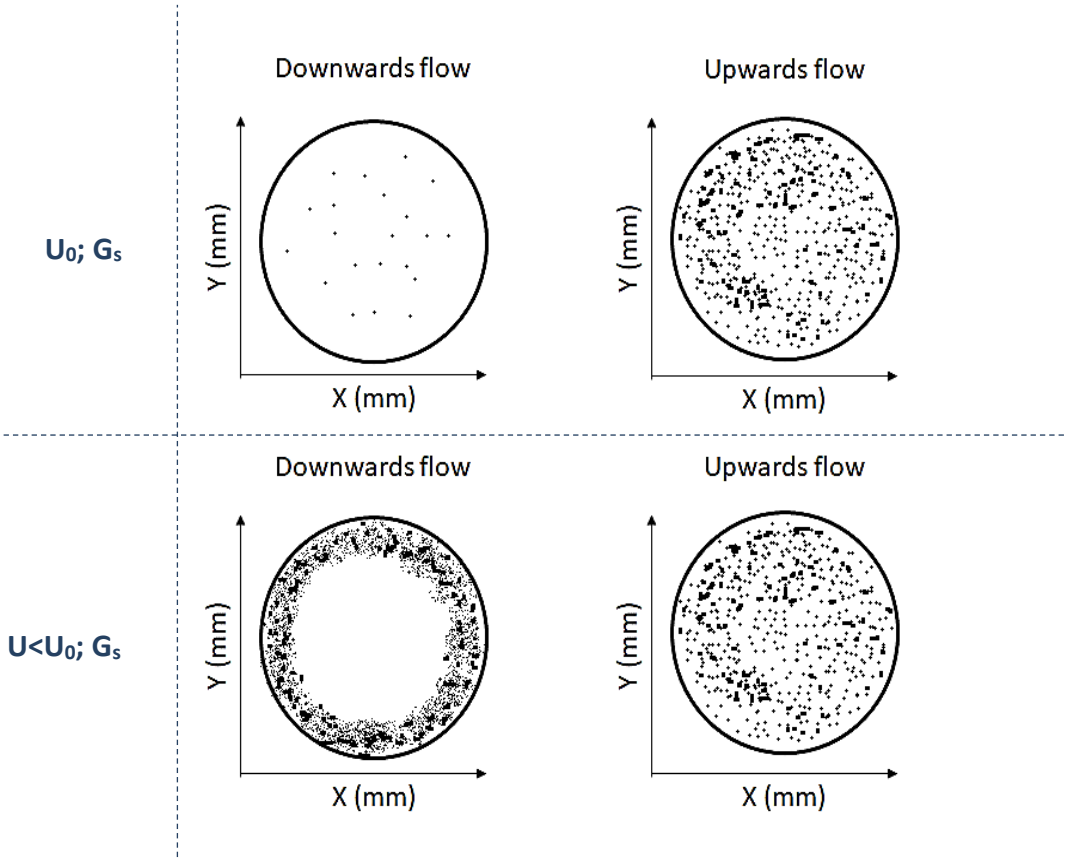

Figure 2.7: *Experimental results indicating enhanced downward flow near the riser wall at a lower superficial gas velocity (Adapted from Van de Velden et al., (2007))*[33]

Particles in the development region near the bottom of the riser respond the most to changes in the superficial gas velocity and the solids flux as opposed to the solids near the top[31,69,78]. Since an increase in the superficial gas velocity or a decrease in the solids flux has been found to increase the uniformity of the particle distribution[24], this will result in a smaller development region and a larger fully developed region while also changing an S-shaped axial solids holdup profile to an exponential profile[24,31,32,69,78]. Li *et al.,* (2019) stated that the more uniform overall particle distributions could be attributed to the increased drag and consequently the enhanced interaction between the gas and solid phases at higher gas velocities[31]. Conversely, an increased solids flux created a greater development region within the riser and enhanced the interaction between the particles in the region. This increased the cluster formation and eventually led to less uniform axial flow[31,78].

By adapting the operation of an FGD-CFB, the sulphur removal efficiency may be changed, but the operational cost should be kept in mind[20,25,26]. For example, an increased superficial gas velocity has been found to reduce the temperature gradient in the reactor, but a greater pressure drop across the riser was induced, and the desulphurisation efficiency decreased[16,64].

The compromised desulphurisation efficiency at higher gas velocities can be explained by the larger volume of unreacted sorbent required to remove the increased flux of SO_2. The additional volume of unreacted sorbent that is required exceeds the increased carrying capacity; thus, stable riser operation with a suitable amount of solids cannot maintained[26]. Furthermore, the reduced residence time of the solid and gas phases means less time is available for the sorbent to react with the SO_2[20,81]. In contrast to this, higher superficial gas velocities have been found to slightly increase the performance of FGD-CFB's in risers with internal baffles, which can be attributed to the increased particle attrition due to the internal flow restrictions[3,18,29,].

Since the flue gas flow rate usually depends on the power plant load, it is seldomly manipulated in practice despite its hydrodynamic significance[23]. Thus, the solids flux remains the subject of many hydrodynamic studies of FGD-CFB's. When the solids load is increased, the particle residence time increases, which improves the sulphur removal efficiency[25,31]. An increased solids flux also results in a higher lime to sulphur dioxide (Ca/S) molar ratio, further enhancing the FGD capability of the reactor[16]. Ollero *et al.,* (2001) noted that one drawback of increasing the Ca/S ratio is a lower sorbent utilisation[23]. This may be explained by the reduced effect of collisions, coalescence and fragmentation on the reaction rate at higher solid fluxes, due to the poor phase mixing[16]. Beyond a certain solid recirculation rate (of up to 98%), the added operational expense associated with the increased pressure drop and low sorbent utilisation outweighs the removal efficiency gained in the process[23,31,37,64,79,81].

2.2.4.3 Particle characteristics

As discussed in Section 2.2.1, the mean size and density of the particles used in a CFB riser are important for effective fluidisation. This is because the saturation carrying capacity increases and the choking velocity of the system decreases as the size and density of both Geldart A and B particles are decreased[49,53]. These two characteristics also influence the solids distribution inside the riser. According to the literature, an increase in the density of the particles increases the radial and axial solids holdup as well as the particle residence time within CFB risers[24]. The higher solids holdup is further accompanied by a slower flow development, thus extending the development region at the bottom of the riser, as illustrated in Figure 2.8[31].

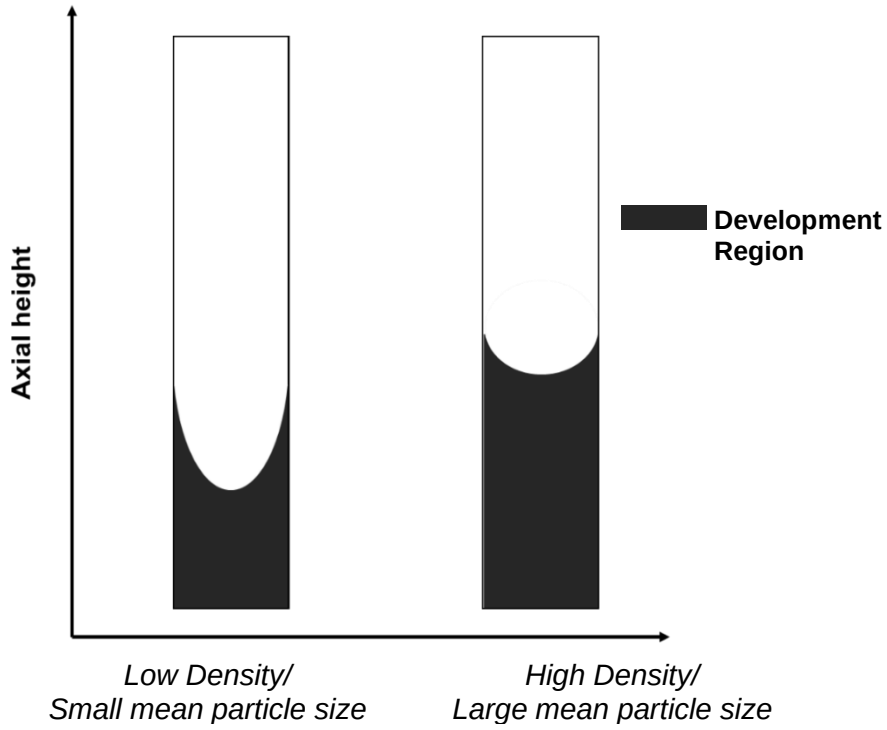

Figure 2.8: *The influence of particle density on the size and shape of the development region inside a riser (adapted from Li et al., (2019))*[31]

An increase in the mean particle size has the same effect on the solids holdup as an increase in the particle density[31,82,93]. That is, a greater solids holdup near the bottom of the riser, a delay in the solids flow development and a higher average particle residence time is to be expected. This can be attributed to the larger drag force between the larger particles and the gas phase and, consequently the tendency of particles to remain near the bottom of the riser[31,82]. Since sorbents with larger particle size or density are more likely to exhibit core annulus or non-uniform flow[31], downward particle flow near the riser walls is also more common[31].

Although larger particles exhibit higher residence times, less surface area is available for the chemical reactions to take place, and this has been found to decrease the sulphur removal efficiency[18]. Therefore, a trade-off between a suitable residence time and an adequate amount of specific surface area exists. Furthermore, the surface roughness of the particles also influences the gas-solid hydrodynamics. The pressure loss induced by particles with rough surfaces is larger than that of smooth particles of the same size and density. This effect is especially pronounced at dilute operating conditions, as discovered by Chang and Louge (1992)[35]. Chang and Louge (1992) ascribed the increased pressure drop to the higher rate of cluster formation and higher quantities of particles flowing downward at the walls of the riser to the rough particle surfaces.

Apart from the mean particle size, the particle size distribution also plays a role in CFB hydrodynamics. This was illustrated by Shi *et al.,* (2014), who reported that inelastic inter-particle collisions consumed more kinetic energy when a narrow PSD was used[94]. They investigated PSD's with spans ranging between approximately 0.5 – 2. This increased the cluster formation as well as the radial non-uniformity at the bottom of the riser, which led to particle downflow near the walls[94]. Conversely, a wider PSD was less sensitive to inter-particle collisions and entrance effects[94]. It was further found that the coarser particles segregated to the bottom of the riser while the particles with a size equal to or smaller than the Sauter mean diameter were easily fluidised to the top[94]. The increased concentration of large particles at the bottom of the riser was reported in another study and can be explained by the different gravitational and drag forces the range of particles experience due to their diverse sizes[93]. Consequently, the segregation of large particles from small particles intensified as the width of the PSD increased[93].

Although particle segregation occurred while using a wide PSD, smaller average residence times were reported, given the reduced particle back mixing (downflow) when compared to the use of a narrow PSD[94]. According to Yang *et al.,* (2021), the superficial gas velocity has a larger impact on the axial solids distribution than the PSD has, although they also reported a lower solids concentration at the bottom of the riser as the width of the PSD increased[93]. These authors also found that the PSD had a negligible effect on the solids' velocity and residence time distribution.

2.3 COMPUTATIONAL FLUID DYNAMICS

CFD modelling is often used to understand the behaviour of multi-phase flow in CFB's. These models either treat all the phases as continua or distinguish between the gas and solid phases using different frameworks. The former is termed an Eulerian-Eulerian approach, while the latter is known as an Eulerian-Lagrangian approach. The finer details of each approach and the fluid mechanics involved are discussed in more detail in Section 4.1.1. In this section, an overview of several publications is provided, and it includes the CFD modelling of CFB's in general as well as the CFD modelling of FGD-CFB's specifically.

2.3.1 CFD and general circulating fluidised beds

2.3.1.1 Large-scale applications

Yang and Wang (2020)[95] studied the hydrodynamics of a CFB system with external particle recirculation which was operated in a dense fluidisation regime and had an inner diameter of 0.2 m. The purpose of their study was to evaluate gas-solid characteristics and transport mechanisms using a multi-phase particle in cell (MP-PIC) numerical approach where the drag coefficient was determined via the Gidaspow drag model. The MP-PIC method is an Eulerian-Lagrangian approach where the particles are represented as parcels instead of being individually modelled. The authors achieved good agreement with experimental data and identified core-annulus flow from their numerical results. Since their findings qualitatively described the experimental trends, they argued that this approach might be used to model CFB's and to identify suitable gas velocity operating limits.

Using a similar MP-PIC approach, a study by Xie *et al.,* (2018)[96] focussed on the applicability of homogeneous and heterogeneous drag models for the numerical simulation of CFB's. The simulation procedure included "riser 1" with an inner diameter of 0.07 m using Geldart A particles and "riser 2" with an inner diameter of 0.4 m using Geldart B particles. Although no experimental data was collected, the CFB operating conditions and dimensions were based on the work of other authors and were validated using their findings. From the six homogeneous and four heterogeneous drag models that were compared, the following conclusions were made:

- For riser 1: The homogeneous models over predicted the solid fluxes, and the accuracy of the void fraction predictions was inconsistent. Conversely, heterogeneous models improved the prediction accuracy and could predict core-annulus flow conditions.
- For riser 2: Both the homogeneous and heterogeneous drag models predicted reasonable flow structures.

Instead of using an Eulerian-Lagrangian approach, a 2017 study by Chen *et al.* focussed on the use of Eulerian-Eulerian methods for CFB applications[97]. The authors attempted to improve the prediction accuracy of existing CFD models by accounting for the anisotropic nature of the velocity fluctuations of particles in CFB's. Accordingly, the gas was modelled within a large-eddy simulation framework, which included a sub-grid scale turbulent kinetic energy model, and the particle behaviour was described via a second order moment (SOM) model.

Since no experimental work was done, the model validity was tested against the experimental findings of previous studies by different authors. The study was simplified further by only considering a 2-dimensional riser. It was found that the CFD model successfully captured the varying solids holdup distributions, turbulent kinetic energy and sub grid energy dissipation under varying solids fluxes and showed good agreement with experimental findings. However, the LES-SOM model requires further development before applying it to a 3-dimensional domain.

2.3.1.2 Small-scale applications

In a study by Zhang *et al.,* (2018) CFD modelling was used to study the influence of temperature and pressure on the hydrodynamics inside a riser filled with Geldart B particles[98]. The CFB had an inner diameter of 0.1 m, and an Eulerian-Eulerian approach with the heterogeneous EMMS drag model was used. The simulation results showed good agreement with the experimental data that was collected. It was found that below 0.4 MPa, changes in the solids flux brought about changes in the fluidisation regime within the riser. In addition, an increase in the operating pressure reduced the solids holdup inside the riser if the solids flux was kept constant. An increase in temperature was found to have a negligible influence on the axial solids holdup profile, although slight increases in the solids velocity in the centre of the vessel were noted.

In a separate study, the EMMS drag model was also used; however, a solids stress model was developed, and the MP-PIC approach was favoured[99]. The adapted model was validated using available literature, which included a study in which the CFB had an inner diameter of 0.09 m. It was concluded that this method reduced the dependence of the CFD prediction accuracy on the resolution of the solution grid. This improvement was attributed to the sub-grid flow structures that were accounted for.

Another study that was dedicated to CFD model improvement was done by Varas *et al.*, (2017)[100]. In this work, the reliability of the Eulerian-Lagrangian approach in the prediction of cluster phenomena using a DEM approach was tested. Given the high computational cost that is associated with DEM modelling techniques, a laboratory-scale CFB riser with an inner diameter of 7 cm was used for validation purposes. The CFB was kept in the fast fluidisation regime, and Geldart D particles were used. Although key cluster characteristics could be predicted using the DEM approach, the number of larger clusters was over-predicted. More research on the influence of drag and collision parameters on clustering was suggested.

2.3.2 CFD and semi-dry FGD processes

2.3.2.1 Large-scale applications

In an article by Xue *et al.,* (2015)[25] the performance of a semi-dry FGD-CFB riser with an inner diameter of 0.2 m was described using both experimental and numerical methods. An unsteady Eulerian-Eulerian approach was selected for the CFD model, and the heterogeneous Syamlal & O'Brien (O-S) drag model and a continuous desulphurisation model were used. The CFD results revealed that the jet water flow rate was the main determining factor of the desulphurisation efficiency, after which the solid circulation rate had the second greatest effect.

In a 2011 study, the performance of a pilot scale semi-dry FGD unit was evaluated[16]. The unit was operated in the dense phase fluidisation regime, and the Eulerian-Lagrangian CFD model included a 1st order reaction model, a k-ε turbulence model and a simple heat transfer model between the gas and solid phases. Good agreement between the experimental and predicted desulphurisation efficiencies, temperature and pressure differentials could be obtained under varying operating conditions. However, the model's predictive capability was reduced with increasing flue gas flow rates and improved with increasing Ca/S ratios. After model validation, the numerical model was applied to study the pressure distribution inside the vessel as well as the trajectory and concentration of circulating ash.

Li *et al.,* (2012)[46] applied an Eulerian-Eulerian model to model a CFB in which a Ca/fly ash-based sorbent was used. The aim of the study was to quantify the effect of impinging streams on desulphurisation efficiency, where impinging streams were defined as two inlets along the same axis with opposing injection directions. It was found that the impingement increased two-phase mixing and increased the desulphurisation efficiency by approximately 5%. From the CFD results, the interaction in the impingement zone could be discussed, and the improvement in the reaction efficiency could be explained. Experiments were also performed, although it was not used for model validation but rather to calculate the residence times in the impingement zones.

2.3.2.2 Small-scale applications

In a study by Wu *et al.,* (2020)[20], CFD was used to describe the influence of enlarged riser sections on the hydrodynamics inside a semi-dry FGD-CFB.

The CFD model was validated using experimental data, and an Eulerian-Eulerian approach, together with the Wen-Yu drag model, was employed. Although no reaction kinetics were incorporated, the study was performed with the intention of improving future FGD applications. From the CFD data, the axial and radial solids holdup profiles could be discussed thoroughly.

In a 2012 publication, the performance of the QL-EMMS drag model was compared to that of the O-S drag model, both of which are heterogeneous models[26]. In this instance, the model employed a unique sulphur capture model, only considered a 2-dimensional geometry and was constructed within an Eulerian-Eulerian framework given the high concentration of solid particles. The QL-EMMS models were constructed such that they could be compared to the experimental findings from the available literature. It was determined that the QL-EMMS model underestimated the increasing drag forces that arose from clustering and that the solid volume fraction within clusters should be determined to improve its performance.

From the various findings, it became clear that experimental work was often used to validate the CFD models, after which the model results were used to explain CFB phenomena. If no experimental work was done, the models were generally validated and compared to the available literature. For the most part, these publications focussed on improving the numerical tools that are available for simulating fluidisation rather than finding optimal operating conditions for specific cases. The qualitative behaviour of multi-phase flows in CFB's has been successfully described using CFD techniques, although the quantitative descriptions still have room for improvement. While attempting to develop a model that would fit the experimental data as accurately as possible, an additional focus of this study was to use CFD data to supplement the discussions that followed from the experimental observations.

CHAPTER 3 - EXPERIMENTAL METHOD

3.1 EXPERIMENTAL SETUP

3.1.1 P&ID and riser dimensions

A new CFB riser was constructed for the purpose of FGD research, and no previous work has been done on the equipment. Therefore, the hydrodynamics inside the riser in its simplest state had to be investigated to lay the groundwork for future investigations. To do this, the interaction between the air and particles at various conditions were studied using the experimental method outlined in Chapter 3. A P&ID of the experimental setup is provided in Figure 3.1 and the description of its streams and units as well as its control and measurement equipment are provided in Table 3-1. The CFB and its auxiliary equipment were constructed for this study according to the design calculations in Annexure C and the additional changes that were made during the commissioning phase of the experimental setup are discussed in Annexure D.

Table 3-1: *Description of stream contents, process units and control equipment in Figure 3.1*

Stream	**Description**	**Item**	**Description**
G – 01	Room temperature air	CLN – 01	Cyclone
M – 01	Air and particle mixture from riser.	FAN – 01	Variable speed fan
M – 02	Air and particles that were not removed by the cyclone	FDR – 01	Variable speed screw feeder
M – 03	Air after passing through the fan	HPR – 01	Sealed sorbent hopper (300 kg capacity)
M – 04	Air after scrubbing	MXR – 01	Fixed speed mixer
M – 05	Water and suspended particles	RSR – 01	CFB riser
S – 01	Sorbent from the hopper	VAL – 01	Variable speed rotary valve
S – 02	Fresh sorbent feed	VEN – 01	Venturi
S – 03	Sorbent particles from cyclone	SCBR – 01	Particle scrubber
W – 01	Water from spray nozzles	●	Port to use for iso-kinetic sampling
Item	**Description**	**Item**	**Description**
FC – 01	Variable speed screw feeder	PT	Flush pressure transmitters

FC – 02	Variable speed fan motor	TT	Resistance temperature detectors
FI – 01	Hot wire anemometer		

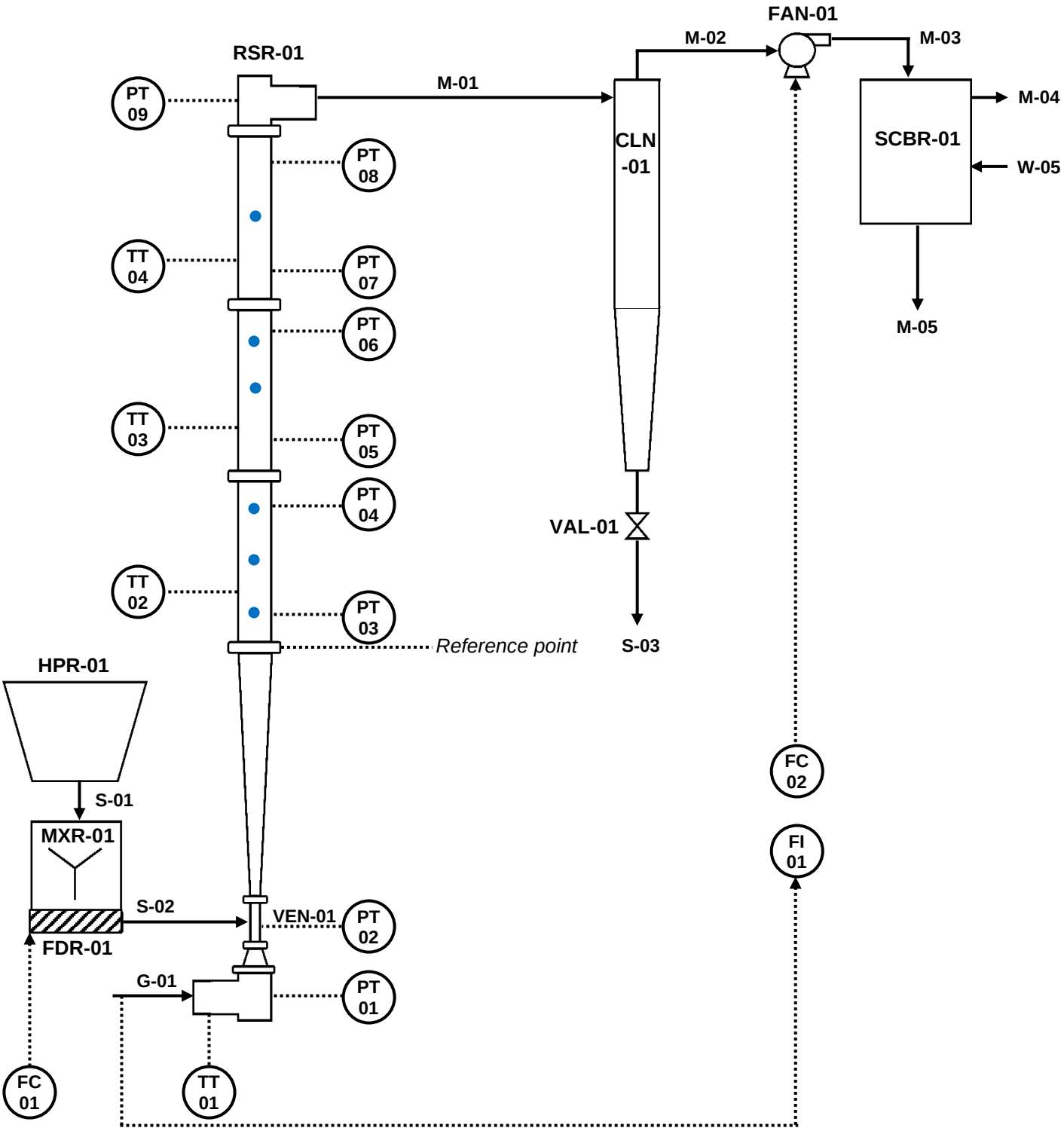

Figure 3.1: *A P&ID of the circulating fluidised bed riser setup that was used throughout the experimental phase.*

Figure 3.2 illustrates the riser's dimensions and one of its three detachable cylindrical sections. Removing one or two cylindrical sections from the riser shown in Figure 3.2 (a) could decrease the riser height to a medium or low setting. These configurations receive further attention in Chapter 4.1. Every cylindrical section has two pressure taps, a port for temperature measurement and a port for water injection, the last of which will be used in future studies. The position of each port is illustrated in Figure 3.2 (b), and the location of the ports was identical on all three riser sections. Additionally, a varying number of solids sampling ports were installed at a 90° angle from the measurement ports, as illustrated in Figures 3.2 (a) and (b).

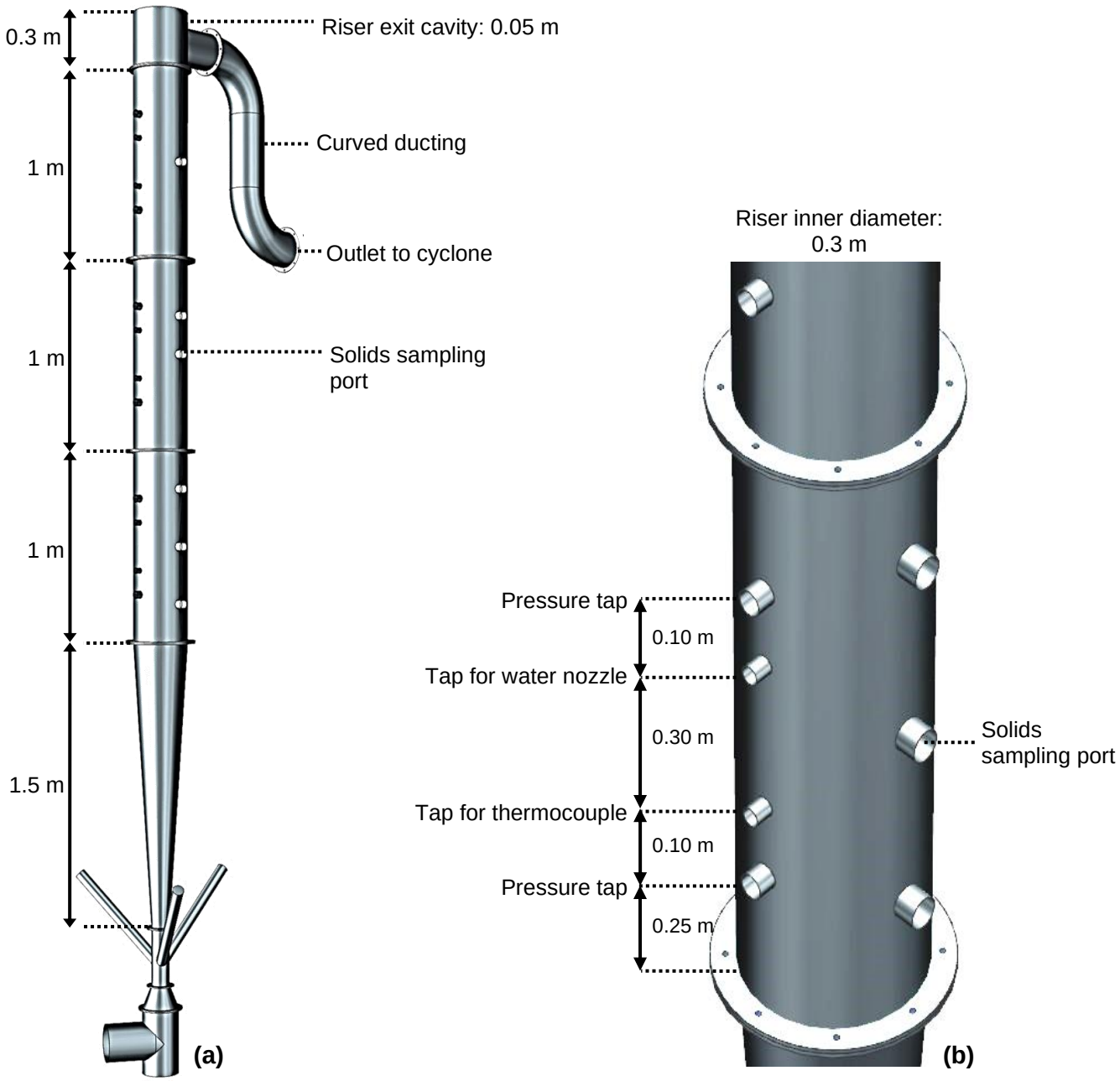

Figure 3.2: (a) *An illustration of the CFB riser and* ***(b)*** *the measurement ports on the one-meter cylindrical sections*

In Figure 3.3, the dimensions of the riser's bottom section are provided. For the purposes of this study, solids inlet numbers one and two were sealed. The former was intended as a recirculation inlet from the cyclone, and the latter as an additional sorbent entry point. However, only one entry port was required for this study and no recycled stream to the riser was included. Furthermore, the position of the solids sampling ports with respect to the other riser elements is illustrated in Figure 3.4.

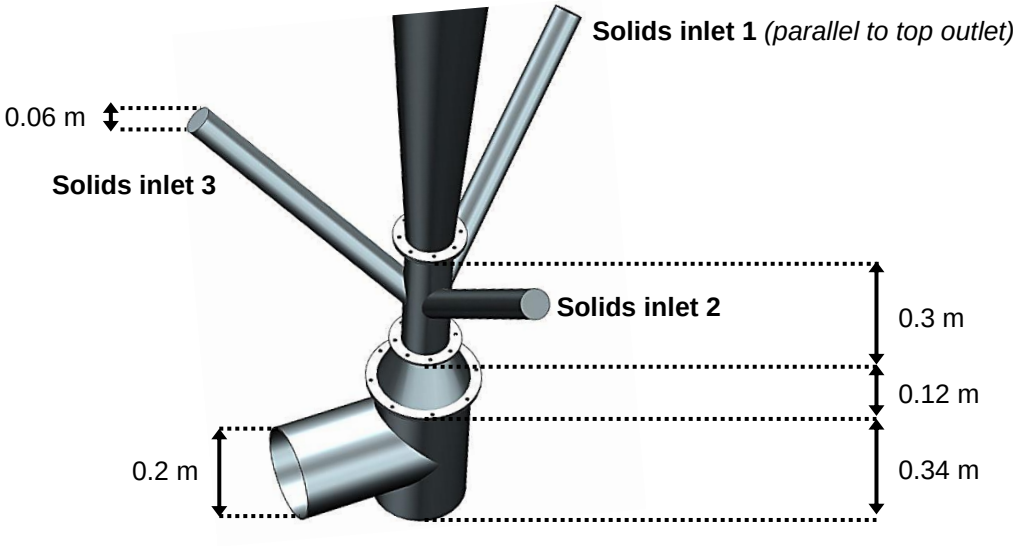

Figure 3.3: *Dimensions of the air and solid inlets at the bottom of the riser*

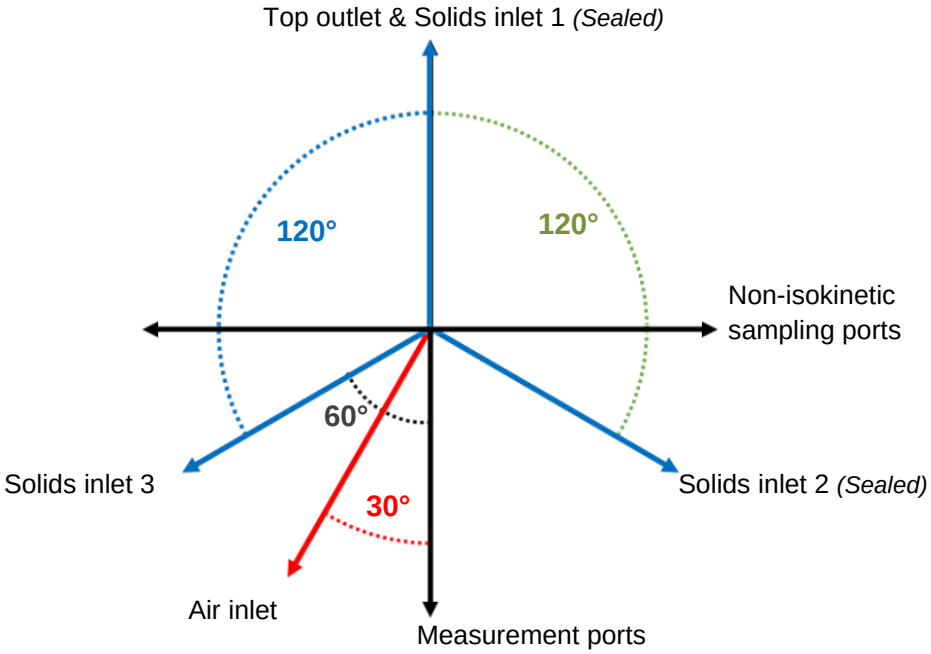

Figure 3.4: *The radial position of different riser elements*

3.1.2 System start-up and operation

An experiment was initiated by changing the fan to a setting that would deliver the desired air inlet velocity according to the calibration curve that is provided in Annexure E2. Following this, the rotary valve below the cyclone was switched to its highest speed setting. Next, the solids mixer was started, and the feeder was changed to the setting that would deliver the desired solids feed rate, according to the calibration curve provided in Annexure E1. While the mixer and feeder were in motion, the hopper above the feeder was filled to capacity. The air flowing into the bottom of the riser fluidised the powder inside the venturi, after which the two-phase mixture travelled towards the top of the riser. From the abrupt riser exit, the suspension travelled towards the cyclone, separating approximately 74 % of the solids from the gas phase. The calculation of the cyclone's removal efficiency has been provided in Annexure F. Air flowing from the top of the cyclone, contained a reduced number of suspended particles and travelled through the fan. A scrubber downstream from the fan reduced the amount of powder that was released into the environment, and its working principle is further discussed in Annexure D2.

The particle flow from the bottom of the cyclone was captured in a 100 L container. Once full, the container contents were reloaded into the hopper, and an empty drum was placed underneath the cyclone. The injection of solids reduced the measured inlet air velocity, and the fan speed was adjusted accordingly. Once the measured inlet air velocity remained within 0.6 m/s of the target value for more than one minute, the riser reached a steady state. From this point onwards, measurements could be made. In order to save time and resources, all of the experimental treatment combinations that required three cylindrical riser sections were completed first. This was followed by those at two sections and the last experiments were those that required only one installed section.

3.2 SORBENT CHARACTERISATION

3.2.1 Sorbent procurement and particle density

Following the discussion from Section 2.1, hydrated lime was chosen as the sorbent for this study. Accordingly, one-kilogram samples of hydrated lime were ordered from four suppliers, namely PPC, Lime distributors (Idwala), Tazchem and Afri-lime and the samples were analysed before choosing the final supplier. Initially, the particle density of each sample was determined. The size of the samples was reduced according to the procedure in Annexure G1 and each batch was analysed using a Micromeritics AccuPyc II 1340. The results are provided in Table 3-2 from which it can be seen that the Afri-lime sorbent had the highest particle density.

Table 3-2: *The particle density of the sample from each of the four suppliers*

Supplier	**Tazchem**	**Idwala**	**PPC**	**Afri-lime**
Particle density (kg/m^3)	2084.6	2040.0	2029.2	2883.0

The PSD of each sample was determined using a Malvern Mastersizer 3000. Ethanol was used as the dispersant since hydrated lime is water soluble. The four samples had similar PSD's; for this reason, only the Afri-lime sample's PSD is provided in Figure 3.5. The three remaining PSD's can be found in Annexure H. Figure 3.5 illustrates that the D[3,2] of the Afri-lime sample was 0.16 µm while the D[4,3] was equal to 14.85 µm and a discussion regarding the relevance of these two parameters is provided in Annexure H. The Afri-lime sample had the highest D[3,2] when compared to the other three suppliers while also having the lowest volume density of sub-micron particles. Given that the sorbents used throughout FGD-CFB literature contain a small volume of sub-micron particles[23,15,25,26], the Afri-lime supplier was deemed the most suitable choice for this study based on the PSD results.

According to the discussion in Section 2.2.1, the hydrated lime that was used in this study can be classified as Geldart C particles. This is in agreement with the Geldart classes that are used in FGD-CFB applications throughout the literature. By determining the average particle size and density of the hydrated lime samples from all four suppliers, it was also seen that the hydrated lime that is available for large-scale applications in South-Africa are limited to Geldart C particles. This was an important finding given that the Geldart class influences the fluidisation properties of the particles, according to the discussion in Section 2.2.1.

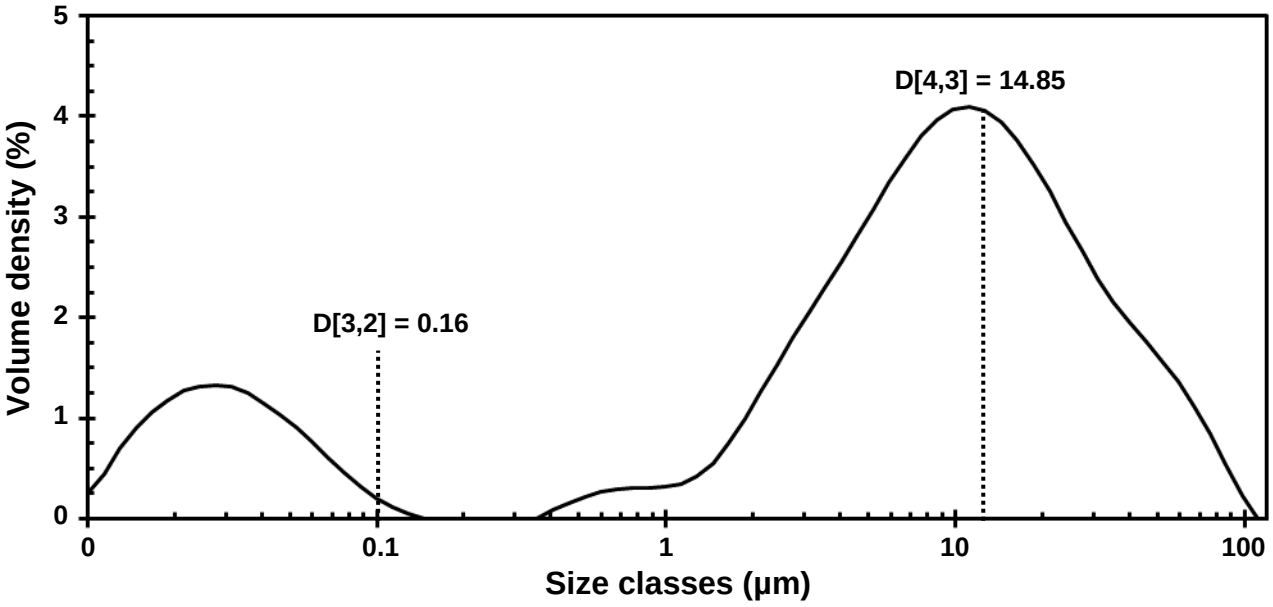

Figure 3.5: *The Sauter mean diameter (D[3,2]) and volume moment mean (D[4,3]) retrieved from the PSD analysis of the hydrated lime sample from Afri-lime*

3.2.2 PSD analysis

The D[4,3] was the preferred definition for the average particle size throughout this study. This was because it represents the size range that makes the sorbent's most significant contribution to the bulk mass and volume. From a hydrodynamic point of view, these parameters are key variables as opposed to the surface area, which would be the preferred parameter when considering reaction chemistry. In the latter case, the D[3,2] would be the more suitable definition of the average particle size. Furthermore, the CFD model calculates a drag force based on the projected particle area. Since the particle volume, rather than the particle surface area, influences the projected particle area, the D[4,3] was the most suitable parameter.

During an experimental run, the solids that were discarded from the bottom of the cyclone were reloaded into the feeder hopper several times. However, only three-quarters of the particles that passed through the cyclone were removed from the carrier air as detailed in Annexure F. Therefore, it was necessary to determine whether the portion of particles that bypassed the cyclone had any effect on the D[4,3] of the remaining sorbent. To this end, a 650 kg batch of hydrated lime was loaded into the CFB system at an inlet air velocity of 6.1 m/s, and a solids feed rate of 0.06 kg/s.

As the batch passed through the system, the sorbent was captured underneath the cyclone in 100 L drums. From the captured lime, a representative sample was prepared according to the procedures summarised in Annexure G2 and Annexure G1. A PSD analysis was performed on the representative sample, and the sorbent that had been captured underneath the cyclone was fed through the system two more times. After every cycle, a representative sample was obtained, as detailed above, and a PSD analysis was performed. The D[4,3] that was recorded after every cycle is provided in Table 3-3 and Figure 3.6 graphically illustrates the change in the PSDs. The shift in the D[4,3] and the PSD after the first pass through the system indicates that a large volume of sub-micron fine particles was removed from the sorbent. Given the reduced number of sub-micron particles after the first pass, consecutive recycling did not alter the span of the PSD significantly and the value of the D[4,3] remained within 20 µm and 30 µm. Thus, fresh sorbent was passed through the system at least once before starting with experimental measurements to minimise the changing D[4,3] effect on the riser hydrodynamics. The final particle size was defined as the average D[4,3] from cycles 1 – 3, as given in Table 3-3.

Table 3-3: *The shift in the D[4,3] that was brought on by sorbent recycling*

Times through cyclone	0	1	2	3	Average of 1 - 3
D[4,3] (µm)	14.8	21.5	22.2	27.2	23.6

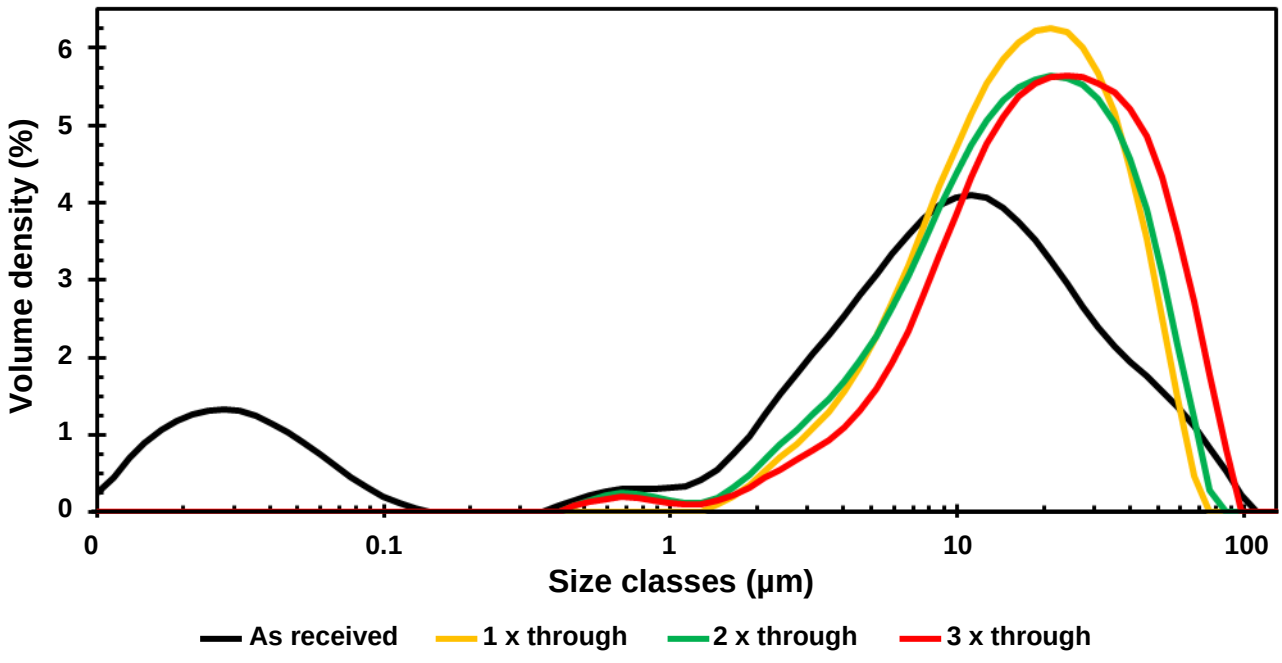

Figure 3.6: *The PSD change that was brought on by sorbent recycling*

3.2.3 XRF analysis

A representative sample of the Afri-lime sorbent was prepared according to the process described in Annexure G1 and sent to an independent laboratory for X-ray fluorescent (XRF) analysis. The results from the analysis are provided in Table 3-4. Initially, the sample was heated to a temperature of 1000°C for two hours until the weight of the sample stabilised. This removed the water content, CO_2 and any additional volatiles while causing the major elements of the sorbent to react with oxygen[101]. From this process, a LOI of 14.37% was obtained. Next, the XRF analysis was performed, and the chemical composition of the sample is provided in its oxidised state in Table 3-4. Approximately 68% of the sample consisted of calcium oxide, which gives an indication of the amount of calcium that was originally present in the form of calcium hydroxide. The main impurities in the sorbent were SiO_2 and Al_2O_3 followed by Fe_2O_3. Although the XRF revealed that the hydrated lime had a low-grade quality, the 68% CaO content falls within the 30% - 90% range required for medium to large-scale FGD applications, as discussed in Chapter 2.1.

Table 3-4: *Result from an XRF analysis of the hydrated lime sorbent*

	Composition (Weight %)										
Component	CaO	LOI	SiO_2	Al_2O_3	Fe_2O_3	P_2O_5	TiO_2	K_2O	Na_2O	MnO	Trace*
Sorbent	68.03	14.37	7.10	4.59	3.71	0.65	0.32	0.16	0.12	0.05	1.83

***Elements present in trace amounts as listed in Annexure H**

3.3 EXPERIMENTAL PROCEDURE

3.3.1 Operating conditions

The influence of the following three factors on the hydrodynamics inside the riser were investigated:

- The inlet air velocity,
- the solids feed rate and
- the riser height.

Three operating levels were specified for each of the three factors, which will be referred to as the low, medium and high settings, as summarised in Table 3-5. Since the riser height was adjusted by adding or removing cylindrical sections the low, medium and high settings were chosen to represent the installation of one, two and three of those sections respectively. However, further calculations and experimental methods were required to select the three settings for the inlet air velocity and the solids feed rate, which are discussed throughout the remainder of this section.

Table 3-5: *The low, medium and high settings of each independent variable*

Factor	Low (-1)	Medium (0)	High (+1)
Inlet air velocity (m/s)	4.3	6.5	8.6
Solids feed rate (kg/s)	0.04	0.05	0.06
Riser height (number of cylindrical riser sections)	1	2	3

3.3.1.1 The low settings

The low setting of the sorbent feeder was determined experimentally. To protect the sorbent feeder, it was always operated at or above its 12% setting. Below this setting, the auger stopped rotating for prolonged periods, placing unnecessary stress on the feeder motor. Therefore, the low setting of the solids feed rate in Table 3-5 corresponds to the 12% setting of the feeder according to the calibration curve in Annexure E1. The low setting of the inlet air velocity was determined mathematically. FGD-CFB's are preferably operated at a riser superficial gas velocity that is equal to twice the particle transport velocity, as discussed in Section 2.2.1.

This condition was defined as the minimum inlet air velocity for this study to ensure sufficient fluidisation at every inlet air velocity setting. The Archimedes number that is associated with this study is provided in the first row of Table 3-6. When comparing this value to those in Table 2-1 it is seen that the correlations from both Khurram *et al.,* (2015)[63] and Smolders and Bayens, (2001)[62] are applicable. However, only the former considered the H/D ratio – which was a key parameter in this study. Therefore, the particle transport velocity of the sorbent was calculated using the empirical correlation from Khurram *et al.,* (2015)[63] and the results are reported in the bottom three rows of Table 3-6.

The value of the riser height, H, is defined as the distance between the top of the riser and the top of the venturi, while the remaining constants that were used for the calculations are provided in Table 3-7. The temperatures at which the air density and viscosity were specified were chosen as the average ambient temperature in the experimental workspace during the month of November. The highest transport velocity was equal to 0.92 m/s and it was multiplied by two to obtain a target superficial air velocity within the cylindrical riser sections. Given the varying diameters of the riser and its air inlet, the superficial air velocity in the riser had to be converted to an inlet air velocity. The resulting value of 4.1 m/s was chosen as the low setting for the air inlet velocity. However, during commissioning it was determined that the riser was prone to slugging at this velocity and the low setting was increased slightly to 4.3 m/s. This value corresponds to the one reported in Table 3-5.

Table 3-6: *Transport velocities at varying riser heights for the FGD-CFB system*

Parameter	Value	Unit
$\boldsymbol{Ar}$	1.33	$(-)$
$\boldsymbol{U_{TR}}$ $(\boldsymbol{H = 4.8})$	0.92	m/s
$\boldsymbol{U_{TR}}$ $(\boldsymbol{H = 3.8})$	0.85	m/s
$\boldsymbol{U_{TR}}$ $(\boldsymbol{H = 2.8})$	0.76	m/s
$\boldsymbol{U_0}$ $(\boldsymbol{U_{TR} \times 2})$	1.84	m/s
$\boldsymbol{U_{inlet,\ min}}$	4.13	m/s

Table 3-7: *Fixed parameters for this study*

Constant	Value	Unit
$\boldsymbol{d_p}$ $(\boldsymbol{D[4,3]})$	23.63	μm
$\boldsymbol{\rho_p}$	2883	kg/m^3
$\boldsymbol{D_{riser}}$	0.30	m
$\boldsymbol{D_{inlet}}$	0.20	m
$\boldsymbol{\rho_f}$	1.19 (@22.9℃)	kg/m^3
$\boldsymbol{\mu_f}$	1.83×10^{-5} (@22.9℃)	$Pa \cdot s$

3.3.1.2 The medium and high settings

The high setting for the solids feed rate was determined experimentally, as illustrated in Table 3-8. The riser was operated at the low inlet air velocity setting, and the feeder was started. The speed setting of the feeder was increased in increments of 5% and allowed to run for five minutes at each setting. During this time, the inlet air velocity of 4.3 m/s was maintained by manipulating the fan setting. At a feeder setting of 22%, the saturation carrying capacity of the air has been exceeded. This caused a solids build-up at the bottom of the riser, which was accompanied by inconsistent pressure readings. Consequently, the feeder setting was decreased in increments of 1% and allowed to run for five minutes at each setting. At the feeders' 20% setting, stable riser operation was once again achieved, and the maximum solids feed rate was fixed at a value of 0.06 kg/s according to the calibration curve in Annexure E1.

Table 3-8: *Process used to decide the high setting of the solids feed rate*

	Feeder setting (%)				
Could the system sustain the solids load in suspension at $U_{inlet} = 4.3$ m/s	12	17	22	21	20
	✓	✓	X	X	✓

The high setting of the inlet air velocity was also determined experimentally. The fan was changed to its 95% setting, and the maximum solids feed rate of 0.06 kg/s was injected into the riser. After five minutes of operation, the inlet air velocity reached an average value of 8.1 m/s, which was selected as the high setting for the experimental program in Table 3-5. This was because the high setting of the solids feed rate would need a substantial amount of air to remain fluidised, thereby creating a maximum air velocity requirement.

In Annexure C2, it was determined that a minimum solids feed rate of 0.03 kg/s would be required to ensure a Ca/S ratio of 1.2 at an inlet air velocity of 13.5 m/s. However, the maximum inlet air velocity for this study was fixed at 8.1 m/s, while the smallest solids feed rate was 0.04 kg/s. Therefore, the condition where Ca/S > 1.2 will be met regardless of the experimental treatment combination.

3.3.2 Experimental design

3.3.2.1 Factorial design and the evaluation of curvature

Simulated data is seldomly validated using experimental procedures[102]. If experimental validation is performed, the experimental outline often entails changing one factor at a time while all other variables are kept constant[102]. This approach is statistically inefficient and fails to account for the combined influence of the different factors on a given response[103]. Instead, the influence of the independent variables (factors) on the hydrodynamics (responses) was described via the statistical design of experiments (DOE) which also minimised the required number of experiments. Two approaches were considered for this purpose. The first was a full factorial design, during which the effect of every possible factor combination on the system was tested[104]. The second, was a central composite design method during which a limited number of experimental combinations were used. For the full factorial design, only the high and low settings that are provided in Table 3-5 were considered and these were denoted by 1 and -1 respectively. Consequently, a total of 8 runs were required[60]. The resulting experimental program is represented by the cube in Figure 3.7 a) with each end of the blue, red and green lines representing the low and high settings of the three factors respectively.

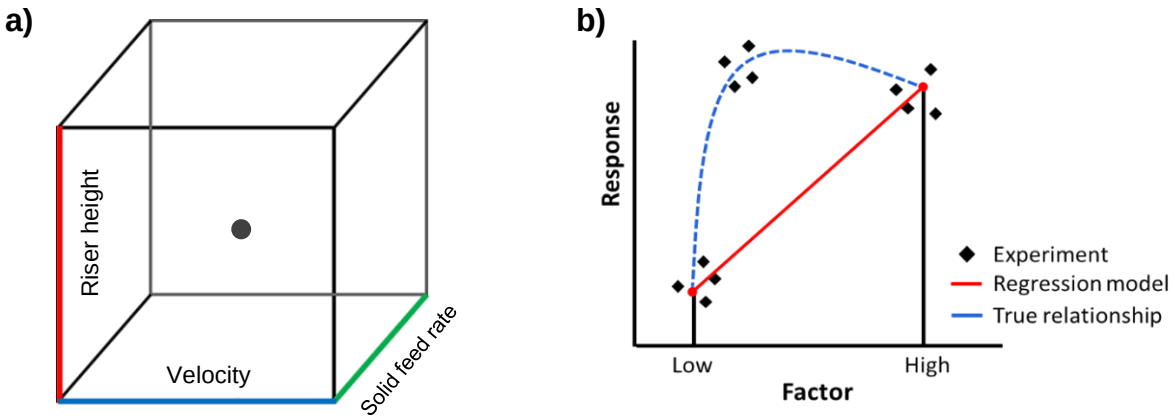

Figure 3.7: *a) The 2^3 full factorial design with a centre point (Adapted from Montgomery and Runger (2014)[105]) and b) a graphical illustration of a linear regression model failing to predict curvature*

In an article by Gutiérrez *et al.,* (2002), a factorial design approach was used to assess the influence of the Ca/S ratio, approach to adiabatic saturation temperature, solids recirculation ratio, SO_2 concentration and the superficial gas velocity on the performance of a semi-dry FGD-CFB[68].

Using a simple linear regression model, they determined that the adiabatic saturation temperature, the recirculation ratio, the Ca/S ratio and the interaction between the Ca/S ratio and the recirculation ratio had the largest influence on the desulphurisation yield[68]. Although the DOE was only one facet of their study, the resulting information was crucial to understanding the most important factors to achieve the plant's objectives. Unfortunately, the analyses techniques associated with a 2^k factorial designs assume a linear relationship between the factors and the response and is therefore unable to account for curvature[105]. This is graphically illustrated in Figure 3.7 b).

To test whether curvature was present, experiments were performed at the centre point of the experimental domain or the medium settings provided for each factor in Table 3-5[104]. A test statistic (t-statistic) was calculated from the generated data to quantify how much the mean of the centre points differed from the mean of the original factorial design points[105]. From the test statistics, P-values were determined, which were compared to a 95% confidence interval. If the P-values were less than the chosen value – the curvature was deemed significant. The t-statistic for curvature is provided in Equation 3-1[104].

$$t_{0_{curvature}} = \frac{\overline{y_F} - \overline{y_C}}{\hat{\sigma}\sqrt{\frac{1}{n_F} + \frac{1}{n_C}}} \qquad \textbf{3-1}$$

Here $\bar{y}$ represents the mean of the measured responses, subscripts F & C refer to the factorial design and centre point measurements respectively, $\hat{\sigma}$ is the standard deviation and n is the number of experimental observations. Since no replicate experiments were performed, the standard deviation was estimated by the square root of the mean square error of the centre point runs (MSE_{cp}) by using Equation 3-2[105].

$$\hat{\sigma}^2 = MSE_{cp} = \frac{SSE_{cp}}{n_c - 1} = \frac{\sum_{centre\ points}(y_i - \bar{y}_c)^2}{n_c - 1} \qquad \textbf{3-2}$$

In the previous expression SSE_{cp} is the sum of squares of the error for the centre point runs and y_i is the measured response of the centre point runs. As a second measure of curvature, the curvature sum of squares, as provided in Equation 3-3, was calculated. If it approached zero, the extent of curvature in the regression analysis was deemed negligible[104].

A linear regression model was chosen for a given response when both tests indicated that the curvature could be ignored. The general form of the linear models is provided in Equation 3-4[104], and the coefficients were determined according to the method in Annexure I.

$$SS_{curvature} = \frac{n_F n_C (\bar{y}_F - \bar{y}_C)^2}{n_c + n_F} \quad \textbf{3-3}$$

$$\hat{y} = \beta_0 + \beta_A A + \beta_B B + \beta_c C + \beta_{AB} AB + \beta_{BC} BC + \beta_{AC} AC + \beta_{ABC} ABC \quad \textbf{3-4}$$

Where β_0 represents the constant, β with a subscript represents the linear and interaction coefficients, $\hat{y}$ is the predicted response, and $A - C$ represents the factors.

3.3.2.2 Modifying the 2^k design

To account for curvature, quadratic terms had to be included in the regression models. This could be achieved by adding a third level or medium operating setting to each factor. However, 3^k full factorial designs require a larger number of experiments and resources when compared to 2^k designs. As a result, alternative solutions were considered, which included[104]:

- Using a response surface method or,
- making use of central composite designs (CCD).

Since a CCD is developed sequentially, the data from the linear regression model analyses and curvature tests could be used. Hence, experimental resources were not wasted. To add quadratic terms, the 2^k designs were augmented by adding axial points at a given distance from the experimental domain's centre point, which will be referred to as the alpha value (α). CCD predictions are optimised when the design is both rotatable and orthogonal[104]. When a design is fully rotatable, the prediction error of all the points at the same distance from the centre point is identical[106]. When a design is fully orthogonal, the predicted effect of a factor will be independent of the effect of other factors or factor interactions[107]. Whether an experimental design is rotatable, orthogonal or a compromise between the two depends on the alpha value[106]. The alpha value is the distance between the centre point and the axial points, and three CCD's are prevalent in the literature.

These are the face-centred (α = 1), circumscribed (α > 1) and inscribed (α < 1) central composite designs, as illustrated in Figure 3.8[108]. For circumscribed and inscribed CCD's, five levels for each factor are required for the experimental runs. These factors are coded as -1, 0, 1 for the low, medium and high factorial runs respectively and -α, +α for the axial runs.

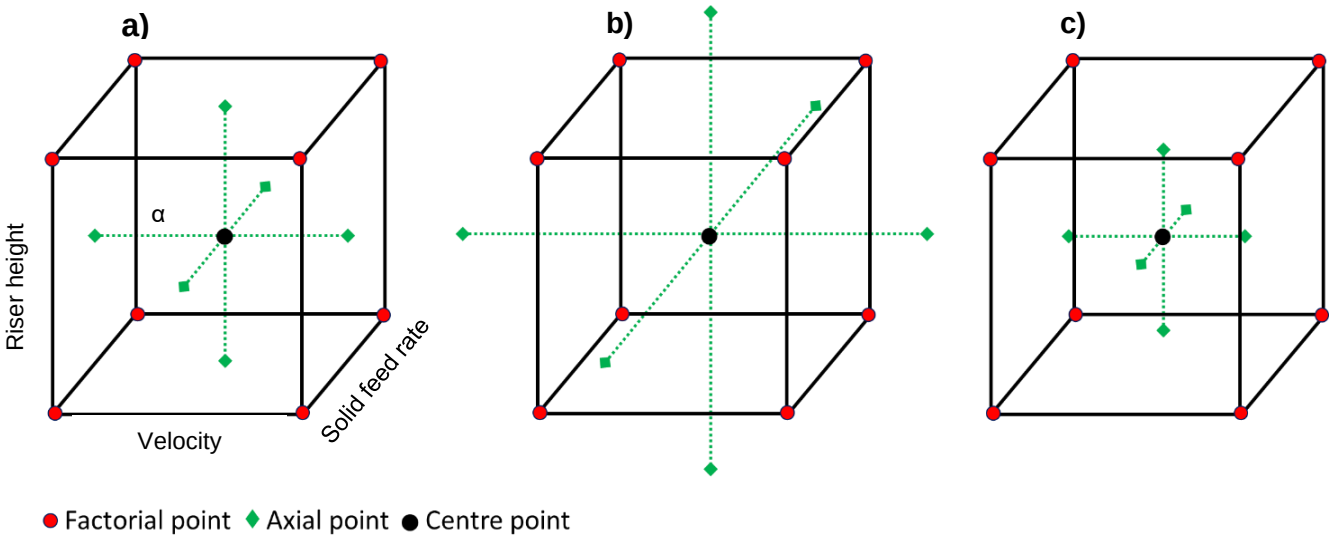

Figure 3.8: a) *Face centred CCD and* ***b)*** *circumscribed CCD and* ***c)*** *inscribed CCD (Adapted from Ranade and Thiagarajan, (2017))*[108]

However, more than three α levels for the riser height were experimentally difficult to achieve, making face-centred CCD's the most suitable option. Unfortunately, face-centred CCD's are not rotatable, but according to the literature good designs may still be achieved in the absence of rotatability[104]. Since axial experimental runs were added, the general regression model from Equation 3-4 could be replaced by Equation 3-5 to include quadratic terms if necessary[107,109,110]. The coefficients (β) in Equation 3-5 were determined according to the method of least squares, as given in Equation 3-6[104]. An example of a typical design matrix X for a face-centred CCD is provided in Table I3 of Annexure I. Equation 3-6 was used to determine the coefficients for an individual regression equation for every measured response y.

$$\hat{y} = \beta_0 + \beta_A A + \beta_A A^2 + \beta_B B + \beta_B B^2 + \beta_c C + \beta_c C^2 + \beta_{AB} AB + \beta_{BC} BC + \beta_{AC} AC \qquad \textbf{3-5}$$

$$\beta = (X^T X)^{-1}(X^T y) \qquad \textbf{3-6}$$

Where $\hat{y}$ is the predicted response, β is a $M \times 1$ coefficient vector matrix, X is the $N \times M$ design matrix (-1, 0, 1 & α, -α if applicable), and y is the measured response in a $N \times 1$ vector matrix. M equals the number of coefficients to be determined (including the constant β_0) whereas N represents the total number of experimental observations.

3.3.2.3 Statistical model adequacy

Coefficient of determination

The coefficient of determination (R^2) of each regression model was determined to indicate the extent to which the various models accounted for variance in the system[103,111]. The method for determining the coefficient of determination remained the same whether a full factorial design or a CCD was used. However, when the number of predictors in a statistical model increases, the R^2 value improves even though the model's fit remains unchanged or worsens, and this is termed R^2 inflation[111]. In such a case, inflation should be accounted for when determining the R^2. Since the number of experimental observations and model coefficients only varied when changing over from a linear to a quadratic approach, the formula used to compute R^2 is provided in Equation 3-7[112]. If the linear model was expanded upon by additional experimental observations or factors, the effect of inflation would have been considered and the same holds true for the quadratic models.

$$R^2 = 1 - \frac{SSE}{SST} \qquad \textbf{3-7}$$

In the previous equations SSE is the sum of the squared residuals as calculated by Equation 3-8, and SST is the total sum of squares for the measurements as calculated by Equation 3-9.

$$SSE = \sum_{i=1}^{n} (y_i - \hat{y}_i)^2 \qquad \textbf{3-8}$$

$$SST = \sum_{i=1}^{n} (y_i - \bar{y})^2 \qquad \textbf{3-9}$$

In the above expressions n refers to the total number of experimental observations (including the centre point runs) and, once again y_i refers to the measured response.

T-statistic

In order to determine the significance of the effect of each factor on the measured response, a test statistic was computed[104]. In the case of a central composite design, Equation 3-10 was used to obtain a vector matrix with each coefficient's t-statistic[104]. In the case of a 2^k full factorial design, the test statistic of all the regression coefficients (except for the constant) was the same, and that value was computed with Equation 3-11[104].

$$t_0 = \frac{\hat{\beta}_0}{\hat{\sigma}\sqrt{(X'X)^{-1}}} \quad \textbf{3-10}$$

$$t_0 = \hat{\sigma} \div \left(\sum_{i=1}^{n}(x_i - \bar{x})\right)^{\frac{1}{2}} \quad \textbf{3-11}$$

In the above equations, $\hat{\beta}_0$ represents the coefficient under investigation, X is the design matrix in coded units (-1,0 & 1) and x_i represents the entries in the i^{th} row of the design matrix. Any column of the design matrix was used to extract the values of x_i, except for the column corresponding to the constant. The constant's column (which is a column filled with 1's) was used to determine the t-statistic of the constant only. The mean $\bar{x}$, was equal to zero for all predictor columns (except the column belonging to the constant) since X was orthogonal. This value was used to determine the t-statistic for the constant as well. For the full factorial design and for the CCD, $\hat{\sigma}$ represents the square root of the mean square error of the predicted response, and it was calculated from Equation 3-12[113]. The computed t-statistic, together with the t-distribution, was then used to calculate a P-value for each model coefficient which will be discussed in the next section.

$$\hat{\sigma}^2 = MSE = \frac{SSE}{n - p - 1} \quad \textbf{3-12}$$

Where n and p represent the total number of experimental observations (including the centre point runs) and the number of model coefficients (excluding the constant), respectively[113].

P-value of the t-statistic

The t-distribution was used to determine P-values, and extracts from the t-distribution at the relevant degrees of freedom, are provided in Table I4 of Annexure I[105]. Once a t-statistic has been determined, the row corresponding to the correct degrees of freedom ($n - p - 1$) or ($n_c - 1$) when evaluating curvature) in the t-distribution was selected, and the t-statistic was compared to each value in that row[105]. Once a matching value has been obtained in the tabulated data, the alpha value corresponding to that table entry was identified. The alpha value was compared to the predefined confidence interval of 0.95[104]. If the alpha value was below 0.05, the null hypothesis was rejected, and the effect of that regression coefficient had a significant effect on the predicted response[105]. Conversely, any alpha value exceeding 0.05 indicated that the regression coefficient did not significantly affect the predicted response. If the t-statistic that was calculated was not equal to a value in the t-distribution table, the two values corresponding to the upper and lower limits of that calculated t-statistic were reported[104]. In addition, interpolation was used to find an alpha value between those two identified alpha values to obtain a single estimate. The interpolation formula is provided and discussed in Annexure I.

3.3.3 Experimental program

As discussed in the preceding subsection, a 2^3 full factorial design approach was followed, which is represented by the treatment combinations in brackets in Table 3-9. To enable the addition of quadratic terms when necessary, axial experimental points were added, and these are indicated without brackets in Table 3-9. Therefore, the final experimental program with all 20 of its treatment combinations is indicated in Table 3-9 where the values (-1, 0, 1) represent the low, medium and high settings of each independent variable, respectively.

The data that was collected from each experimental treatment combination was used to calculate the seven parameters in Table 3-10. The response of each parameter to the changing conditions was captured within the regression models that were constructed from the 2^3 as well as the CCD design approaches. The VBA code that was written for each analysis method is provided in Annexure J. Finally, the adequacy of the linear and quadratic models was determined according to Section 3.3.2.3.

Table 3-9: *Face-centred CCD that was used as the experimental program for this study*

Experiment number	Inlet gas velocity	Solids feed rate	Riser height
[1]	-1	1	1
2	-1	0	0
[3]	1	1	-1
[4]	1	1	1
[5]	0	0	0
[6]	0	0	0
7	0	0	0
8	0	0	0
9	0	-1	0
10	0	1	0
11	0	0	0
12	1	0	0
[13]	-1	-1	1
[14]	-1	1	-1
15	0	0	-1
[16]	1	-1	-1
[17]	-1	-1	-1
[18]	1	-1	1
19	0	0	1
20	0	0	0

Table 3-10: *Responses considered in the factorial design analysis*

Response	Unit	Description	Calculation
$\boldsymbol{RNI(\varepsilon_s)_{bot}}$	-	RNI(ε_s) at the bottom port.	Equation 2-12
$\boldsymbol{RNI(\varepsilon_s)_{mid}}$	-	RNI(ε_s) at the middle port.	Equation 2-12
$\boldsymbol{RNI(\varepsilon_s)_{top}}$	-	RNI(ε_s) at the top port.	Equation 2-12
$\bar{\varepsilon}_{s_{low}}$	-	Average solids holdup at the bottom port.	Equation 2-10
$\bar{\varepsilon}_{s_{med}}$	-	Average solids holdup at the middle port.	Equation 2-10

$\bar{\varepsilon}_{s_{high}}$	-	Average solids holdup at the top port.	Equation 2-10
ΔP_{riser}	Pa	Pressure drop across the riser.	$\Delta P_{riser} = P_{(PT-09)} - P_{(PT-01)}$
$\Delta P_{section}$	Pa	Pressure drop across the installed cylindrical sections.	$[\Delta P_{riser} = P_{(PT-09)} - P_{(PT-03)}]$*

PT-09, PT-03 and PT-01 refer to the transmitters indicated in Figure 3.1.

3.3.4 Experimental data collection

3.3.4.1 Velocity data

All the air velocity measurements were made using a Testo 440 hot-wire anemometer, and further details of the instrument are provided in Annexure K1. When measuring velocity at the riser inlet, the tip of the anemometer was placed at the centre of the riser inlet during operation, and the velocity data was displayed on a handheld device that communicated with the probe via Bluetooth. The influence of the anemometer's position on the velocity measurement was investigated by recording the average velocity at 5 locations across the inlet area, as illustrated by Figure 3.9. At each measurement point, the velocity was recorded every three seconds for one minute, and a correction factor was calculated using Equation 3-13. In all cases, the riser inlet velocity measurements were multiplied by the correction factor, which was equal to 1.06, to adjust for flow variations across the riser inlet.

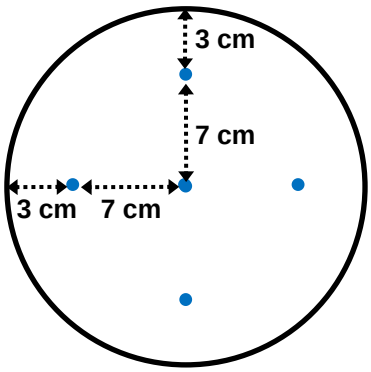

Figure 3.9: *Velocity measurement locations at the riser inlet*

$$correction = \frac{U_{Average}}{U_{measured}} = 1.06 \quad \textbf{3-13}$$

Where $U_{Average}$ and $U_{measured}$ represent the average of the five measurement locations and the value of the inlet air velocity in the centre of the riser, respectively.

3.3.4.2 Pressure and temperature data

The pressure and temperature at various points along the riser were measured using installed flush (i.e., non-intrusive) pressure transmitters and resistance temperature detectors. The details of these instruments are provided in Annexure K1. All of the electronic equipment was connected to and controlled from a PLC. During sorbent sampling, the non-isokinetic probe had to be inserted or withdrawn from the sampling ports. This temporarily altered the flow conditions within the riser since fluctuations in the pressure indicators could be observed. For this reason, the pressure and temperature data was recorded after the sorbent sampling has been completed and before an experimental run was ended. Once the sampling ports were sealed and the fluctuations in the pressure data reached a minimum, the pressure and temperature data was recorded every five seconds for a duration of five minutes and the data was exported to an excel file.

3.3.4.3 Non-isokinetic sampling

To determine the local mass flow rates of the hydrated lime inside the riser during a run, a non-isokinetic sampling probe was constructed. A diagram of the probe is provided in Figure 3.10, and photos as well as the dimensions thereof, have been included in Annexure K2. The probe was connected to a vacuum line which could be partially opened or closed using a ball valve. A toggle valve was used to shut off the suction line while repositioning the sampler in the riser such that the ball valve could be kept open at a given setting. These valves were selected since the pressure drop across a needle valve was too severe and limited the suction velocity that could be obtained at the sampling tip. Behind the sampling tip of the probe, a lid was fastened across the sampling port of the riser. This ensured that the 90° angle between the probe and the riser wall remained in-tact while also minimising air flow into the riser through the port during sampling. The hydrated lime sample was allowed to accumulate on top of a glass fibre filter paper encased in a Perspex cylinder and held in place with a rubber seal. At every experimental treatment combination, the non-isokinetic sampler was used to collect samples at three different riser heights.

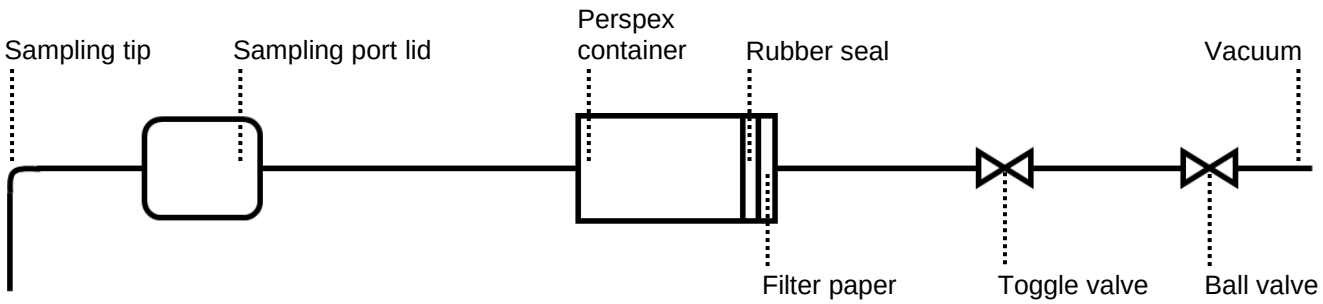

Figure 3.10: *Non-isokinetic sampling probe*

The height of every available sampling port that is illustrated in Figure 3.11 (a) is provided in Table 3-11. While one cylindrical section was installed, the three measurement ports labelled “B” in Figure 3.11 (a) were used. However, while two sections were installed, measurement ports “B1”, “B3” and “M2” were used. Lastly, in the case when three sections were installed, measurement ports “B2”, “M1” and “T1” were used. At each of the three ports chosen for an experiment, the iso-kinetic sampler was traversed from one radial sampling point to the next across the riser’s diameter. The seven radial sampling points that were used are illustrated in Figure 3.11 (b), and their positions are also provided in Table 3-11. A description of the non-isokinetic sampling procedure that was followed to extract solids from the riser during an experiment is provided in Annexure K2.

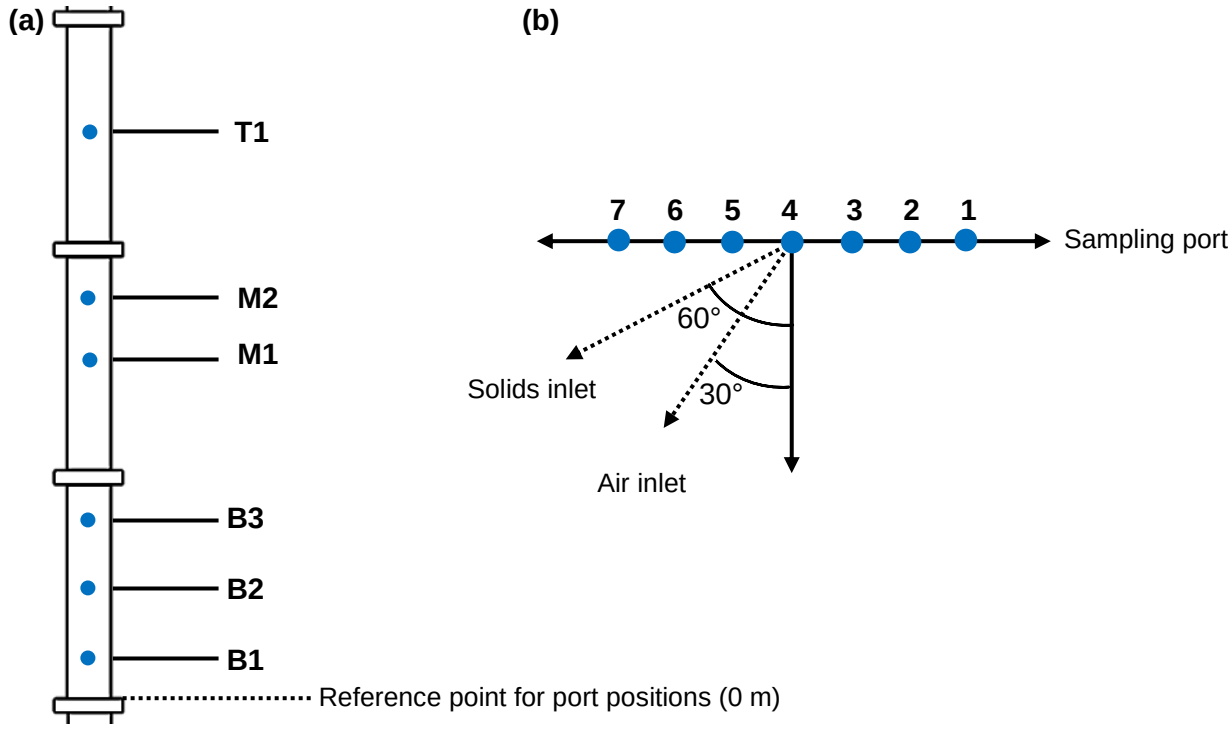

Figure 3.11: *The location of the* ***(a)*** *axial and* ***(b)*** *radial sampling points*

Table 3-11: *Axial and radial position of the sampling ports illustrated in Figure 3.11*

Distance from the reference point (m).	B1	B2	B3	M1	M2	T1
	0.2	0.5	0.8	1.5	1.7	2.5
Distance from the sampling port (cm).	**1**	**2**	**3**	**4**	**5**	**6**	**7**
	0	5	10	15	20	25	30

A difference exists between the suction velocity at the probe tip and the gas velocity at the measurement location when using a non-isokinetic sampling procedure. When the suction velocity is less than that of the carrier gas, a portion of the particles bypass the probe during sampling. On the other hand, too many particles are pulled into the sampler when its suction velocity exceeds that of the carrier gas. For this reason, the influence of the probe's suction velocity on the sampled mass was investigated. These tests were performed at an inlet air velocity of 6 m/s, and a solids feed rate of 0.04 kg/s and the riser at its medium height setting. Furthermore, the samples were collected at radial positions 3, 4 and 5 in Figure 3.11 (b) and at riser port "B3" in Figure 3.11 (a) according to the procedure in Annexure K2. The average of the three radial samples was computed and converted to a solids flux using Equation 3-14. This process was repeated at four additional probe suction velocities, and the result is illustrated in Figure 3.12.

$$G = \frac{\dot{m}}{A_{probe}} \qquad \textbf{3-14}$$

In the previous equation G is the mass flux in the probe tip in kg/m^{2}s, $\dot{m}$ is the mass flow rate in kg/s and A_{probe} is the area of the probe tip in m^2. Figure 3.12 illustrates that the solids flux at 2 m/s and 2.5 m/s deviated from the values of the remaining three measurements and this can be attributed to the unsteady nature of CFBs. However, from Figure 3.12, it can also be seen that the measured solids flux at 1.5 m/s and 3.5 m/s were equal. Furthermore, the standard deviation of the data was equal to 0.16 kg/m^{2}s, which equates to a percentage deviation of 9%. Thus, the probe's suction velocity was found to have a negligible influence on the collected sample mass. Consequently, the use of a non-isokinetic sampler was justified despite the observed fluctuations.

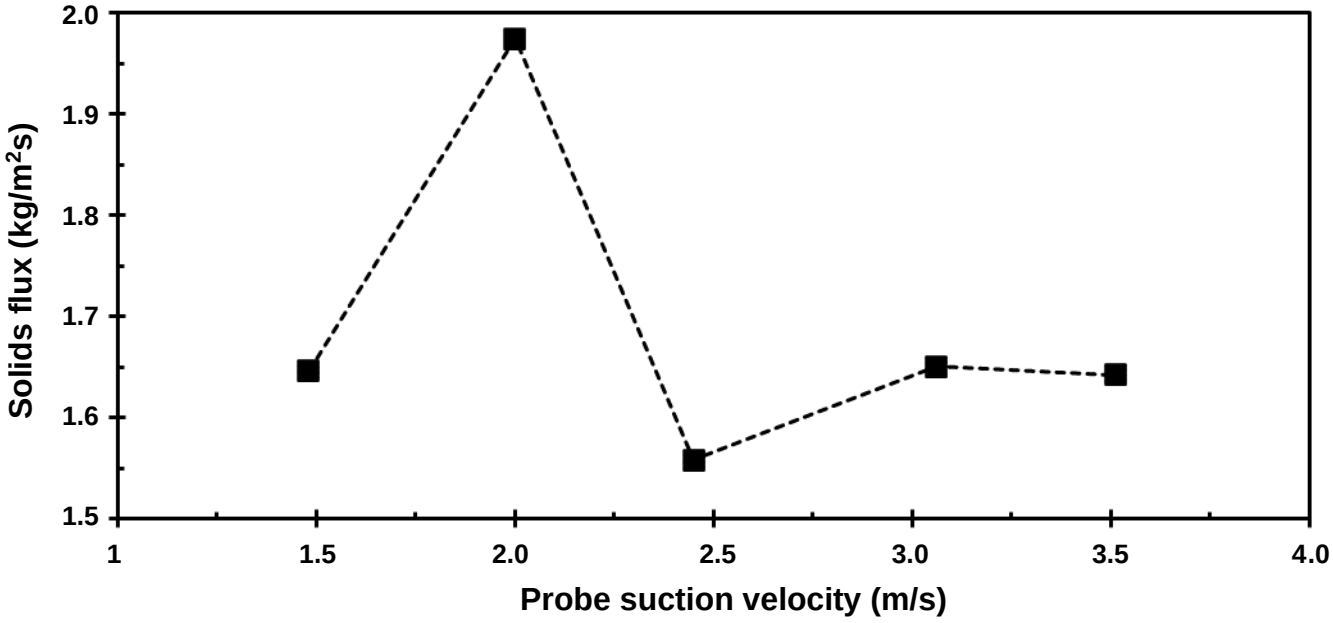

Figure 3.12: *The effect of probe suction velocity on the measured average solids flux in the centre of the riser (U_0= 2.8 m/s and G = 0.57 kg/m^{2}s)*

3.4 APPLICATION OF SIMILARITY PARAMETERS

By applying the similarity parameters from Section 2.2.2, the operating parameters of large-scale FGD-CFB units can be adapted for a laboratory-scale unit and vice versa. Upon inspection of Table 2-2 in Section 2.2.2, it can be seen that the operating conditions provided by Zhou et al. (2011) are within the range of acceptable values reported for industrial-scale FGD-CFB units throughout the literature. For this reason, their operating conditions were plugged into the three similarity parameters most often used for scaling purposes. The results are provided in Section A of Table 3-12. Target operating conditions for the setup in this study could be determined via the data in Section A of Table 3-12. To do this, the fixed experimental parameters pertaining to this work, as provided in Section B of Table 3-12, were used. These parameters included the air and particle densities, the riser's inner diameter and the fluidising air viscosity. From the Froude number in Section A together with the riser's inner diameter from Section B, a target superficial air velocity within the riser could be determined, and the result is provided in Section C. From the second similarity parameter in Section A in Table 3-12 and the newly calculated air velocity, a target solids flux for the system could be specified.

Table 3-12: *Similarity parameters of an industrial scale FGD-CFB unit*

A: Similarity parameters from Zhou *et al.*, (2011)[64]		
Similarity parameter	Value	Unit
$\boldsymbol{Fr_D = U_0^2/gD}$	0.47	$(-)$
$\boldsymbol{G_s/\rho_p U_0}$	1.61×10^{-4}	$(-)$
$\boldsymbol{U_0/U_t}$	36.08	$(-)$
B: Fixed parameters for this study		
Fixed parameter	Value	Unit
$\boldsymbol{\rho_p}$	2883	kg/m^3
$\boldsymbol{D}$	0.30	m
$\boldsymbol{\rho_f}$	1.19 (@22.9℃)	kg/m^3
$\boldsymbol{\mu_f}$	1.83×10^{-5} (@22.9℃)	$Pa \cdot s$
C: Resulting operating parameters applicable to this study		
Calculated parameter	Value	Unit
$\boldsymbol{U_0}$	1.18	m/s
$\boldsymbol{G_s}$	0.54	$kg/m^2 s$
$\boldsymbol{d}$	19.44	μm

In addition to the operating parameters, a target diameter for the hydrated lime particles was obtained using the third similarity parameter in Section A of Table 3-12. This was done by populating Equation 3-15 with the fixed parameters for this study and calculating the particle size that would ensure a $\mathrm{U_0/U_t}$ ratio equal to that in Table 3-12. The resulting operating parameters that were applicable to this study are given in Section C of Table 3-12.

$$U_t = \left(\rho_p - \rho_f\right) \times \frac{{d_p}^2 g}{18\mu_f} \qquad \textbf{3-15}$$

The superficial gas velocity from Section C in Table 3-12 was converted to an inlet velocity, and the solids flux was converted to a solids feed rate.

The final target operating conditions obtained for this study through the similarity parameters are provided in the third column of Table 3-13. The true operating conditions that were specified for this study, according to Section 3.3.1, are reported in the fourth column of Table 3-13 for comparison.

Table 3-13: *The operating conditions obtained via similarity parameters versus those truly used during the experimental phase*

Experimental parameter	Unit	Values obtained from scaling parameters	Values specified for this study
$\boldsymbol{U_{inlet}}$	m/s	2.65	$4.3 - 8.6$
$\boldsymbol{U_{riser}}$	m/s	1.18	1.84
$\dot{\boldsymbol{m}}$	kg/s	0.04	$0.04 - 0.06$
$\boldsymbol{d}$	μm	19.49	23.63
$\boldsymbol{U_{TR,max} \times 2}$	m/s	1.69	1.84

When comparing the data in Table 3-13, it is seen that the lower end of the conditions that were used in this study are comparable to the values obtained via the similarity calculations. The only exception was the inlet air velocity which had a minimum value of 4.3 m/s, which is 60% higher than the recommended value. Upon further investigation, it was determined that the unit described by Zhou *et al.,* (2011)[64] in their publication operated at a riser superficial gas velocity that exceeded twice its transport velocity as recommended throughout the literature. The calculation procedure is provided in Annexure L. However, the target inlet air velocity of 2.65 m/s would deliver a superficial gas velocity of 1.18 m/s for this study according to the similarity parameters. In the final row of Table 3-13, the superficial gas velocity, which would be equal to twice the transport velocity, is reported. By comparing this condition to the riser's superficial gas velocity in the same column, it can be seen that compliance with the recommended operating velocity would be lost since the recommended superficial gas velocity (1.18 m/s) is less than twice the transport velocity (1.69 m/s). Consequently, higher velocities were used in this work which explains the discrepancy between the specified values for this work and those recommended by the similarity parameters. In conclusion, the chosen operating conditions facilitated dynamic similarity between this study and FGD-CFB units from the literature, enabling the comparison of the findings in Chapter 5 to the previous work.

CHAPTER 4 – CFD MODEL CONSTRUCTION

4.1 MODEL DEVELOPMENT

In this chapter the CFD model construction is explained. Initially, the most suitable model equations for this hydrodynamic study are motivated. The following paragraphs explain the simplifications that were made with regards to the turbulence model, the Eulerian-Lagrangian model and the drag model since these parameters are often adjusted throughout literature to achieve improved predictions. Afterwards, the discretization of the geometry and the solution algorithms within the model were motivated. Based on these discussions, the software specific actions are provided in Section 4.2 and 4.3.

4.1.1 Fluid mechanics

4.1.1.1 Conservation equations

In computational fluid dynamic (CFD) applications, the Navier-Stokes equations are applied to model the flow of incompressible fluids. When a fluid has a Mach number lower than 0.2 and a sufficiently low solid volume fraction, a general rule of thumb is to treat it as incompressible[60]. Hence, the Mach number based on the flow velocity of the fluid that will allow for the assumption of incompressibility to be evaluated was calculated using Equation 4-1[60].

$$M = \frac{\boldsymbol{U_f}}{c} < 0.2 \qquad \textbf{4-1}$$

The speed of sound in dry air is approximately 331.5 m/s at 0°C, with speed increasing by approximately 0.6 m/s for each 1 degree Celsius rise in temperature[114]. It further increases as the humidity of the fluid rises[115]. According to these conditions, the fluid velocity would have to be at least 66.3 m/s at 0°C before compressibility would have to be considered. Furthermore, the discussions in Section 4.1.1.3 and 4.3.2.2 indicates that the solids volume fractions were sufficiently low. Because of this and the low velocities that were used in the study, incompressible flow could be assumed, and the Navier stokes equations as provided in Equation 4-2 could be used[60].

$$\rho \frac{d\boldsymbol{u}}{dt} = \rho \boldsymbol{g} - \nabla \mathrm{P} + \mu \nabla^2 \boldsymbol{u} \qquad \textbf{4-2}$$

Where, u represents the fluid velocity, ρ, μ, P represent the fluid density, dynamic viscosity and pressure, respectively and $\nabla = \partial/\partial x + \partial/\partial y + \partial/\partial z$ represents the divergence in cartesian coordinates. However, the fluid and flow variables' instantaneous values differed from their mean values due to turbulence[60,116,117]. This is illustrated in Figure 4.1, where the blue line illustrates the mean value of the velocity at a point, and the black line represents the instantaneous value thereof.

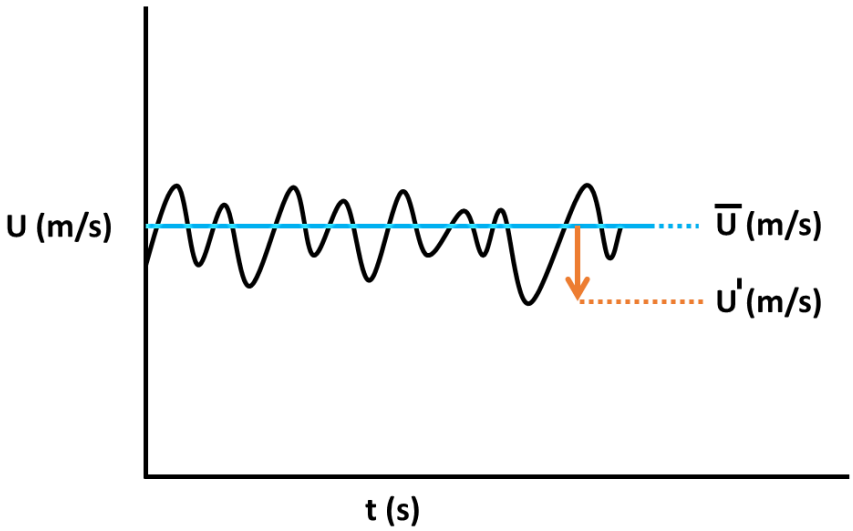

Figure 4.1: *The fluctuating nature of velocity over time in turbulent flow (Adapted from Welty et al., 2015)*[60]

The CFD grid that would have been required to capture these fluctuations would have such a fine resolution that a numerical solution would be impractical (it would take too much time to converge). For this reason, the Reynolds averaged Navier-Stokes (RANS) equations were used instead. During the time averaging process, all the fluid and flow variables were written in terms of their mean and fluctuating components as illustrated by Equation 4-3, where velocity was used as an example[60].

$$\boldsymbol{U_x} = \overline{\boldsymbol{U_x}}(x, y, z) + \boldsymbol{U'_x}(x, y, z, t) \qquad \textbf{4-3}$$

Where $\bar{\phi}$ and ϕ',with ϕ any variable represents the mean and fluctuating components of that variable.

The resulting RANS equations are presented by Equation 4-4 to the following assumptions[60,116]:

- Incompressible flow,
- Constant fluid viscosity and
- Steady flow.

$$\rho \frac{\partial \overline{\boldsymbol{U_\iota U_J}}}{\partial x_i} = -\frac{\partial \bar{P}}{\partial x_i} + \frac{\partial}{\partial x_j}\left(\mu \frac{\partial \overline{\boldsymbol{U_\iota}}}{\partial x_j} - \rho \overline{\boldsymbol{U'_\iota U'_J}}\right) + \boldsymbol{F_B} \qquad \textbf{4-4}$$

In the above expression μ is the dynamic viscosity of the fluid and F_B represents the body forces per unit volume. Since CFB's are unsteady by nature, the RANS equations were instead written as the URANS (unsteady RANS) equations. As will be discussed in the following sections, two-way coupled Eulerian-Lagrangian simulations were performed, and the applicable URANS formula is presented by Equation 4-5[118,96,119]. The RANS and URANS equations represent the conservation of momentum. Equation 4-6 represents the conservation of energy from the first law of thermodynamics, while Equation 4-7 represents the conservation of mass[15,97].

$$\frac{\partial \varepsilon_f \overline{\boldsymbol{U_\iota}}}{\partial t} + \frac{\partial \varepsilon_f \overline{\boldsymbol{U_\iota U_J}}}{\partial x_i} = -\frac{\varepsilon_f \partial \bar{P}}{\rho_f \partial x_i} + \frac{\partial}{\partial x_j}\left(\varepsilon_f \left(\nu_f \frac{\partial \overline{\boldsymbol{U_\iota}}}{\partial x_j} - \overline{\boldsymbol{U'_\iota U'_J}}\right)\right) + \varepsilon_f \boldsymbol{F_B} + \boldsymbol{F_M} \qquad \textbf{4-5}$$

$$\frac{\partial(\rho E)}{\partial t} + \nabla\left(\rho E \boldsymbol{U_f}\right) = \boldsymbol{F_B} \cdot \boldsymbol{U_f} + \nabla \cdot \left(\boldsymbol{U_f} \cdot \boldsymbol{\sigma}\right) - \nabla \cdot q + \boldsymbol{S_E} \qquad \textbf{4-6}$$

$$\frac{\partial\left(\varepsilon_f \rho_f\right)}{\partial t} + \nabla \varepsilon_f \rho_f \boldsymbol{u_f} = 0 \qquad \textbf{4-7}$$

In this set of equations ν represents the kinematic viscosity of the fluid, F_M is the momentum source per unit volume, E represents the energy per unit mass, q and σ is the heat flux and stress tensor, respectively and S_E is the energy source per unit volume.

4.1.1.2 Turbulence model

Three methods exist with which the turbulence in fluid flow may be resolved, and they are provided for comparison in Table 4.1[120]. In the table RANS and URANS methods were identified as the least computationally expensive, and this can be attributed to their reliance on empirical correlations.

However, numerous CFB studies followed a large eddy simulation (LES) approach[29,90,97]. This means that the turbulence scales above a certain threshold were directly resolved using a sufficiently fine grid, whereas the remaining scales were modelled using the Smagorinsky turbulence model. However, the LES as well as the direct numerical simulation (DNS) approaches, proved to be too computationally expensive for the large-scale CFB application in this work. For this reason, only the turbulence models belonging to the RANS and URANS categories were considered.

Table 4-1: *Simulation aspects associated with different turbulence modelling techniques (Adapted from Xiao & Cinnella, 2019)*[120]

Turbulence modelling method	***RANS/ URANS***	***LES***	***DNS***
Degree of modelling required	Full	Only for flow scales below a cut-off threshold	Zero
Degree of resolved turbulence	Zero	Only for flow scales above a cut-off threshold	Full
Comparison of computational cost	Lowest	Intermediate	Highest
Comparison of mesh	Coarsest	Intermediate	Finest
Simulation time required	Lowest	Intermediate	Highest

The second to last term in Equation 4-4 arose during the Reynolds averaging process and is called the Reynolds stress term. The Reynolds stress quantified the contribution of turbulence to the total shear stress tensor in the fluid[60]. In order to calculate the Reynolds stress, the Boussinesq hypothesis as given by Equation 4-8, was used[62,119,115].

$$\tau_{ij} = -\overline{\boldsymbol{U'_i U'_j}} = -\frac{2\kappa}{3} + \mu_t \left(\frac{\partial \boldsymbol{U_i}}{\partial x_j} + \frac{\partial \boldsymbol{U_j}}{\partial x_i} \right) \qquad \textbf{4-8}$$

Here κ represents the turbulent kinetic energy and μ_t the turbulent eddy viscosity. Closure of the RANS and unsteady RANS equations was therefore achieved by solving the turbulent eddy viscosity (μ_t) in Equation 4-8. To do this, the eddies had to be considered.

Eddies are present in a wide range of sizes (henceforth referred to as length scales) in turbulent flow and are responsible for the dissipative nature thereof. Within the larger length scales, energy and momentum transport occur, and within the smallest length scale (Kolmogorov scale), energy is dissipated to heat[121]. To explicitly solve the RANS equations, it would be necessary to account for all the eddy length scales present in a specific flow. Unfortunately, this would be computationally expensive for the simplest cases, which is why the mean influence of eddies on the overall flow profile was approximated using turbulence models, as discussed previously[120].

Various turbulence models are available to calculate the turbulent eddy viscosity (from Equation 4-8), and the oldest solution technique entails algebraically calculating a mixing length[60]. However, solution techniques incorporating transport equations have become more popular given the improved accuracy when compared to algebraic approximations such as the mixing length approach[122]. For example, one-equation models contain one additional non-linear second-order partial differential equation that needs to be solved before the turbulent eddy viscosity can be determined[122]. Such equations have the general form given in Equation 4-9.

$$\mu_t = c\sqrt{\bar{e}} \qquad \textbf{4-9}$$

Where c is a model constant and $\bar{e}$ is the mean kinetic energy. The mean kinetic energy in Equation 4-9 has to be solved using both its transport equation and an algebraic specification of the mixing length, which is incorporated into the calculation of $\bar{e}$. In the near-wall sublayer, the algebraic approximation of the mixing length is reasonably successful, which is why one-equation models are mainly limited to near-wall flow investigations[122,123]. However, two-equation models are prevalent in industrial applications since it eliminates the need to algebraically specify a mixing length[122,123]. From the available two-equation models, the k-ε and k-ω models are popular choices for most applications, with the latter being preferred for swirling flows[15]. The standard k-ε (SKE) equation has a PDE for the turbulent kinetic energy (Equation 4-10) and for the dissipation rate (Equation 4-11), after which the calculation of the turbulent eddy viscosity follows in Equation 4-12[121,124]. With the turbulent eddy viscosity calculated, all of the terms in the RANS equations could be solved[16,20,125].

$$\frac{\partial}{\partial t}(\rho\kappa) + \nabla(\rho\kappa\overline{\boldsymbol{u}}) = \nabla\left[\left(\mu + \frac{\mu_t}{\sigma_\kappa}\right)\nabla\kappa\right] + P_\kappa - \rho(\varepsilon_d - \varepsilon_{d0}) + S_\kappa \qquad \textbf{4-10}$$

$$\frac{\partial}{\partial t}(\rho\varepsilon_d) + \nabla(\rho\varepsilon_d\overline{\boldsymbol{u}}) = \nabla\left[\left(\mu + \frac{\mu_t}{\sigma_{\varepsilon_d}}\right)\nabla\varepsilon_d\right] + \frac{\varepsilon_d}{\kappa}C_{\varepsilon_d 1}P_\varepsilon - C_{\varepsilon_d 2}f_2\rho\left(\frac{{\varepsilon_d}^2}{\kappa} - \frac{{\varepsilon_{d0}}^2}{\kappa}\right) + S_{\varepsilon_d} \quad \textbf{4-11}$$

$$\mu_t = \rho C_\mu f_\mu \frac{\kappa^2}{\varepsilon_d} \quad \textbf{4-12}$$

Where all quantities pertain to the fluid phase, κ is the turbulent kinetic energy, ε_d is the turbulent dissipation rate and $\sigma_\kappa, \sigma_{\varepsilon_d}, C_\mu, C_{\varepsilon_d 1}, C_{\varepsilon_d 2}$ are model constants, P_κ & P_ε are production terms, f_μ and f_2 are damping factors and S_κ & S_{ε_d} are user defined source terms. Another factor to consider was that the k-ε equations perform poorly in the presence of adverse pressure gradients and cannot predict flow separation accurately as a result thereof[121,123]. Modifications to the k-ε equation enhance its predictive capability and lessen its shortcomings. Such a modification is the realizable k-ε (RKE) equation, which differs from the SKE in two ways. The first difference is a different set of equations for the dissipation rate presented by Equations 4-13 - 4-15[126,127].

$$\frac{\partial}{\partial t}(\rho\varepsilon_d) + \nabla(\rho\varepsilon_d\overline{\boldsymbol{u}}) = \nabla\left[\left(\mu + \frac{\mu_t}{\sigma_{\varepsilon_d}}\right)\nabla\varepsilon_d\right] + C_{\varepsilon_d 3}S_\varepsilon - C_{\varepsilon_d 2}\frac{\kappa}{\kappa + \sqrt{\overline{\boldsymbol{u}}\varepsilon_d}}\rho\left(\frac{{\varepsilon_d}^2}{\kappa} - \frac{{\varepsilon_{d0}}^2}{\kappa}\right) + S_{\varepsilon_d} \quad \textbf{4-13}$$

$$C_{\varepsilon_d 3} = max\left(0.43, \frac{\eta}{\eta + 5}\right) \quad \textbf{4-14}$$

$$\eta = \frac{S(\kappa)}{\varepsilon_d} \quad \textbf{4-15}$$

S_ε in the equations above is a source term, and S may be calculated using **4-16**. The second difference lies within the calculation of the turbulent eddy viscosity, where the value of C_μ is approximated using Equation 4-16 rather than a constant[126,127]. This version of the standard equation normally produces superior results when compared to the original equations and, at the very least, provides similar results. However, since the degree of flow separation was insignificant in this study, the SKE equations proved to be sufficient.

$$C_\mu = \left(A_0 + A_s\overline{\boldsymbol{u}}^*\frac{\kappa}{\varepsilon_d}\right)^{-1} \quad \textbf{4-16}$$

Where A_0 = 4.04 with A_s, ϑ, W, S (which is the strain rate), $\bar{u}^*$and $\widetilde{\Omega_{ij}}$ are calculated by Equations 4-17 - 4-22 respectively.

$$A_s = \sqrt{6}\cos(\vartheta) \quad \textbf{4-17}$$

$$\vartheta = \frac{1}{3}\arccos\left(\sqrt{6}W\right) \quad \textbf{4-18}$$

$$W = 2^{1.5}\frac{\widetilde{S_{ij}}\widetilde{S_{jk}}\widetilde{S_{ki}}}{S^3} \quad \textbf{4-19}$$

$$S = \sqrt{2\widetilde{S_{ij}}\widetilde{S_{ij}}} \quad \textbf{4-20}$$

$$\bar{u}^* = \sqrt{\widetilde{S_{ij}}\widetilde{S_{ij}} + \widetilde{\Omega_{ij}}\widetilde{\Omega_{ij}}} \quad \textbf{4-21}$$

$$\widetilde{\Omega_{ij}} = \frac{1}{2}\left(\frac{\partial\overline{\boldsymbol{u_i}}}{\partial x_j} - \frac{\partial\overline{\boldsymbol{u}}_{\boldsymbol{j}}}{\partial x_i}\right) \quad \textbf{4-22}$$

4.1.1.3 Eulerian-Lagrangian and Eulerian-Eulerian models

Both the Eulerian-Lagrangian (E-L) and Eulerian-Eulerian (E-E) techniques are available to solve multi-phase flows in a CFD environment. When the former is chosen, the carrier phase is modelled within an Eulerian reference frame and the dispersed phase within a Lagrangian reference frame[30,128]. When using the E-L approach to model intermediate and high particulate loadings, particles may be grouped together based on their properties to create numerous parcels[15,129]. Thus, the carrier phase is modelled as a continuum, while parcels are individually tracked throughout the domain[99]. Some of the advantages of the E-L approach lie in its ability to more accurately account for particle collisions, including size distributions in drag calculations and its validity at a wide range of Stokes and Knudsen numbers[128].

The E-E approach, unfortunately, does not provide the same advantages and is less descriptive of individual particle physics. Nevertheless, it requires significantly less computational effort by using empirical correlations (or the kinetic theory) and by representing the phases as interpenetrating continua[20,25,30,99,130]. The lower computational effort together with its reasonable prediction capability, has increased its use for the simulation of industrial scale processes. Choosing between the E-E and E-L approach can at times be more straightforward than others. For example, when stratified or slug flow occurs, the two phases in the mixture can easily be distinguished from one another as illustrated by Figure 4.2.

In this case the E-E approach would achieve satisfactory results, since it regards all phases as continua[130]. However, most of the cases involving CFB's do not involve stratified or slug flows and this necessitates further analysis to determine which modelling approach is the most suitable for the application.

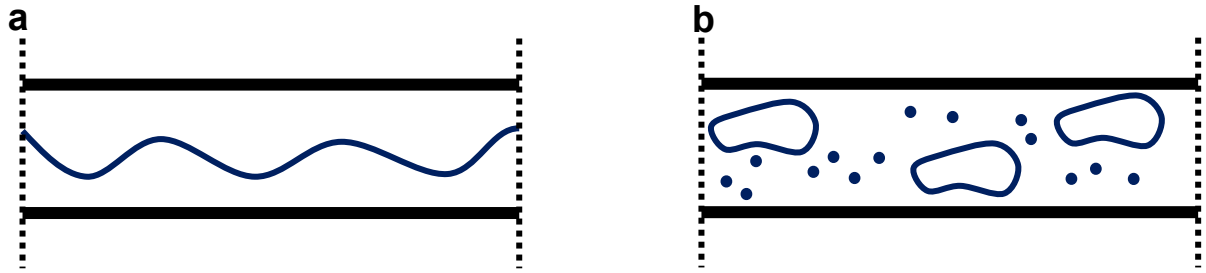

Figure 4.2: *Visual representation of* ***a)*** *stratified and* ***b)*** *slug flow*

If the volume fraction of the particles/dispersed phase is less than 10-12%, an Eulerian-Lagrangian approach is suitable since the high computational effort associated with this approach is accommodated by the lower amount of particles present[15,49]. Consequently, the user's guide for Fluent 6.1™ recommends using either the E-L or E-E method based on the particulate loading level. To quantify the particulate loading level, the inter-particle spacing can be approximated using Equation 4-23[130]:

$$\frac{L_k}{d_p} = \left(\frac{\pi}{6}\frac{1+\kappa}{\kappa}\right)^{1/3} \qquad \textbf{4-23}$$

Where L_k is a characteristic length, d_p the mean diameter of the dispersed phase and $\kappa = \frac{\epsilon}{\gamma}$. The particulate loading parameter and the material density ratio are calculated using Equation 4-24 and Equation 4-25 respectively[130,131].

$$\epsilon = \frac{\bar{\varepsilon}_s\, \rho_p}{\varepsilon_f \rho_f} \qquad \textbf{4-24}$$

$$\gamma = \frac{\rho_p}{\rho_f} \qquad \textbf{4-25}$$

Where $\bar{\varepsilon}_s$ is the solid volume fraction, ε_f is the void fraction, ρ is the density and subscripts p and f refer to the solid and fluid phases, respectively.

For high values of $\frac{L_k}{d_d}$ the two-phase flow is still sufficiently dilute to make use of the E-L approach[15]. However, should an intermediate load be identified using Equation 4-23, the dimensionless form of the Stokes number can be determined using Equation 4-26 for further analysis[130].

$$St = \frac{\rho_d \, d_d^2 \, \boldsymbol{U_k}}{18 \, \mu_c \, L_k} \qquad \textbf{4-26}$$

Where St is the Stokes number and subscripts, c & d refer to the carrier and dispersed phase, respectively, while subscript k refers to a characteristic quantity. Depending on the value of the dimensionless Stokes number, the following can be deduced for intermediately loaded flows[131]:

- If St << 1, then the particle follows the flow nicely, and the E-L method may be used.
- If St ~ 1, any model approach is applicable, and the least computationally expensive method may be chosen.
- If St >> 1, an E-E approach is recommended, although an E-L approach remains a possibility for certain simulations.

If an E-L approach is found to be applicable, the type of mathematical interaction between the fluid and particle phases has to be specified. A strong correlation exists between the solid volume fraction within the domain and the magnitude of the forces exerted between and within the different phases that are present. The first possible scenario is when the carrier phase governs the flow of the particles via drag and turbulence, but the forces that are exerted by the particles have a small to negligible effect on the fluid[132,133]. The parcels will almost exactly follow the streamlines in the flow, and this is termed one-way coupling[130]. The second scenario is termed two-way coupling and is observed when the forces of the carrier phase and the dispersed phase have a significant influence on each other[128,133]. This coupling should be expected when the mass loading becomes higher[134]. A third scenario is two-way coupling but with particle-particle interaction (friction and collision) and particle-fluid-particle interaction (streamlines in a dense phase) taken into consideration. This case is termed four-way coupling[133]. In such a case, the flow parcels can become completely dislodged from the carrier phase at regions with large gradients.

As can be expected, the computational effort increases as the coupling is increased from one-way coupling to two- or four-way coupling. Thus, Crowe *et al.,* (2012) stated that the choice of coupling is generally based on experience or parameter estimation techniques[135]. In an article by Elghobashi (1994) a map was presented which can be used to decide between one-, two- and four-way coupling based on the solid volume fraction, and the map was later adapted by Cortes and Gil (2007) to include the interparticle spacing at the boundaries using Equation 4-23[136,137].

In Figure 4.3, the map illustrating the most suitable coupling option for different particulate loading levels is illustrated, together with the limit at which E-E methods become more practical. From Figure 4.3 it is clear that one-way coupling is sufficient when the volume fraction of the solids (α_p) is less than 10^{-6} and the interparticle spacing (L_k/d_p) is more than 80. Between $10^{-6} < \alpha_p < 10^{-3}$ and $8 < L_k/d_p < 80$ two-way coupling should be considered since the increased volume of particles will alter the energy and momentum of the fluid phase. At higher solid volume fractions four-way coupling becomes necessary until such time as the solid volume percentage increases above 10%, in which case the E-E approach would be more practical given its lower computational resource requirement.

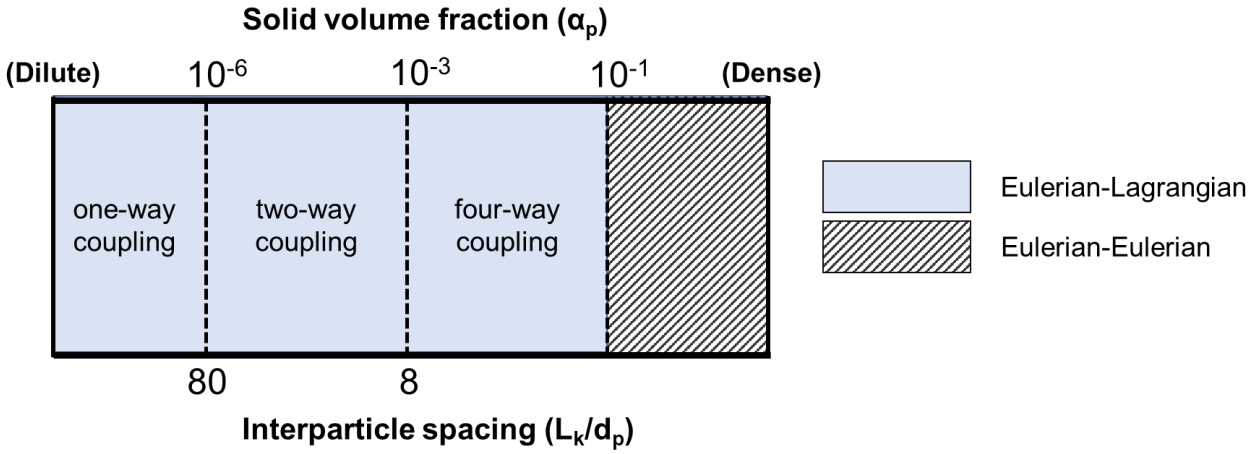

Figure 4.3: *Conditions under which different coupling types should be considered (Adapted from Elghobashi (1994) and Cortes and Gil (2007))*[136,137]

Another parameter to determine how closely a particle will follow the streamlines of the carrier phase is termed the particle relaxation time. The smaller the value of this parameter, the faster the particle will respond to forces exerted by the carrier phase. However, long particle relaxation times cause parcels to behave independently from the carrier phase. This parameter is easily calculated without the use of CFD modelling techniques using Equation 4-27[138,139,140].

$$t_p = \frac{\rho_p {d_p}^2}{18\mu_f} \quad \textbf{4-27}$$

Apart from being a useful indicator of the type of approach to be used, the force balance used to model the parcels in the E-L approach is often written in a way to include the relaxation factor. As mentioned previously, parcels of particles are individually tracked throughout the domain when using an Eulerian-Lagrangian approach. The properties of these individually tracked parcels are reported at fixed points within the domain as the particles pass through them. Essentially, the desired outcome of Lagrangian particle tracking is the parcel velocities since the velocity and position will differ from the streamlines of the carrier fluid due to various forces acting on the particles. For this reason, Newton's second law of motion is used to account for such forces and is provided in Equation 4-28[99,141,142]. By determining the parcel velocity, the position of the particles may be determined. The different forces that act on the particles are added together to equal the term on the left-hand side of Equation 4-28. In gas-solid two-way coupled systems, this usually includes the forces due to gravity, buoyancy, fluid pressure and drag[142].

$$\boldsymbol{Fnet} = m_p \boldsymbol{a} = m_p \frac{d\boldsymbol{U_p}}{dt} \quad \textbf{4-28}$$

Discrete element method (DEM) Eulerian-Lagrangian models differ from the general Eulerian-Lagrangian approach in the sense that it tracks individual particles instead of parcels[143]. By explicitly modelling the inter-particle interactions it requires more computational effort making the parcel approach more desirable for large-scale applications. Consequently, Equation 4-28 is solved for each parcel using information from previous time steps in order to obtain the particle trajectories that correspond to various groups of particles throughout the solution domain[129].

Once the particle trajectories have been obtained, the solid and fluid phases are coupled through the void fraction. The fluid phase treats the volume that is occupied by the solid phase as a void and vice versa, thereby limiting the available space through which the respective phases may flow. Furthermore, the change in momentum experienced by the parcels throughout the domain is accumulated across all cells and treated as a momentum source in the last term of Equation 4-5[29,143]. In the case of four-way coupling, an additional contact force is considered when solving Newton's second law of motion to account for inter-particle forces[143]. However, in general, this approach is not feasible for the simulation of large-scale applications, as was discussed previously.

4.1.1.4 Drag model

The drag force acting on the particles had to be calculated to solve Equation 4-28. This was done via Equation 4-29[50,144] while various drag models are available to calculate the drag coefficient C_D.

$$\boldsymbol{F_D} = \frac{1}{2}\rho_f \boldsymbol{U^2} C_D A \qquad \textbf{4-29}$$

Here F_D , C_D and A represent the drag force, drag coefficient and projected particle area respectively. The drag model that would be the most appropriate for any given simulation depends on the type of coupling required. When considering one-way and two-way coupling, the effect of inter particle interaction is negligible in comparison to the gas-particle interactions as discussed previously. Consequently, the effect of the particle volume fractions on the drag coefficient are usually neglected. Furthermore, CFD models are often simplified by assuming that all of the particles are spherical and these assumptions enable the use of the Schiller-Neumann drag model that is represented by Equation 4-30[50]. The Schiller-Neumann drag model is capable of providing a drag coefficient which has a maximum deviation of 5% from the standard drag coefficient for all particle Reynolds numbers below 800 – 1000[50,135].

$$\begin{aligned} C_D &= \frac{24}{Re_d}\left(1 + 0.15{Re_d}^{0.687}\right) && Re_d < 1000 \\ &= 0.445 && Re_d > 1000 \end{aligned} \qquad \textbf{4-30}$$

From a Reynolds number of 800 to 3000, the drag coefficient remains reasonably constant until the critical Reynolds number has been reached[135]. However, in dense particle flows, the particle-particle interactions significantly affect the hydrodynamics and must be accounted for when solving each particle position using Newton's second law of motion. Thus, much work has been done to improve existing drag formulations, the most notable being the development of heterogeneous drag models. Such models account for non-uniform and time-varying multiscale flow structures (such as clusters)[145], making these especially useful for CFB analysis.

Homogeneous drag models

Since homogenous drag models do not account for clustering during the calculation procedure, these require less computational effort[96,145]. However, reasonably accurate predictions may be obtained using homogeneous models if extremely fine grids of 2-4 times the particle diameter are used[145]. The previously discussed Shiller-Neuman drag model is an example of a homogeneous drag model. Other popular homogeneous drag models that have been mentioned in CFB studies include the Haider & Levenspiel, Clift, Liu, Koch-hill, Wen-Yu, Syamlal & O'Brien (O-S) and Gidaspow drag models. From these drag models the Haider & Levenspiel and Clift drag models are tailored for non-spherical particles while the Liu drag model is useful for deforming particles (such as droplets)[146,147,148].

The remaining four drag models were developed with the assumption that the particles of interest are spherical and rigid. Unfortunately, the Koch-hill model was originally designed for applications with fluid Reynolds numbers that are below 120[29,149] while the Wen-Yu model's peak performance is limited to dilute particle flows[20,90]. However, the O-S and Gidaspow drag models remain and are suited for CFB modelling since these account for the local void fractions in the riser. This is necessary since areas with high concentrations of particles will experience different drag forces when compared to dilute regions. Both of these models perform similarly but the Gidaspow model that is provided by the conditional formulas in Equation 4-31 is the predominant choice throughout literature that are centred around CFB's[30,96,97,125,99].

$$\boldsymbol{F_D} = \; 150\left(\frac{\mu_f \varepsilon_p}{\rho_p {\varepsilon_f}^2 {d_p}^2}\right) + 1.75\left(\frac{\rho_f \left|\boldsymbol{U_f} - \boldsymbol{U_p}\right|}{\varepsilon_f \rho_p d_p}\right) \qquad if\ \varepsilon_f > \varepsilon_{f,min}$$

$$\boldsymbol{F_D} = \; C_D \frac{3}{4}\frac{\rho_f}{\rho_p}\frac{\left|\boldsymbol{U_f} - \boldsymbol{U_p}\right|}{d_p}{\varepsilon_f}^{-2.65} \qquad if\ \varepsilon_f < \varepsilon_{f,min} \qquad \textbf{4-31}$$

$$C_D = \; 24\left(\frac{1 + 0.15(Re_d)^{0.687}}{Re_d}\right) \qquad if\ Re_d \; < \; 1000$$

$$C_D = 0.445 \qquad if\ Re_d \; \geq \; 1000$$

In this model $\varepsilon_{f,min}$ refers to the cut-off void fraction which is usually set to a value of 0.8. From Equation 4-31 it becomes apparent that the drag force and the drag coefficient will be approximated with different models depending on the average void fraction and the particle Reynolds number. The Gidaspow model is a combination of the Ergun equation and the Wen-Yu drag model, with the former being used under normal circumstances and the latter being preferred under dilute operating conditions[150]. Although this model accounts for local solid volume fractions, it is predominantly used in DEM modelling or in conjunction with LES turbulent methods to obtain more accurate particle or fluid information which aids with drag calculations[96,97,125].

Heterogeneous drag models

The most popular heterogeneous drag model found in numerical studies of CFB's is the Energy minimisation multiscale (EMMS) model[30,99,46,98]. This model is favoured since it accounts for the effect of clusters on the overall drag force experienced by the particles[99,145]. It achieves this by dividing the gas-solid flow into a dense phase, a dilute phase and an intermediate phase between the two, thereby capturing the effect of mesoscale structures on the hydrodynamics[99]. This has led to a drastic improvement in the predictive capability of CFD models that are applied to circulating fluidised beds. Although the EMMS models and all variations thereof outperform homogeneous drag models, these are computationally expensive especially when used in conjunction with DEM modelling[151]. That being said, the EMMS method has been successfully applied to the general Eulerian-Lagrangian approach as well[99].

4.1.2 Discretization

In the CFD environment, the partial differential equations (PDE's) that describe the flow of fluids and solids are solved using numerical methods. In general, either the finite difference method (FDM), finite element method (FEM) or finite volume method (FVM) can be used for this purpose[152]. The FVM is usually preferred of these three options, given its independence from the type of mesh structure chosen[29]. STAR-CCM+™ uses the FVM for most simulations and utilises an integral form of the governing equations. Three main steps are performed during the FVM, which are (i) the mesh generation, (ii) the discretisation of PDE's and (iii) the solution of the system of equations[153].

During step one, the geometry is separated into discrete control volumes. Figure 4.4 provides the three most common geometrical shapes used for meshing. From left to right, a hexahedral, tetrahedral and polyhedral cell can be seen. A hexahedral mesh is known to cause minimal numerical diffusion, leading to more accurate predictions[154,155]. Unfortunately, the construction of hexahedral meshes is time-consuming and presents difficulties when used in complex geometries. Conversely, a tetrahedral mesh is easier to construct, but the cells aren't suitable for excessive stretching. Thus, a large number of cells are required to divide the domain into control volumes which increases the computational effort[154,155,156].

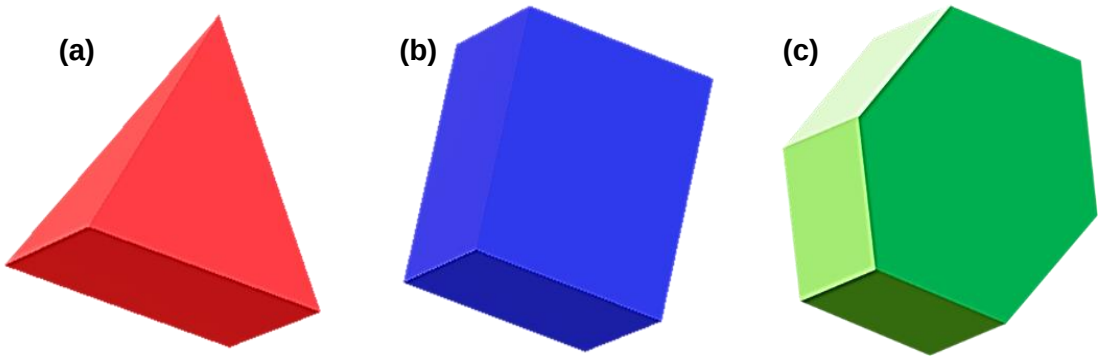

Figure 4.4: *Different cells used for CFD discretisation:* ***(a)*** *Hexahedral* ***(b)*** *tetrahedral and* ***(c)*** *polyhedral cells (Adapted from Sosnowski et al., (2017))*[154]

A polyhedral mesh combines the advantages of both hexahedral and tetrahedral meshes. Polyhedral meshes are often derived from tetrahedral cells, which makes these suitable for complex geometries[154]. However, the cells of a polyhedral mesh can be stretched to lower the number of control volumes that are required for a CFD solution. Furthermore, the numerical diffusion associated with a polyhedral mesh is lower than that of tetrahedral meshes and in some cases outperform hexahedral meshes as well, since a larger number of neighbouring cells are present[154]. These characteristics lead to a better approximation of the gradients between different mesh cells[155]. The control volumes resulting from the meshing procedure are distributed such that the faces are situated midway between two nodes, as illustrated by Figure 4.5. Regardless of the type of mesh chosen, the information pertaining to each variable is stored in the nodes during the calculation procedure.

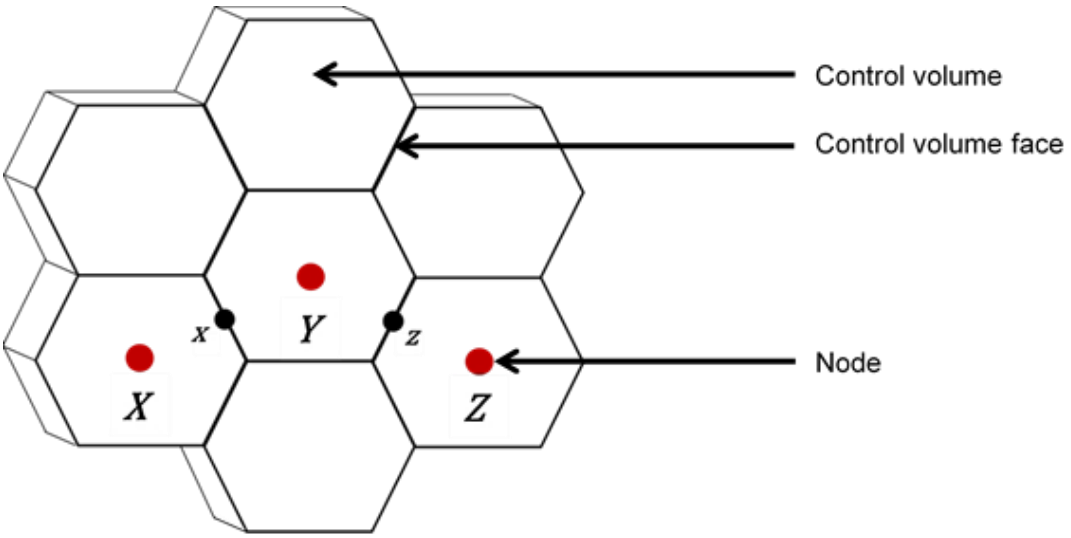

Figure 4.5: *The position of nodes and control volume faces after mesh generation (Adapted from Versteeg & Malalasekera (2007:116)*[153]

During step two of the FVM, the governing equations that were discussed in Section 4.1.1 are integrated across the control volumes to yield a discretised numerical equation at each of the various nodes[153]. Furthermore, the values and gradients of the variables at the control volume face, as indicated in Figure 4.5, are required, in addition to those stored at the nodes[28]. These are generally approximated using interpolation schemes such as central differencing, upwind or linear upwind models. Of the three, the simplest method is central differencing, provided in Equation 4-32 for an arbitrary variable[153].

$$\psi_z = \frac{\psi_Y + \psi_Z}{2} \qquad \textbf{4-32}$$

Where ψ_z, ψ_Y and ψ_Z represent a variable of interest at the control volume interface, at the active node and at the following node respectively. Once the discretisation process is complete, a system of equations is constructed and solved using matrix algebra. A finer grid is associated with more nodes and a larger system of equations, which explains the increased computational effort in the CFD environment. The third step of the FVM is the solution of the discretised equations and for this purpose a solution algorithm, as discussed in the next section, must be chosen.

4.1.3 Solution algorithm

4.1.3.1 Steady flow conditions without a Lagrangian phase

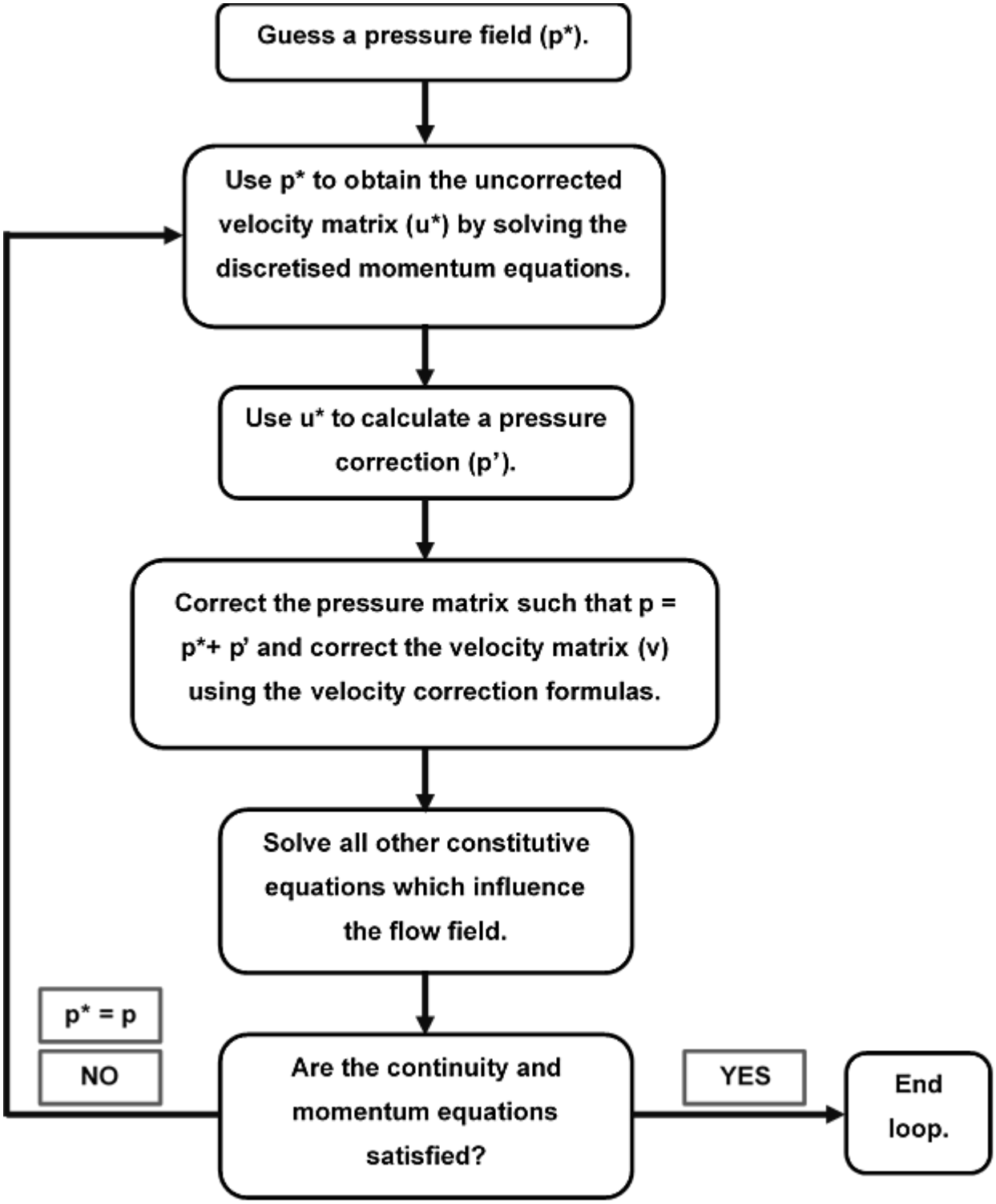

Figure 4.6: *Flow diagram illustrating the steps of the SIMPLE algorithm (Adapted from Versteeg & Malalasekera (2007:190))*[153]

Two main methods exist with which the discretised set of PDEs of the fluid phase may be solved. The first is a coupled solver during which the pressure field is solved from a suitable equation of state, the energy equation and the continuity equation[143,153]. When this method is chosen, the velocity field matrix and the pressure matrix are solved simultaneously, which requires a lot of computational effort[143]. The second method is a segregated solver, and this approach is suitable if the gas is assumed to be incompressible[153]. Since the density of an incompressible gas remains constant, a correct guess of the pressure field matrix should deliver a velocity field matrix which satisfies the continuity equation[153]. A segregated solver therefore solves the pressure and velocity fields separately using an iterative procedure which is less computationally expensive[143,153,157].

The semi-implicit method for pressure-linked equations (SIMPLE) algorithm is the most notable segregated solution algorithm throughout the literature and was chosen for this study. The SIMPLE algorithm is initiated by guessing a pressure field[153]. Using the pressure field, the momentum equations are solved to yield a velocity field matrix. Once this has been completed, the velocity field matrix is used to calculate a pressure correction term for subsequent calculations. The pressure corrections are used to update the pressure field matrix and the velocity field matrix with which all other constitutive equations are closed[153]. If the resulting velocity field matrix does not satisfy the continuity equation, the process is repeated using the updated pressure field matrix as the new guess with which the loop is initialised[153]. This process is schematically illustrated in Figure 4.6.

4.1.3.2 Unsteady flow conditions with a Lagrangian phase

When transient conditions are simulated, the SIMPLE algorithm may be adapted by adding an outer loop for time marching[153]. This updated procedure is illustrated in Figure 4.7. During the solution procedure, a time step size is chosen after which the SIMPLE algorithm is allowed to converge[153]. Once convergence has been achieved the SIMPLE algorithm may be applied for a given number of inner iterations after which the time is updated and the process is repeated until a user defined time constraint has been achieved[153]. As discussed in Section 4.1.1.3, parcel trajectories are solved by completing a force balance to use in conjunction with Newton's second law of motion. However, certain forces can only be computed with information from the surrounding carrier fluid[143]. To accomplish this goal, the Lagrangian solution process is performed before the SIMPLE algorithm by using the pressure and velocity information from the previous time step[143]. After a set amount of sub steps, the solution procedure is terminated and the resulting volume fraction and momentum source terms are fed to the SIMPLE loop to populate the source terms in the URANS equations[143].

The general order of calculations is as follows:

- Initialise a pressure and velocity field matrix.
- Solve Newton's second law of motion for each parcel.
- Run the SIMPLE algorithm.
- Update the time step.
- Repeat these steps until the user-defined time constraint has been reached.

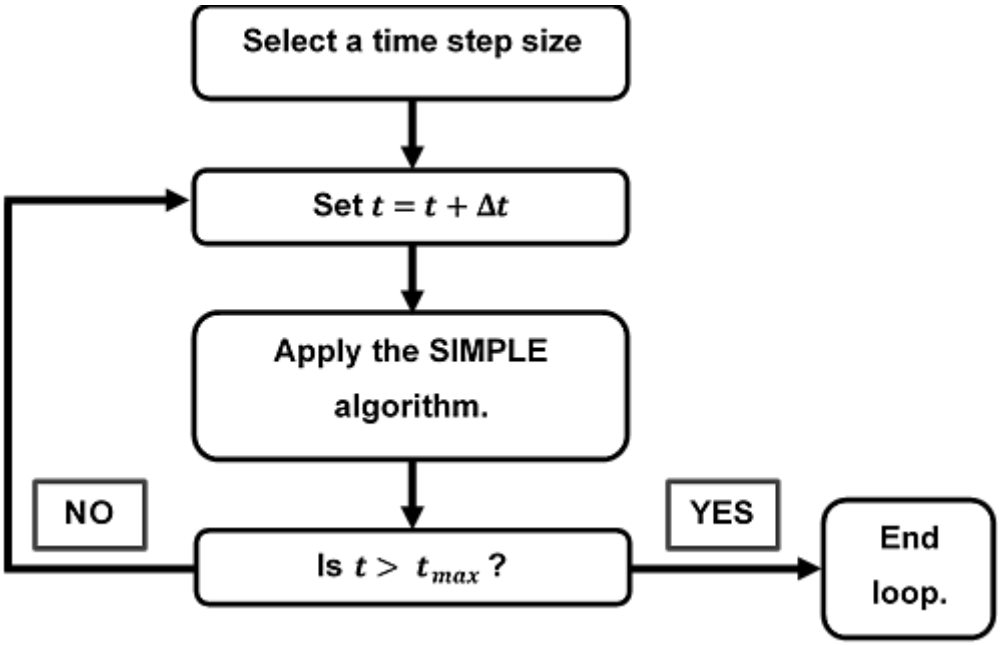

Figure 4.7: *Flow diagram illustrating the steps of the unsteady SIMPLE algorithm (Adapted from Versteeg & Malalasekera (2007:190))*[153]

4.1.4 Residuals

As mentioned, a guessed pressure difference is used to eventually obtain corrected pressure and velocity matrices with which the continuity, momentum and energy equations are solved. During the solution process, the values of key variables are compared from one iteration to the next. If the values between two consecutive iterations change, the difference between the values is called the residual error. A CFD simulation would be perfectly converged once the residual error in every mesh cell and of every variable is equal to the machine's representation of "zero"[153]. In a computer, a real number has a finite number of decimals and all terms after that number of decimal places are neglected. Thus, zero on a computer is not truly equal to its mathematical definition.

Nonetheless, computers used for CFD calculations have a sufficiently high number of decimal places such that it would take an impractical amount of time for every residual in every cell to reach zero[153]. Instead of stopping the iterative process once all cells have a residual error equal to zero, another stopping criterion is desired[153]. Generally, a global residual term for every monitored variable is created to eliminate the need for inspecting every cell in the domain. The global residual of all variables then has to satisfy a maximum value chosen by the user. In the STAR-CCM+™ environment, this is done by calculating the root mean square (RMS) of the residuals of every monitored variable using Equation 4-33[156]. By taking the square of the residual in every cell, negative values will not cancel positive values during the calculation of the global residual term[156].

$$R_{rms} = \sqrt{\frac{1}{n}\sum_{i=1}^{n} {r_i}^2} \qquad \textbf{4-33}$$

Where r_i is a local cell residual, n refers to the number of cells in the mesh and R_{rms} is the global residual term using an RMS calculation. Upon inspection of Equation 4-33, it becomes clear that the magnitude of R_{rms} depends on the magnitude of the flow variables throughout the domain[153]. For example, if a velocity of 0.1 m/s changed to 0.01 m/s in all the cells, the R_{rms} would be equal to 0.09 m/s. However, if the velocity changed from 10 m/s to 1 m/s in all of the cells, the R_{rms} would equal 9 m/s. Although both global residuals decreased by 90%, a user criterion of 10^{-3} would end the calculation procedure for the former case and not the latter. Since the global residual will be larger for variables with greater orders of magnitude, the stopping criterion specified by the user would have to be case specific[153]. Furthermore, the example only considered velocity, whereas many different variables are monitored simultaneously, each with its own unit and order of magnitude. To collectively consider the global residual of all key variables and to specify a single stopping criterion, normalisation of the global residuals is performed using the general formula given by Equation 4-34[156].

$$R_{norm} = \frac{R_{rms}}{F} \qquad \textbf{4-34}$$

Where R_{norm} is the normalised residual for any given variable and F is a normalisation factor. Versteeg and Malalasekera provided commonly used normalisation factors (F), two of which can be represented in the form of Equation 4-35 and Equation 4-36[153].

$$F = {R_{rms}}^{k_0}, \qquad 2 < k_0 < 10 \tag{4-35}$$

$$F = \sum_{j}^{inlet\ cells} (\rho AU.n)_j \theta_j \tag{4-36}$$

With k_0 the iteration number, j the cell number and θ the flow variable of interest. STAR-CCM+™ uses an adapted form of Equation 4-35 in the sense that it only considers the first five iterations of the simulation[156]. For the remainder of the simulation, the normalisation factor remains constant. This can be presented mathematically by Equation 4-37.

$$F = max\{|R_{rms}|^1, |R_{rms}|^2, \dots, |R_{rms}|^{k_0}\}\ with\ k_0 = 5 \tag{4-37}$$

All things considered, a residual plot reaching an asymptotic value indicates that the average deviation of a variable remains the same from one iteration to the next. If the asymptotic values are sufficiently low, the effect of the deviation is low enough that the simulation may be stopped. However, convergence issues may be hidden during the averaging process if many cells have decreasing residuals and only a few have increasing residuals[153]. For this reason, a simulation is not necessarily converged in every cell once the residual plots indicate asymptotic behaviour and further investigation of the variables of importance is recommended.

4.2 Computer-aided design of the riser

Computer-aided design (CAD) drawings of the riser were created in Siemens NX-12™ according to the dimensions in Section 3. Figure 4.8 (a)–(c) illustrates the assembly at its high, medium and low height settings, respectively. A “mould” of the open space inside the riser through which particle-entrained flow could occur was subsequently generated in the CAD software. Therefore, the fluid region was represented as a single solid body. If the “moulds” were halved, each half would be entirely solid as illustrated by Figure 4.9 (a). This was done since the modelling software regards an imported solid as a fluid region unless it is specified otherwise. Furthermore, the three tubes through which solids could be introduced to the riser were excluded to reduce residual noise and the overall solution time of the CFD models. As an alternative, three circular indentations with a diameter of 60 mm and a depth of 2 mm were added to the surface of the venturi, as illustrated by Figure 4.9 (b). Once completed, each of the three riser drawings were exported as parasolid files to enable compatibility with the Siemens STAR-CCM+™ software.

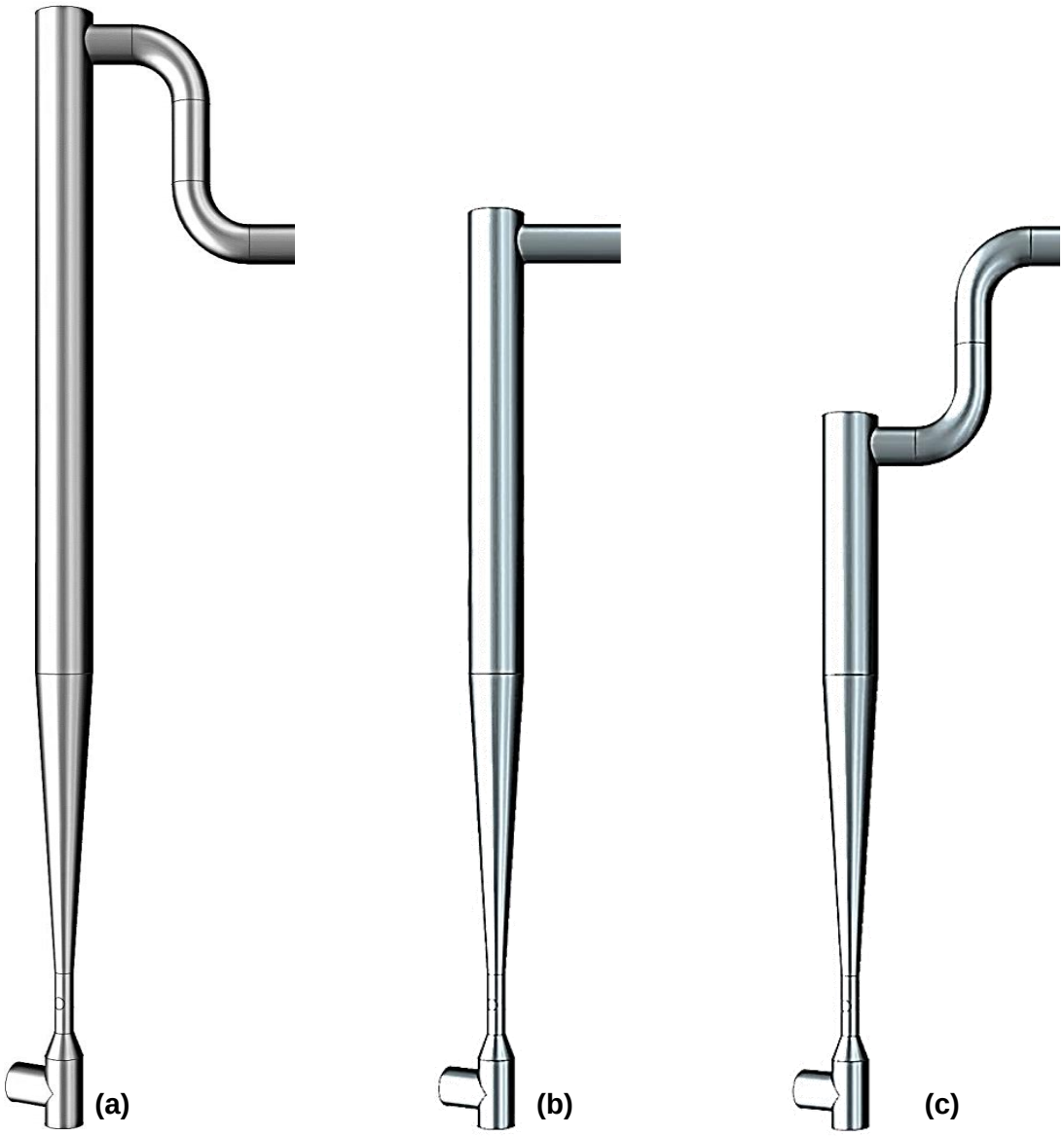

Figure 4.8: *CAD drawings of the riser at its* ***(a)*** *high,* ***(b)*** *medium and* ***(c)*** *low height settings*

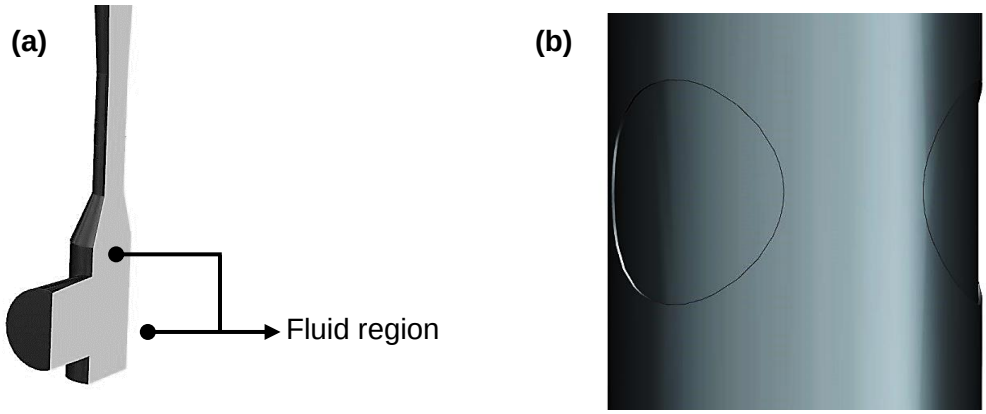

Figure 4.9: (a) *The fluid region within the riser which is represented as a solid and* ***(b)*** *indentations on the venturi that were used to represent the solids entry points*

4.3 Construction of the CFD simulations

4.3.1 Start up

For all three riser geometries, the modelling procedure was similar, with the only exception being the parasolid file that was imported into the *STAR-CCM+*^{TM} software. Once imported, the software automatically creates a part with a single surface area. The surface was separated at every curve such that the air inlet at the bottom, the outlet at the top and the three solids entry ports could be distinguished from the remaining surface area. Consequently, six boundaries were created. Both the air inlet and the entry port used for solids injection were specified as stagnation inlets. This allowed the air flow at those boundaries to start from a state of rest. To achieve and maintain the desired inlet air velocity at the bottom of the riser for a given simulation, the negative gauge pressure at the top of the riser had to be varied. For this reason, the boundary at the top of the riser was specified as a pressure outlet. The two remaining solids entry ports and the remaining surfaces of the riser were specified as walls with a roughness height of 0.02 mm. The method through which the wall roughness height was determined is provided in Annexure N.

4.3.2 Physics models

4.3.2.1 Model selection

The fluid region was specified as a gas phase. Since the gas never reached nor exceeded a Mach number of 0.2, the RANS equations could be selected to describe its flow. The model was solved in a three-dimensional domain, and the segregated flow model was used, given its ease of computation, as was discussed in Section 4.1.3. Turbulence was accounted for through the k-ε turbulence model, given its computational ease and the small amount of flow separation in the modelling application. An implicit unsteady solver was used, which employs the algorithm that was discussed in Section 4.1.3.2, while the fluid and particle properties, as well as the constants that were adjusted from their default values, are provided in Table 4-2. The normal and tangential wall restitution coefficients were adjusted but the chosen values still indicated near-elastic collisions. Adjusted values from CFB literature are usually between 0.95 – 0.99[20,29,97,99] and are in some cases chosen form a sensitivity analysis[25]. However, in this instance it was obtained from time averaged data that was collected for a range of particles between 10 to 500 µm which were imparted on a wall at 10 m/s[158].

Given the large experimental setup as well as the great number of conditions to be simulated, heterogeneous drag models would be too computationally expensive, as discussed in Section 4.1.1.4. Accordingly, a homogeneous model was selected. The particles would have to travel at a velocity of 520 m/s to reach a particle Reynolds number of 800, and this calculation is provided in Annexure O.

Table 4-2: *List of constants used in the STAR-CCM+™ environment*

Constant	Symbol	Unit	Value
Density of air (@ 22.9°C)	ρ_f	kg/m^3	1.19
Dynamic viscosity of air (@ 22.9°C)	μ_f	$Pa \cdot s$	1.83×10^{-5}
Density of particles	ρ_p	kg/m^3	2883
Wall normal restitution coefficient[158]	-	-	0.97
Wall tangential restitution coefficient[158]	-	-	0.94
Particle size	d_p	μm	23.63
Particle mass flow rate	$\dot{m}_p$	kg/s	0.04 / 0.05 / 0.06

Beyond this limit, the increasing error in the Schiller-Neumann drag coefficient predictions would justify the use of more complex drag models as discussed in Section 4.1.1.4. However, this study never reached a particle velocity of 520 m/s, which meant that the Schiller Neumann drag model would suffice. This model was also deemed sufficient given the low average solid volume fraction inside the riser as a result of operating in the transport fluidisation regime. Consequently, the inter-particle interaction, which could contribute to large errors in drag calculations, were reduced. Hence, the Schiller-Neumann drag model was chosen from the group of homogeneous drag models that were discussed in Section 4.1.1.4. A surface injector was specified for the particles, and the solids were introduced to the riser in a direction that was normal to the entry port. 30 000 Injection points were used, and the sorbent particle size was specified according to the average D[4,3] obtained from the analysis in Section 3.1.2. Finally, the inlet mass flow rate of the injected particles was entered according to the experimental conditions that were being simulated.

4.3.2.2 Choice of approach and phase coupling

In Table 4-3 the minimum and maximum solid volume fractions from the experimental data is provided. When following the discussion from Section 4.1.1.3, a Eulerian-Lagrangian approach would be a suitable method for particle description since $10^{-6} < \bar{\varepsilon}_s < 10^{-1}$. Furthermore, the Stokes number was calculated using Equation 4-26. The slip velocity was obtained by simulating the experiment in which the highest $\bar{\varepsilon}_s$ was found. This occurred at the lowest air velocity, highest solids feed rate and lowest riser height setting. The result is reported in the final column of Table 4-3 and since the Stokes number was significantly larger than one, a Eulerian-Eulerian approach also had to be considered according to Section 4.1.1.3.

In Section 4.1.1.3, it was further shown that two-way coupling is recommended when $10^{-6} < \bar{\varepsilon}_s < 10^{-3}$ and $8 < L_k/d_p < 80$. Consequently, the interparticle spacing was calculated from Equations 4-23 – 4-25 and the results are reported in the third column of Table 4-3. Since 100% of the calculated $\bar{\varepsilon}_s$ and L_k/d_p parameters fell within the required range, a Eulerian-Lagrangian method was chosen despite the high stokes number. Additionally, the particle relaxation time was calculated using Equation 4-27 and found to have a value of 0.005 s. The relaxation time was large enough for the particles to dislodge from gas streamlines in regions where sudden changes in gas velocity occurred. For this reason, two-way coupling was chosen to account for the interaction between the phases in addition to the Eulerian-Lagrangian approach.

Table 4-3: *Indicators that were calculated to choose a suitable method of representation for the solid phase in the CFD models*

	$\bar{\varepsilon}_s$	L_k/d_p	$t_p\ (s)$	St
Maximum value	8.43×10^{-4}	21.8	0.005	4.8
Minimum value	5.07×10^{-5}	8.5		

4.3.3 Simulation procedure

After the physics models had been selected and the necessary adjustments had been made, the CFD model was started with a steady-state solver. The simulation was allowed to run until the 700th iteration, during which no solid particles were added to the riser.

This was done to reduce the overall solution time by providing better initial values for the unsteady and Lagrangian phase solvers. Throughout the entire simulation time, the air flow through the riser was controlled by specifying a negative pressure across the outlet boundary at the top of the riser, as is also experimentally induced by the draught fan. The specified value was adjusted until the inlet air velocity at the bottom of the riser exceeded the target value by 0.2 m/s. By starting the unsteady simulations at a slightly higher inlet gas velocity, the increased pressure drop that resulted from the addition of particles was accounted for. At the 700th iteration, the steady state solver was replaced by the implicit unsteady solver, and the Lagrangian phase was injected. The number of inner and outer iterations were chosen as 3000 and 7, respectively. The former refers to the number of iterations that the SIMPLE algorithm was allowed to converge, whereas the latter refers to the number of times this process was repeated before updating the time step. This procedure was applied to all of the CFD simulations, which include the grid and time-step independence analyses. Nine CFD models were constructed at the conditions that correspond to the corners and the centre point of the 2^3 experimental domain. This was graphically illustrated in the factorial design discussion in Section 3.3.2.2 and corresponds to the experimental runs that were indicated in brackets in Table 3-9.

4.3.4 Meshing and grid independence study

After selecting the relevant physics models, the geometry was divided into control volumes across which the governing equations could be solved. Based on the discussion in Section 4.1.2, the decision was made to use polyhedral cells. Since finer grids outperform coarser grids at the cost of added solution time, the size of the cells had to be chosen carefully. For this reason, a grid independence study was performed.

4.3.4.1 Mesh quality

The quality of a mesh in the *STAR-CCM+*^{TM} environment can be measured by extracting cell metrics – three of which were used for this study. The first was the cell skewness angle, which is the angle between the cell face normal and the line connecting two cell centroids as illustrated by the red arrow in Figure 4.10 (a). When the cell skewness angle is equal to 90°, the dot product used within certain denominators becomes zero, which could lead to convergence issues[156]. The second metric was the volume change which is the ratio between the volume of a given cell and that of its neighbouring cells. An example of a small volume change ratio is provided in Figure 4.10 (b). When this happens, the solvers used during the solution procedure experience stability issues[156]. The third metric was cell quality which indicates cell non-orthogonality.

When the cell quality has a value approaching zero, it is considered an inadequate cell, as illustrated by Figure 4.10 (c)[156].

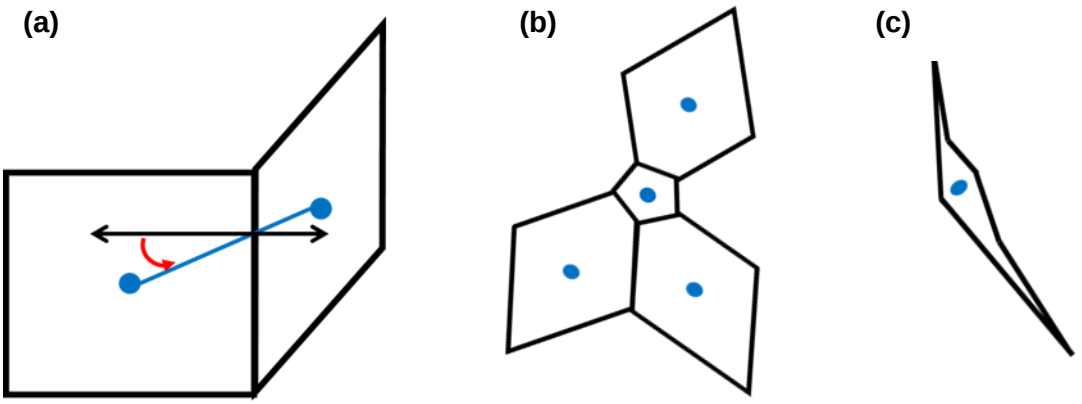

Figure 4.10: *An example of* ***a)*** *cell skewness,* ***b)*** *cells with a small volume change ratio and* ***c)*** *a highly non-orthogonal cell (Adapted from the STAR-CCM+™ user guide, 2019)*[156]

With regards to the three metrics, cells were flagged as invalid if one of the following criteria were true:

- The cell skewness angle was greater than 85°,
- the volume change of a cell was smaller than 0.01 and
- the cell quality of a cell had a value below 0.0001.

4.3.4.2 Mesh properties

Seven different grids were constructed for evaluation, and the coarsest mesh had a base size of 80 mm. Global mesh refinement was achieved by decreasing the base size three times. Three of the four grids were further refined at the top of the riser and the bottom venturi section to capture large velocity gradients in those regions. This was achieved by creating the volumetric controls that are illustrated in Figure 4.11 Volumetric controls in *STAR-CCM+™* are user-specified regions in which the properties of the mesh can be varied from the general properties specified for the global grid. The properties of the grids that were used for the independence study is provided in Table 4-4. The different grids were labelled according to their base size in mm and their level of refinement. The latter was either “global” which indicated that no volumetric controls were added or “local” which indicated the alternative.

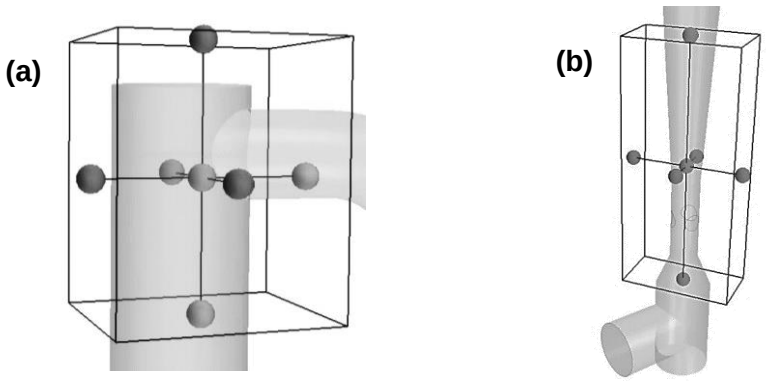

Figure 4.11: *Region in which local mesh refinement was done at* ***(a)*** *the top of the riser and* ***(b)*** *the bottom venturi section*

Apart from varying the cell size, the number of prism layers that were used were varied until the best mesh quality has been achieved. Only the final number of prism layers that were chosen for each mesh is reported in Table 4-4. Prism layers refer to the cells that are adjacent to the walls in which wall functions are used to solve the velocity gradient of the fluid phase. Since this approach depends on empirical correlations instead of resolved physics, it was possible to use larger cells near the wall region in order to reduce the computational effort.

Table 4-4: *Grid independence analysis mesh properties*

Grid name	Mesh base size (mm)	Cells	Prism layers	Volumetric control base size (mm)
80_Global	80	74791	4	-
80_Local	80	78379	4	20
60_Global	60	74594	2	-
60_Local	60	100439	2	12
40_Global	40	85976	2	-
40_Local	40	191437	2	8
20_Local	20	174607	4	-

4.3.4.3 Mesh quality comparison

Figure 4.12 indicates that the lowest percentage of invalid cells were present in the 20_Global, 60_Local and 60_Global grids, making these the most suitable candidates for further analyses.

However, all seven grids were considered in subsequent analyses since a sufficiently low percentage (<0.03%) of invalid cells were yielded. From Figure 4.12 it is further seen that the addition of local mesh refinement considerably reduced the number of invalid cells of the 80 mm and 60 mm grids while the improvement of the 40 mm grid was less pronounced.

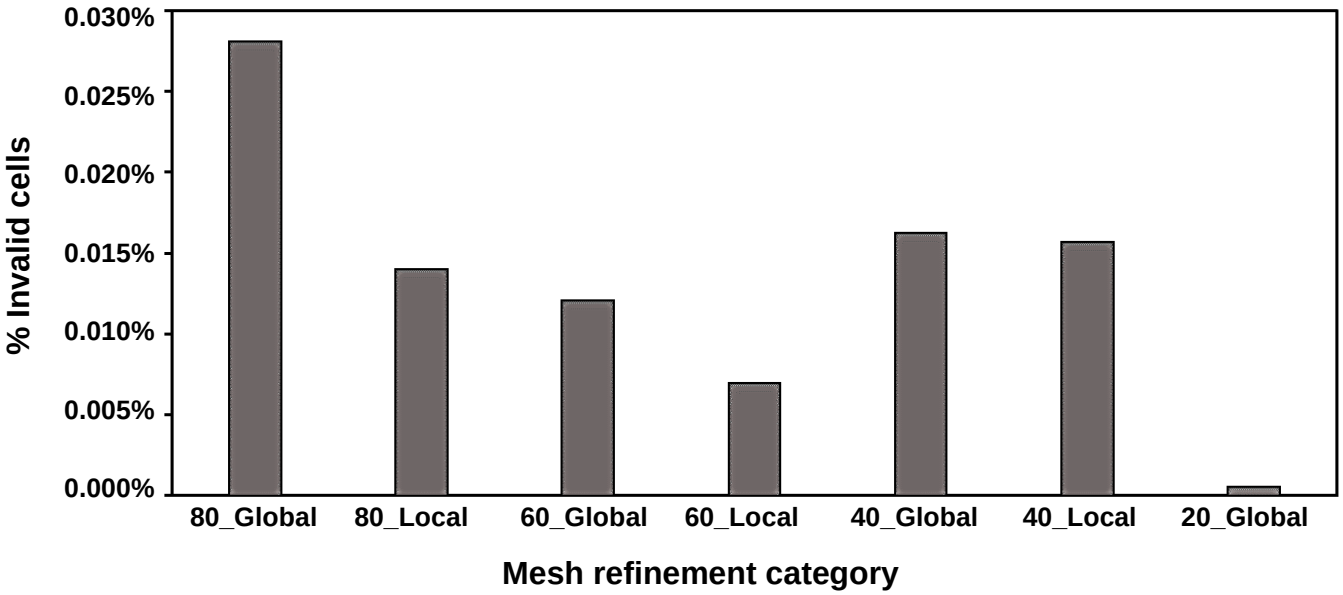

Figure 4.12: *The percentage of invalid cells that were present in every grid that was used for the independence study*

Only a portion of the remaining valid cells within each mesh category had superior metric values, which were defined as:

- Cell quality > 0.5
- Skewness angle < 40°
- Volume change > 0.5

The percentage of cells with the abovementioned metric values for every grid is provided in Figure 4.13. The 40_Local grid had the highest percentage of good cells in all three metric categories. Nevertheless, in all seven grids, more than 60% of the cells had good metrics and were therefore considered in subsequent analyses. Figure 4.13 further shows that local grid refinement had an overall favourable effect on the cell metrics. However, when considering the grids without volumetric controls, a decrease in cell size improved the cell skewness but negatively influenced the volume change metric.

When comparing the overall quality of the seven grids, the 60_Global, 60_Local and 20_Global grids were superior based on their low percentage of invalid cells. Additionally, the 40_Local grid contained a larger percentage of superior cells compared to the other grids, making these four grids desirable options for further analysis.

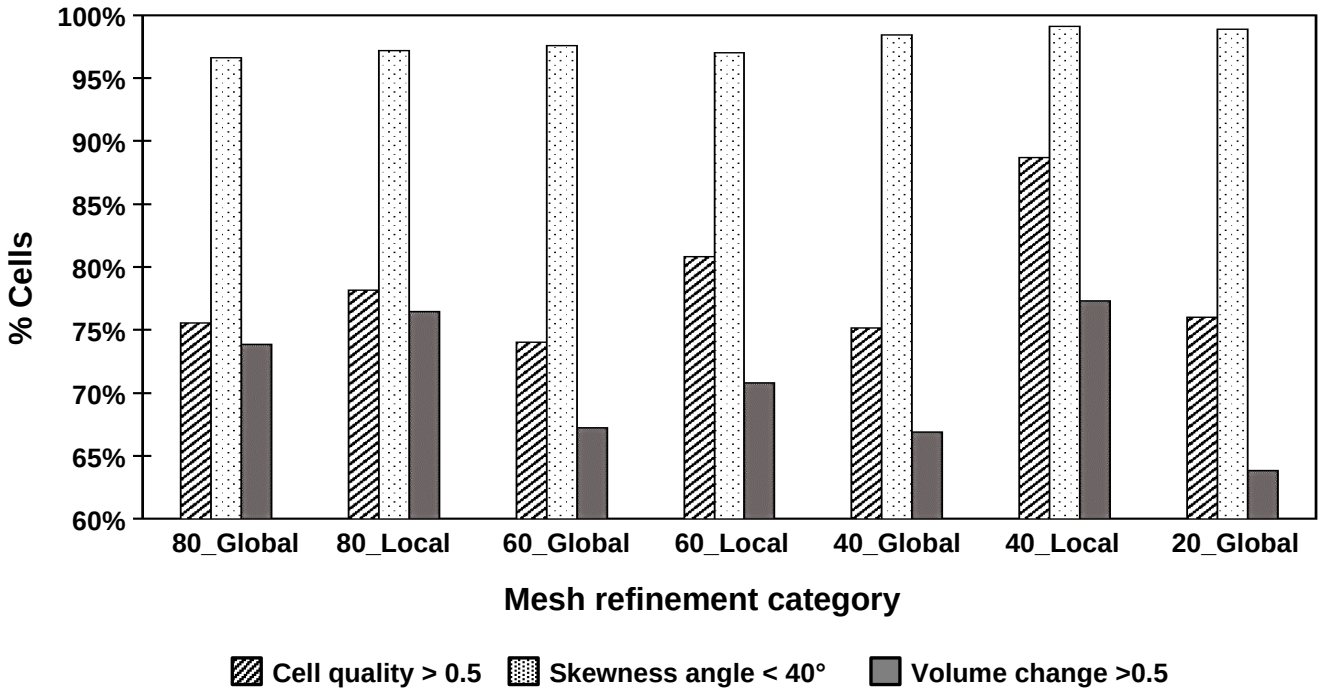

Figure 4.13: *The percentage of cells with good metrics in every mesh category*

4.3.4.4 Mesh performance comparison

Three seconds of riser operation was simulated with each of the seven grids. The performance parameters that were compared after three seconds included the:

- solution time,
- predicted gauge pressure at the top of the riser and
- the predicted average solid volume fractions at the bottom, middle and top riser measurement ports.

As the predicted conditions inside the riser after three seconds was not representative of the experimental conditions at the time of data collection, the CFD data at this point was not compared to experimental data during the grid-independence analysis. Instead, the simulation with the 20_Global mesh was used as a benchmark given its large degree of refinement and exceptionally small number of invalid cells. Illustrations of each grid and its influence on the particle velocity at the top and bottom of the riser can be found in Annexure P. Figure 4.14 shows that the addition of local grid refinement increased the solution time with the exception of the 80 mm grid. Furthermore, the shift from a 60_Global to a 60_Local mesh increased the solution time by more than 30 minutes. The highest solution time of 256 minutes (4.3 hours) was recorded when using the 40_Local grid, which is expected for a finer grid, but then also slightly contradicts the observation for the 20 mm grid size.

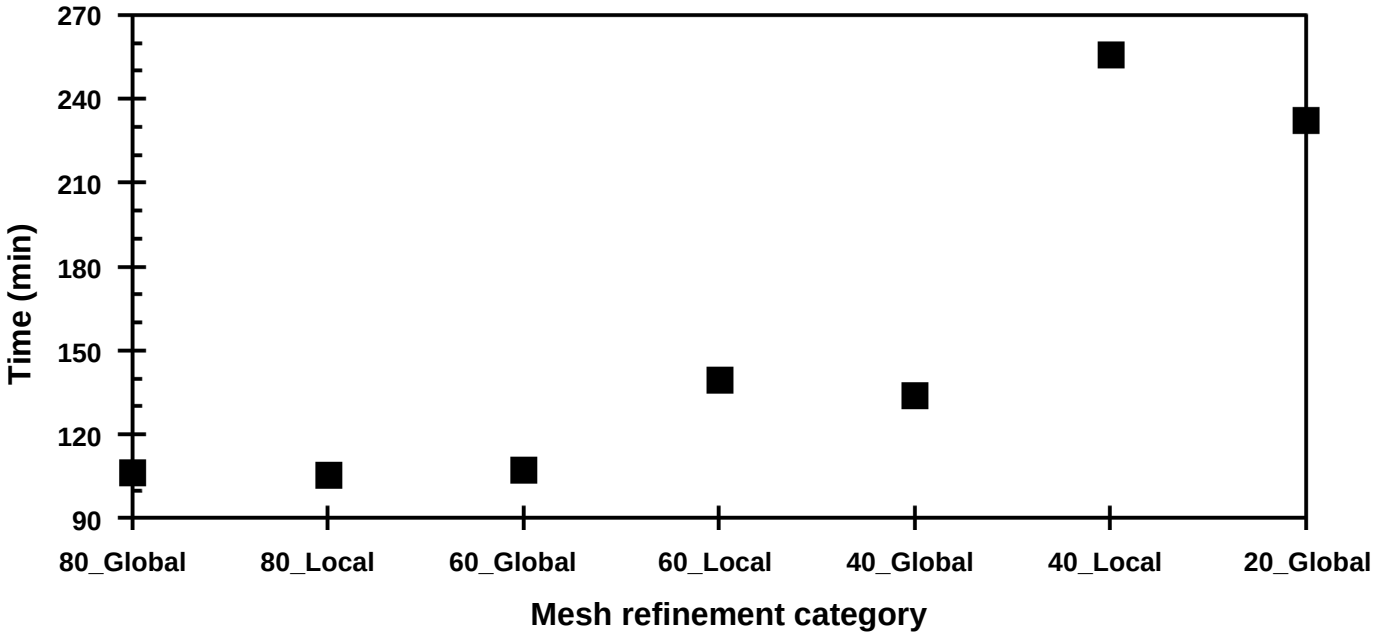

Figure 4.14: *The time required to simulate three seconds of riser operation for every mesh used in the grid independence study*

Figure 4.15 illustrates that the addition of local grid refinement decreased the predicted value of the gauge pressure at the top of the riser. The consecutive refinement from the 60_Global to the 40_Local grids brought on a decrease in the gauge pressure prediction, while an increased value was observed at the 20_Global grid. Furthermore, all seven grids delivered a gauge pressure prediction within a standard deviation of 3%.

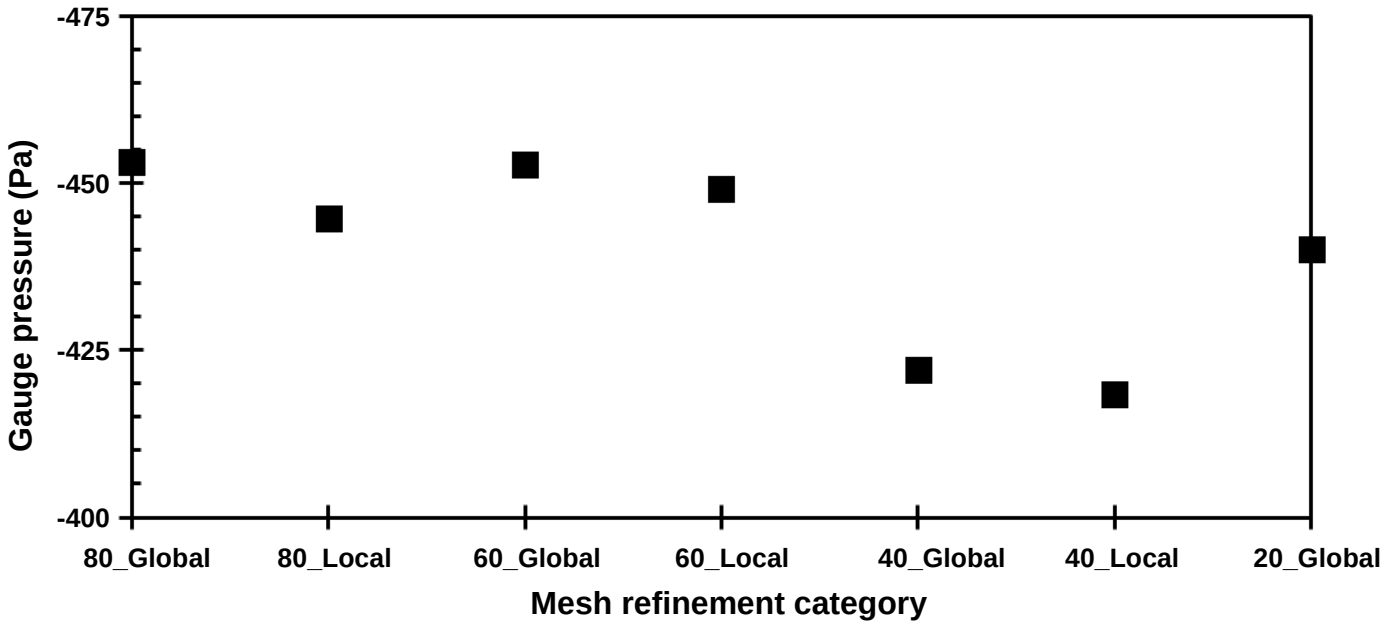

Figure 4.15: *The CFD predictions of gauge pressure at the top of the riser for different mesh refinement categories*

In Figure 4.16 the average solid volume fraction ($\bar{\varepsilon}_s$) prediction at every riser port and every mesh refinement category is provided. It was found that the predictions obtained with the 60-Global grid exhibited the greatest deviation from those with the 20_Global grid. With the 20_Global grid, the bottom port had the highest predicted value of $\bar{\varepsilon}_s$ and the middle port the lowest, whereas the opposite was true with the 60_Global grid. Apart from these two grids, the highest $\bar{\varepsilon}_s$ prediction was always achieved at the top port while the lowest prediction was achieved at the bottom port. Nonetheless, none of the CFD models predicted the same trend as the 20_Global grid.

The most suitable grid was chosen through the process of elimination. Due to the large amount of solution time associated with the 20_Global and the 40_Local grids, these two were not deemed suitable for the aim of this study. From the remaining five grids, the 40_Global grid produced the worst prediction of the gauge pressure at the top of the riser when compared to the 20_Global grid and was therefore eliminated from the list of suitable grids. When referring to Figure 4.16, the CFD simulation with the 60_Global grid predicted the opposite order of $\bar{\varepsilon}_s$ values than the 20_Global grid and was eliminated as a consequence. From the three remaining grids, the 60_Local mesh was chosen as the most suitable grid due to its low number of invalid cells when compared to the 80 mm grids and its high percentage of superior cells in general.

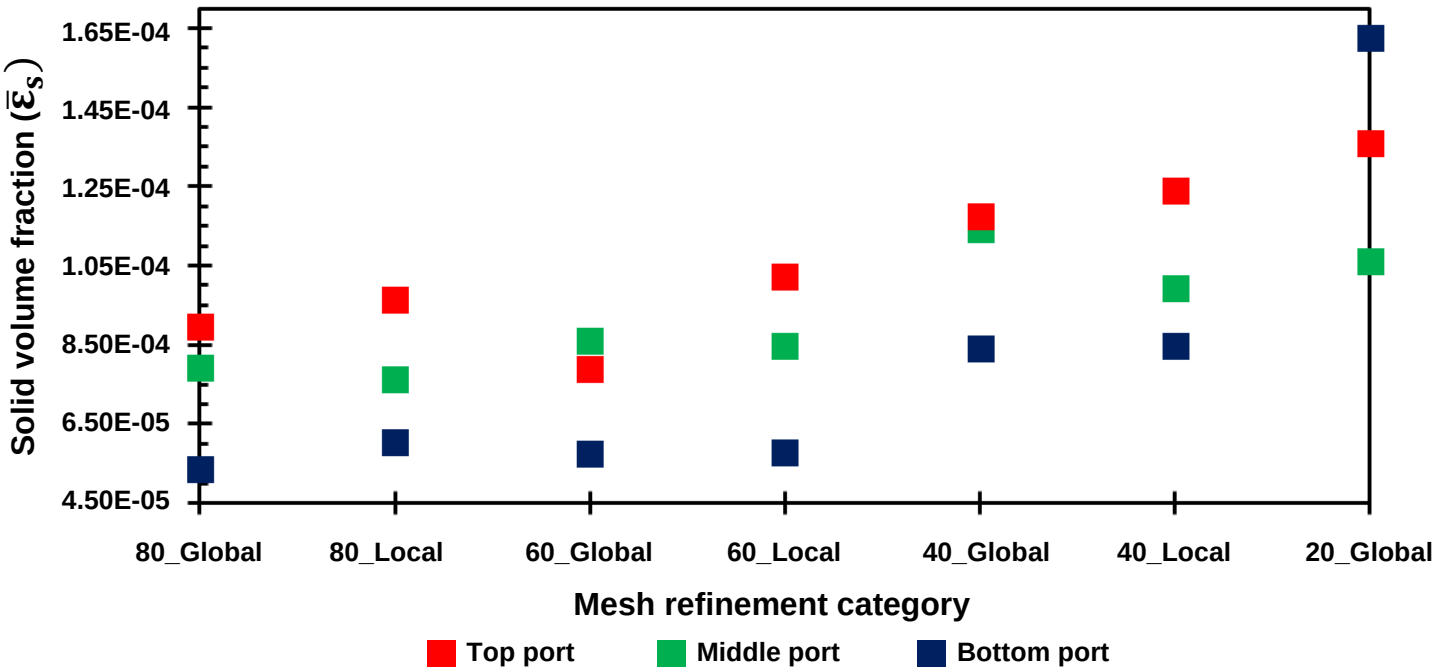

Figure 4.16: *CFD predictions of the average solid volume fraction at the bottom, middle and top riser ports after three seconds for various mesh refinement categories*

4.3.5 Time-step independence study

When using an explicit numerical method to solve the PDEs in CFD modelling, the information from the current time step dictates the prediction values at the next. Therefore, the time-steps should be small enough to ensure that sufficient information is captured at every cell node. Consequently, the time-step size requirements for explicit solvers are determined by using the Courant–Friedrichs–Lewy (CFL) condition, which is also referred to as the Courant number as defined by Equation 4-38[130,159].

This condition provides a ratio between the distance travelled by the flow in a given time step to the size of the cell. If the Courant number is greater than one, the flow has overshot the cell during a time step and stability issues may occur. Therefore, it is recommended that the Courant number should be lower than one[159]. Unlike explicit solvers which determine the node values one-by-one, implicit solvers are inherently stable since these solvers solve a system of equations across the entire solution domain[160]. For implicit schemes, the maximum CFL number is often set to a value above 5 or completely disregarded given the solver's inherent stability[130,159,160].

$$Co = \frac{t_{CFD} \times U_{cell}}{x_{cell}} \quad \textbf{4-38}$$

Here, Co is the Courant number, t_{CFD} is the time step size chosen, U_{cell} is the velocity at a cell face and x_{cell} is the size of the cell. An implicit approach was used in this study and despite its stability, the influence of the time-step size on the CFD model predictions were evaluated. This was done by testing three time-steps in combination with the 60 mm mesh with local mesh refinement. After simulating three seconds of riser operation, the models were compared by their:

- average courant number,
- gauge pressure at the top of the riser,
- solution time and
- the average solid volume fractions at the bottom, middle and top riser measurement ports.

The results from the time-step analyses are presented in Table 4-5. From the table it can be seen that only the largest time-step size produced an average Courant number above one. Moreover, the value of 1.5 is still sufficiently small for an implicit solver when considering the inherent stability detailed in the previous discussion. When looking at the third column in Table 4-5 it becomes apparent that the time-step size had a negligible influence on the prediction of gauge pressure at the top of the riser as expected from an implicit solver application. Finally, it was seen that a decrease in the time step size significantly increased the solution time as illustrated by the final column in Table 4-5.

Table 4-5: *Values recorded from three CFD models at 3 s of simulated time with varying time-step sizes*

Time-step size (s)	Average Courant number	Gauge pressure at the top of the riser (Pa)	Solution time (hr)
0.005	1.4	-449	2.3
0.0025	0.7	-449	4.5
0.001	0.3	-450	11.5

In Figure 4.17, the influence of the time-step size on the solid volume fraction ($\bar{\varepsilon}_s$) prediction is illustrated. By reducing the time-step size from 0.005 s to 0.0025 s, the difference between the $\bar{\varepsilon}_s$ at the top and bottom ports reduced. A further reduction to 0.001 s decreased the prediction of the $\bar{\varepsilon}_s$ at the middle port to its lowest value. With the smallest time-step, the difference between the $\bar{\varepsilon}_s$ at the top and bottom ports was less than with the largest time-step. The subtle changes in Figure 4.17 did not justify the large amount of time required to complete the simulations with the smaller time-steps. Additionally, Figure 4.17 illustrates that the top port had the highest $\bar{\varepsilon}_s$ while the bottom port had the lowest $\bar{\varepsilon}_s$ for all three time-step sizes. Thus, the trends were captured regardless of the time-step size. Consequently, the largest time-step size of 0.005 s was used in all of the CFD models.

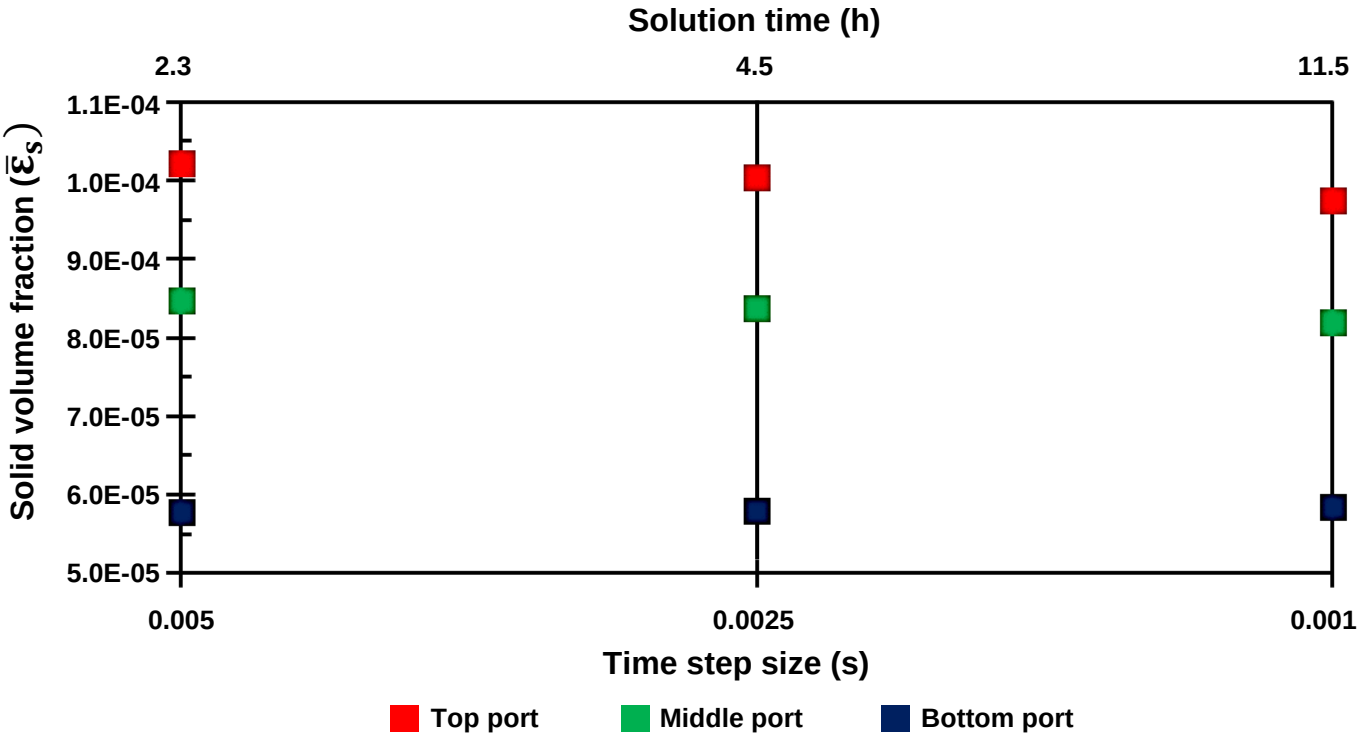

Figure 4.17: *The influence of the time-step size on the solid volume fraction prediction at every riser port and the time taken to simulate three seconds of riser operation*

CHAPTER 5 - RESULTS AND DISCUSSION

5.1 EXPERIMENTAL DESCRIPTION OF THE HYDRODYNAMICS

5.1.1 Radial solids holdup

The local solid volume fraction (ε_s) at seven radial points along the three axial sampling ports were recorded during each experiment, as discussed in Section 3.3.4.3. In order to discuss the radial solids holdup profiles, only the results pertaining to the low riser height setting were provided. The profiles pertaining to the maximum riser height setting can be found in Annexure Q and exhibit the same trends that will be discussed within this section. In addition, the confidence intervals that are associated with the radial solids holdup profiles have been indicated along the light blue profile for reference. The confidence intervals are discussed in more depth in Annexure R. In Figure 5.1, the solids holdup profiles that were obtained at the bottom sampling port are illustrated. The graph shows the solids volume fraction presented on the y-axis versus the radial position indicated on the x-axis with a zero-value implying the axial centre of the riser. The arrow on the riser's top-view plane at the sampling point in the legend of Figure 5.1 denotes the travel direction of the sampling probe.

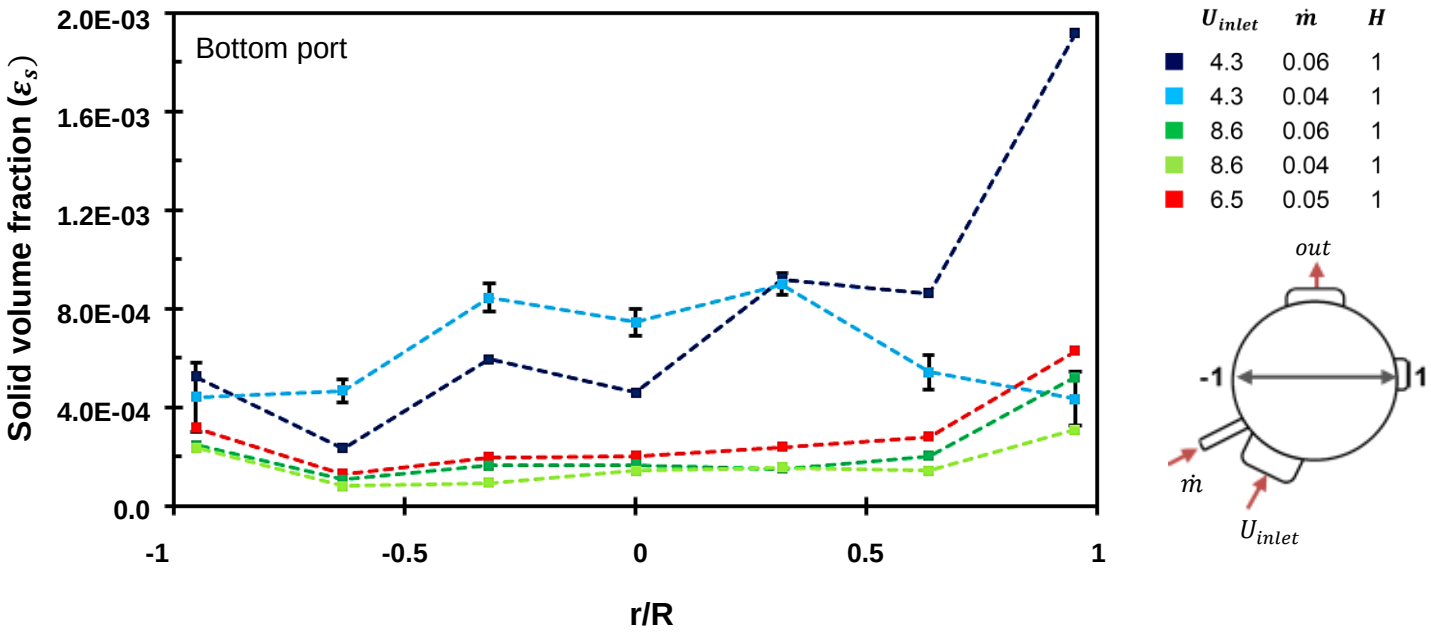

Figure 5.1: *The radial solids holdup profile at the* ***bottom sampling port*** *under varying inlet velocity and solid feed rate settings*

The dark blue line in Figure 5.1, had the least uniform solids distribution given the high concentration of particles to the right-hand side of the sampling axis. To explain this trend, the top view of the riser has been provided for reference next to the graph in Figure 5.1. The momentum of the solids ($\dot{m}$) and the air (U_{inlet}) that was injected in the lower left quadrant of the reference image, resulted in preferential particle flow towards the upper right quadrant. This caused the increased solid volume fraction near the right wall of the riser in most of the profiles in Figure 5.1. The large particle concentration facilitated an increased number of inter-particle interactions which further increased the solids holdup in such regions.

The light blue profile in Figure 5.1 was obtained at a decreased solids feed rate setting. Under those conditions, a flatter solid volume fraction profile was observed, and the solids holdup near the right riser wall was less. This suggests that a decrease in the solids feed rate resulted in more uniform particle flow, especially near the riser walls. As discussed in Section 2.2, uniform flow refers to the even distribution of particles along the radial plane of the riser. The increase in uniformity as the solids feed rate is decreased was also observed at the high inlet air velocity settings as indicated by the green lines in Figure 5.1, although the effect was less prominent. This is consistent with the literature findings that were presented in Section 2.2.4.2. An increase in the inlet air velocity resulted in a lower solid volume fraction at nearly every radial sampling point in Figure 5.1. During high inlet air velocity experiments, the increased momentum transfer from the carrier phase to the particles compensated for momentum losses due to inter-particle interactions and friction. Hence, more uniform profiles were created. However, particle accumulation was observed near the riser walls in Figure 5.1 regardless of the inlet air velocity setting. This observation is attributed to the momentum losses at the walls of the riser due to friction. Nevertheless, the relationship between the inlet air velocity and the radial solids holdup agrees with the findings discussed in Section 2.2.4.2.

In Figure 5.2, the solids holdup profiles that were obtained at the middle sampling port are illustrated. The blue profiles in were flatter than those in Figure 5.1 which suggests a higher degree of flow development. However, the same could not be said about the red and green profiles. Figure 5.2 further illustrates that an increase in the inlet air velocity or a decrease in the solids feed rate increased the uniformity of the solids holdup profiles. Once again, these changes were more noticeable near the wall region of the riser whereas the centre region ($-0.3 < r/R < 0.3$) remained unchanged and this is consistent with literature findings.

The influence of the operating parameters on the solids holdup at the top port is illustrated in Figure 5.3. The operating conditions had the same influence on the radial solids holdup profiles at the top sampling port as it did at the bottom and middle ports. However, a higher degree of non-uniformity was present at the top port when compared to the middle port. This could have been due to an exit effect as defined in Section 2.2.4.1 and this hypothesis is further explored in Section 5.2.

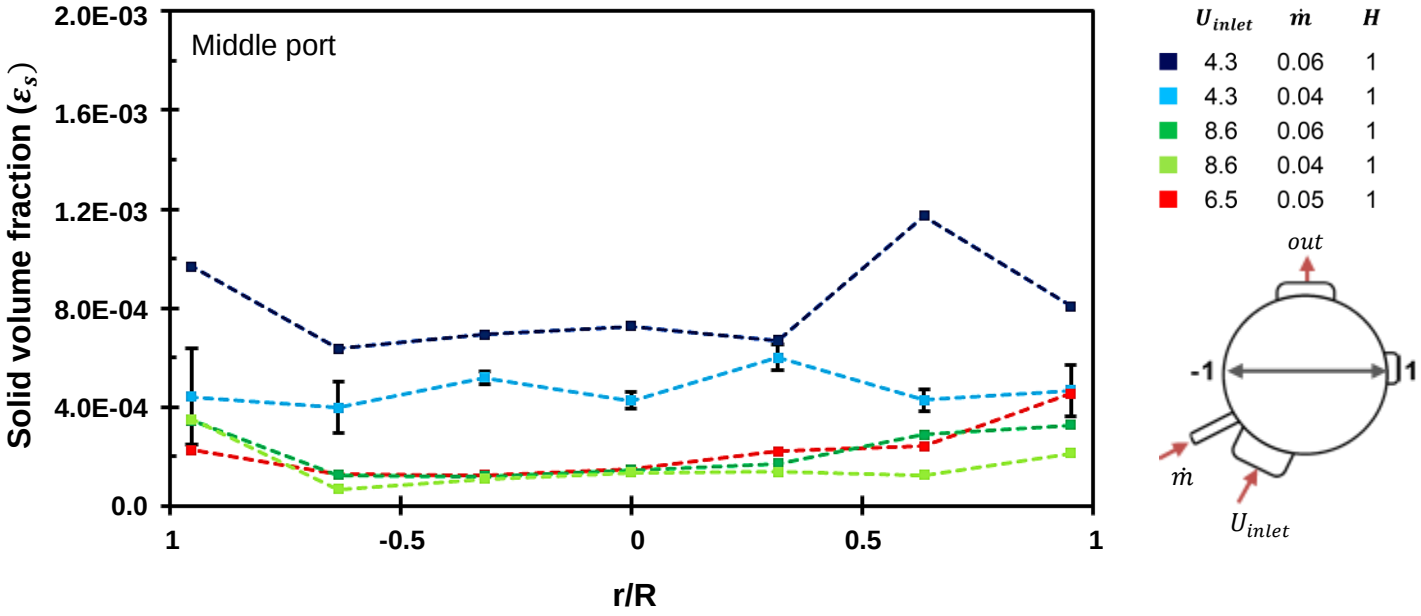

Figure 5.2: *The radial solids holdup profile at the* ***middle sampling port*** *under varying inlet velocity and riser height settings*

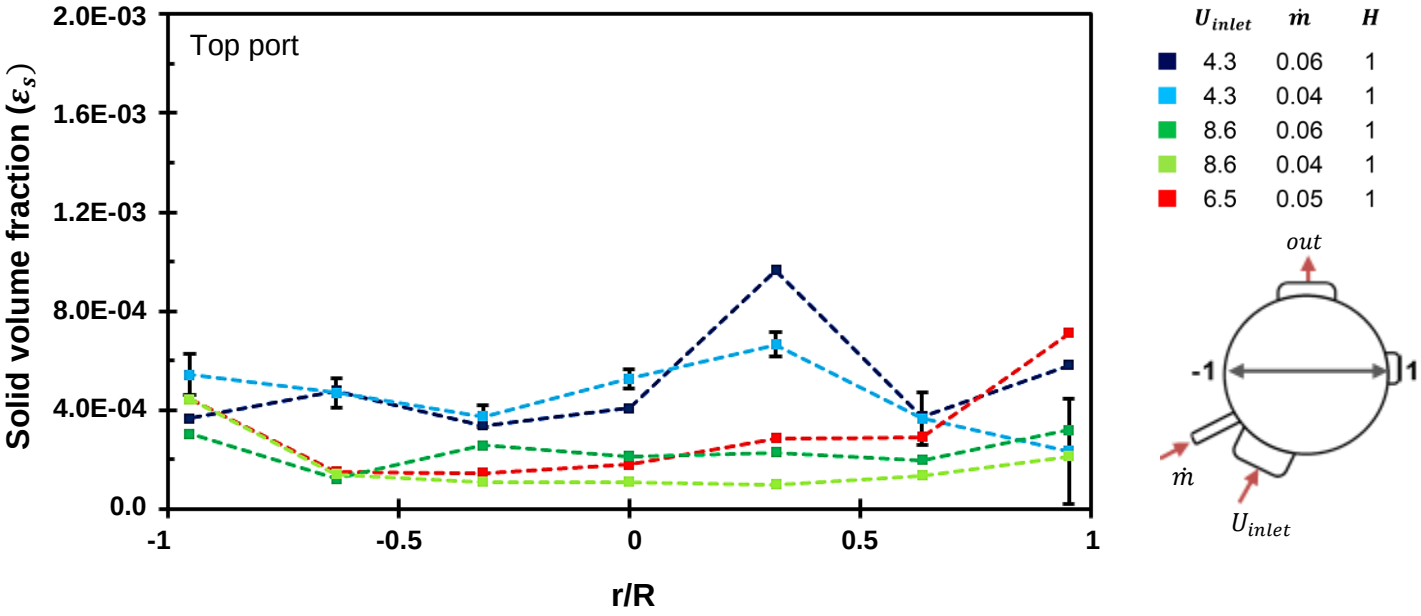

Figure 5.3: *The radial solids holdup profile at the* ***top sampling port*** *under varying inlet velocity and riser height settings*

The influence of the riser height setting on the radial solids holdup profiles at the bottom port is indicated in Figure 5.4 whereas the remainder of the radial solids holdup profiles are available in Annexure Q. An increase in the riser height from one to three sections shifted the skewness of the radial profiles and the same shift was observed at the middle sampling port but not at the top sampling port. The maximum solids holdup was shifted more towards the middle and the left riser wall with the top-view of the riser in the legend of Figure 5.3 as reference frame.

When comparing the dark blue profiles in Figure 5.4, the high solids volume fraction at the right riser wall reduced when the height setting was increased. Although this seemed to increase its uniformity, the shape of the dark blue profile in the bottom of Figure 5.4 indicates core annulus flow which is by definition a non-uniform distribution according to Section 2.2.3.2 During core annulus flow, a high concentration of low velocity or even downward flowing particles are present near the riser walls while the centre of the riser contains a dilute suspension of upward flowing particles. This results in the highest solids holdup being present along the riser walls. However, only upwards flowing particles were sampled given the sampling angle of the probe. As a result, the opposite trend is revealed since the upward flowing particles were increased near the riser centre when compared to the walls. Nevertheless, this hypothesis could be confirmed by considering the CFD results which will be discussed in Section 5.2.1.

For the light blue profile, an increase in the riser height created a spike in the solids holdup near the left riser wall which also increased the non-uniformity of the profile. The red and green profiles exhibited a decrease in the upwards flowing particles near the right riser wall as the height of the riser was increased. This had a different effect depending on the remaining independent variables. In the case of the dark green profile, a greater riser height increased the non-uniformity since a high concentration of particles were obtained in an isolated part of the radial area towards the left riser wall Similarly, the red profile was deemed less uniform but the particles were concentrated towards the right centre region of the riser. The only exception was the light green profile which exhibited more uniform flow upon an increase in riser height. However, in general an increase in the riser height and therefore an increase in the H/D ratio reduced the uniformity of the particle distributions.

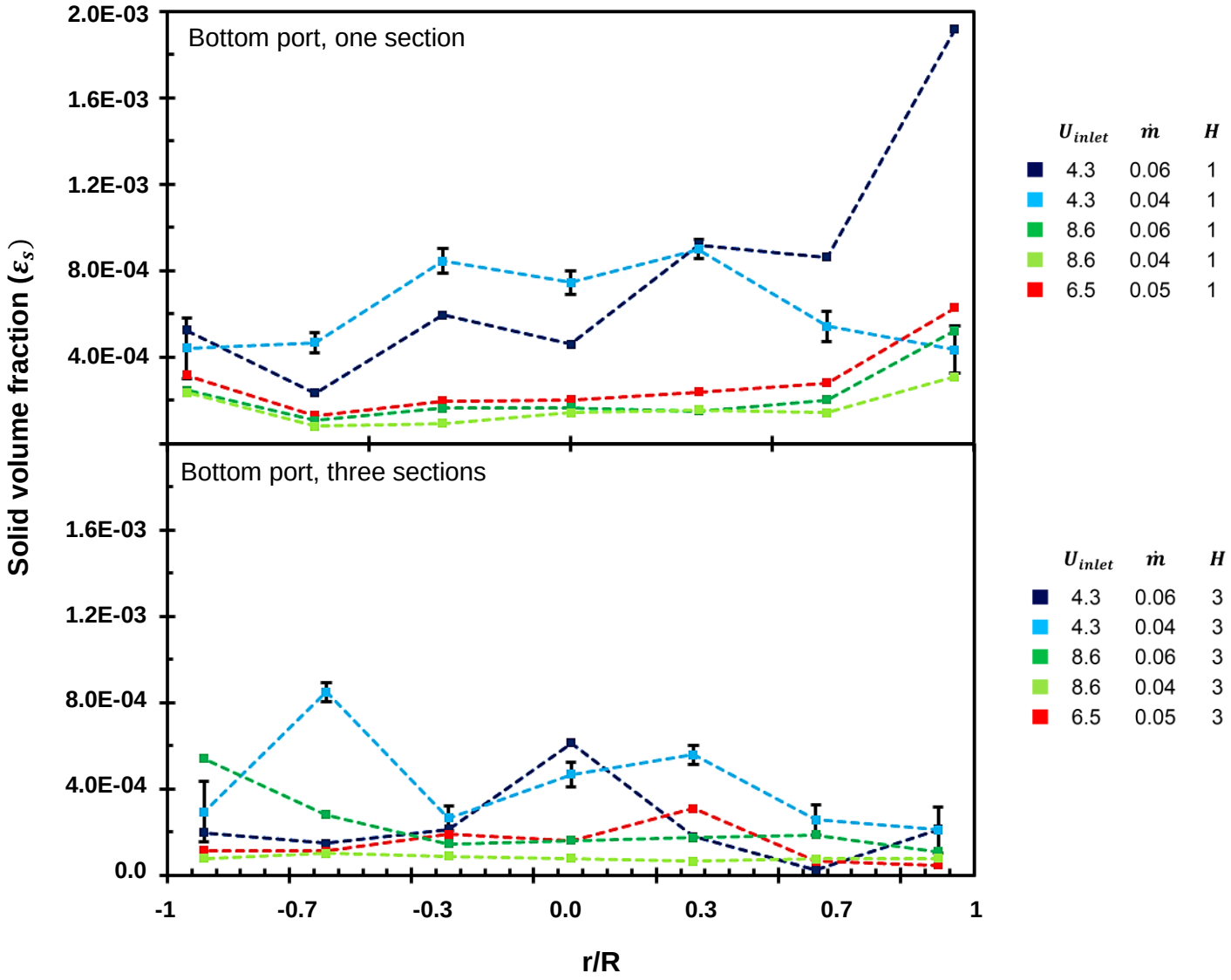

Figure 5.4: *The influence of riser height on the radial solids holdup profiles at the bottom sampling port*

According to literature[32,69], an increase in the H/D ratio created more uniform or flatter radial distributions. However, by examining Figure 5.4 and the remaining solids holdup profiles in Annexure Q, it was determined that an increase in the riser height (and therefore in the H/D ratio), had the opposite effect. The low solids flux operation may have contributed to the deviation from literature. Similar studies were performed at solids fluxes of between 1 – 200 kg/m^{2}s whereas this study was performed at fluxes below 1 kg/m^{2}s. Hence, the particles occupied a smaller cross-sectional area than would have been the case if higher solids fluxes were used.

Furthermore, in this study the riser height was changed in order to investigate the influence of the H/D ratio on the solids holdup. Conversely, the riser diameter was varied to assess the same influence throughout literature. This means that the ratio of the wall surface area to riser volume remained unchanged in this work while it was varied throughout literature and this will be discussed in more depth in Section 5.2.1.

5.1.2 Axial solids holdup

In Section 2.2.3, two methods for calculating the average solid volume fraction ($\bar{\varepsilon}_s$) were proposed. The first was an integral method which relies on local solid volume fraction measurements whereas the second was an approximation using pressure differential data. Both were evaluated in Annexure S after which it was decided to use the integral method represented by Equation 2-10. The average solid volume fraction at the three sampling ports were plotted against the riser height under varying operating conditions. In Figure 5.5 the axial solids holdup profiles in the tallest riser are illustrated. On the y-axis, the height of the sampling point from the reference height is provided and the x-axis represents the average solid volume fraction at a given height. The reference point is indicated in the image below the legend on the right of the figure. The confidence intervals associated with the data at each measurement port has been determined in Annexure R and added to the light blue profiles from Figure 5.5 - Figure 5.7 for reference.

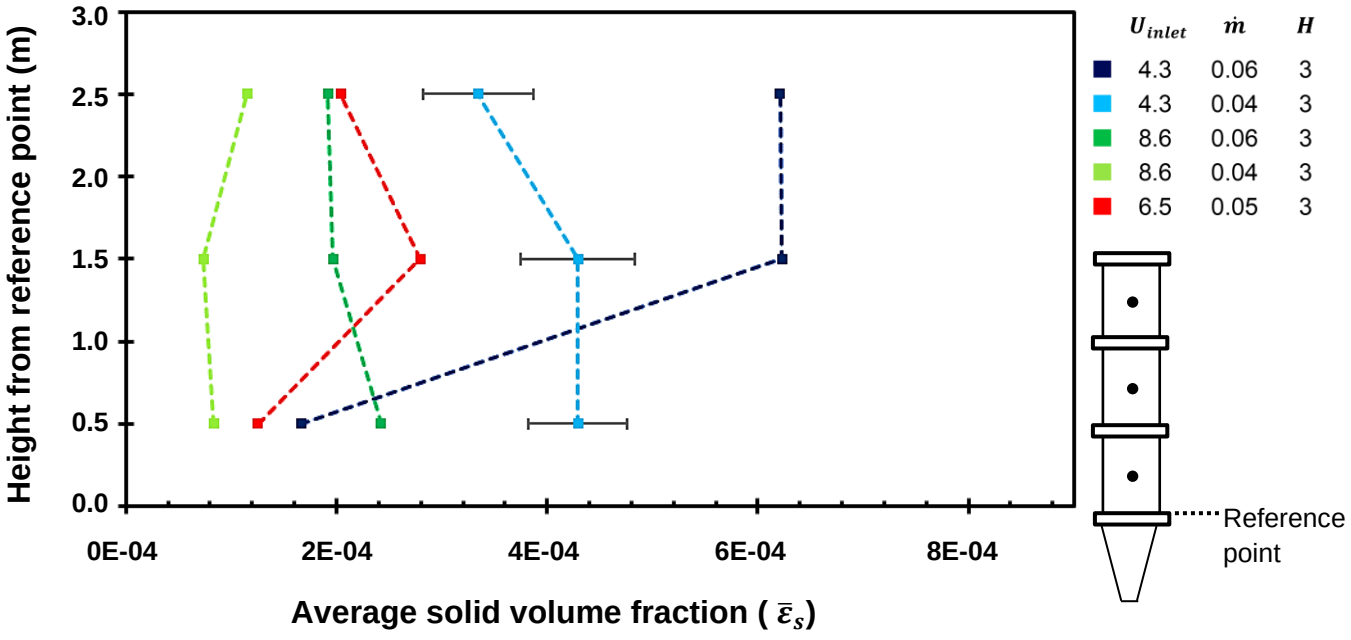

Figure 5.5: Experimental axial solids holdup profiles under varying operating conditions at the high riser height setting

Due to the confidence intervals, no conclusions could be made regarding the shape of the light green, dark green or light blue axial solids holdup profiles in Figure 5.5. However, some conclusions could be made regarding the red and dark blue average solid volume fractions in Figure 5.5. The $\bar{\varepsilon}_s$ at the top of the riser exceeded the $\bar{\varepsilon}_s$ values at the bottom for the dark blue profile. The maximum solids holdup at the top suggests the presence of an exit effect which was defined in Section 2.2.4.1, and this will be discussed in more depth throughout Section 5.2.2. An increase in the inlet air velocity together with a decrease in the solids load seemed to have reduced the exit effect as illustrated by the shift from the dark blue to the red line in Figure 5.5. In addition, a decrease in the inlet air velocity settings shifted the entire axial profile towards the right of Figure 5.5. This is in line with the literature findings from Section 2.2.4.2 despite the large confidence intervals that were obtained in this work.

In Figure 5.6 the axial solids holdup profiles that were obtained for the medium riser height setting are illustrated. Once again, the discussion will be limited to the red and dark blue profiles due to the associated experimental error. The velocity of the red axial profile in Figure 5.6 is equal to that of the two green profiles in Figure 5.5 and the velocity of the dark blue profile in Figure 5.6 is similar to the velocity of the two blue profiles in Figure 5.5. At a high velocity (the red profile in Figure 5.6) an exit effect was created when decreasing the riser height setting. This is indicated by the high solid holdup at the top sampling port when compared to the bottom when operating with two installed cylindrical riser sections. At a low velocity (the dark blue profile in Figure 5.6) the maximum solids holdup shifted towards the bottom of the riser when its height was reduced. Hence, the exit effect at the medium riser height setting was less than at the high setting when operating at 4.3 m/s.

The axial solids holdup profiles at the low riser height setting are provided in Figure 5.7. In this case, the confidence intervals were such that conclusions regarding the shape of the blue profiles could be discussed with more certainty when compared to the others. Both the dark and light blue profiles exhibited a higher $\bar{\varepsilon}_s$ at the bottom of the riser when compared to the top, however, this difference was less pronounced at the lower solid feed rate setting as depicted by the light-blue profile. This indicates that the exit effect was negligible in the shortest riser; at least for the low velocity experiments. Furthermore, when comparing the dark blue profiles from Figure 5.5 - Figure 5.7 the directly proportional relationship between the riser height setting and the exit effect can be seen. This phenomenon is explained further in Section 5.2.

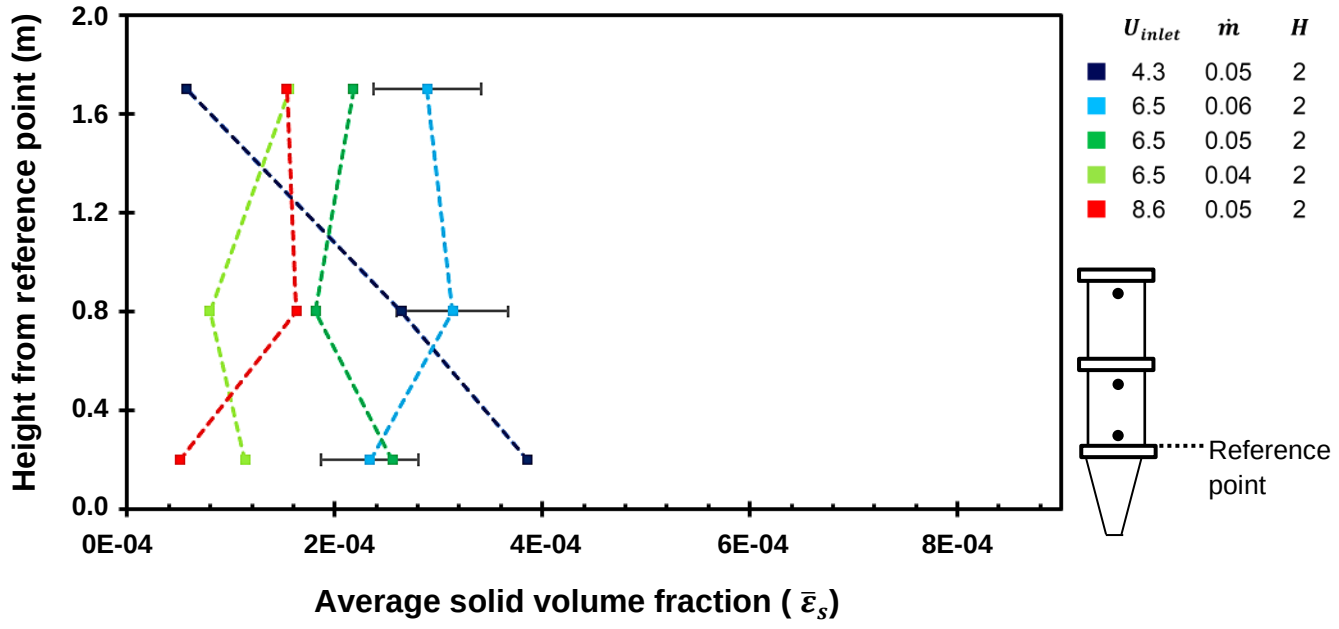

Figure 5.6: *Experimental axial solids holdup profiles under varying operating conditions at the medium riser height setting*

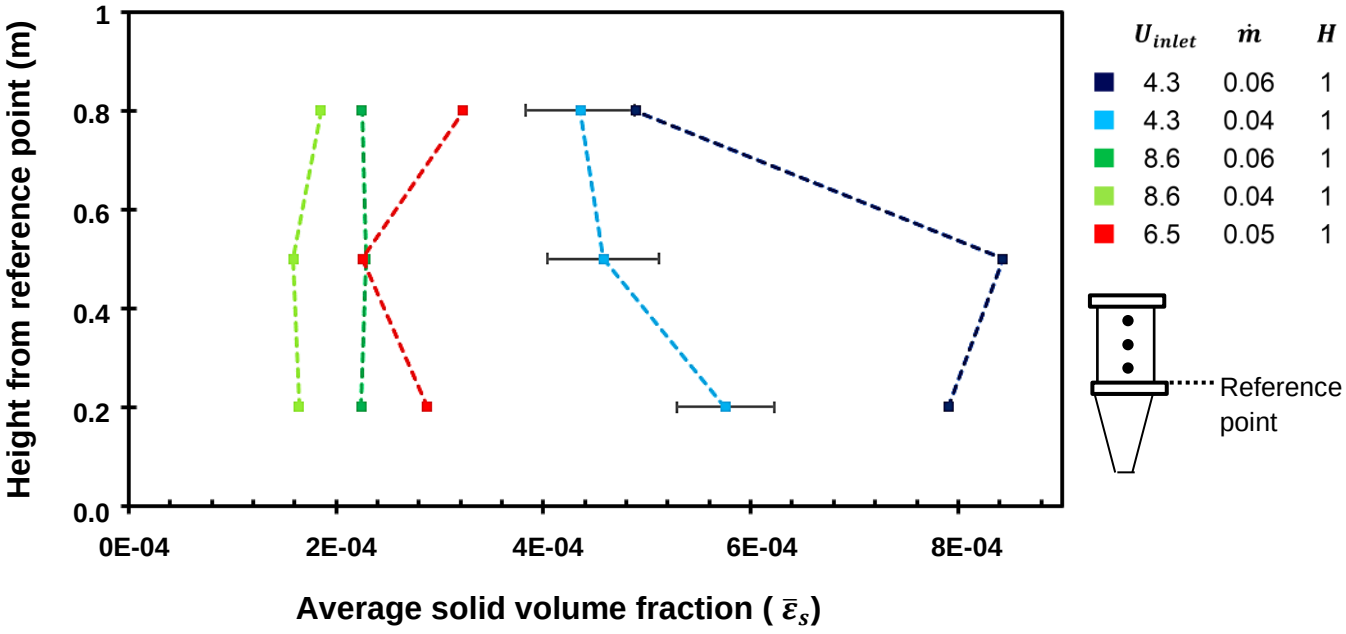

Figure 5.7: *Experimental axial solids holdup profiles under varying operating conditions at the low riser height setting*

According to Yan and Zhu (2004)[69], a change in the riser diameter has no influence on the shape of the axial solids holdup profile. However, the preceding discussion implies that a change in the riser height does. Furthermore, no exponentially decaying or C-shaped profile can be seen throughout Figure 5.5 - Figure 5.7 even though such profiles have been associated with numerous CFB-FGD systems throughout literature. This may have been due to the presence of the venturi at the bottom of the riser which accelerated the two-phase flow. As a result, the high velocity at the bottom of the riser mitigated the particle accumulation that was required for the formation of a C-shaped or exponentially decaying profile.

5.1.3 Pressure differential

To further evaluate the influence of the independent variables on the riser hydrodynamics, two pressure differentials were considered. The first was the pressure differential across the installed cylindrical sections while the second was the differential across the entire length of the riser. These differentials are defined in Table 3-10 in Section 3.3.2. The experimental results are provided in Table 5-1 along with the applicable confidence intervals determined and reported on in Annexure R. When comparing the fourth and fifth columns in Table 5-1 it can be seen that the pressure differential across the cylindrical sections ($\Delta P_{sections}$) were lower than those across the entire riser (ΔP_{riser}). The difference between the two may be regarded as the pressure drop across the venturi. Furthermore, the pressure drop across the installed sections can be represented as a percentage of the total pressure drop by applying Equation 5-1. These percentages have been included in the final column of Table 5-1. According to literature, an increase in the inlet air velocity reduces the average solids holdup and thereby the clustering and phase interactions inside the riser[20,31,35,69] Consequently, the overall pressure losses due to particle interactions are reduced at higher air velocities. This explains why $\Delta P_{sections}(\%)$ decreased as the inlet air velocities in Table 5-1 increased.

$$\Delta P_{sections}(\%) = \frac{100 \times (\Delta P_{sections})}{\Delta P_{riser}} \qquad \textbf{5-1}$$

From Table 5-1, it can be seen that when three cylindrical sections were installed, the venturi caused 93% - 97% of the overall pressure drop. This can be attributed to the greater momentum requirement that arose from increasing the tower height. When this was done, the frictional, drag and gravitational forces acting on the particles while travelling towards the riser outlet increased. In a response to this, the vacuum at the top of the riser had to be increased to maintain the same inlet air velocity. Given the higher suction, the venturi effect was enhanced, which increased the pressure differential across the restriction.

This will be discussed in more detail in Section 5.2.4. However, in the medium and short risers, the resistance to flow was less, which lowered the contribution of the venturi to the overall pressure drop. This explains the higher $\Delta P_{sections}(\%)$, at the medium and maximum height settings. Since the contribution of $\Delta P_{sections}$ to ΔP_{riser} was more pronounced, the influence of the air velocity on the negation of particle interactions and the reduction of pressure losses can be seen more clearly.

Table 5-1: *The pressure differentials across the riser and its installed sections under varying operating conditions and riser configurations*

$\boldsymbol{Installed\ sections}$	$\boldsymbol{U_{inlet}}$ $\boldsymbol{(m/s)}$	$\boldsymbol{\dot{m}_{solids}}$ $\boldsymbol{(kg/s)}$	$\boldsymbol{\Delta P_{riser}}$ $\boldsymbol{(Pa)}$	$\boldsymbol{\Delta P_{sections}}$ $\boldsymbol{(Pa)}$	$\boldsymbol{\Delta P_{sections}}$ **(%)**
3	4.3	0.04	**390**	**26**	7
	4.3	0.06	**585**	**34**	6
	8.6	0.04	**1001**	**29**	3
	8.6	0.06	**254**	**10**	4
	6.5	0.05	**626**	**42**	7
2	4.3	0.05	**586**	**399**	68
	8.6	0.05	**1211**	**391**	32
	6.5	0.04	**637**	**390**	61
	6.5	0.05	**888**	**389**	44
	6.5	0.06	**897**	**392**	44
1	4.3	0.04	**469**	**339**	72
	4.3	0.06	**594**	**360**	61
	8.6	0.04	**1219**	**323**	26
	8.6	0.06	**1184**	**354**	30
	6.5	0.05	**869**	**363**	42
		$CI =$	± 48	± 3	

The second to last column in Table 5-1 has been colour coded. As the pressure differential increases in Table 5-1 the cells change to a darker green or yellow colour, and finally, a dark red colour as the upper limit of the recorded values is approached.

The pressure differential across the installed cylindrical sections was one order of magnitude lower while operating at the high riser height settings compared to the medium or low riser height settings. This suggests a lower superficial gas velocity within the tallest riser which is consistent with the increased resistance to flow as discussed earlier. In Table 5-1, it can further be seen that the pressure differential across the riser sections was the highest at the medium riser height setting. The most probable explanation for the high-pressure differential across the medium riser is its exit assembly. The exit structures were curved at the low and high riser height settings, as shown in Section 4.1, whereas straight ducting was used at the medium riser height setting. This means that the flow resistance due to the exit assembly within the medium riser was the lowest, which would have increased the velocity gradient and the pressure differential. In Section 5.2, this idea is explained in more detail. Apart from the varying exit structures, any variations in the solids inventory between the riser height settings would have influenced the pressure differential. However, the overall average solids holdup inside the riser was not determined experimentally. In addition, the uncertainty associated with the axial solids holdup profiles in Section 5.1.2 was too large to formulate definitive explanations for the different pressure differentials in this section. Therefore, alternative explanations of the different pressure differentials will be provided from a CFD perspective.

5.2 CFD DESCRIPTION OF THE HYDRODYNAMICS

As discussed in Section 4.3.3, results from nine CFD simulations were obtained so that the influence of the three variables of interest on the riser hydrodynamics, could be evaluated. The simulation conditions of the nine models corresponded to the 2^3 full factorial design points as discussed in Section 3.3.2 and 4.3.3. From the nine CFD models, the radial solids holdup, axial solids holdup, pressure differentials and exit effects could be investigated. Additional CFD models were evaluated where necessary to supplement the discussions throughout this section.

5.2.1 Radial solids holdup

The simulated radial solids distribution at the middle sampling port under varying conditions is illustrated in Figure 5.8. In order to compare the results to those in Section 5.1.1, the CFD riser geometry was cut into planes along its z-axis and viewed from the top, where the orientation corresponds to that in Figure 5.9. Figure 5.8 was divided into four quadrants to highlight the changing operating and design parameters.

The horizontal division between the quadrants separates the high, and low solids feed rate settings, while the vertical line separates the high and low inlet air velocity settings. Furthermore, the effect that a change in the riser height setting had on the solids distribution is illustrated within each quadrant in Figure 5.8. The particles on each plane is represented by parcels, where each dot represents several particles which were grouped together to increase the ease of computation within the simulation software. The varying colours of the parcels indicate the velocity magnitude with the lowest velocity being represented by a dark blue and the highest velocity by a red colour as shown in the legend at the bottom of Figure 5.8. As mentioned previously, the parcels are directed towards the reader to indicate upwards movement through the cut plane. In addition, the empty space within the riser should be assumed to contain an insignificantly small concentration of particles, as no parcels were present in those regions.

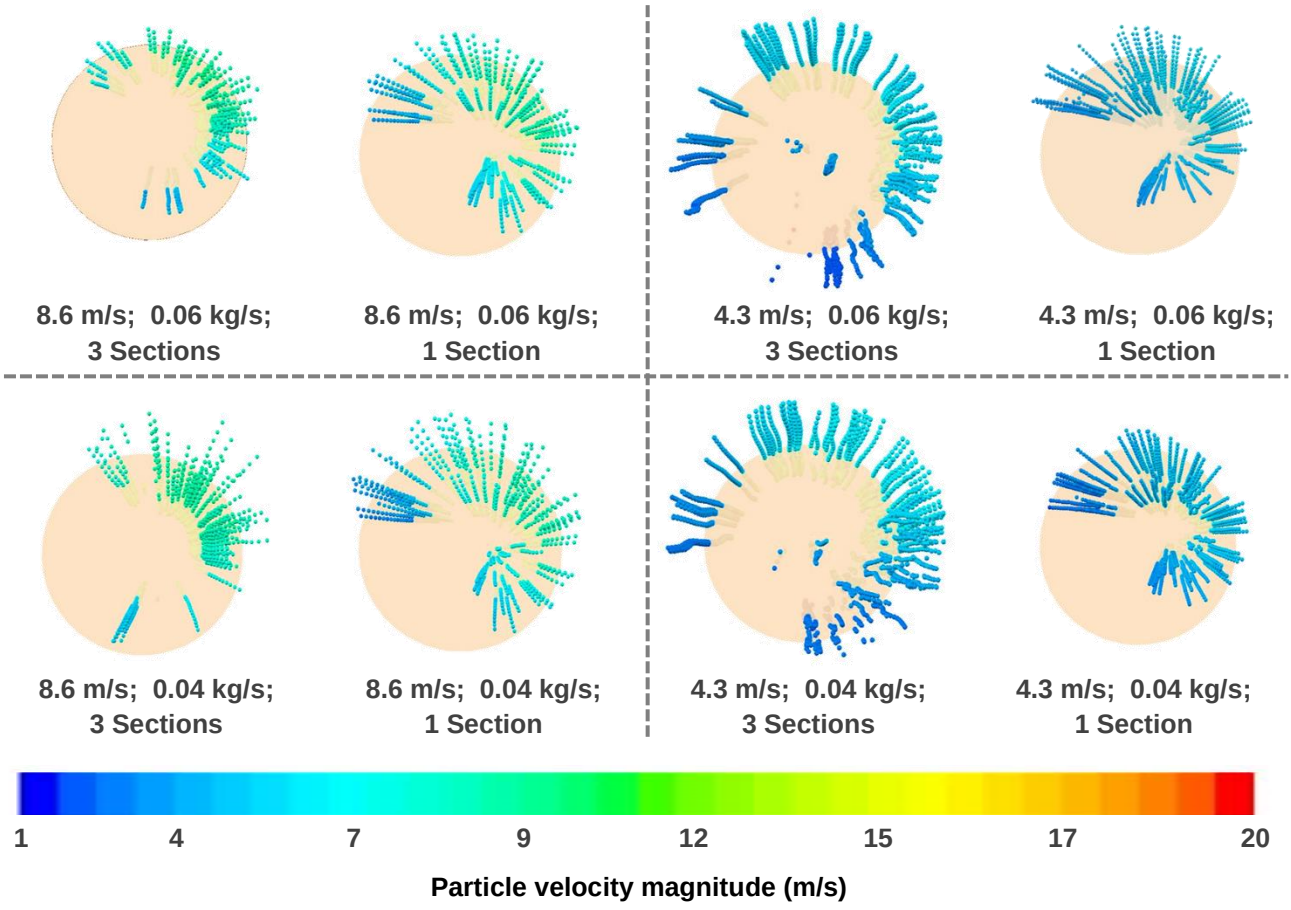

Figure 5.8: *The influence of varying operating and design parameters on the radial solids distribution at the middle sampling port according to the CFD models*

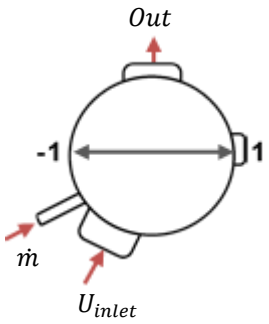

Figure 5.9: *Reference image for Figure 5.8, which indicates the relative position of various riser elements*

When considering Figure 5.8, a decrease in the riser height setting reduced the percentage of concentrated particles near the riser's walls (r/R > 0.75). The particles covered a greater area in the middle of the riser (0.5 < r/R < 0.75) instead. This means that the uniformity of the particle distribution deteriorated as the riser height was increased, which agrees with the experimental findings from Section 5.1.1. The influence of the H/D ratio on the solids holdup was discussed in chapter 2. When the riser diameter is increased, the ratio between the wall area to the riser volume will decrease according to Equation 5.2. However, the authors explained that although less wall friction was present under such conditions, the increase in the available cross- sectional area could facilitate a greater radial velocity gradient. Due to the greater velocity gradient, preferential gas flow was observed in the centre of the riser and preferential particle flow was observed near the walls of the riser, which increased the radial non-uniformity. In risers with a smaller diameter the opposite was true and the momentum exchange from the gas to the near wall particles increased. This increased the uniformity of the radial solids distributions within these risers despite the increased effect of wall friction.

$$\frac{Wall\ area}{Riser\ volume} = \frac{2\pi R \times h}{\pi R^2 \times h} = \frac{2}{R} \qquad \textbf{5-2}$$

In this study, the height was varied instead of the riser diameter, which means that the ratio between the wall area to the riser volume remained unchanged. However, in the taller riser, the two-phase flow was in contact with the riser wall for a longer distance before reaching the top of the riser. The additional friction meant that the near-wall particles in the medium and tall risers were subject to lower near-wall gas flows when compared to the shortest riser. This increased the volume of particles that concentrated near the walls, and, by definition, the non-uniformity of the radial particle distribution was higher.

To summarise, an increase in the riser diameter increased the non-uniformity of the solids distribution according to literature findings. In contrast, an increase in the riser height setting had the same effect, according to the conclusions of this study. Apart from the riser height setting, variations in the simulated inlet air velocity also had an influence on the radial solids distributions in Figure 5.8. As the inlet air velocity decreased, the solids distribution became less uniform because the particle accumulation near the riser walls increased. This is consistent with literature findings and is due to the reduced momentum transfer to the particles at lower carrier gas velocities. Consequently, the extent to which the particles deviated from the gas streamlines increased, and a more significant percentage accumulated within areas of lower flow. Compared to the riser height setting and the inlet air velocity, the solids feed rate had a negligible effect on the radial solids holdup.

Regardless of the operating and design conditions, the upper right corner of the scenes in Figure 5.8 contained the highest volume of particles. This suggests that the radial solids holdup in Figure 5.8 was influenced by the direction of particle and inlet air injection. The air that entered the riser at the lower left corner of the riser, as depicted in Figure 5.9, directed the particle flow, which also entered from the lower left corner, towards the opposite wall at the upper right corner of the riser as shown in Figure 5.9. As a result, the air velocity in the riser did not reach a maximum value in the centre as would be the case during core annulus flow. Instead, the maximum upwards particle flow was obtained at the opposite side of the air inlet which agrees with the experimental findings from Section 5.1.1. The implication of this was that possible core annulus flow could only be observed at 4.3 m/s since the momentum transfer from the inlet air to the injected particles was lower. In addition, the influence of the particle flow on the air flow through the two-way coupling selection was increased at low velocities. Accordingly, the trajectory of the particle and air streamlines changed at low inlet air velocities and at sufficiently high riser height settings. Since the same trends could be identified at the top and bottom ports, those scenes were provided in Annexure T.

5.2.2 Exit effects

As discussed in Section 2.2.4.1, an exit effect is an increase in the average solid volume fraction at the top of a CFB riser due to the internal recirculation or the deceleration of particles near the exit. The particles collide with the walls around the exit or lose momentum before reaching the top of the riser, resulting in decelerated or downward particle flow.

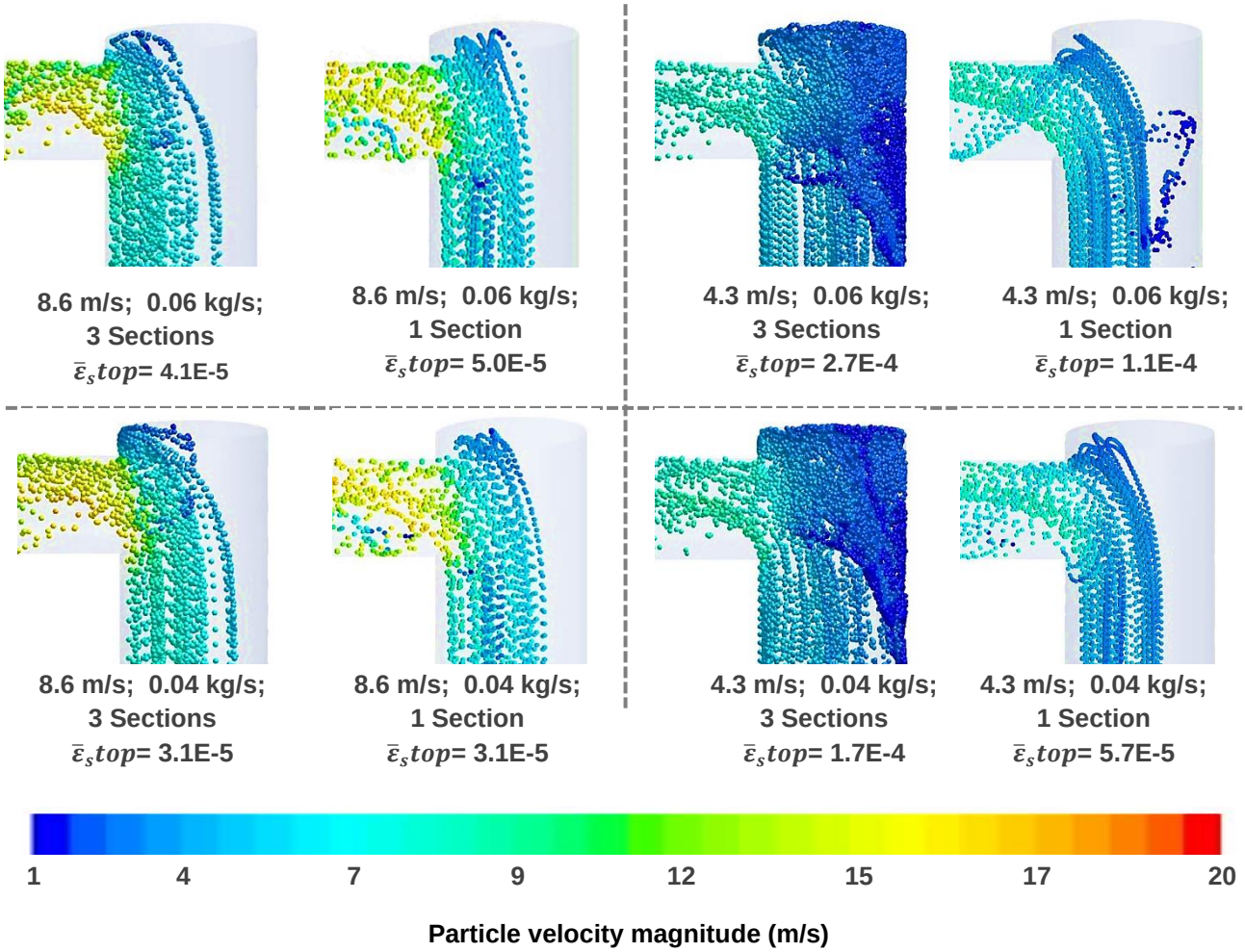

Figure 5.10: *The influence of varying operating conditions on the exit effect*

In this section, exit effects from the CFD models and their response to the varying design and operating parameters will be discussed. Scenes were created to visualise the particle behaviour at the top of the riser for each of the eight CFD models, which are provided in Figure 5.10. Figure 5.10 is divided into four quadrants to highlight the changing operating and design parameters. The horizontal and vertical divisions between the quadrants separate the high and low solids feed rate settings and the high and low inlet air velocity settings, respectively. In addition, the influence of the riser height setting is illustrated within each quadrant, while the average solid volume fractions within the top 0.5 m of each riser assembly were also included. Once again, the particles are represented by parcels, where each dot represents several particles which were grouped together to increase the ease of computation within the simulation software. The varying colours of the parcels indicate the velocity magnitude with the lowest velocity being represented by a dark blue and the highest velocity by a red colour as shown in the legend at the bottom of Figure 5.10.

In this case, a side view of the top of the riser is provided and the parcel flow occurs in 3 dimensions. In addition, the empty space may again be assumed to contain an insignificantly small concentration of particles, as no parcels were present in those regions. Upon inspection of Figure 5.10, an increase in the solids feed rate resulted in a higher solid volume fraction at the top of the riser ($\bar{\varepsilon}_s top$). Given that the inlet air velocity settings were kept constant for all four scenes in the left-hand plane or for all four scenes in the right-hand plane, the number of particles inside the riser increased together with the higher solids feed rate. Accordingly, the particle flow shifted towards a denser fluidisation region, and the two-phase flow decelerated. Because of this, a higher solid volume fraction throughout the riser was observed, and the exit effect became more pronounced.

It is further noticed that the shift in the operating conditions from the left to the right quadrants in Figure 5.10, which is associated with a change in gas velocity, brought about a more drastic visual change in the exit effect than the shift from the top to the bottom quadrants, which is associated with a change in solids feed rate. This indicates that the inlet air velocity had a stronger influence on the exit effect when compared to that of the solids feed rate. In accordance with literature findings as well as the experimental findings detailed in Section 5.1, a decrease in the inlet air velocity brought about an increase in the solids inventory inside the riser. Furthermore, the exit effect increased as a result thereof. When one riser section was installed, a reduction in the inlet air velocity decelerated the upwards flow. Therefore, the solids inventory inside the riser as well as the exit effect, increased. Although the same trend was observed when three sections were installed, internal particle recirculation occurred in addition to the higher overall solids holdup.

To understand the influence of the riser height on the exit effect, two additional CFD models were created to represent the medium riser height settings. The results are provided in Figure 5.11, where it can be seen that the degree of internal particle recirculation was limited in the shortest riser (with one cylindrical section installed). It can further be seen that when the riser was at its medium height setting (with two installed sections), the particles collided with the cavity walls above the exit but also with the roof of the riser. This is indicative of a more significant exit effect when compared to that in the short riser. At the maximum riser height setting, the largest exit effect could be observed at 4.3 m/s, while the exit effect was smaller when compared to the medium riser at 8.6 m/s.

Consequently, the combined influence of the riser height settings and the inlet air velocity governed the degree of internal particle recirculation at the top of the riser. This was because the riser height governed the degree of flow development, whereas the inlet air velocity governed swirling. Both these factors will be discussed subsequently. The first factor that will be discussed is the influence of riser height on the exit effect. Scenes of the gas velocity magnitude obtained from the two-phase simulations throughout the riser at varying riser height settings are provided in Figure 5.12.

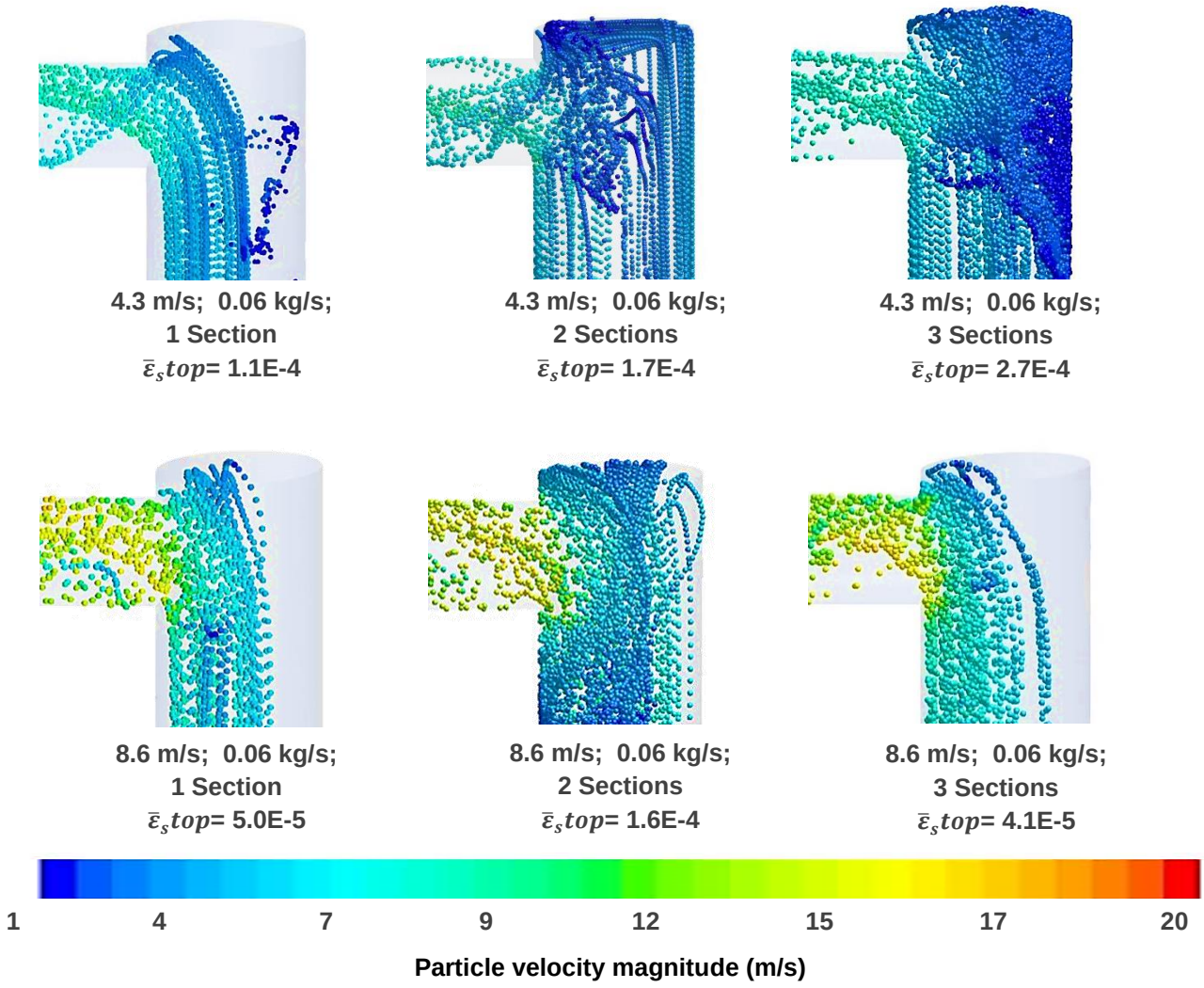

Figure 5.11: *The influence of riser height on the exit effect*

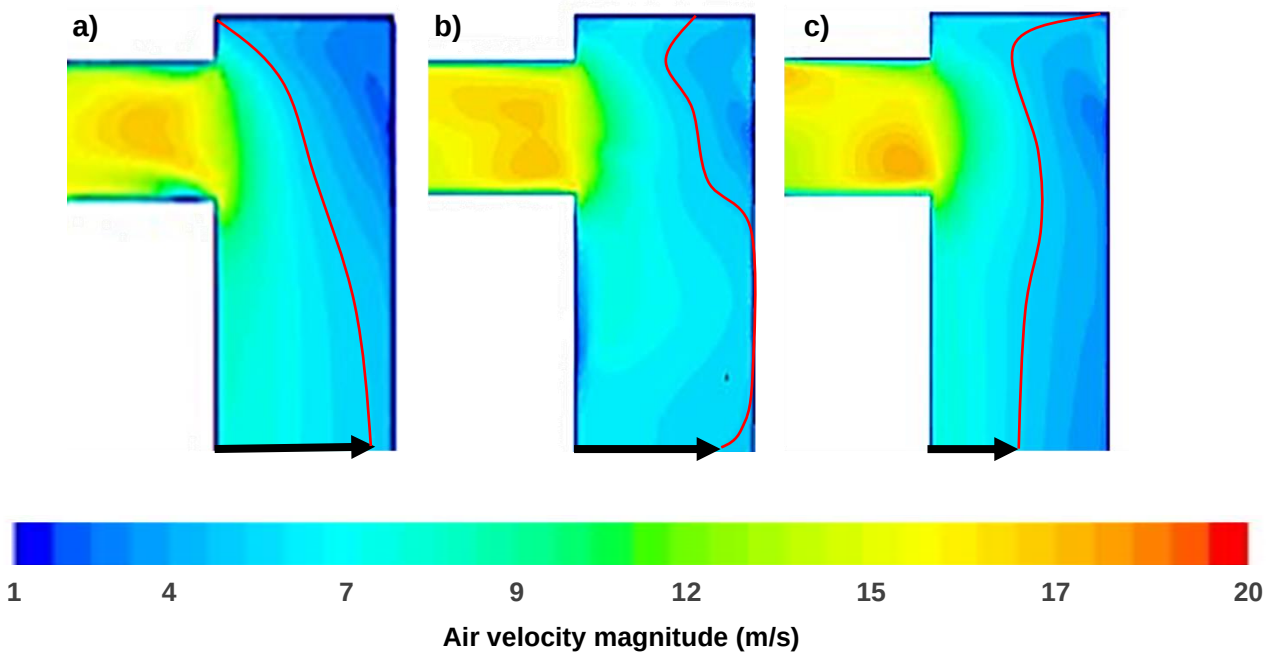

Figure 5.12: *Gas velocity magnitude profiles at the top of the riser at its (a) high, (b) medium and (c) low height settings*

The black arrows in Figure 5.12 point towards the edge of each 5.2 m/s velocity contour, which was further highlighted by a red line. As the riser height decreased from three sections in Figure 5.12 a) to one section in Figure 5.12 c), the length of the black arrows decreased. This suggests that the two-phase flow reached the riser exit in a lower state of development at lower riser height settings. Since the flow in the taller risers was at a later stage of development, the particles were more evenly distributed, as noticed and discussed in Section 5.2.1. Because of this, more particles were located further away from the exit and had to travel a greater horizontal distance before leaving the riser. Unfortunately, the upwards momentum of the particles caused these to overshoot the riser exit and collide with the walls above the exit instead. In the medium and short risers, the particles followed the gas streamlines more closely and were concentrated in one radial region upon reaching the exit at the top. The approximate radial region where the majority of the particle flow was present is indicated by the red cross in Figure 5.13. Since the particles had a smaller horizontal distance to travel towards the riser exit, less overshooting became apparent. Consequently, the likelihood of internal particle recirculation at the top of the riser decreased. Since the riser height governed flow development and the degree to which particle concentration positions deviated from the red cross in Figure 5.13, it had a large influence on the likelihood of internal recirculation at the top of the riser. The increasing exit effect together with the riser height at the top of Figure 5.12 corresponds to the experimental conclusions from Section 5.1.2.

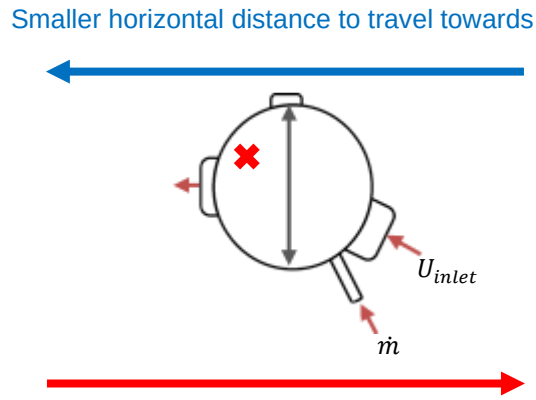

Figure 5.13: *Top view of the riser for reference*

The second factor which governed the exit effect was swirling. To illustrate the swirling effect at the riser's exit, the geometry in Figure 5.14 was rotated 90° in a clockwise direction around its z-axis, and a plane was used to cut the geometry along the red arrow. Given that particle recirculation was negligible in the short riser, according to the preceding discussion, the effect of swirling on the internal particle recirculation was only considered in the medium and tall risers. The scenes of the swirling air flow that was present at the riser exit under varying riser height settings and operating conditions are indicated in Figure 5.15. In Figure 5.15, the gas velocity vectors at the riser exit is indicated where the velocity magnitude is represented on a colour scale as indicated in the legend at the bottom of the figure. In this case, the length of each vector was kept constant to avoid confusion but as the vectors were rotated away from the reader the arrow appeared shorter.

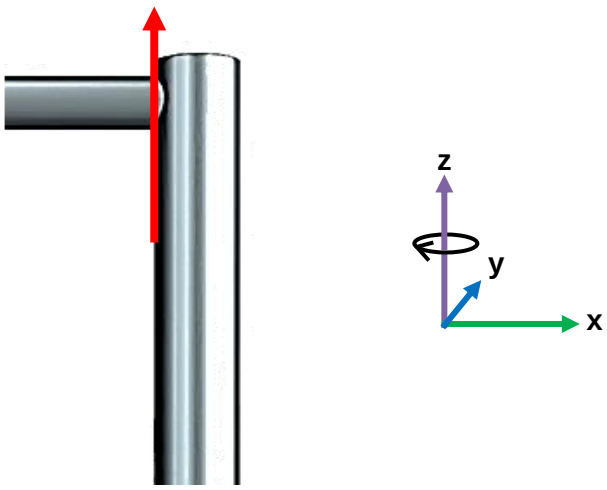

Figure 5.14: *Reference image for the swirling scenes*

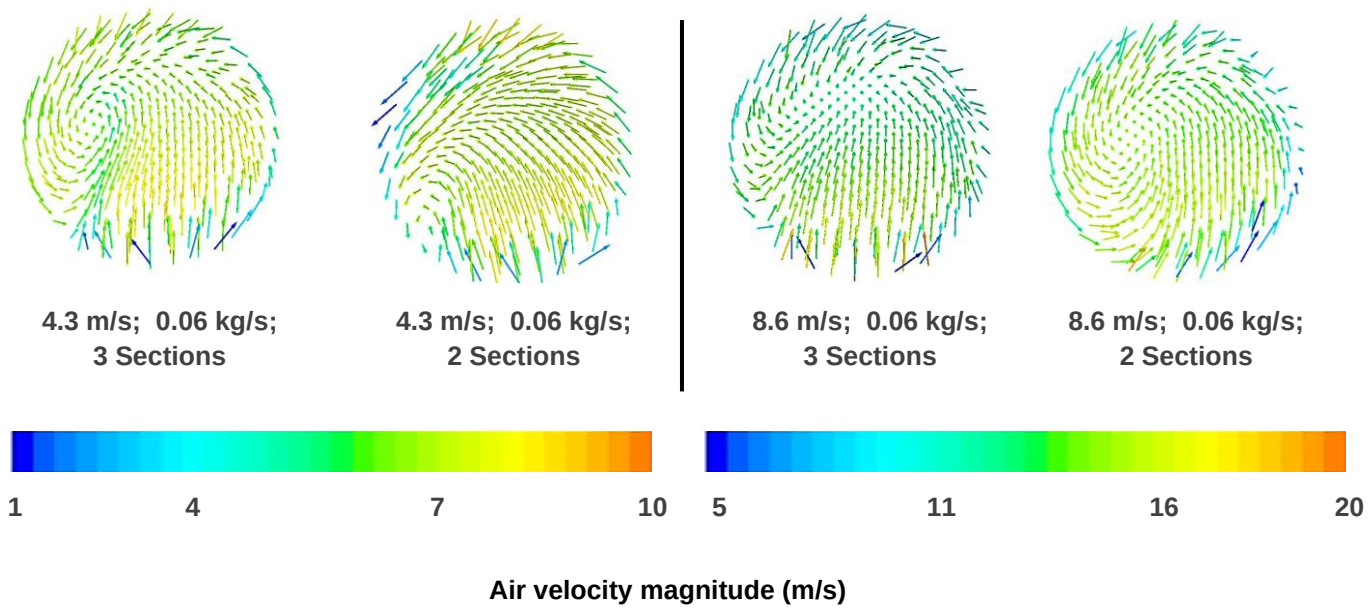

Figure 5.15: *Swirling effects at varying riser heights and inlet air velocities*

The degree of swirling at a given riser height varied based on the air velocity setting. The counterclockwise swirling altered the particles' trajectories to spiral towards the exit instead of exiting in a straight line. However, this rapid directional change caused particles to dislodge and collide with the walls of the riser instead. This is illustrated in Figure 5.16, where the particles collide with the back wall of the riser due to the swirling. These particles collide with the walls, travelled downwards and eventually re-joined the gas streamlines which flowed out through the exit. In Figure 5.15, it can be seen that the swirling in the tall riser was more significant than the swirling in the medium riser at 4.3 m/s. Consequently, the exit effect in the tall riser was more pronounced.

However, at 8.6 m/s, the swirling in the medium riser exceeded that of the tall riser, and as a result, the exit effect in the medium riser was greater. This explains the different solid volume fractions at the top of the riser under varying height and velocity settings in Figure 5.11. To summarise, the riser height determined whether particles would overshoot the exit, whereas the velocity settings and exit assembly determined the degree of flow swirling. This implies that the medium and tall risers were more likely to facilitate internal particle recirculation and that the degree of swirling determined at which height setting the exit effect would be more pronounced.

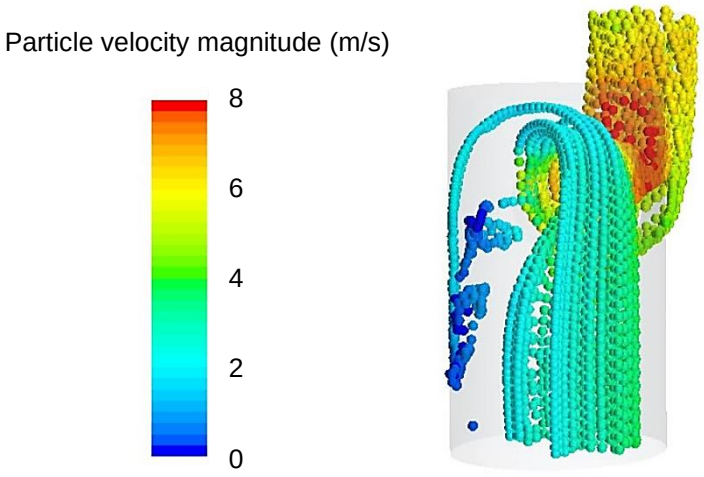

Figure 5.16: *Dislodged particles travelling towards the back riser wall due to inertia*

5.2.3 Axial solids holdup

In order to assess the influence of the operating conditions on the axial solids holdup, the profiles in Figure 5.17 were generated. This was done by creating circular planes along the height of the riser and extracting the surface averaged solids volume fraction from the simulation output. Figure 5.17 only contains the axial solids holdup profiles that correspond to the shortest riser since the same trends were identified in the simulations of the taller risers. These profiles have been provided in Annexure T. The reference point for the y-axis in Figure 5.17 is at the top of the conical section which was attached to the venturi. The riser's conical section was inaccessible during this study's experimental phase and was therefore not included in the axial solids holdup discussion in Section 5.1.2. Figure 5.17 shows that a higher average solid volume fraction was present at the bottom and top of the riser when compared to the middle.

Although the profiles were seemingly C-shaped, the gradually decreasing solids holdup within the conical section can be attributed to the increasing pipe diameter rather than to flow development. The increased solids holdup near the top of the riser was caused by the exit effects that were discussed in the previous section. Compared to the solids feed rate setting, the inlet air velocity had a larger influence on the shape of the axial solids holdup profiles in Figure 5.17. As the inlet air velocity was reduced, the exit effect became more pronounced, and this is consistent with the discussion in the previous section. In addition, the overall solids holdup increased as the inlet air velocity was reduced or the solids feed rate was increased. This relationship is well documented throughout the literature, as discussed in Section 2.2.4.2. In Figure 5.18 and Figure 5.19, the effect of the riser height on the axial solids holdup profiles can be seen, and the average overall solids holdup inside the riser is indicated next to each profile

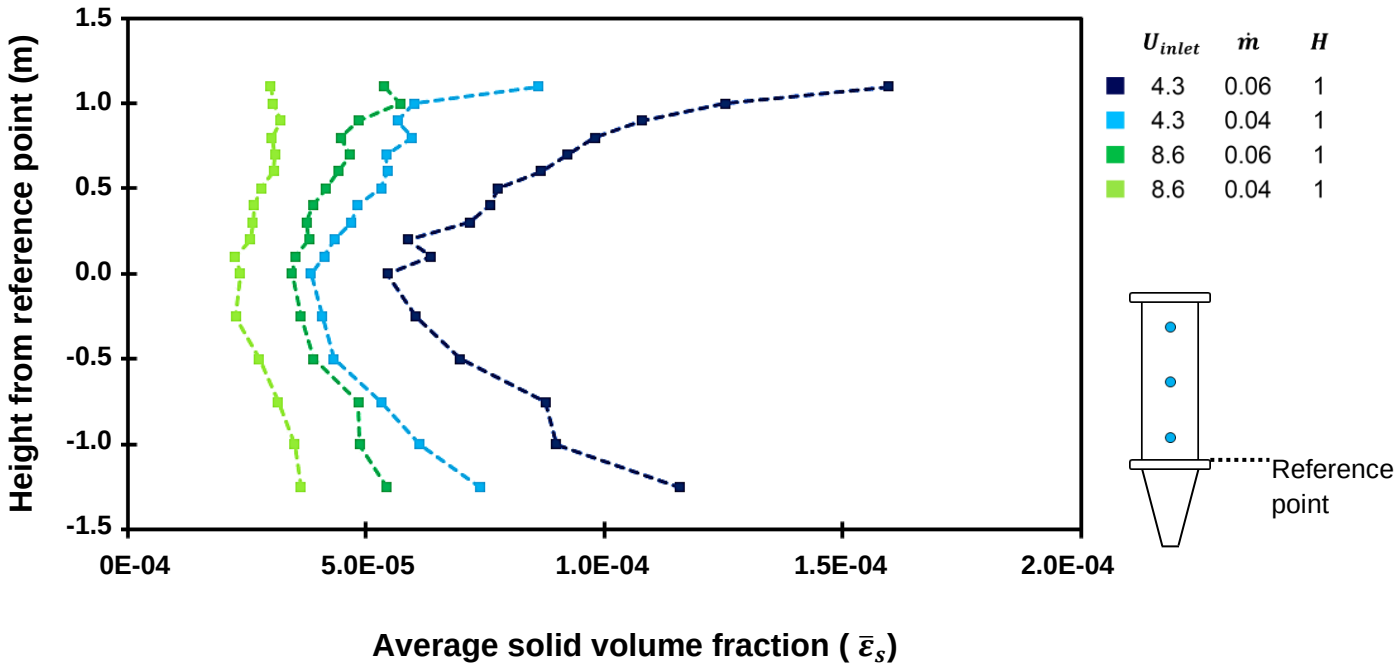

Figure 5.17: *Predicted axial solids holdup profiles under varying operating conditions at the low riser height settings*

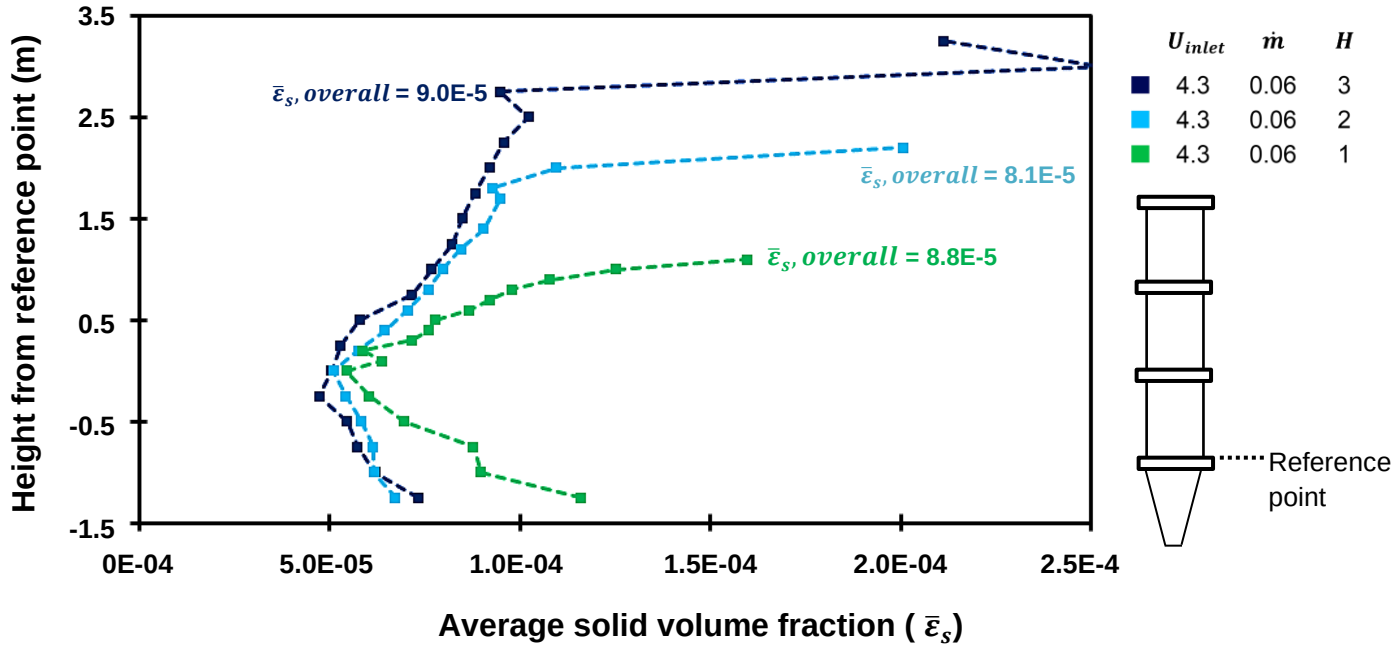

Figure 5.18: *Predicted axial solids holdup profiles under varying riser height settings at low inlet air velocity and high solids feed rate*

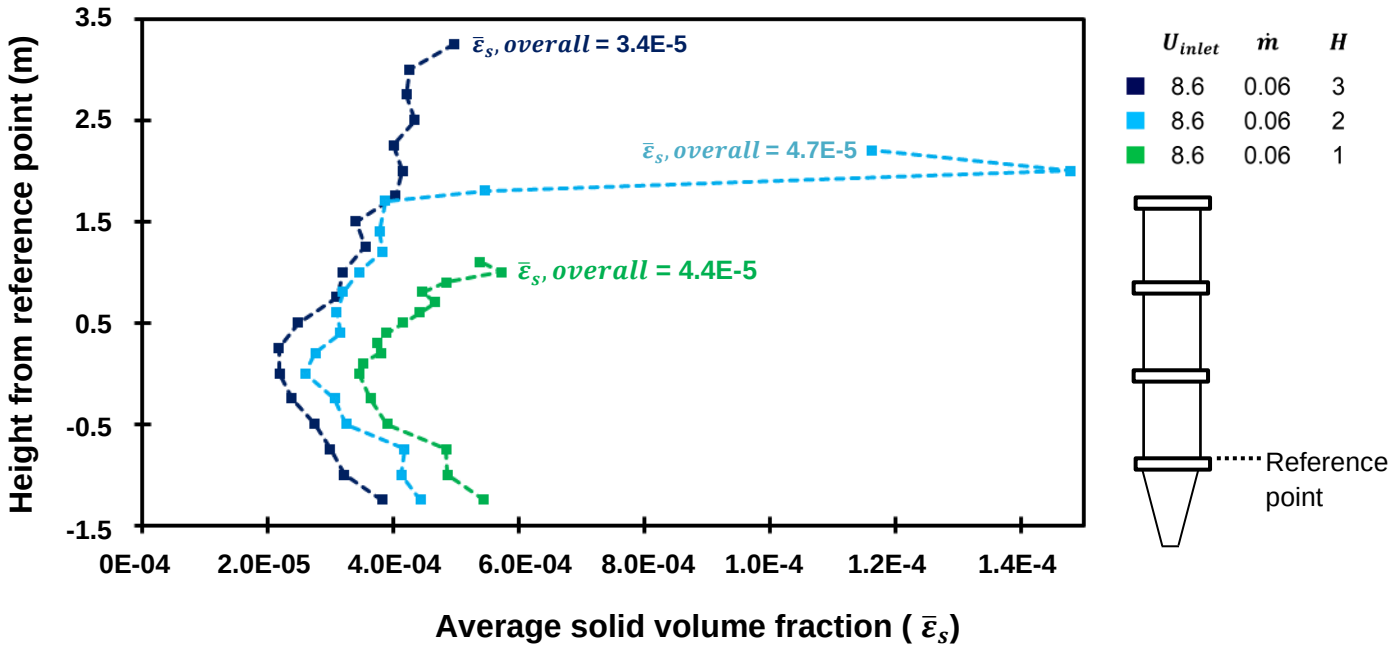

Figure 5.19: *Predicted axial solids holdup profiles under varying riser height settings at high inlet air velocity and solids feed rate*

In Figure 5.18, the presence of a prominent exit effect did not necessarily translate to a higher overall solids holdup, since $\bar{\varepsilon}_s, overall$ in the shorter riser was greater than that at the medium riser. This is because the flow resistance that was caused by the varying exit structures also had to be accounted for. When the riser height was changed to its high or low setting, bent ducting was used to connect the riser exit structure to the cyclone. Given the double elbow, the extent of flow separation, as well as the length of the exit duct, increased. Hence, the bent ducting created an additional resistance to flow that was not present in the straight exit duct used for the medium riser. Because of this, the pressure differential across the cylindrical sections in the medium riser was greater, as illustrated in Table 5-2.

Table 5-2: *Pressure differential between the base of the bottom cylindrical section and the riser outlet before particle injection*

	Number of installed sections		
Inlet air velocity (m/s)	**1**	**2**	**3**
4.3	5.2 Pa	6.5 Pa	4.8 Pa
8.6	22.2 Pa	23.3 Pa	15.5 Pa

Because of this, a trade-off existed between the pressure gradient across the cylindrical sections and the presence of an exit effect. Depending on these two factors, the overall solid volume fraction within the riser varied. At 4.3 m/s, the overall solids holdup was primarily determined by the pressure differentials in Table 5-2. This means that the medium riser had the lowest overall solids volume fraction due to straight ducting on the riser exit. In addition, the tall riser had the highest solids holdup, given the low-pressure differential across its cylindrical sections. However, at 8.6 m/s, the capacity of the carrier gas to overcome the flow resistance across the riser exit ducting was higher. Hence, the extent of the exit effects governed the overall solids holdup. For example, the medium riser height setting had the greatest exit effect as well as the greatest overall solids holdup, whereas the tallest riser had the lowest overall solids holdup given its reduced exit effect.

5.2.4 Pressure differential

From the experimental data, it was determined that between 28% and 98% of the pressure losses occurred across the venturi before the two-phase flow entered the installed cylindrical sections. From the CFD models, further information regarding this occurrence could be obtained. In Figure 5.20 the general pressure gradient across the venturi at the bottom of the riser is illustrated. The static pressure values corresponding to positions labelled (a) and (b) in Figure 5.20 have been provided in Table 5-3 for various operating and design settings.

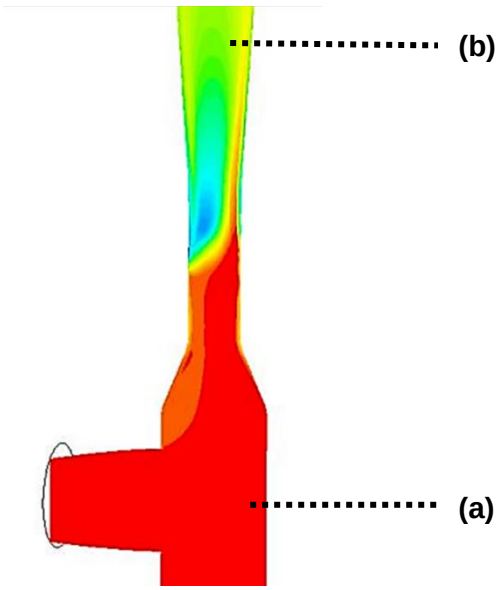

Figure 5.20: *Static pressure gradient across the riser inlet*

When considering both Figure 5.20 and Table 5.3, the predicted pressure at position (a) was close to atmospheric pressure. After the restriction, the two-phase flow accelerated which created the low static pressures observed inside and after the venturi around label (b). This was due to the venturi effect, wherein the pressure upstream of the restriction increased, as indicated by the red colour, and the flow velocity through the restriction increased as a result thereof. The predicted static pressure at the top of the riser can be found in the second to last column of Table 5-3. The data was extracted from the position corresponding to the top pressure transmitter (PT-09) from the experiments. Furthermore, the pressure at the top of the riser was subtracted from the pressure at the inlet to estimate ΔP_{riser} and the results are reported in the final column of Table 5-3. Since the venturi caused flow acceleration around label (b), it had a higher velocity and lower static pressure value when compared to P_{top} in Table 5-3. In addition, no noticeable trend between the solids feed rate and the riser's pressure drop could be identified from the CFD data. As discussed previously, the low solids flux operation (less than 1 kg/m^{2}s) may have contributed to this deviation from literature. The absence of a heterogeneous drag model also caused an underestimation of the overall solid volume fraction within the riser, given that the effect of varying particle distributions on the drag forces was not accounted for. In turn, the pressure differential across the riser was underestimated.

Table 5-3: *Predicted static gauge pressure values for Figure 5.20 and the top of the riser*

$\boldsymbol{Installed\ sections}$	$\boldsymbol{U_{inlet}}$ $(\boldsymbol{m/s})$	$\boldsymbol{\dot{m}_{solids}}$ $(\boldsymbol{kg/s})$	$\boldsymbol{a}$: $\boldsymbol{Inlet}$ $(\boldsymbol{Pa})$	$\boldsymbol{b}$: $\boldsymbol{Cone}$ $(\boldsymbol{Pa})$	$\boldsymbol{P_{top}}$ $(\boldsymbol{Pa})$	$\boldsymbol{\Delta P_{riser}}$ $(\boldsymbol{Pa})$
3	4.3	0.04	−9	−546	−432	423
	4.3	0.06	−9	−521	−449	440
	8.6	0.04	−36	−2299	−1573	1537
	8.6	0.06	−37	−2125	−1570	1533
2	4.3	0.06	−9	−478	−458	449
	8.6	0.06	−31	−1919	−1456	1425
1	4.3	0.04	−10	−521	−407	397
	4.3	0.06	−9	−474	−409	400
	8.6	0.04	−35	−2081	−1383	1348
	8.6	0.06	−34	−2125	−1386	1352

In Table 5-3, it can be seen that ΔP_{riser} increased together with the inlet air velocity setting. However, the percentage of the pressure losses that occurred across the venturi overshadowed the pressure losses across the riser sections. Since low solids feed rates were used, the superficial gas velocity, which would sustain the fast fluidisation regime within the cylindrical riser sections, was less. Hence, a greater force was required to achieve the desired air velocity after the restriction than what was required to maintain the fluidisation regime within the riser. This explains why the pressure differential across the venturi was one order of magnitude larger than that across the cylindrical sections that contained the bulk of the particles. Consequently, the simulation trends are comparable to the experimental findings in section 5.1.3.

The influence of the riser height on the outlet gauge pressure and the overall solids holdup was similar. This is indicated in Figure 5.21 and Figure 5.22, where the overall solids holdup is presented on the left axis and the outlet gauge pressure is presented on the right axis. The gauge pressure at the riser outlet is indicative of the gas velocity in the riser with lower pressure values indicating higher suction velocities. In both figures, the predicted overall solids holdup increased or decreased together with the gauge pressure. Consequently, the lower gas velocities that are associated with the less negative gauge pressures resulted in a higher solids holdup. This inversely proportional relationship between the carrier gas velocity and the solids holdup has been well established by previous researchers as discussed throughout Section 2.2

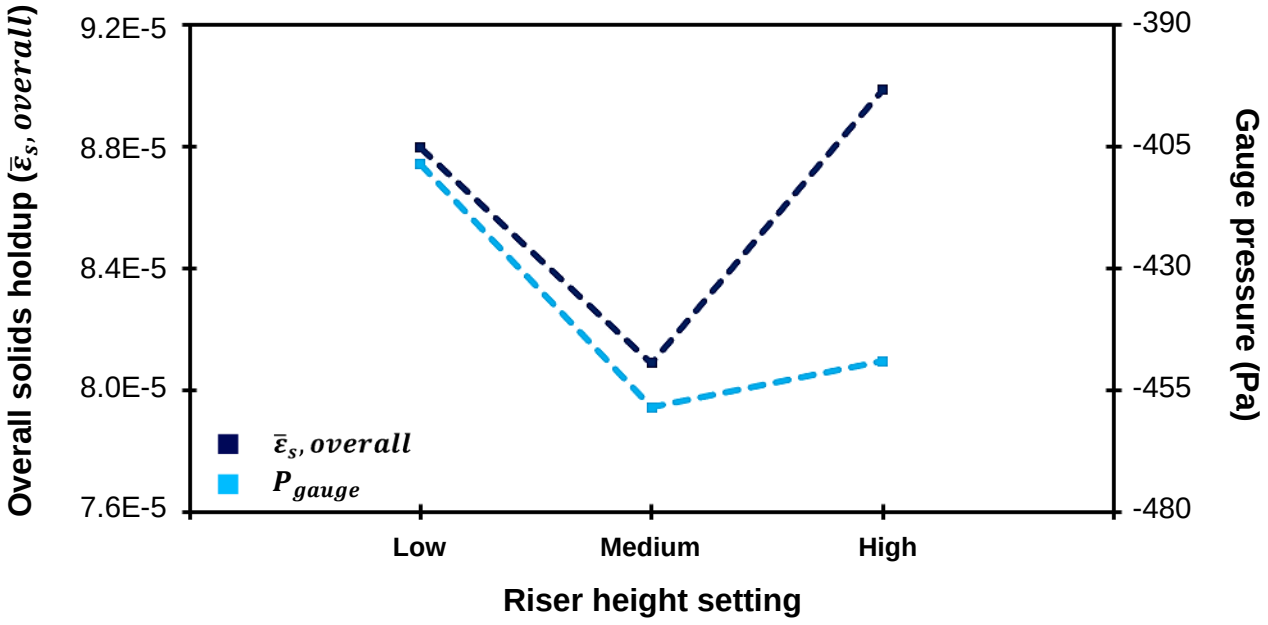

Figure 5.21: *The predicted overall solids holdup and gauge pressure at the top of the riser* ($U_{inlet} = 4.3\ m/s$ & $\dot{m}_{solids} = 0.06\ kg/s$)

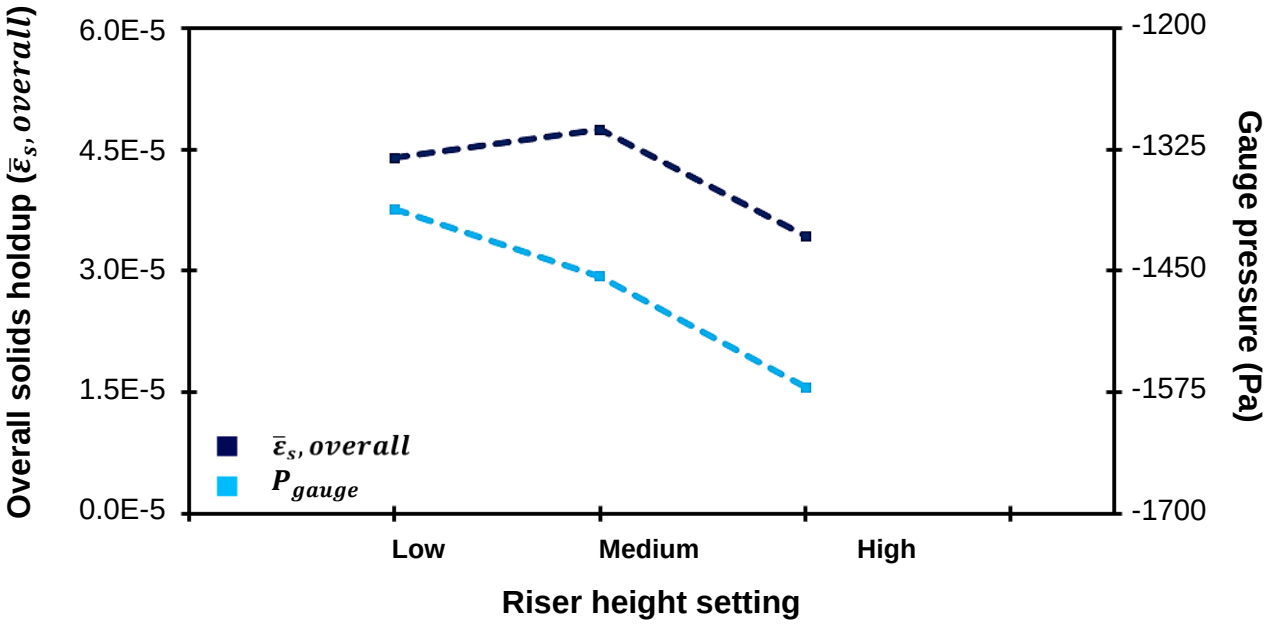

***Figure 5.22**: The predicted overall solids holdup and gauge pressure at the top of the riser ($U_{inlet} = 8.6\ m/s$ & $\dot{m}_{solids} = 0.06\ kg/s$)*

5.3 STATISTICAL DESCRIPTION OF THE HYDRODYNAMICS

5.3.1 Radial non-uniformity index

As discussed in Section 2.2.3.2, the radial non-uniformity index ($RNI(\varepsilon_s)$) indicates the extent to which particles deviate from a flat radial profile at a given riser height. From experimental data, regression models were constructed to predict the $RNI(\varepsilon_s)$ at each of the three sampling ports under varying inlet velocities, solids feed rates and riser height settings. The necessity to account for curvature in the regression models was evaluated through the parameters in Table 5-4. According to the P-values of curvature, it was unnecessary to include quadratic terms in the regression models. However, the curvature sum of squares ($SS_{curvature}$) at the top measurement port was significantly larger than zero, with the maximum obtainable value being one. This indicated that curvature had to be accounted for when predicting the $RNI(\varepsilon_s)$ at the top sampling port after all. For this reason, linear regression models were used to describe the $RNI(\varepsilon_s)$ at the bottom and middle ports while a quadratic model was used at the top. The three applicable regression models have been provided in Annexure U.

***Table 5-4**: Analysis of curvature in the relationship between the $RNI(\varepsilon_s)$ and the varying operating conditions and riser height settings*

Response	$\lvert t_{0_{curvature}} \rvert$	$P_{curvature}$	$SS_{curvature}$ $(\times 10^{-3})$	Regression model
$RNI(\varepsilon_s)_{bot}$	0.69	0.64	9.45	Linear
$RNI(\varepsilon_s)_{mid}$	2.30	0.31	4.49	Linear
$RNI(\varepsilon_s)_{top}$	0.52	0.72	106.97	Quadratic

After the regression models were generated, the predicted and experimental $RNI(\varepsilon_s)$ values at each of the three sampling ports were compared and the comparison is illustrated in Figure 5.23 (a) – (c). The regression models that were used for the bottom and middle ports described 96% and 99% of the variance respectively. This is indicated in Figure 5.23 (a) and (b) together with the mean squared errors (MSE) associated with each regression model. Given the small MSE and the large R^2 in both instances, the regression models provided a good fit for the data. The quadratic regression model that was used to predict the $RNI(\varepsilon_s)$ at the top port described 46% of the variance in the data and had a MSE of 0.07 as illustrated in Figure 5.23 (c). Given the low R^2 value, the $RNI(\varepsilon_s)$ at the top port proved difficult to describe via a quadratic regression model.

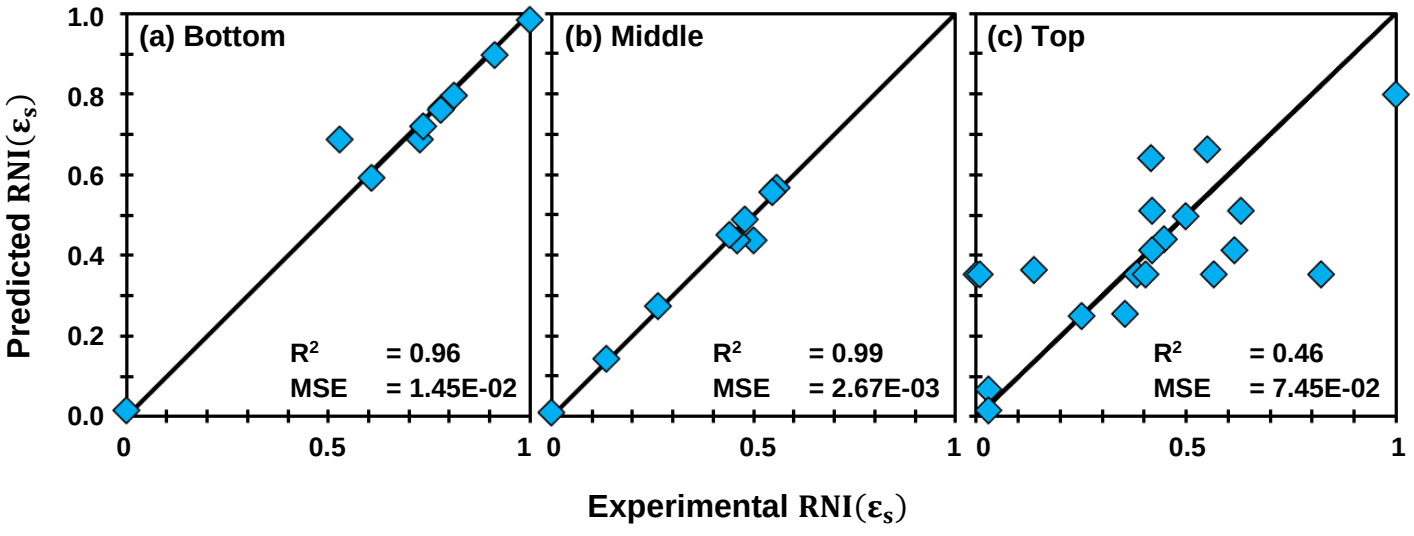

***Figure 5.23:** Normalised experimental versus predicted $RNI(\varepsilon_s)$ values at the **(a)** bottom port, **(b)** middle port and **(c)** top port*

The inlet air velocity, riser height, and solids feed rate were the independent variables in the regression models throughout the entirety of Section 5.3. The P-values that were associated with each factor and factor combination in the $RNI(\varepsilon_s)$ regression models, are reported in Table 5.5. The P-values that were equal to or less than 0.05 indicated that the corresponding factor had a significant correlation with the response and was therefore highlighted in blue.

At the bottom port, none of the factors had a significant statistical influence on the $RNI(\varepsilon_s)$. However, the inlet air velocity and solids feed rate had the lowest P-values even though these exceeded 0.05. This agrees with literature since the chances of particle clustering at the bottom of the riser is higher than that at the top due to incomplete flow development at the bottom. As a result, a change in the solids feed rate and inlet air velocity usually generates the greatest response at the bottom of the riser. The span of the sorbent PSD may have contributed to the weak correlations. Throughout literature, PSDs with spans ranging between 0.5 – 2 were used where 2 was considered to be large[82,94]. However, in this study the sorbent had a span of 2.3 which indicates that a comparatively wide PSD was used. Furthermore, the hydrated lime had an average particle size of 24 µm, which is less than the sizes reported throughout literature. According to the discussion in Section 2.2.4.3, the wider span and smaller particle size likely reduced the occurrence of particle clustering at the bottom port, which would have weakened the influence of the operating conditions on the $RNI(\varepsilon_s)$.

At the middle port, most of the factors and factor combinations had a significant effect on the $RNI(\varepsilon_s)$ according to the data in Table 5-5. The only insignificant factor, pointed out by a high P-value was the solids feed rate. However, when combined with other factors, the influence of the solids feed rate on the $RNI(\varepsilon_s)$ at the middle port was deemed significant. To discuss the influence of these factors on the $RNI(\varepsilon_s)_{mid}$, it may be useful to compare the findings to the CFD results in Section 5.2.1. From the CFD models, it was determined that an increase in the riser height or a decrease in the inlet air velocity increased the non-uniformity of the radial particle distributions within the riser. The former was due to increased friction and flow development, while the latter was due to the limited carrying capacity of the air at lower inlet air velocities.

Table 5-5: *P-values that were associated with each factor and factor combination from the regression analysis of the* $RNI(\varepsilon_s)$

Factor	$RNI(\varepsilon_s)_{bot}$	$RNI(\varepsilon_s)_{mid}$	$RNI(\varepsilon_s)_{top}$
U_{inlet}	0.105	0.019	0.406
$\dot{m}$	0.060	0.104	0.686
H	0.368	0.016	0.676
$U_{inlet} \times \dot{m}$	0.455	0.033	0.617
$U_{inlet} \times H$	0.109	0.051	0.418
$\dot{m} \times H$	0.189	0.029	0.736
$U_{inlet} \times \dot{m} \times H$	0.140	0.038	N/A
U_{inlet}^2	N/A	N/A	0.050
$\dot{m}^2$	N/A	N/A	0.719
H^2	N/A	N/A	0.089

According to the regression model of the $RNI(\varepsilon_s)_{mid}$, this was only true under specific conditions, namely:

- Two or three installed cylindrical sections and
- Inlet air velocities of between 4.3 m/s and 6.5 m/s.

Outside of these parameter limits, an increase in the riser height or a decrease in the inlet air velocity decreased the $RNI(\varepsilon_s)_{mid}$ instead. Put differently, these changes resulted in more uniform distributions. This is illustrated by the response surface that was constructed from the regression model of the $\mathrm{RNI}(\varepsilon_s)_{\mathrm{mid}}$ in Annexure V. The discrepancy between the experimental findings and the CFD results may be explained by considering Figure 5.24. Since samples were collected along the dashed lines in Figure 5.24 the $\mathrm{RNI}(\varepsilon_s)$ value of both cases would be equal, despite the less uniform distribution in the second image. Furthermore, downwards flowing particles were not sampled. Thus, if another set of radial data was collected at a 90° angle and the downwards flowing particles were quantified, the non-uniformity would be better described by this parameter.

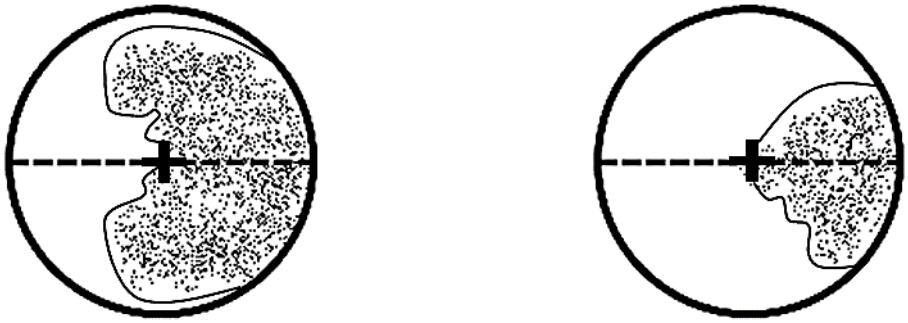

Figure 5.24: *Hypothetical radial solids holdup distributions to illustrate the shortcomings in the* $RNI(\varepsilon_s)$ *calculations*

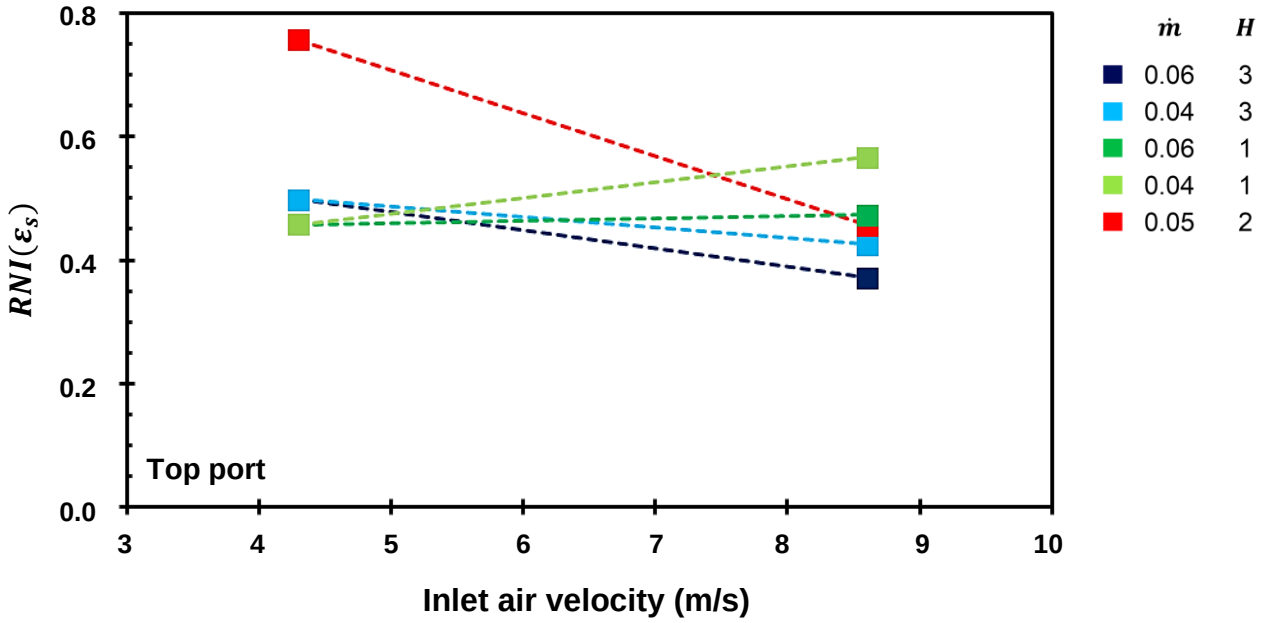

Figure 5.25: *The experimentally determined relationship between the* $RNI(\varepsilon_s)_{top}$ *and the inlet air velocity at varying solids feed rates and riser height settings*

The regression model and CFD models only predicted similar hydrodynamic behaviour when the non-uniformity of the radial solids distribution translated to the dashed measurement line in Figure 5.24. This only occurred at the conditions discussed previously. The quadratic regression model that was constructed to predict the $RNI(\varepsilon_s)$ at the top port indicated a strong second order relationship between the $RNI(\varepsilon_s)$ and the inlet air velocity. However, the experimental findings were considered without applying the regression model, given the poor fit of the model, as indicated in Figure 5.23 (c).

The experimental results indicated that the $RNI(\varepsilon_s)$ at the top port decreased as the inlet air velocity was increased if the riser height remained sufficiently large. This is illustrated in Figure 5.25, where the $RNI(\varepsilon_s)$ decreased along the x-axis when the riser was at or above its medium height setting. Once again, the reason for the riser height limitation on the $RNI(\varepsilon_s)_{top}$ calculation can be attributed to the sampling procedure. The non-uniformity was only captured through sampling at the greater riser height settings since those conditions were associated with the least uniform radial solids distributions.

5.3.2 Average solid volume fraction

From experimental data, regression models were generated to predict the average solid volume fraction ($\bar{\varepsilon}_s$) at each of the three sampling ports under varying inlet velocities, solids feed rates and riser height settings. Similar to the previous section, the P-values of curvature and the curvature sum of squares for each of the three parameters were determined and reported in Table 5-6. Since the P-value of curvature for the average solid volume fraction at the top port was smaller than 0.05, it was necessary to include quadratic terms in its regression model. Furthermore, the curvature sum of squares ($SS_{curvature}$) of the average solid volume fraction at all the measurement ports were significantly smaller than zero. For this reason, linear regression models were used to describe the $\bar{\varepsilon}_s$ at the bottom and middle port while a quadratic model was used at the top port. The three applicable regression models have been provided in Annexure U.

Table 5-6: *Analysis of curvature in the relationship between the average solid volume fraction ($\bar{\varepsilon}_s$) and the varying operating conditions and riser height settings*

Response	$\lvert t_{0_{curvature}} \rvert$	$P_{curvature}$	$SS_{curvature}$ $(\times 10^{-3})$	Regression model
$\bar{\varepsilon}_{s_{bot}}$	14.34	0.05	22.64	Linear
$\bar{\varepsilon}_{s_{mid}}$	3.00	0.21	60.80	Linear
$\bar{\varepsilon}_{s_{top}}$	86.02	0.01	69.41	Quadratic

A comparison between the predicted and experimental average solid volume fractions at every sampling port together with their goodness of fit indicators is provided in Figure 5.26 (a) – (c). The linear regression models which represented the average solid volume fractions at the bottom and middle sampling ports, described 97% and 92% of the variance, respectively.

Given the small MSE and the large R^2 in both Figure 5.26, (a) and (b), the linear models were deemed suitable to describe the experimental trends. However, the quadratic regression model that was used to predict the $\bar{\varepsilon}_s$ at the top port only accounted for 74% of the variance in the data points. Hence, the low R^2 value limited the conclusions that could be made regarding the average solid volume fraction at the top port via regression analysis.

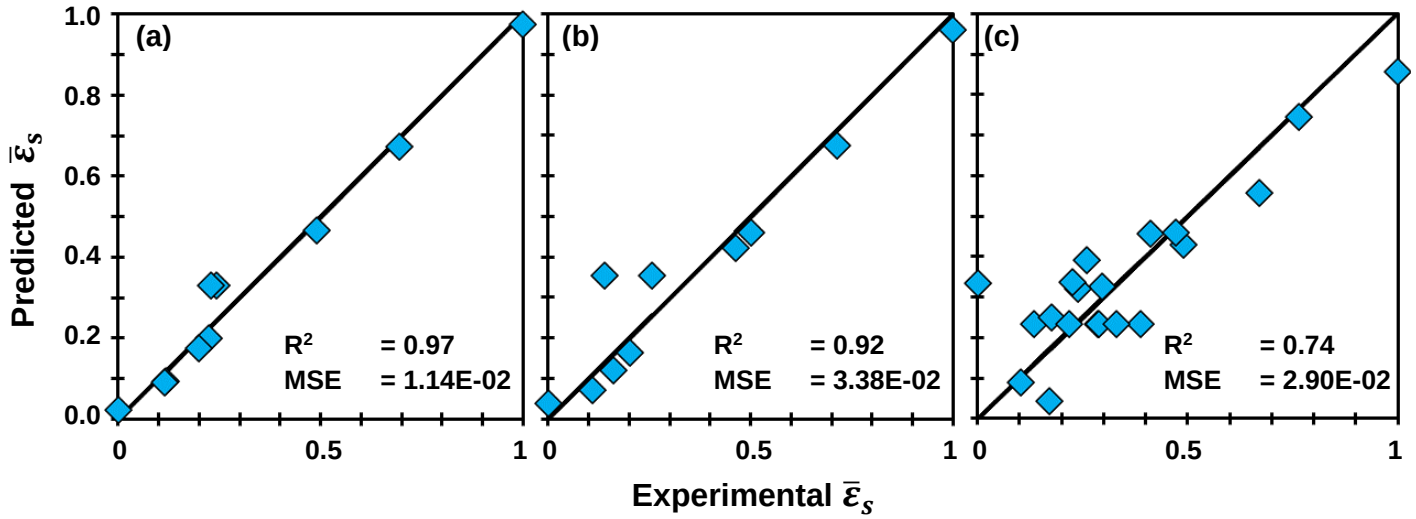

Figure 5.26: *Normalised experimental versus predicted average solid volume fraction* $(\bar{\varepsilon}_s)$ *at the* ***(a)*** *bottom port using a linear regression model,* ***(b)*** *middle port using a linear regression model and* ***(c)*** *top port using a quadratic regression model*

In Table 5-7, the P-values of the various factors and factor combinations are provided. The inlet air velocity was the only factor that had a P-value below 0.05 for all three of the $\bar{\varepsilon}_s$ predictions as indicated by the blue blocks in Table 5-7. This indicates that the inlet air velocity had the strongest influence on the average solid volume fraction regardless of the sampling point. According to the three regression models in Annexure U, an increase in the inlet air velocity resulted in a lower average solid volume fraction. This held true regardless of the riser height setting, or the solids feed rate and is consistent with literature findings. Since lower average solid volume fractions are often associated with lower $RNI(\varepsilon_s)$ values throughout literature, the influence of the inlet air velocity on both parameters should be similar. However, in the previous section, it was found that an increased air velocity only decreased the $RNI(\varepsilon_s)$ values under specific circumstances.

Table 5-7: *P-values that were associated with each factor and factor combination from the regression analysis of the* $\bar{\varepsilon}_s$

Factor	$\bar{\varepsilon}_{s_{bot}}$	$\bar{\varepsilon}_{s_{mid}}$	$\bar{\varepsilon}_{s_{top}}$
U_{inlet}	0.033	0.052	0.006
$\dot{m}$	0.509	0.196	0.084
H	0.064	0.472	0.531
$U_{inlet} \times \dot{m}$	0.379	0.459	0.442
$U_{inlet} \times H$	0.086	0.776	0.592
$\dot{m} \times H$	0.229	0.767	0.367
$U_{inlet} \times \dot{m} \times H$	0.121	0.617	N/A
${U_{inlet}}^2$	N/A	N/A	0.432
$\dot{m}^2$	N/A	N/A	0.290
H^2	N/A	N/A	0.093

5.3.3 Pressure differential

Regression models were also composed to investigate the relationship between the pressure differentials and the inlet velocity, solids feed rate and the riser height setting. Once again, the pressure differential across the riser (ΔP_{riser}) as well as the installed cylindrical sections ($\Delta P_{sections}$) were considered. The P-values of curvature and the curvature sum of squares of both regression models are provided in Table 5-8. A strong quadratic relationship between $\Delta P_{sections}$ and the factors were identified through the low $P_{curvature}$ and high $SS_{curvature}$. On the other hand, a linear model was sufficient to describe the total pressure differential across the riser due to the high $P_{curvature}$ and low $SS_{curvature}$. Accordingly, a linear regression model was used to describe the pressure differential across the riser, while a quadratic model was used to describe the pressure differential across the riser sections. These regression models are provided in Annexure U.

Table 5-8: *Analysis of curvature in the relationship between the pressure differentials and the varying operating conditions and riser height settings*

Response	$\lvert t_{0_{curvature}} \rvert$	$P_{curvature}$	$SS_{curvature}$ $(\times 10^{-3})$	Regression model
$\Delta P_{sections}$	117.23	0.01	460.00	Quadratic
ΔP_{riser}	10.47	0.07	63.66	Linear

A comparison between the predicted and experimental values of both pressure differentials is illustrated in Figure 5.27. Both regression models could describe more than 90% of the variance in the data according to their R^2 values. Furthermore, the MSE of both regression models were significantly smaller than one, indicating a good fit between the predicted and experimental values. The quadratic regression model, which described $\Delta P_{sections}$, slightly outperformed the linear regression model, which described ΔP_{riser}. However, both models were deemed suitable to describe the correlation between the pressure differentials and the various factors of interest.

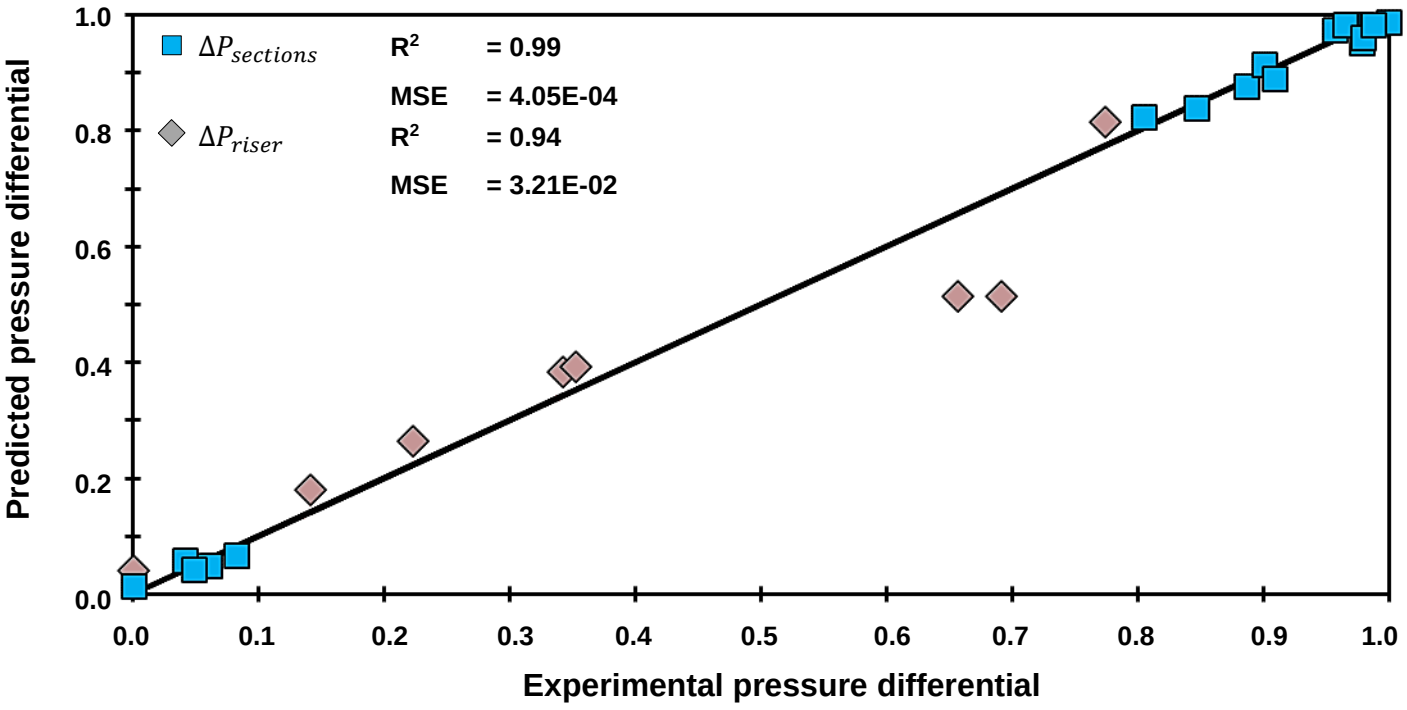

Figure 5.27: *Normalised experimental versus predicted pressure differential across the installed riser sections and across the entire riser*

The P-values of the various factors and factor combinations are tabulated in Table 5-9. According to these values, no statistically significant relationship could be identified between the three independent variables and ΔP_{riser}. This corresponds to the CFD findings in Section 5.2.4, where it was determined that the greatest pressure gradient was found across the venturi. Hence, any variations in the overall pressure differential due to the changing factors were overshadowed by the pressure drop across the venturi. According to Section 5.2.4, the pressure differential across the venturi was mainly a factor of the velocity setting of the run, which explains why the inlet air velocity factor had the lowest P-value in the first column of Table 5-9, although it was not less than 0.05. When the pressure losses across the venturi were removed from the equation, the influence of the factors on the pressure differential became more apparent. This is represented by the highlighted data of $\Delta P_{sections}$ in Table 5-9. In Table 5-9, the riser height and certain factor combinations containing the riser height had a strong connection to $\Delta P_{sections}$. According to the regression model in Annexure U, the adjustment from one to two cylindrical sections increased the pressure differential. Upon a further increase in the riser height, $\Delta P_{sections}$ started to decrease. This is graphically illustrated by the response surface in Annexure V.

Table 5-9: *P-values that were associated with each factor and factor combination from the regression analysis of the pressure differentials*

Factor	$\boldsymbol{\Delta P_{riser}}$	$\boldsymbol{\Delta P_{sections}}$
$\boldsymbol{U_{inlet}}$	0.086	0.072
$\boldsymbol{\dot{m}}$	0.464	0.115
$\boldsymbol{H}$	0.138	0.000
$\boldsymbol{U_{inlet} \times \dot{m}}$	0.165	0.485
$\boldsymbol{U_{inlet} \times H}$	0.173	0.777
$\boldsymbol{\dot{m} \times H}$	0.360	0.016
$\boldsymbol{U_{inlet} \times \dot{m} \times H}$	0.281	N/A
$\boldsymbol{U_{inlet}{}^2}$	N/A	0.494
$\boldsymbol{\dot{m}^2}$	N/A	0.171
$\boldsymbol{H^2}$	N/A	0.000

This means that the medium riser height setting had the greatest pressure differential across its cylindrical sections between the three. This agrees with the CFD data in Table 5-2 and was due to the straight ducting that was used as the exit assembly in the medium riser. Since a straight pipe was connected to the T-shaped outlet instead of a curved duct, the degree of flow separation and swirling within the duct was reduced. In turn, the resistance to flow that was caused by the exit geometry was less, and the velocity in the riser increased. For these reasons, a larger pressure differential was observed.

5.4 COMPARISON BETWEEN EXPERIMENTAL AND CFD DATA

5.4.1 Solids holdup

Given the substantial amount of data, only a selected number of data sets were compared throughout this section. The data sets were chosen at a fixed solids feed rate and riser height setting but at varying inlet air velocity settings. This is because the inlet air velocity setting had a larger influence on the various parameters in the CFD environment when compared to the remaining two factors. In Figure 5.28, the radial solids holdup profiles at the bottom sampling port can be seen. The figure has the same layout as those in Section 5.1.1 but in this case the experimental and predicted profiles are compared. The blue profiles represent the comparison at a low inlet air velocity while the green profiles represent the comparison at a high inlet air velocity. The CFD data was extracted from a line probe across the same direction that the experimental samples were obtained.

All four profiles in Figure 5.28 exhibit an increased solid volume fraction at $0 < r/R < 1$. This indicates that in both the modelling and experimental environment, the sorbent was directed towards the opposite side of the air inlet upon entry as explained in Sections 5.1.1 and 5.2.1. In Figure 5.28, a decrease in the inlet air velocity from 8.6 m/s to 4.3 m/s caused an increase in the experimental and predicted solid volume fraction at most radial positions. Another resemblance between the predicted and experimental data was identified upon inspecting the non-uniformity of the profiles. At the middle sampling port in Figure 5.29, the radial profiles were more uniform when compared to those at the bottom port in Figure 5.28. This is indicative of flow development along the riser height in both the CFD and experimental environment. In addition, the non-uniformity of the radial profiles at the top was higher than that at the middle due to exit effects, regardless of the data type. This can be seen when comparing Figure 5.30 to Figure 5.29. For the light green profile, this non-uniformity manifested as the particles being isolated to a smaller area of the radial plane whereas the non-uniformity of the remaining profiles were more apparent.

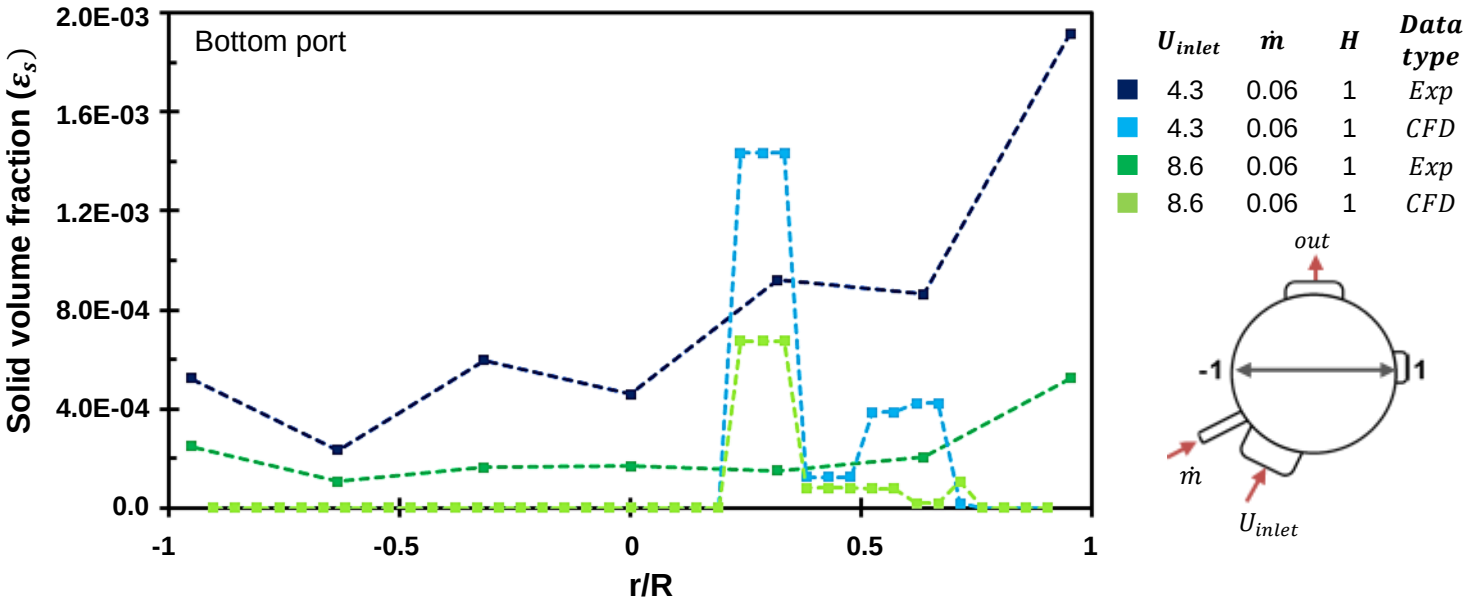

Figure 5.28: *The predicted and experimental radial solids holdup profiles at the bottom sampling port*

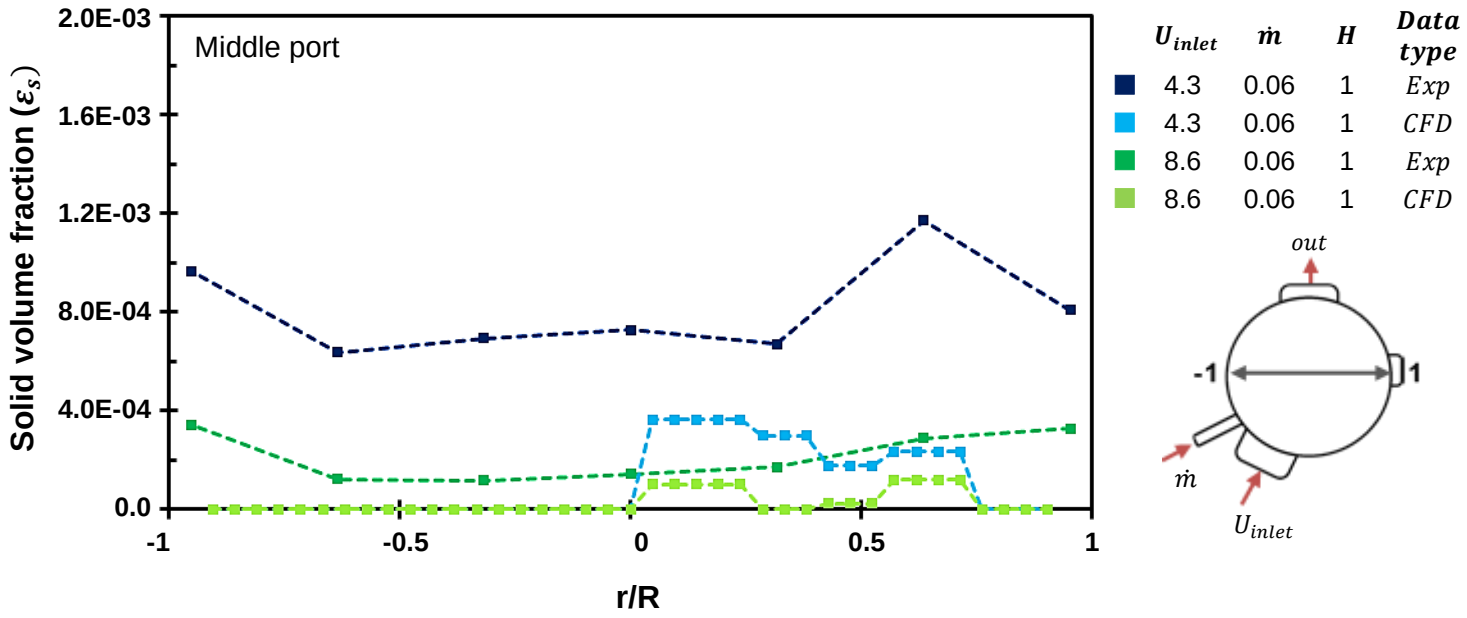

Figure 5.29:*The predicted and experimental radial solids holdup profiles at the middle sampling port*

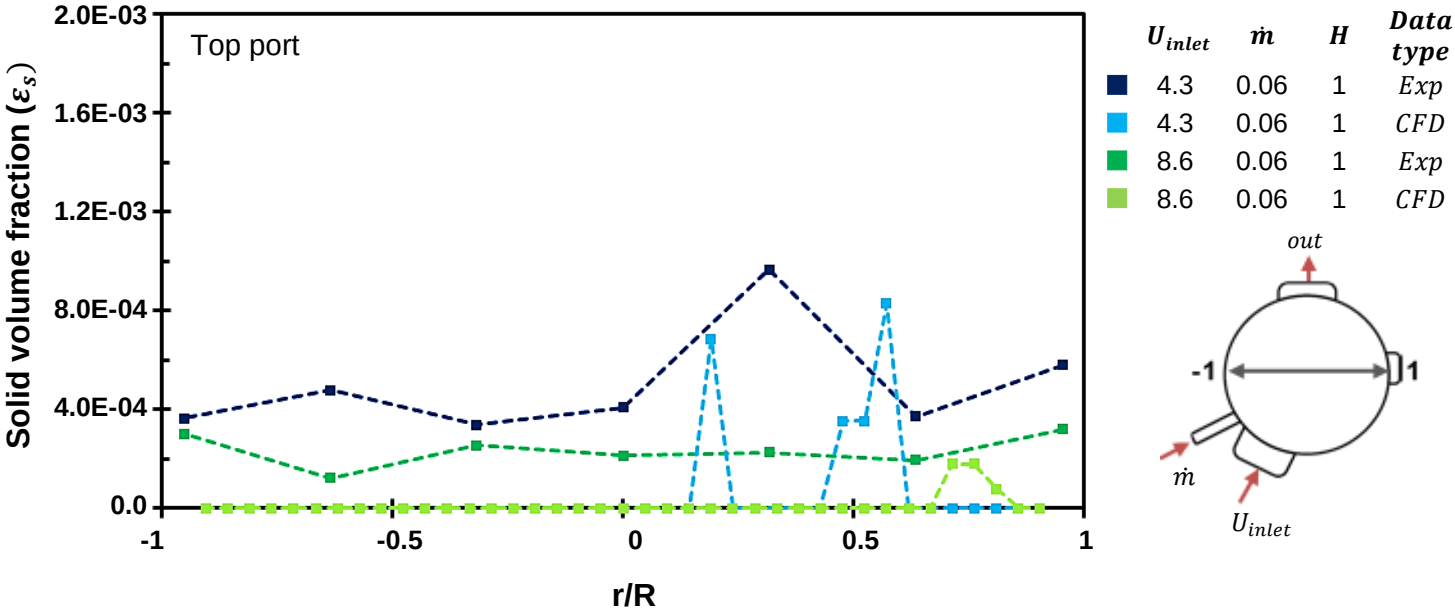

Figure 5.30: *The predicted and experimental radial solids holdup profiles at the top sampling port*

Some key differences between the experimental and CFD radial solids holdup profiles can be identified from Figure 5.28 - Figure 5.30. At the bottom and middle ports, the experimental data suggest that the maximum solids holdup was present near the riser wall. In contrast to this, the CFD data indicates that the middle region of the riser (0.25 < r/R < 0.75) contained most of the particles. The underestimation of near-wall particles was likely caused by the application of the homogeneous drag model as well as the selection of two-way coupling during the construction of the CFD models. Due to these selections, the effect of clustering and inter-particle interactions on the drag forces were not accounted for, as explained in Section 4.1.1. This increased the prediction error in regions with high concentrations of particles since those regions were more likely to be affected by inter-particle interactions and clustering. The reporting method used may also have contributed to the underestimation of the near wall particles. This is because the particles that may have been situated at a slight angle with respect to the data sampling line would not have been captured. The number of predicted particles near the walls of the riser only exceeded the predicted particle concentration in the centre under limited conditions, as discussed in Section 5.2. At the top port, the position of the maximum particle concentrations was similar in both the predicted and experimental profiles, as indicated in Figure 5.30. This was likely due to the swirling effect and internal recirculation, as discussed in Section 5.2.2, which increased the predicted solids holdup despite the absence of a heterogeneous drag model.

The predicted and experimental axial solids holdup profiles are presented in Figure 5.31. The layout of Figure 5.31 is similar to those in Section 5.1.2, however the predicted and experimental data is compared. The blue profiles correspond to the low inlet air velocity setting while the green profiles correspond to the high setting. As the inlet air velocity decreased from 8.6 m/s to 4.3 m/s, the difference between the overall solid volume fraction at the top half of the riser and the bottom half of the riser increased. In addition, the entire profile shifted towards the right of the x-axis. These observations suggest that the inlet air velocity had an inversely proportional relationship with the exit effect and the overall solid volume fraction, regardless of the data type. Despite the comparable trends, the predicted average solid volume fractions were significantly less than that of the experimental data. When considering the experimental data, the average solid volume fraction at each of the three sampling points was calculated from the local solid samples. Since no information was obtained from additional radial angles, these values likely under or overshot the true values. From a modelling perspective, the choice of phase coupling and drag models likely gave rise to the observed prediction error, as mentioned repeatedly throughout the previous discussions. The underestimation of the average solid volume fractions could therefore have been due to both experimental and modelling shortcomings. Regardless of the poor predictive capabilities, the CFD models proved valuable in explaining the hydrodynamics within inaccessible regions during the experimental phase of this study.

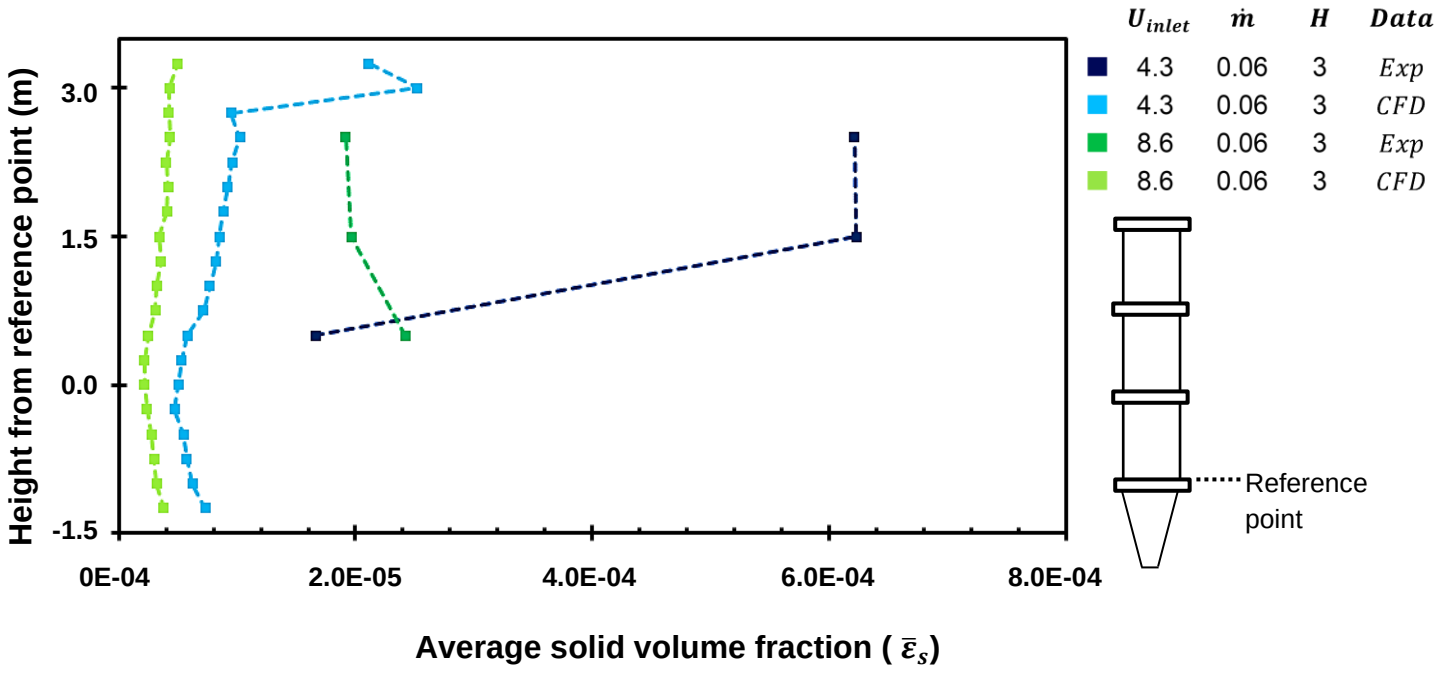

Figure 5.31: *Predicted and experimental axial solids holdup profiles*

5.4.2 Pressure differential

A comparison between the experimental and predicted static pressure differentials across the riser is illustrated in Figure 5.32. In order to determine those differentials, the gauge pressure values were recorded at PT-09, which is situated 0.15 m from the roof of the riser. The gauge pressure at the inlet was then subtracted from these values to determine the pressure differential across the riser. In Figure 5.32, the dark and light blue lines correspond to the predicted and experimental pressure differentials. On the x-axis, placeholders for the various operating conditions were used, and the value of each is provided in Table 5-10. From Figure 5.32, it can be seen that the predicted pressure differential followed the same trend as the experimental pressure differential with the exception of placeholder one. Point one represents the high setting of all three independent variables, as reported in Table 5-10. Under those conditions, the prediction error was the greatest, and this was likely due to the negligible influence of the solids feed rate on the hydrodynamics in the CFD environment. This can be seen by comparing points one and two, three and four, five and six or seven and eight of the dark blue profile in Figure 5.32. Each of these pairs represents a change in the solids feed rate setting, and in each case, the more significant prediction error belongs to the high solids feed rate.

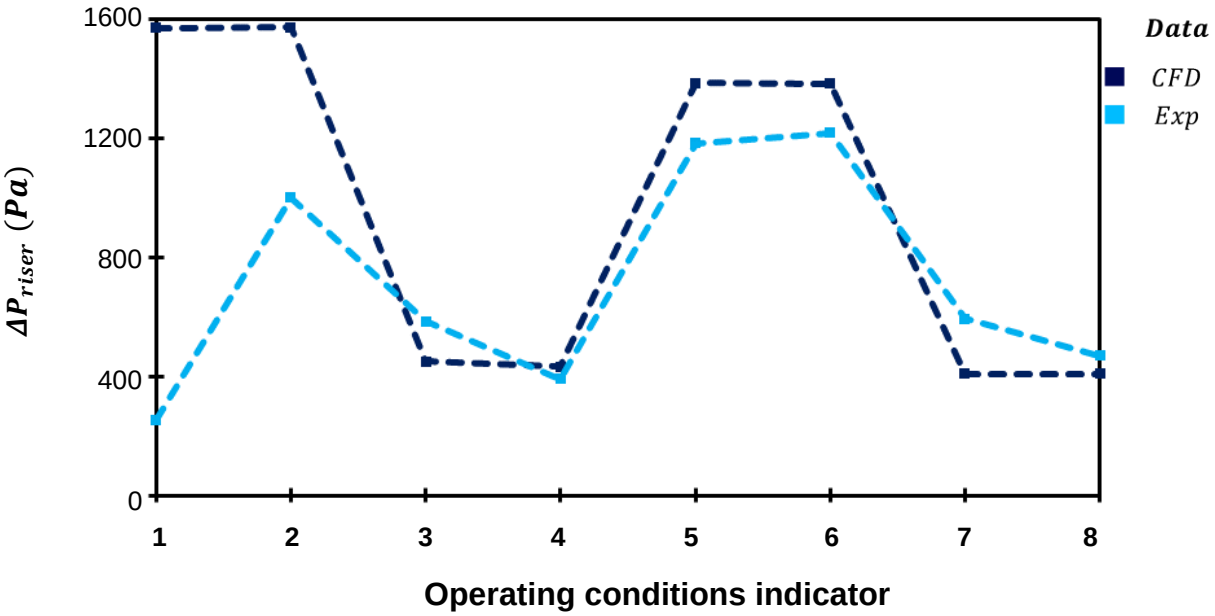

Figure 5.32: *The experimental and predicted static pressure drop across the riser*

In Figure 5.33, a comparison between the experimental and predicted pressure differential across the riser sections is illustrated. In this case, the pressure differential was computed by subtracting the static pressure at the base of the bottom cylindrical section from the pressure value at P-09. The CFD models underestimated the pressure differentials across the riser sections from points four to eight in Figure 5.33. Since these points represent the lowest riser height setting, the data suggests that the CFD models could not sufficiently describe the influence of riser height on the pressure differential. Since a good resemblance was found between the experimental and CFD data at the top of the riser, the prediction error in Figure 5.33 could only be due to faulty pressure values at the base of the cylindrical sections.

The low predicted pressure differential across the shortest riser is also an indication that the predicted solids inventory was underestimated when one riser section was installed. As discussed previously, the most likely reason for this deviation is the absence of four-way phase coupling and a heterogeneous drag model. Accordingly, from an experimental point of view, a decrease in the riser height caused an increase in the particle inventory at the bottom of the riser while also increasing the pressure differential across its sections. However, a decrease in the riser height had a negligible effect on the pressure differential across its sections from a CFD perspective.

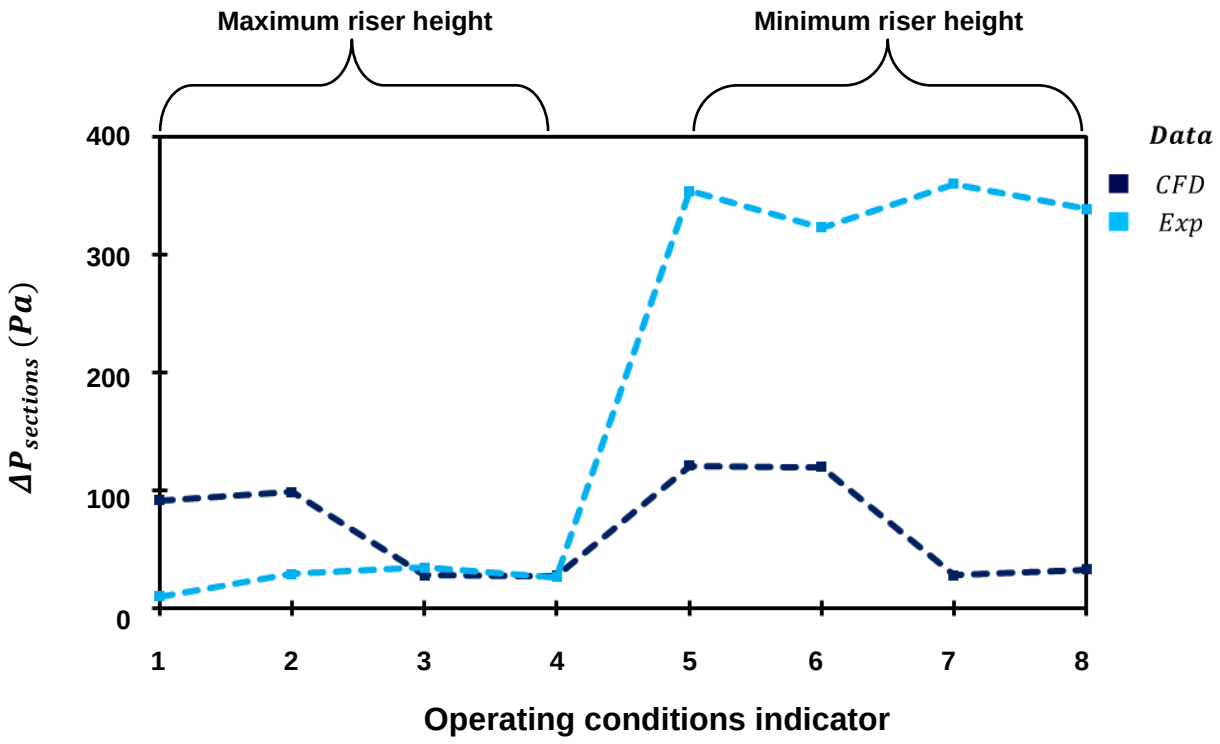

Figure 5.33: *The experimental and predicted static pressure drop across the riser sections*

Table 5-10: *Operating conditions corresponding to the indicators in Figure 5.32 and Figure 5.33*

$\boldsymbol{Indicator}$	**1**	**2**	**3**	**4**	**5**	**6**	**7**	**8**
$\boldsymbol{Installed\ sections}$	3	3	3	3	1	1	1	1
$\boldsymbol{U_{inlet}\ (m/s)}$	8.6	8.6	4.3	4.3	8.6	8.6	4.3	4.3
$\boldsymbol{\dot{m}_{solids}\ (kg/s)}$	0.06	0.04	0.06	0.04	0.06	0.04	0.06	0.04

CHAPTER 6 - CONCLUSIONS AND RECOMMENDATIONS

6.1 CONCLUSIONS

The first objective of this study was to quantify the influence of design and operating conditions on the hydrodynamics inside the CFB riser using an experimental approach. Conclusions drawn from the experimental results are as follows:

- The particles were not uniformly distributed over the cross-sectional area of the riser during operation. This non-uniformity was mainly due to an accumulation of particles at the wall that was located on the opposite side of the air inlet. As a result, changing conditions had a more prominent effect on the near-wall particles when compared to those in the centre of the riser.

- An increase in the inlet air velocity, a decrease in the solids feed rate, or a reduction in the riser height (a smaller H/D ratio) improved the uniformity of the radial solids holdup profiles. Between these three variables, the inlet air velocity had the most significant influence.

- An increase in the inlet air velocity decreased the pressure losses across the installed cylindrical sections with respect to the losses across the entire riser.

- The maximum pressure drop across the installed cylindrical sections occurred at the medium riser height setting. This suggests that the exit structure that was installed on top of the medium riser provided less resistance to flow.

- At high inlet air velocities, the exit effect inside the medium riser was the largest. However, at low and medium inlet air velocities, the tower height determined whether an exit effect would be present. Under these circumstances, the exit effect enlarged as the riser height was increased.

The regression analysis indicated the following:

- A decrease in the riser height or an increase in the inlet air velocity decreased the non-uniformity, but only under limited conditions. These conditions were at inlet air velocities of less than 6.5 m/s and at or above the medium riser height settings. Outside of these limits, the opposite influence was observed.
- An increase in the inlet air velocity reduced the average solids holdup at the bottom and middle sampling ports.

- The riser height greatly influenced the pressure differential across the installed cylindrical riser sections. When adjusting the riser from one to two cylindrical sections, the pressure differential across these ($\Delta P_{sections}$) increased. However, upon a further increase $\Delta P_{sections}$ started to decrease.

The second objective of this study was to quantify the influence of design and operating conditions on the hydrodynamics inside the CFB riser using a numerical approach. The findings from the CFD analysis were as follows:

- An increase in the inlet air velocity or the riser height improved the uniformity of the radial solids holdup profiles. When compared to the other two factors, the solids feed rate had a negligible influence on the radial solids holdup
- Possible core annulus flow was only observed at 4.3 m/s and the maximum riser height setting.
- Two factors were necessary to create an exit effect. The first factor was the riser height, which determined whether particles would collide with the walls above the exit. This mainly occurred inside the medium and tall risers, which means that these were more likely to facilitate internal particle recirculation. The second factor was the degree of flow swirling which varied based on the air velocity setting. Between the medium and tall riser, the vessel with the highest degree of flow swirling always contained the largest exit effect.
- A decreased inlet air velocity or an increased solids feed rate increased the overall solids volume fraction inside the riser. At 4.3 m/s, the exit assembly governed the overall solids volume fraction. However, at 8.6 m/s, the extent of the exit effect governed the overall solids volume fraction.
- The pressure differential across the venturi overshadowed the pressure losses across the installed cylindrical riser sections. However, the predicted overall solids volume fraction increased or decreased together with the predicted pressure differential across the entire riser.

The objectives of this study were realised to a great extent. The influence of the three main operating and design conditions on the two-phase flow behaviour inside the CFB riser has been thoroughly discussed. In addition, the CFD models demonstrated the same trends as the experimental findings, despite its inability to reproduce exact experimental values. The results from this study are comparable to literature findings, except for the influence of the H/D ratio on the hydrodynamics. However, this deviation was due to the varying riser height, whereas the riser diameter was changed in previous work.

Fast fluidisation could be achieved within the experimental setup with the sorbent required for FGD applications and suitable operating conditions could be maintained. Furthermore, the CFD model was a useful tool for the description of the hydrodynamics. In general, the groundwork for future FGD technology research has been lain.

6.2 RECOMMENDATIONS

Given that the overall solids volume fractions were underestimated together with the pressure differential across the cylindrical sections, the CFD models can be improved in future studies. The addition of a heterogeneous drag model should be considered to better approximate the drag forces acting on the dispersed phase in regions of high particle concentrations. In addition, the CFD post-processing could be refined by investigating more effective methods for reporting the solids volume fraction. This is especially true for the description of near wall particles, for which further model development may be necessary. Furthermore, DEM modelling should be considered in the event of adequate computing capacity and less restrictive time constraints.

From an experimental point of view, the accuracy of the average solids volume fraction and $RNI(\varepsilon_s)$ calculations could be improved by increasing the number of radial solids sampling angles. In addition, the sampling nozzle should be rotated 180°, and the suction through the nozzle should be set to a smaller value to quantify the downward flow of particles inside the riser. It is further recommended that the hydrodynamic study should be expanded to include the influence of the cyclone and the riser exit ducting configuration in order to quantify the influence of these units on the exit effect. Given that the eventual goal will be to remove SO_2 from flue gas, the temperature and relative humidity inside the riser should be increased while operating within the conditions specified in this work. If the experimental conditions are altered, the CFD models should be adapted accordingly.

REFERENCES

1. Sangeetha SK, Sivakumar V. Long-term temporal and spatial analysis of SO2 over Gauteng and Mpumalanga monitoring sites of South Africa. *J Atmos Solar-Terrestrial Phys*. 2019;191(1):1-19. doi:10.1016/j.jastp.2019.05.008

2. Benko T, Teichmann C, Mizsey P, Jacob D. Regional effects and efficiency of flue gas desulphurization in the Carpathian Basin. *Atmos Environ*. 2007;41(38):8500-8510. doi:10.1016/j.atmosenv.2007.07.018

3. Srivastava RK, Jozewicz W. Flue gas desulfurization: The state of the art. *J Air Waste Manag Assoc*. 2001;51(12):1676-1688. doi:10.1080/10473289.2001.10464387

4. Khaniabadi YO, Polosa R, Chuturkova RZ, et al. Human health risk assessment due to ambient PM10 and SO2 by an air quality modeling technique. *Process Saf Environ Prot*. 2017;111:346-354. doi:10.1016/j.psep.2017.07.018

5. Chen B, Hong C, Kan H. Exposures and health outcomes from outdoor air pollutants in China. *Toxicology*. 2004;198:291-300. doi:10.1016/j.tox.2004.02.005

6. Li R, Cui L, Meng Y, Zhao Y, Fu H. Satellite-based prediction of daily SO 2 exposure across China using a high- quality random forest-spatiotemporal Kriging (RF-STK) model for health risk assessment. *Atmos Environ*. 2019;208:10-19. doi:10.1016/j.atmosenv.2019.03.029

7. Chiang TY, Yuan TH, Shie RH, Chen CF, Chan CC. Increased incidence of allergic rhinitis, bronchitis and asthma, in children living near a petrochemical complex with SO2 pollution. *Environ Int*. 2016;96:1-7. doi:10.1016/j.envint.2016.08.009

8. von Stackelberg K. Power Generation and Human Health. In: *Encyclopedia of Environmental Health*. Vol 5. Second Edi. Elsevier; 2011:333-341. doi:10.1016/b978-0-444-63951-6.00186-8

9. Shashadin MS, Mutalib NSA, Latif MT, Greene CM, Hassan T. Lung Cancer Challenges and future direction of molecular research in air pollution- related lung cancers. *Lung cancer*. 2018;118(1):69-75. doi:10.1016/j.lungcan.2018.01.016

10. Ji P, Li Z, Dong J, Yi H. SO2 derivatives and As co-exposure promote liver cancer metastasis through integrin αvβ3 activation. *Ecotoxicol Environ Saf*. 2019;181:572-578. doi:10.1016/j.ecoenv.2019.06.029

11. Department of environmental affairs (South Africa). 2020. National Environmental Management: Air Quality Act 2004 (Act no. 39 of 2004). (Notice 421). Government Gazette, 43174:421, 27 March.

12. Makgato SS, Chirwa EMN. Waterberg coal characteristics and SO2 minimum emissions standards in South African power plants. *J Environ Manage*. 2017;201(2):294-302. doi:10.1016/j.jenvman.2017.06.049

13. Koralegedara NH, Pinto PX, Dionysiou DD, Al-Abed SR. Recent advances in flue gas desulfurization gypsum processes and applications – A review. *J Environ Manage*. 2019;251:1-13. doi:10.1016/j.jenvman.2019.109572

14. Neathery JK. A fundamental study of circulating bed absorption for flue gas desulfurization. [PhD thesis]. Lexington, Kentucky: University of Kentucky. 1993.

15. Marocco L, Mora A. CFD modeling of the Dry-Sorbent-Injection process for flue gas desulfurization using hydrated lime. *Sep Purif Technol*. 2013;108(1):205-214. doi:10.1016/j.seppur.2013.02.012

16. Chang G, Song C, Wang L. A modeling and experimental study of flue gas desulfurization in a dense phase tower. *J Hazard Mater*. 2011;189(1-2):134-140. doi:10.1016/j.jhazmat.2011.02.009

17. Córdoba P. Status of Flue Gas Desulphurisation (FGD) systems from coal-fired power plants: Overview of the physic-chemical control processes of wet limestone FGDs. *Fuel*. 2015;144:274-286. doi:10.1016/j.fuel.2014.12.065

18. Chen YC, Shyh JH. Flue gas desulfurization in an internally circulating fluidized bed reactor. *Powder Technol*. 2005;154(1):14-23. doi:10.1016/j.powtec.2005.03.017

19. Scala F, D'Ascenzo M, Lancia A. Modeling flue gas desulfurization by spray-dry absorption. *Sep Purif Technol*. 2004;34(1-3):143-153. doi:10.1016/S1383-5866(03)00188-6

20. Wu G, Chen W, He Y. Investigation on gas–solid flow behavior in a multistage fluidized bed by using numerical simulation. *Powder Technol*. 2020;364(1):251-263. doi:10.1016/j.powtec.2020.01.078

21. Gutiérrez Ortiz FJ, Ollero P. A pilot plant technical assessment of an advanced in-duct desulphurisation process. *J Hazard Mater*. 2001;83(3):197-218. doi:10.1016/S0304-3894(00)00364-2

22. Sauer H, Leuschke F, Baege R. What is possible to achieve on flue gas cleaning using

the CFB technology. In: *8th International Conference on Circulating Fluidized Beds*. May 2015; 10-13. Hangzhou, China. https://www.researchgate.net/publication/286016536_What_is_possible_to_achieve_on_flue_gas_cleaning_using_the_CFB_technology. Accessed September 15, 2020.

23. Ollero P, Gutiérrez Ortiz FJ, Cabanillas A, Otero J. Flue-gas desulfurization in circulating fluidized beds: An empirical model from an experimental pilot-plant study. *Ind Eng Chem Res*. 2001;40(23):5640-5648. doi:10.1021/ie010152i

24. Berruti F, Pugsley TS, Godfroy L, Chaouki J, Patience GS. Hydrodynamics of circulating fluidized bed risers: A review. *Can J Chem Eng*. 1995;73(5):579-602. doi:10.1002/cjce.5450730502

25. Wang X, Li Y, Zhu T, Jing P, Wang J. Simulation of the heterogeneous semi-dry flue gas desulfurization in a pilot CFB riser using the two-fluid model. *Chem Eng J*. 2015;264:479-486. doi:10.1016/j.cej.2014.11.038

26. Chen C, Li F, Qi H. Modeling of the flue gas desulfurization in a CFB riser using the Eulerian approach with heterogeneous drag coefficient. *Chem Eng Sci*. 2012;69(1):659-668. doi:10.1016/j.ces.2011.11.035

27. Spengler JD, Chen Q. Indoor air quality factors in designing a healthy building. *Annu Rev Energy Environ*. 2000;25(1):567-600. doi:10.1146/annurev.energy.25.1.567

28. Patankar SV. *Numerical Heat Transfer and Fluid Flow*. 1st ed. Hemisphere Publishing Corporation; 1980.

29. Fang M, Luo K, Yang S, Zhang K, Fan J. LES-DEM investigation of gas-solid flow dynamics in an internally circulating fluidized bed. *Chem Eng Sci*. 2013;101(1):213-227. doi:10.1016/j.ces.2013.06.038

30. Wu Y, Peng L, Qin L, Wang M, Gao J, Lan X. Validation and application of CPFD models in simulating hydrodynamics and reactions in riser reactor with Geldart A particles. *Powder Technol*. 2018;323(1):269-283. doi:10.1016/j.powtec.2017.10.003

31. Li Y, Zhai G, Zhang H, Li T, Sun Q, Ying W. Experimental and predictive research on solids holdup distribution in a CFB riser. *Powder Technol*. 2019;344:830-841. doi:10.1016/j.powtec.2018.12.082

32. Yan A, Ball J, Zhu J. Scale-up effect of riser reactors (3) axial and radial solids flux distribution and flow development. *Chem Eng J*. 2005;109(1):97-106.

doi:10.1016/j.cej.2005.03.017

33. Van de Velden M, Baeyens J, Smolders K. Solids mixing in the riser of a circulating fluidized bed. *Chem Eng Sci*. 2007;62(8):2139-2153. doi:10.1016/j.ces.2006.12.069

34. Squires AM. The story of fluid catalytic cracking: The first “circulating fluid bed.” *Circ Fluid Bed Technol*. 1985:18-20. doi:10.1016/B978-0-08-031869-1.50007-7

35. Chang H, Louge M. Fluid dynamic similarity of circulating fluidized beds. *Powder Technol*. 1992;70(3):259-270. doi:10.1016/0032-5910(92)80061-Z

36. Liu Y, Bisson TM, Yang H, Xu Z. Recent developments in novel sorbents for flue gas clean up. *Fuel Process Technol*. 2010;91(10):1175-1197. doi:10.1016/j.fuproc.2010.04.015

37. Zhou Y, Peng J, Zhu X, Zhang M. Hydrodynamics of gas-solid flow in the circulating fluidized bed reactor for dry flue gas desulfurization. *Powder Technol*. 2011;205(1-3):208-216. doi:10.1016/j.powtec.2010.09.013

38. Zhang Y, Wang T, Yang H, Zhang H, Zhang X. Experimental study on SO2 recovery using a sodium-zinc sorbent based flue gas desulfurization technology. *Chinese J Chem Eng*. 2015;23(1):241-246. doi:10.1016/j.cjche.2014.10.007

39. Krammer G, Brunner C, Khinast J, Staudinger G. Reaction of Ca(OH)2 with SO 2 at Low Temperature. *Ind Eng Chem Res*. 1997;36(5):1410-1418. doi:10.1021/ie960628b

40. Deng Y, Ansart R, Baeyens J, Zhang H. Flue gas desulphurization in circulating fluidized beds. *Energies*. 2019;12(20):1-19. doi:10.3390/en12203908

41. Fernández I, Garea A, Irabien A. SO2 reaction with Ca(OH)2 at medium temperatures (300-425°C): Kinetic behaviour. *Chem Eng Sci*. 1998;53(10):1869-1881. doi:10.1016/S0009-2509(98)00029-3

42. Karatepe N, Erdoğan N, Ersoy-Meriçboyu A, Küçü S. Preparation of diatomite/Ca(OH)2 sorbents and modelling their sulphation reaction. *Chem Eng Sci*. 2004;59(18):3883-3889. doi:10.1016/j.ces.2004.04.013

43. Krammer G, Brunner C, Khinast J, Staudinger G. Reaction of Ca(OH)2 with SO2 at Low Temperature. *Ind Eng Chem Res*. 1997;36(5):1410-1418. doi:10.1021/ie960628b

44. Klingspor J, Stromberg A., Karlsson HT, Bjerle I. Similarities between lime and limestone in Wet-Dry Scrubbing. *Chem Eng Process*. 1984;18:239-247.

45. Geldart D. Types of Gas Fluidization. *Powder Technol*. 1973;7:285-292. doi:10.1016/0032-5910(73)80037-3

46. Li Y, Li F, Qi H. Numerical and experimental investigation of the effects of impinging streams to enhance Ca-based sorbent capture of SO 2. *Chem Eng J*. 2012;204-206:188-197. doi:10.1016/j.cej.2012.05.115

47. Leuschke F, Bleckwehl S, Ratschow L, Werther J. Flue gas desulphurization in a circulating fluidized bed: Investigation after 10 years of successful commercial operation at the facility of PILSEN/CZ. In: *The 9th Int. Conference on Circulating Fluidized Beds, in Conjunction with the 4th International VGB Workshop "Operating Experience with Fluidized Bed Firing Systems."* May 2008; 13-16. Hamburg, Germany. https://www.researchgate.net/publication/288575373_Flue_gas_desulphurization_in_a_circulating_fluidized_bed_Investigation_after_10_years_of_successful_commercial_operation_at_the_facility_of_PILSENCZ/download. Accessed August 10, 2020.

48. Grace JR. Contacting modes and behaviour classification of gas—solid and other two-phase suspensions. *Can J Chem Eng*. 1986;64:353-363. doi:https://doi.org/10.1002/cjce.5450640301

49. Zhang HL, Degrève J, Dewil R, Baeyens J. Operation diagram of Circulating Fluidized Beds (CFBs). *Procedia Eng*. 2015;102:1092-1103. doi:10.1016/j.proeng.2015.01.232

50. Rhodes M. *Introduction to Particle Technology*. 2nd ed. West Sussex: John Wiley & Sons, Ltd; 2008.

51. Timsina R, Thapa RK, Moldestad BME, Eikeland MS. Effect of particle size on flow behavior in fluidized beds Effect of particle size on flow behavior in fluidized beds. 2019;(January 2020). doi:10.2495/EQ-V4-N4-287-297

52. Bi HT, Grace JR, Zhu JX. Types of choking in vertical pneumatic systems. *Int J Multiph Flow*. 1993;19(6):1077-1092. doi:https://doi.org/10.1016/0301-9322(93)90079-A

53. Zhang G, Chen Z, Bao J, Wei W, Bi X. A revisit to saturation carrying capacity and saturated solid fraction in gas-solid upward fl ow. *Powder Technol*. 2020;373:627-636. doi:10.1016/j.powtec.2020.07.011

54. Yang W. *Handbook of Fluidization and Fluid Particle Systems*. 1st ed. Pittsburgh, Pennsylvania: CRC Press; 2003.

55. Balasubramanian N, Srinivasakannan C, Ahmed Basha C. Transition velocities in the riser

of a circulating fluidized bed. *Adv Powder Technol*. 2005;16(3):247-260. doi:10.1163/1568552053750198

56. Subramanian, Saravanan N. K. Regime Classification of Geldart B Food Particles in Circulating Fluidized Bed. *Appl Math Inf Sci*. 2019;13(4):589-594. doi:10.18576/amis/130410

57. Smolders K, Bayens J. Hydrodynamic modeling of circulating fluidized beds. *Adv powder Technol*. 1998;9(1):17-38. doi:10.1016/S0921-8831(08)60591-9

58. Basu P. *Combustion and Gasification in Fluidized Beds*. 1st ed. Florida: CRC Press; 2006.

59. Bi HT, Grace JR. Flow regime diagrams for gas-solid fluidization and upward transport. *Int J Multiph Flow*. 1995;21(6):1229-1236. doi:10.1016/0301-9322(95)00037-X

60. Welty JR, Rorrer GL, Foster DG. *Fundamentals of Momentum, Heat and Mass Transfer*. 6th ed. Singapore: John Wiley & Sons; 2015.

61. Kim D, Sube Y, Shahzad M, Bong J, Choi J, Ryu H. A model for predicting transport velocity in gas fluidized-beds. *Adv Powder Technol*. 2018;29(12):3070-3078. doi:10.1016/j.apt.2018.08.006

62. Smolders K, Baeyens J. Gas fluidized beds operating at high velocities: A critical review of occurring regimes. *Powder Technol*. 2001;119(2-3):269-291. doi:10.1016/S0032-5910(01)00267-4

63. Khurram MS, Choi JH, Won YS, et al. Effects of angle on the transport velocity in an inclined fluidized-bed. *Korean J Chem Eng*. 2015;32(12):2542-2549. doi:10.1007/s11814-015-0157-0

64. Zhou Y, Peng J, Zhu X, Zhang M. Hydrodynamics of gas – solid flow in the circulating fluidized bed reactor for dry fl ue gas desulfurization. *Powder Technol*. 2011;205(1-3):208-216. doi:10.1016/j.powtec.2010.09.013

65. Van Der Meer EH, Thorpe RB, Davidson JF. Dimensionless groups for practicable similarity of circulating fluidised beds. *Chem Eng Sci*. 1999;54(22):5369-5376. doi:10.1016/S0009-2509(99)00270-5

66. Masayuki H, Hiroyuki I, Yo K, Noboru Y. A Scaling law for cirulating fuidized beds. *J Chem Engnerring Japan*. 1989;22(6):587-592. doi:10.1252/jcej.22.587

67. Monazam ER, Shadle LJ. Analysis of the acceleration region in a circulating fluidized bed

riser operating above fast fluidization velocities. *Ind Eng Chem Res*. 2008;47(21):8423-8429. doi:10.1021/ie8009445

68. Gutiérrez FJ, Ollero P, Cabanillas A, Otero J. A technical pilot plant assessment of flue gas desulfurisation in a circulating fluidised bed. *Adv Environ Res*. 2002;7(1):73-85. doi:10.1016/S1093-0191(01)00114-9

69. Yan A, Zhu J. Scale-up effect of riser reactors (1): Axial and radial solids concentration distribution and flow development. *Ind Eng Chem Res*. 2004;43(18):5810-5819. doi:10.1021/ie049578y

70. Noymer PD, Hyre MR, Glicksman LR. The effect of bed diameter on near-wall hydrodynamics in scale-model circulating fluidized beds. *Int J Heat Mass Transf*. 2000;43(19):3641-3649. doi:10.1016/S0017-9310(00)00002-8

71. Silva GG, Jiménez NP, Salazar OF. Fluid Dynamics of Gas - Solid Fluidized Beds. In: *Advanced Fluid Dynamics*. 1st ed. Rijeka, Croatia: InTech; 2012. doi:10.5772/25791

72. van Ommen JR, Mudde RF. Measuring the Gas-Solids Distribution in Fluidized Beds - A Review. *Int J Chem React Eng*. 2008;6(1):31-46. doi:10.2202/1542-6580.1796

73. Zhang W, Tung Y. Radial Voidage Profiles in Fast Fluidized Beds of Different Diameters. *Chem Eng Sci*. 1991;46(12):3045-3052. doi:10.1016/0009-2509(91)85008-L

74. Collado FJ. Hydrodynamics model for the dilute zone of circulating fl uidized beds. *Powder Technol*. 2018;328:108-113. doi:10.1016/j.powtec.2018.01.007

75. Rodrigues S, Forret A, Montjovet F, Lance M, Gauthier T. CFD modeling of riser with Group B particles. 2015;283:519-529. doi:10.1016/j.powtec.2015.05.020

76. Reinhardt B, Cordonnier A, Florent P. Use of an isokinetic sampling probe. Results in a cyclone. *Powder Technol*. 1999;101(1):81-90. doi:10.1016/S0032-5910(98)00155-7

77. van Breugel JW, Stein JJM, de Vries RJ. Isokinetic Sampling in a Dense Gas-Solids Stream. *Proc Inst Mech Eng Conf Proc*. 1969;184(3):18-23. doi:10.1243/pime_conf_1969_184_075_02

78. Wang C, Zhu J, Barghi S, Li C. Axial and radial development of solids holdup in a high flux/density gas-solids circulating fluidized bed. *Chem Eng Sci*. 2014;108:233-243. doi:10.1016/j.ces.2013.12.042

79. Monazam ER, Breault RW, Shadle LJ. Pressure and apparent voidage profiles for riser

with an abrupt exit (T-shape) in a CFB riser operating above fast fluidization regimes. *Powder Technol*. 2016;291:383-391. doi:10.1016/j.powtec.2015.12.041

80. Sun YK, Lu QG, Bao SL, et al. Commercial operation test and performance analysis of a 200 MWe super-high-pressure circulating fluidized bed boiler. *Ind Eng Chem Res*. 2011;50(6):3517-3523. doi:10.1021/ie101271x

81. Harris AT, Davidson JF, Thorpe RB. Particle residence time distributions in circulating uidised beds. 2003;58:2181-2202. doi:10.1016/S0009-2509(03)00082-4

82. Qi X, Zhu J, Huang W. A new correlation for predicting solids concentration in the fully developed zone of circulating fl uidized bed risers. *Powder Technol*. 2008;188(1):64-72. doi:10.1016/j.powtec.2008.03.012

83. Feng X, Shen L, Wang L. Effect of baffle on hydrodynamics in the air reactor of dual circulating fluidized bed for chemical looping process. 2018;340:88-98. doi:10.1016/j.powtec.2018.09.012

84. Wang S, Cheng M, Zhu X, et al. Effect of swirling gas nozzles on gas-solid flow patterns inside a novel multi-regime riser. *Powder Technol*. 2020;367:233-242. doi:10.1016/j.powtec.2020.03.048

85. Breault RW, Monazam ER, Shadle LJ, Rowan S, Macfarlan LH. The effect of riser end geometry on gas-solid hydrodynamics in a CFB riser operating in the core annular and dilute homogeneous flow regimes. *Powder Technol*. 2017;316:181-189. doi:10.1016/j.powtec.2017.02.017

86. Bai D, Kato K. Quantitative estimation of solids holdups at dense and dilute regions of CFB. *Powder Technol*. 1999;101(3):183-190. doi:10.1016/S0032-5910(98)00159-4

87. Cahyadi A, Anantharaman A, Yang S, et al. Review of cluster characteristics in circulating fluidized bed (CFB) risers. *Chem Eng Sci*. 2017;158:70-95. doi:10.1016/j.ces.2016.10.002

88. Zhang R, Yang H, Wu Y, Zhang H, Lu J. Experimental study of exit effect on gas-solid flow and heat transfer inside CFB risers. *Exp Therm Fluid Sci*. 2013;51:291-296. doi:10.1016/j.expthermflusci.2013.08.011

89. Pugsley T, Lapointe D, Hirschberg B, Werther J. Exit Effects in Circulating Fluidized Bed Risers. *Can J Chem Eng*. 1997;75(6):1001-1010. doi:10.1002/cjce.5450750602

90. Dwivedi K, Dutta S, Loha C, Karmakar M, Chatterjee P. A numerical study on the wall erosion impact and gas-particle hydrodynamics in circulating fluidized bed riser. *Therm Sci*

Eng Prog. 2021;22:100852. doi:10.1016/j.tsep.2021.100852

91. Zhang J, You C, Chen C. Effect of internal structure on flue gas desulfurization with rapidly hydrated sorbent in a circulating fluidized bed at moderate temperatures. *Ind Eng Chem Res*. 2010;49(22):11464-11470. doi:10.1021/ie100988r

92. Xu G, Nomura K, Nakagawa N, Kato K. Hydrodynamic dependence on riser diameter for different particles in circulating fluidized beds. *Powder Technol*. 2000;113(1-2):80-87. doi:10.1016/S0032-5910(99)00317-4

93. Yang S, Wang S, Wang H. Impact of polydispersity on the flow dynamics in the riser of a circulating fluidized bed. *Powder Technol*. 2021;381:489-502. doi:10.1016/j.powtec.2020.12.015

94. Shi X, Lan X, Liu F, Zhang Y, Gao J. Effect of particle size distribution on hydrodynamics and solids back-mixing in CFB risers using CPFD simulation. *Powder Technol*. 2014;266:135-143. doi:10.1016/j.powtec.2014.06.025

95. Yang S, Wang S. Eulerian-Lagrangian simulation of the full-loop gas-solid hydrodynamics in a pilot-scale circulating fluidized bed. *Powder Technol*. 2020;369:223-237. doi:10.1016/j.powtec.2020.05.043

96. Xie J, Zhong W, Yu A. MP-PIC modeling of CFB risers with homogeneous and heterogeneous drag models. *Adv Powder Technol*. 2018;29(11):2859-2871. doi:10.1016/j.apt.2018.08.007

97. Chen J, Meng C, Wang S, Yu G, Hu T, Lin F. Effect of solid mass flux on anisotropic gas–solid flow in risers determined with an LES-SOM model. *Particuology*. 2017;34:70-80. doi:10.1016/j.partic.2016.12.003

98. Zhang Y, Lei F, Xiao Y. The influence of pressure and temperature on gas-solid hydrodynamics for Geldart B particles in a high-density CFB riser. *Powder Technol*. 2018;327:17-28. doi:10.1016/j.powtec.2017.12.040

99. Jiang Y, Li F, Ge W, Wang W. EMMS-based solid stress model for the multiphase particle-in-cell method. *Powder Technol*. 2020;360(1):1377-1387. doi:10.1016/j.powtec.2019.09.031

100. Carlos Varas AE, Peters EAJF, Kuipers JAM. CFD-DEM simulations and experimental validation of clustering phenomena and riser hydrodynamics. *Chem Eng Sci*. 2017;169:246-258. doi:10.1016/j.ces.2016.08.030

101. Kang S, Kwon Y, Moon J. Quantitative Analysis of CO 2 Uptake and Mechanical Properties of Air Lime-Based Materials. *Energies*. 2019;12(15):1-12.

102. Wu C, Hamada M. *Experiments: Planning, Analysis, and Parameter Design Optimization*. 1st ed. New York: Wiley; 2000.

103. Lorscheid I, Heine BO, Meyer M. Opening the “Black Box” of Simulations: Increased Transparency and Effective Communication Through the Systematic Design of Experiments. *Comput Math Organ Theory*. 2012;18(1):22-62. doi:10.1007/s10588-011-9097-3

104. Montgomery DC. *Design and Analysis of Experiments*. 8th ed. Hoboken, NJ: John Wiley & Sons, Inc; 2013.

105. Montgomery D., Runger G. *Applied Statistics and Probability for Engineers*. 6th ed. Singapore: John Wiley & Sons Singapore Pte. Ltd.; 2014.

106. Ait-Amir B, Pougnet P, El hami A. Meta-model development. In: Hami A El, Pougnet P, eds. *Embedded Mechatronic Systems 2*. 1st ed. London, UK: Elsevier Ltd.; 2015:151-179.

107. St-Pierre NR, Weiss WP. Technical note: Designing and analyzing quantitative factorial experiments1. *J Dairy Sci*. 2009;92(9):4581-4588. doi:10.3168/jds.2009-2267

108. Ranade SS, Thiagarajan P. Selection of a design for response surface. *IOP Conf Ser Mater Sci Eng*. 2017;263(2):1-14. doi:10.1088/1757-899X/263/2/022043

109. Asghar A, Raman AAA, Daud WMAW. A Comparison of Central Composite Design and Taguchi Method for Optimizing Fenton Process. *Sci World J*. 2014;2014:1-14. doi:10.1155/2014/869120

110. Nekkanti V, Muniyappan T, Karatgi P, Hari MS, Marella S, Pillai R. Spray-drying process optimization for manufacture of drugcyclodextrin complex powder using design of experiments. *Drug Dev Ind Pharm*. 2009;35(10):1219-1229. doi:10.1080/03639040902882264

111. Zhang D. A Coefficient of Determination for Generalized Linear Models. *Am Stat*. 2017;71(4):310-316. doi:10.1080/00031305.2016.1256839

112. Myers RH, Montgomery DC, Anderson-Cook CM. *Response Surface Methodology: Process and Product Optimization Using Designed Experiments*. 1st ed. Hoboken: John Wiley & Sons; 2009.

113. James G, Witten D, Hastie T, Tibshirani R. *An Introduction to Statistical Learning*. 1st ed. New York City: Springer Science & Business Media; 2013.

114. Kroes MJ, Nolan M. *Aircraft Basic Science*. 8th ed. New York City: McGraw Hill; 2013.

115. Everest FA, Pohlmann K. *Master Handbook of Acoustics*. 6th ed. New York City: McGraw Hill Professional; 2015.

116. Davidson L. *Fluid Mechanics , Turbulent Flow and Turbulence Modeling*. Goteborg, Sweden; 2020. http://www.tfd.chalmers.se/~lada/postscript_files/solids-and-fluids_turbulent-flow_turbulence-modelling.pdf. Accessed April 10, 2021. .

117. Lindberg S. Numerical simulation of particle soiling in the engine compartment of a bus. [Masters thesis]. Goteborg, Sweden: Chalmers university of technology. 2015.

118. Schwarze R, Obermeier F. Performance and limitations of the unsteady RANS approach. *Appl Math Mech*. 2006;6(1):543-544. doi:10.1002/pamm.200610252

119. Narasimhamurthy VD. Unsteady-RANS Simulation of Turbulent Trailing-Edge Flow. [Masters thesis]. Goteborg, Sweden: Chalmers university of technology. 2004.

120. Xiao H, Cinnella P. Quantification of model uncertainty in RANS simulations: A review. *Prog Aerosp Sci*. 2019;108:1-31. doi:10.1016/j.paerosci.2018.10.001

121. Argyropoulos CD, Markatos NC. Recent advances on the numerical modelling of turbulent flows. *Appl Math Model*. 2015;39(2):693-732. doi:10.1016/j.apm.2014.07.001

122. Kundu PK, Cohen IM, Dowling DR. *Fluid Mechanics*. 5th ed. Cambridge, Massachusetts: Academic Press; 2012.

123. Ercoftac special interest group. *Best Practice Guidelines for Cfd*. 1st ed. (Casey M, Wintergerste T, eds.). Ercoftac; 2000. https://www.ercoftac.org/downloads/watermarks/not_in_use/bpg_spf_version_1.pdf. Accessed February 7, 2021.

124. Liu J, Heidarinejad M, Pitchurov G, Zhang L, Srebric J. An extensive comparison of modified zero-equation, standard k-ε, and LES models in predicting urban airflow. *Sustain Cities Soc*. 2018;40:28-43. doi:10.1016/j.scs.2018.03.010

125. Li S, Shen Y. Multi-fluid modelling of hydrodynamics in a dual circulating fluidized bed. *Adv Powder Technol*. 2020;31(7):2778-2791. doi:10.1016/j.apt.2020.05.010

126. Van Maele K, Merci B. Application of two buoyancy-modified k-ε turbulence models to different types of buoyant plumes. *Fire Saf J*. 2006;41(2):122-138. doi:10.1016/j.firesaf.2005.11.003

127. Lateb M, Masson C, Stathopoulos T, Bédard C. Comparison of various types of k-ε models for pollutant emissions around a two-building configuration. *J Wind Eng Ind Aerodyn*. 2013;115:9-21. doi:10.1016/j.jweia.2013.01.001

128. Subramaniam S. Lagrangian-Eulerian methods for multiphase flows. *Prog Energy Combust Sci*. 2013;39(2-3):215-245.

129. Nijdam JJ, Guo B, Fletcher DF, Langrish TAG. Lagrangian and Eulerian models for simulating turbulent dispersion and coalescence of droplets within a spray. *Appl Math Model*. 2006;30(11):1196-1211. doi:10.1016/j.apm.2006.02.001

130. FLUENT. Fluent 6.1 User Guide. http://jullio.pe.kr/fluent6.1/help/pdf/ug/fl61ug.pdf. Published 2003. Accessed April 14, 2020.

131. Faghri A, Zhang Y. Chapter 3: Modeling Multiphase flow and Heat transfer. In: *Fundamentals of Multphase Heat Transfer and Flow*. 1st ed. Berlin: Springer Nature; 2019:820.

132. García M, Sommerer Y, Schönfeld T, Poinsot T. Evaluation of Euler-Euler and Euler-Lagrange Strategies for Large-Eddy Simulations of Turbulent Reacting Flows. *ECCOMAS Themat Conf Comput Combust*. 2005;30:1-18. https://citeseerx.ist.psu.edu/document?repid=rep1&type=pdf&doi=8460d38217f40ab5c6299336609ee4fe9776398d. Accessed July 27, 2021.

133. Alletto M, Breuer M. One-way, two-way and four-way coupled LES predictions of a particle-laden turbulent flow at high mass loading downstream of a confined bluff body. *Int J Multiph Flow*. 2012;45(1):70-90. doi:10.1016/j.ijmultiphaseflow.2012.05.005

134. Vié A, Pouransari H, Zamansky R, Mani A. Comparison between Lagrangian and Eulerian methods for the simulation of particle-laden flows subject to radiative heating. *Annu Res Br*. 2014;(1):15-25. https://web.stanford.edu/group/ctr/ResBriefs/2014/05_vie.pdf. Accessed August 13, 2021.

135. Crowe CT, Schwarzkopf JD, Sommerfeld M, Tsuji Y. *Multiphase Flows with Droplets and Particles*. 2nd ed. Boca Raton, Florida: CRC Press; 2012.

136. Elghobashi S. On predicting particle-laden turbulent flows. *Appl Sci Res*. 1994;52(4):309-

329. doi:10.1007/BF00936835

137. Cortez C, Gil A. Modeling the gas and particle flow inside cyclone separators. 2007;33:409-452. doi:10.1016/j.pecs.2007.02.001

138. Stroh A, Alobaid F, Hasenzahl MT, Hilz J, Ströhle J, Epple B. Comparison of three different CFD methods for dense fluidized beds and validation by a cold flow experiment. *Particuology*. 2016;29:34-47. doi:10.1016/j.partic.2015.09.010

139. Dehbi A, Martin S. CFD simulation of particle deposition on an array of spheres using an Euler/Lagrange approach. *Nucl Eng Des*. 2011;241(8):3121-3129. doi:10.1016/j.nucengdes.2011.05.031

140. Almohammed N, Alobaid F, Breuer M, Epple B. A comparative study on the influence of the gas flow rate on the hydrodynamics of a gas-solid spouted fluidized bed using Euler-Euler and Euler-Lagrange/DEM models. *Powder Technol*. 2014;264:343-364. doi:10.1016/j.powtec.2014.05.024

141. Mahdavimanesh M, Noghrehabadi AR, Behbahaninejad M, Ahmadi G, Dehghanian M. Lagrangian Particle Tracking: Model Development. *Life Sci J*. 2013;10(8):34-41. http://www.lifesciencesite.com/lsj/life1008s/005_19229life1008s_34_41.pdf. Accessed November 20, 2020.

142. Pagalthivarthi K V., Gupta PK. Particle tracking in rotating channel flow. *Indian J Eng Mater Sci*. 2008;15(5):365-376. https://www.researchgate.net/publication/238101554_Particle_tracking_in_rotating_channel_flow. Accessed November 25, 2020.

143. Persson T. Eulerian-Lagrangian Modeling of Multicomponent Spray for Aseptic Treatment of Carton Bottles in the Food Process and Packaging Industry. [Masters thesis]. Gotenburg, Sweden: Chalmers university of technology. 2013.

144. Incropera FP, Dewitt DP, Bergman TL, Lavine AS. *Incropera's Principles of Heat and Mass Transfer*. 8th ed. Singapore: John Wiley & Sons, Ltd; 2017.

145. Gao X, Li T, Sarkar A, Lu L, Rogers WA. Development and validation of an enhanced filtered drag model for simulating gas-solid fluidization of Geldart A particles in all flow regimes. *Chem Eng Sci*. 2018;184:33-51. doi:10.1016/j.ces.2018.03.038

146. Zhang H, Xiong B, An X, Ke C, Chen J. Numerical prediction on the drag force and heat transfer of non-spherical particles in supercritical water. *Powder Technol*. 2020;361:414-

423. doi:10.1016/j.powtec.2019.07.032

147. Loth E. Drag of non-spherical solid particles of regular and irregular shape. *Powder Technol*. 2008;182(3):342-353. doi:10.1016/j.powtec.2007.06.001

148. Liu A., Mather D, Reitz R. Modeling the Effects of Drop Drag and Breakup on Fuel Sprays. 1993;298:1-13. doi:10.4271/930072

149. Beetstra R, van der Hoef M., Kuipers J. Drag Force of Intermediate Reynolds Number FlowPast Mono- and Bidisperse Arrays of Spheres. *AIChE J*. 2007;53(2):489-501. doi:10.1002/aic

150. Lundberg J, Halvorsen BM. A review of some exsisting drag models describing the interaction between phases in a bubbling fluidized bed. In: *49th Scandinavian Conference on Simulation and Modeling (SIMS 2008)*. October 2008; 7-8. Oslo, Norway. https://www.researchgate.net/publication/228515089_A_review_of_some_existing_drag_models_describing_the_interaction_between_phases_in_a_bubbling_fluidized_bed. Accessed December 4, 2021.

151. Jurtz N, Kruggel-Emden H, Baran O, Aglave R, Cocco R, Kraume M. Impact of Contact Scaling and Drag Calculation on the Accuracy of Coarse-Grained Discrete Element Method. *Chem Eng Technol*. 2020;43(10):1959-1970. doi:10.1002/ceat.202000055

152. Peiro J, Sherwin S. *Handbook of Materials Modelling*. 1st ed. (Yip S, ed.). Netherlands: Springer; 2005.

153. Versteeg H., Malalasekera W. *An Introduction to Computational Fluid Dynamics*. 2nd ed. Essex, England: Pearson Education Inc; 2007. doi:10.1002/9781119369189

154. Sosnowski M, Krzywanski J, Gnatowska R. Polyhedral meshing as an innovative approach to computational domain discretization of a cyclone in a fluidized bed CLC unit. *E3S Web Conf*. 2017;14:1-10. doi:10.1051/e3sconf/20171401027

155. Balafas G. Polyhedral Mesh Generation for CFD-Analysis of Complex Structures. [Masters thesis]. Munchen, Germany: Technische Universitat Munchen. 2014.

156. STAR-CCM+. STAR-CCM+ User guide. file:///C:/Program Files/Siemens/14.02.010/STAR-CCM+14.02.010/doc/en/online/index.html#page/connect%2Fsplash.html. Published 2019. Accessed March 1, 2020.

157. Honório H., Maliska C. On the performance of coupled and segregated methods for solving

two-dimensional incompressible flows employing unstructured grids. In: *15th Brazilian Congress of Thermal Sciences and Engineering*. November 2014; 10-13. Belém, Brazil. https://www.researchgate.net/publication/309174725_ON_THE_PERFORMANCE_OF_COUPLED_AND_SEGREGATED_METHODS_FOR_SOLVING_TWO-DIMENSIONAL_INCOMPRESSIBLE_FLOWS_EMPLOYING_UNSTRUCTURED_GRIDS. Accessed August 1, 2020.

158. Shaffer F, Massah H, Sinclair J, Shahnam M. *Measurement of Time-Averaged Particle-Wall Collision Properties Using Particle Tracking Velocimetry. [Report]*. Pittsburgh, Pennsylvania; 1995. https://digital.library.unt.edu/ark:/67531/metadc675596/m2/1/high_res_d/3715.pdf. Accessed December 15, 2020.

159. Caughey DA. Chapter 2: Computational Aerodynamics. In: Johnson W, ed. *Rotorcraft Aeromechanics*. Cambridge, England: Cambridge University Press; 2013:462-492. doi:10.1017/cbo9781139235655.014

160. Thuburn J. Numerical Models: Methods. In: *Encyclopedia of Atmospheric Sciences: Second Edition*. Vol 4. 2nd ed. Elsevier; 2015:161-166. doi:10.1016/B978-0-12-382225-3.00246-2

161. Qi G, Cheng S, Liu Y, Guo Q. Pilot scale test of wet dust removal by high gravity intensification technology in fertilizer plant. *J Environ Chem Eng*. 2021;9(6):106424. doi:10.1016/j.jece.2021.106424

162. Venables HJ, Wells JI. Powder sampling. *Drug Dev Ind Pharm*. 2002;28(2):107-117. doi:10.1081/DDC-120002443

163. Crosby NT, Patel I. *General Principles of Good Sampling Practice*. 1st ed. (Crosby NT, ed.). London: Royal Society of Chemistry; 1995.

164. Michaud D. Laboratory Methods of Sample Preparation. https://www.911metallurgist.com/blog/laboratory-methods-of-sample-preparation. Published 2015. Accessed May 27, 2021.

165. Rawle A. Basic principles of particle size analysis. *Surf Coatings Int Part A Coatings J*. 2003;86(2):58-65. http://cat.inist.fr/?aModele=afficheN&https://www.researchgate.net/publication/279693634_The_Basic_Principles_of_Particle_Size_Analysis. Accessed June 22, 2021.

166. Niemi T. Particle Size Distribution in CFD Simulation of Gas-Particle Flows. [Masters

thesis]. Espoo, Finland: Aalto university. 2012.

167. Malvern. MASTERSIZER 3000 USER MANUAL. www.malvern.com. Published 2013. Accessed January 2, 2021.

168. Saluja R, Moeed KM. Modeling and Parametric Optimization using Factorial Design Approach of Submerged Arc Bead Geometry for Butt Joint. *Int J Eng Res Appl*. 2012;2(3):505-508.

169. Felder RM, Rousseau RW. *Elementary Principles of Chemical Processes*. 3rd ed. John Wiley & Sons, Inc; 2005.

ANNEXURES

CHAPTER 2

Annexure A: Operating velocity vs. transport velocity

Three articles reported operating conditions in large-scale FGD-CFB applications which included an industrial and two pilot scale reactors. Using the reported operating conditions, the transport velocities were calculated using the three correlations from Table 2-1[57]. Furthermore, if a range of velocities were reported, the highest velocity was used for the calculation. The results are provided in Table A1. The average ratio of the operating superficial gas velocity to the transport velocity associated with a given study varied between 2.5 and 3.1.

Table A1: *Calculation results of the average ratio between the superficial gas velocity and the transport velocity*

Parameter	Unit	CFB-FGD scale		
		Industrial[64]	Pilot[25]	Pilot[26]
d_p	μm	48	100	83
ρ_f	kg/m^3	0.78	0.36	0.36
ρ_p	kg/m^3	2250	2240	1000
μ_g	$Pa \cdot s$	2.3×10^{-5}	4.2×10^{-5}	4.2×10^{-5}
Ar	-	3.60	4.56	1.16
U_0	m/s	4.43	10.00	5.00
$U_{TR,\ Bi\ \&\ Grace}$	m/s	1.78	3.77	2.29
$U_{TR,\ Smolders\ \&\ Bayer}$	m/s	1.96	4.11	2.61
$U_{TR,\ Khurram}$	m/s	1.55	2.35	1.43
$(\boldsymbol{U_0/U_{TR}})_{\boldsymbol{average}}$	-	2.54	3.12	2.53

Annexure B: Similarity parameters

Chang and Louge (1992)[35]:

$$Fr^* = \frac{U}{\left(g\overline{d_p}\phi^{\alpha}\right)^{1/2}} \quad \textbf{B-1}$$

$$M = \frac{G}{\rho_g U} \quad \textbf{B-2}$$

$$Ar^* = \frac{\rho_p \rho_g \left(d_p \phi^{\alpha}\right)^3 g}{\mu^2} \quad \textbf{B-3}$$

$$R = \frac{\rho_p}{\rho_g} \quad \textbf{B-4}$$

$$L^* = \frac{D}{d_p \phi^{\alpha}} \quad \textbf{B-5}$$

CHAPTER 3

Annexure C: Additional design calculations (equipment specifications)

For this study, a CFB system was designed and constructed. The laboratory scale CFB riser was designed to test the effect of three H/D ratios which were 16, 12.7 and 9.3 and these were chosen from the range of H/D ratios that were reported for similar systems in Section 2.2.4.1. Furthermore, the position of each riser inlet and the outlet were chosen to reflect those reported in literature[25]. The riser, ducting and cyclone were constructed from carbon steel and covered with one coat of phenoline-187 paint and one coat of thermaline-1248 paint to protect the steel surfaces from corrosion and to provide insulation. The design and construction of the cyclone and initially-used bag filters were outsourced. The specifications that were provided to the fan and sorbent feeder suppliers were determined and detailed in this section.

C-1. Fan requirements

To size the auxiliary equipment, the following assumptions were made based on FGD-CFB literature[25,26,37]:

- Particle size: 100 μm
- Particle density: 2240 kg/m^3
- Air density: 1.21 kg/m^3
- Air dynamic viscosity: 1.85 x 10^{-5} Pa·s
- Ca/S ratio of 1.2
- SO_2 content of 2% in flue gas

From these properties the transport velocity of hypothetical particles was determined using the Archimedes and transport Reynolds numbers from the correlations provided in Section 2.2.1. The results are reported in Table C1. Since FGD-CFB's are generally operated at superficial gas velocities that are equal to twice the transport velocity, the minimum value of 1.3 m/s from Table C1 was selected as the minimum velocity in the riser. If the largest transport velocity from Table C1 is multiplied by two, it is seen that approximately 6 m/s would be required and this was used as an approximate maximum velocity within the riser. This concluded the determination of the minimum and maximum air velocities that were required within the riser.

Table C1: *Transport velocities that were used during the design phase of the laboratory-scale FGD unit*

Correlation used	Unit	Value	Riser height (m)
$U_{TR,\ Bi\ \&\ Grace}$	m/s	2.06	N/A
$U_{TR,\ Smolders\ \&\ Bayens}$	m/s	2.05	N/A
$U_{TR,\ Zhang\ et\ al.}$	m/s	3.23	N/A
$U_{TR,\ Khurram}$	m/s	1.54	4.8
$U_{TR,\ Khurram}$	m/s	1.41	3.8
$U_{TR,\ Khurram}$	m/s	1.28	2.8

C-2. Feeder requirements

The solids feed rate that was required to ensure a Ca/S ratio of 1.2 at the maximum superficial gas velocity of 6 m/s (which is equal to an inlet velocity of 13.5 m/s) was determined. By specifying the minimum feed rate of the feeder at this value, the Ca/S ratio would always be sufficient. Consequently, the superficial gas velocity was converted to a mass flow rate by using Equation C-1. With the mass flow rate known, the molar flow rate of air was determined with Equation C-2.

$$\dot{m}_{air} = U_{0,air} \times A_{riser} \times \rho_{air} = 0.51\ kg/s \qquad \textbf{C-1}$$

$$\dot{n}_{air} = \frac{\dot{m}_{air} \times 1000}{M_{air}} = 17.71\ mole/s \qquad \textbf{C-2}$$

Where $\dot{m}_{air}$ is the mass flow rate of air, A_{riser} is the cross sectional area of the riser, ρ_{air} is the density of air, $\dot{n}_{air}$ is the molar flow rate of air and M_{air} is the molar mass of air which is equal to 28.97 g/mole. It was assumed that 2% of the air consisted of SO_2 and the corresponding molar flowrate was determined using Equation C-3. Since the molar flow rate of sulphur (S) would be equal to that of the sulphur dioxide (SO_2), the moles of Ca required to satisfy a Ca/S ratio of 1.2 was calculated using Equation C-4. This was converted to a mass flow rate through Equation C-5.

$$\dot{n}_{SO2} = \dot{n}_S = \dot{n}_{air} \times 2\% = 0.35\ mole/s \qquad \textbf{C-3}$$

$$\dot{n}_{Ca} = \dot{n}_S \times 1.2 = 0.43\ mole/s \qquad \textbf{C-4}$$

$$\dot{m}_{Ca} = \dot{n}_{Ca} \times M_{Ca} = 17.04\ g/s \qquad \textbf{C-5}$$

Where $\dot{n}_S$ and $\dot{n}_{Ca}$ represent the molar flow rates of sulphur and calcium respectively, $\dot{m}_{Ca}$ is the mass flow rate of calcium and M_{Ca} is the molar mass of calcium which is equal to 40.08 g/mole. Once the required mass flow rate of calcium has been determined it had to be converted to a mass flow rate of sorbent in order to size the feeder. With no information regarding the chemical composition of the sorbent, it was assumed to consist of 70 % CaO on a mass basis during the design phase of the FGD unit. Thus a 100 g of the sorbent would contain 70 g of the CaO compound which was written in terms of moles through Equation C-6. From here, the mass of Ca that would be present in a 100 g sample was determined from Equation C-7 which may also be defined as its weight percentage in the sorbent.

$$n_{CaO} = \frac{m_{CaO}}{M_{CaO}} = n_{Ca} = 1.25\ moles \qquad \textbf{C-6}$$

$$m_{Ca} = n_{Ca} \times M_{Ca} = W\%_{Ca} = 50.03\% \qquad \textbf{C-7}$$

Where n_{CaO} is the molar amount of CaO; m_{CaO} is equal to 70 g; M_{CaO} is the molar mass of CaO which is equal to 56.08 g/mole and $W\%_{Ca}$ is the percentage of calcium present in the sorbent on a mass basis. With the required mass flow rate of calcium as determined in Equation C-5 and the weight percentage of Ca in the sorbent as determined with Equation C-7, the overall mass flow rate of the sorbent could be determined using Equation C-8. According to these calculations, the feeder had to deliver at least 0.03 kg/s to meet the required Ca/S ratio of 1.2 at the highest gas flow rate of 6 m/s.

$$\dot{m}_{sorbent} = \frac{\dot{m}_{Ca}}{W\%_{Ca}} = 34.06\ g/s \qquad \textbf{C-8}$$

Here $\dot{m}_{Ca}$ was determined by Equation C-5 as the required Calcium feed rate and $\dot{m}_{sorbent}$ is the corresponding sorbent feed rate after adjusting for impurities.

C-3. Pressure drop and summary

The pressure drop across the system was estimated using Equation C-9. From literature, the maximum pressure drop across a laboratory scale FGD riser was used in the calculation (ΔP_{riser})[81] while that of the cyclone and filters were estimates from the respective suppliers.

$$\Delta P = \Delta P_{riser} + \Delta P_{cyclone} + \Delta P_{filters} \quad \textbf{C-9}$$

$$5.5\ kPa = 2.5 + 1.5 + 1.5$$

To summarise, the instruments and process units were ordered according to the requirements specified. These included a superficial gas velocity of between 1.3 – 6.0 m/s, a pressure drop of 5.5 kPa and a minimum solids feed rate of 0.03 kg/s together with the assumptions that were listed in Section C1.

Annexure D: Changes made during commissioning

D1. Sorbent feeder

The sorbent feeder consisted of a hopper in which the hydrated lime could be loaded before starting with experiments, a constant speed mixer and a variable speed auger. However, the diameter of the auger outlet was greater than the riser inlet and originally a fitting was used to connect the two as illustrated in Figure D1. During operation, the powder was forced through the fitting and the declining diameter caused a blockage within the pipe.

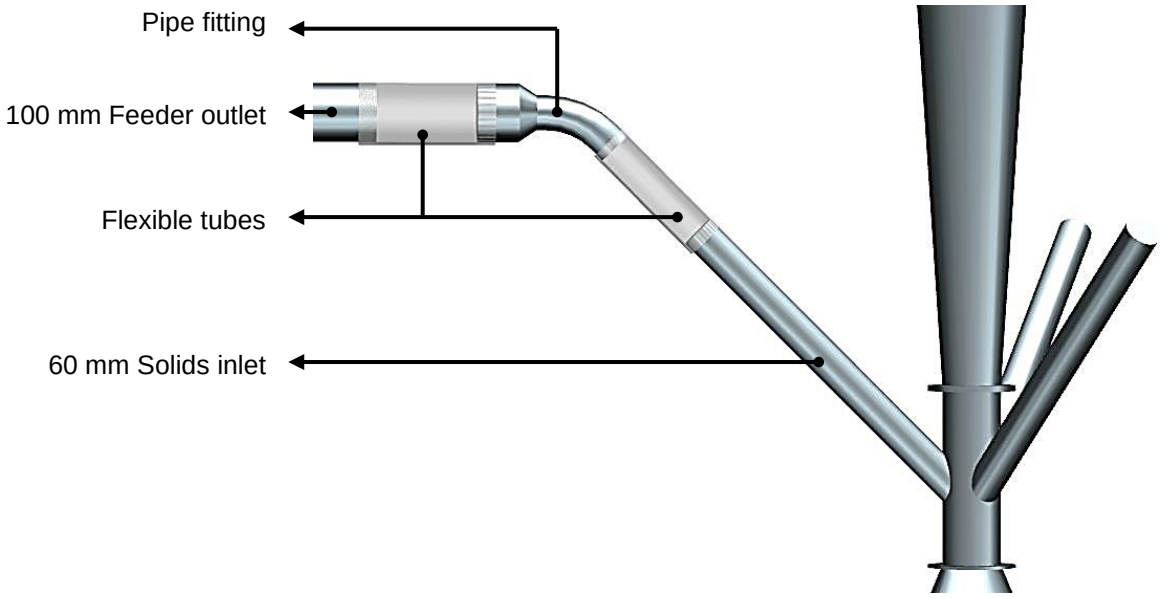

Figure D1: *Original connection between the feeder outlet and the riser inlet*

Several attempts were made to solve the problem as illustrated in Figure D2. The fitting was replaced by a wide flexible tube which was fixed over the riser inlet using a narrow flexible tube as shown in Figure D2 (a). Furthermore, compressed air was introduced at the bottom of the wide tube through a small cavity. Although these changes ensured a more gradual change in diameter and allowed for particle agitation, a dense powder cake eventually formed within the tubes and the flow of sorbent stopped.

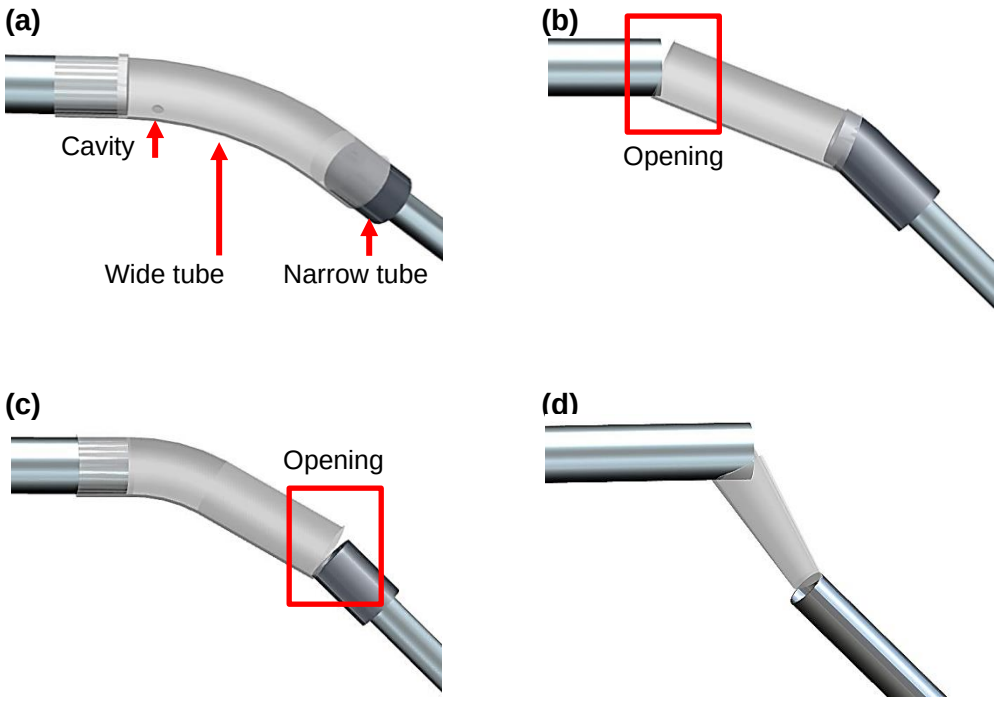

Figure D2: *Various feeder configurations tested during system commissioning*

Next, the wide tube was left partially open as illustrated in Figure D2 (b) and (c) which allowed the riser to pull in additional air through the sorbent feed pipe. This ensured particle agitation either as the sorbent was discharged from the auger or at the sudden decline in diameter brought on by the narrow tube. Although a longer operating period could be achieved with these adjustments, the inlet blocked within five minutes of riser operation. For all three options a build-up of powder started along the edge of the riser inlet as illustrated in Figure D3. The powder collapsed into the pipe causing a blockage after a few minutes of operation. Furthermore, the build-up of sorbent was more significant when operating at low inlet air velocities (< 4 m/s). This was attributed to the frictional forces acting on the sorbent being in excess of the force applied by the suction air in the opposite direction.

With the acquired knowledge a ramp was installed across which the sorbent could enter the riser inlet as illustrated by Figure D2 (d). The steep ramp increased the downward component of the gravitational force which prevented particle accumulation on top of its surface at low operating velocities. Additionally, the solids were fed into the centre of the riser inlet to prevent particle accumulation along the pipe edges at low operating velocities. This solved the problem and the commissioning of the system could continue.

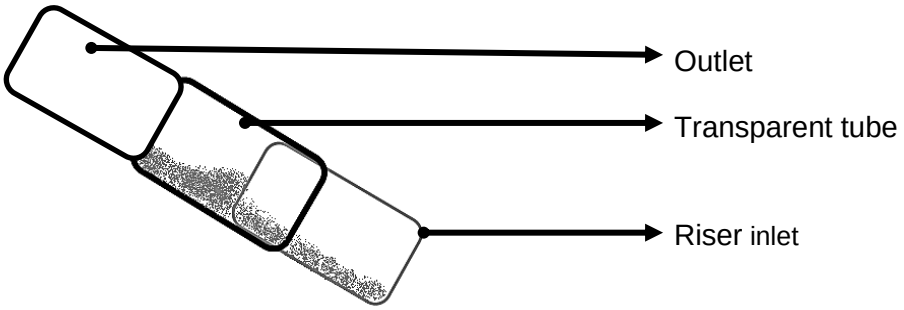

Figure D3: *Powder build-up caused by the edge of an inner pipe*

D2. Scrubber

The original design of the CFB unit included a primary HEPA filter and a secondary bag filter to trap the particles that were not removed by the cyclone. This is illustrated in Figure D4 where BFL-01 represent the filters and H-01 - H-03 refer to hypothetical material streams. The remaining descriptions from Figure D4 received attention in Section 3.1.1. After sorbent characterisation as discussed in Section 3.1.2 it was found that the mean diameter of the sorbent was equal to approximately 23 µm which was much smaller than the anticipated 100 µm that was assumed during the design phase. Consequently, the cyclone's efficiency was compromised, and a large volume of hydrated lime bypassed the cyclone and collected on-top of the filters. This increased the pressure drop across the system which prevented the desired fluidisation regime within the upstream riser. To circumvent this problem, the filters were removed and a scrubber was designed and installed after FAN-01 as represented by SCBR-01 in Figure D5.

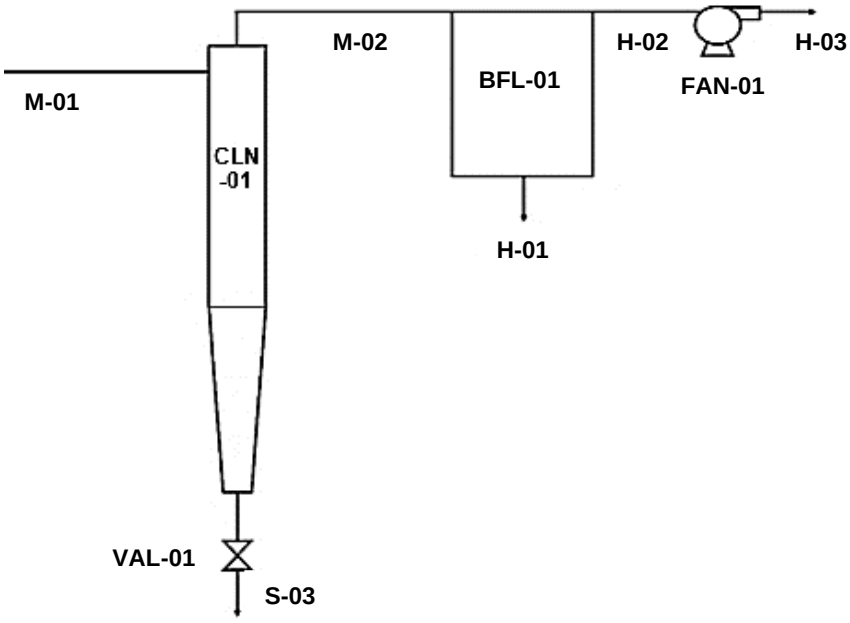

Figure D4: *A partial P&ID with the original filter setup*

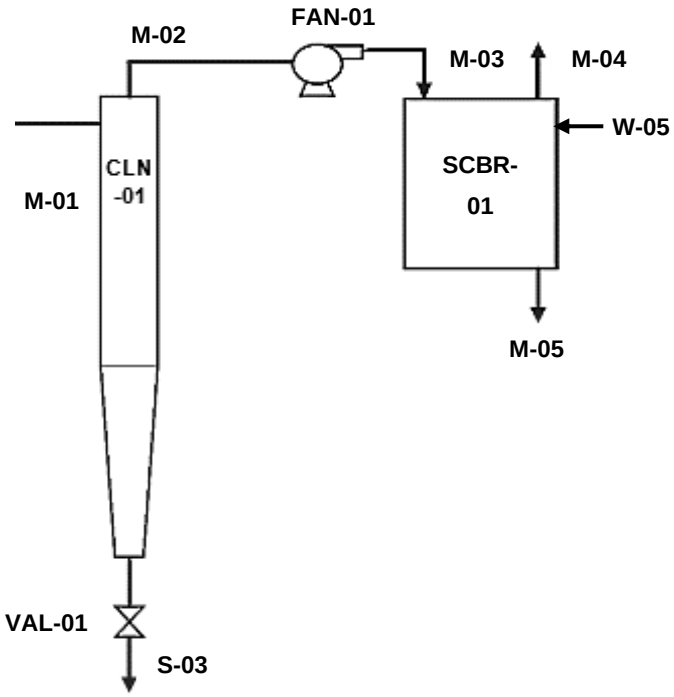

Figure D5: *A partial P&ID with the updated filter setup*

The most important features of the scrubber are illustrated in Figure D6. With the scrubber, the sorbent could be removed from the air without compromising the fluidisation regime in the upstream riser. This was possible since enough space was allowed between the water surface at the bottom of the tank and the air outlet to the top as illustrated in Figure D6.

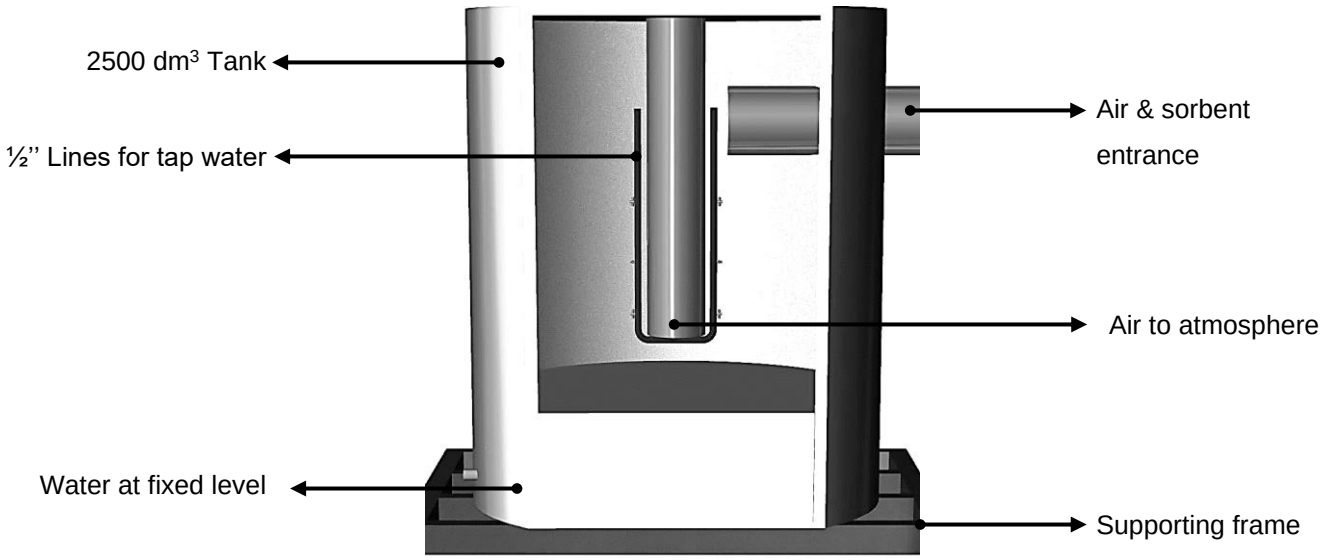

Figure D6: *Scrubber concept design*

In Figure D7 (a) the nine misting nozzles that were installed inside and around the gas outlet at the top of the tank are depicted. As the air and particle suspension entered the tank, the particles collided with water mist and settled to the bottom of the scrubber. Given that the unit reduced the amount of particles that were released to the atmosphere, it was deduced that the water droplets were sufficiently small to capture the sorbent. If the size of the water droplets were increased, the particles would likely travel past the droplets in streamlines instead of colliding with them[161]. A final design feature was the pump that was used to recirculate the water at the bottom of the tank to prevent particle settling and to ensure that a homogeneous water-particle mixture was discarded through the tank overflow. The discarded slurry was stored in sealed containers for future work.

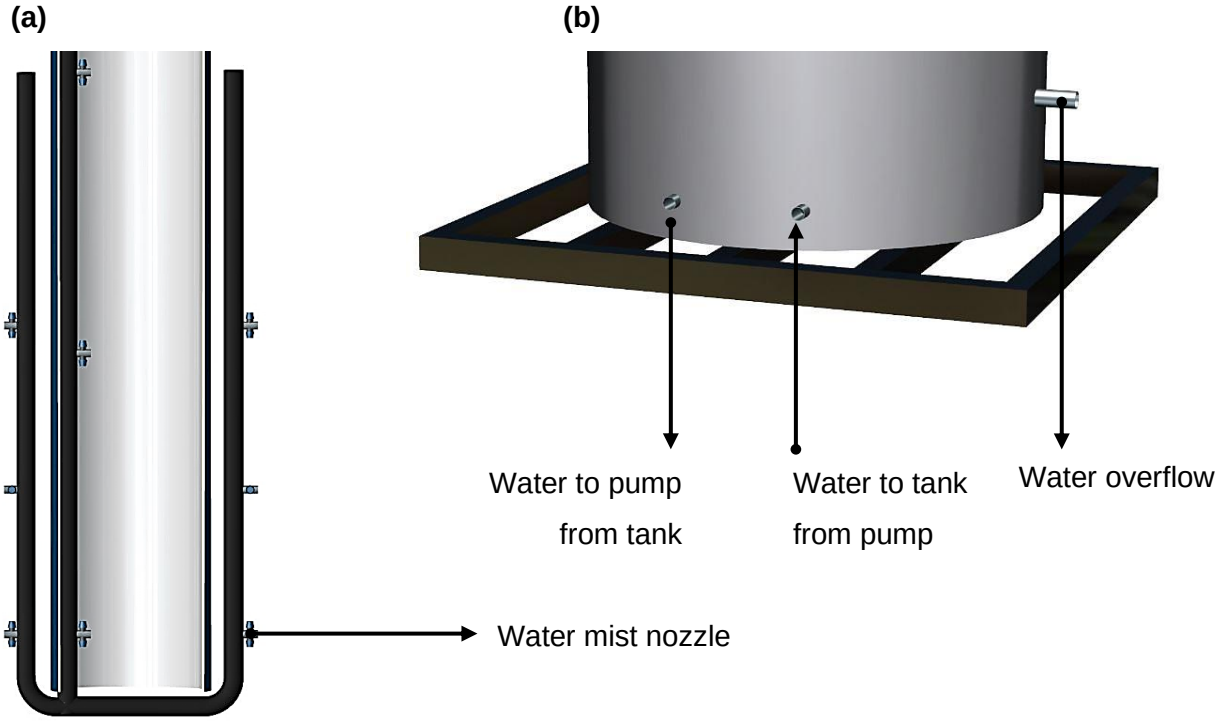

Figure D7: *Design features of the scrubber used for sorbent capture*

Annexure E: Calibration curves

E1. Sorbent feeder calibration curve

To construct the sorbent feeder's calibration curve, the following procedure was followed:

1. Before loading, the feeder and its mixer was switched on. This was done to protect the feeder motor since a loaded hopper placed unnecessary strain on the auger during start-up. The feeder was started at its twelve percent setting to further protect the motor and it was never operated below this point. Next, two containers were collected.
2. Container 1 was placed at the feeder outlet to capture the discharged sorbent after which the hopper was loaded.
3. Container 2 was weighed and the speed setting of the feeder was changed to twelve percent.
4. Container 1 was replaced by container 2 and a stopwatch was started.
5. After 60 seconds has passed, container 2 was removed and container 1 was placed in its stead once again.
6. Container 2 was weighed while the feeder was left at or changed to its 12% speed setting. This was to reduce the sorbent flow while weighing the container and to prevent frequent starting and stopping of the feeder.
7. The weight difference determined from container 2 was divided by 60 seconds to determine the feed rate at that specific speed setting.
8. The contents of container 2 was loaded into the hopper and the hopper was refilled.
9. Container 2 was weighed.
10. The speed setting was increased by five percent.
11. Steps 4 – 10 were repeated until the feed rate at the 100% setting has been established.
12. The hopper was allowed to empty and the feeder and its mixer was switched off.

In Figure E1 the calibration curve of the sorbent feeder is illustrated. The sorbent feeder could deliver approximately 0.35 kg/s while running at its highest setting and 0.04 kg/s while running at its lowest setting. According to the design calculations that were provided in Annexure C2, the feeder delivered a sufficient feed rate to ensure that the Ca/S ratio in the riser would be greater than 1.2 regardless of the superficial gas velocity.

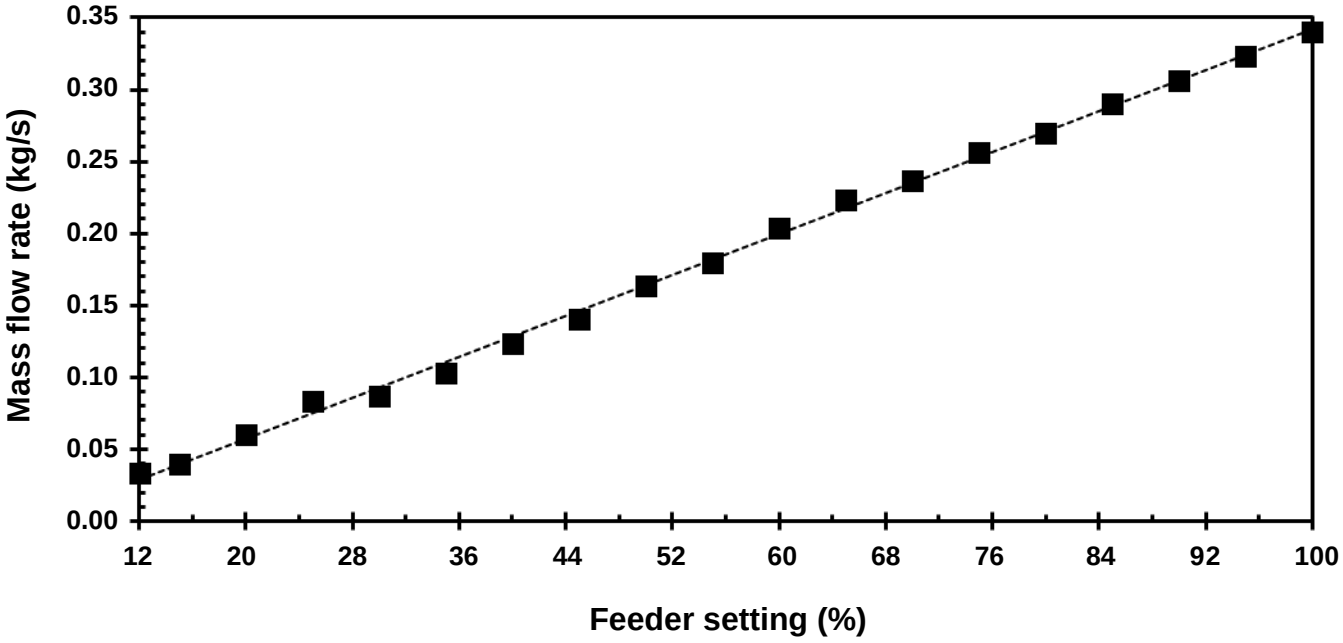

Figure E1: *Calibration curve of the sorbent feeder*

E2. <u>Fan calibration curve</u>

To construct the fan's calibration curve as represented in

Figure E2, the following procedure was followed:

1. The hot-wire anemometer was placed at the centre of the air inlet at the bottom of the riser.
2. The fan was changed to its ten percent setting.
3. The fan was allowed to run until the inlet velocity fluctuations were at a minimum.
4. Every three seconds a velocity reading was recorded using the handheld device and this was done for a duration of one minute.
5. The average air velocity which corresponded to the given fan setting was recorded.
6. The fan speed was increased by five percent.
7. Steps 3 – 6 were repeated until the inlet velocity at the 100% setting of the fan had been established.
8. The fan was switched off and the anemometer removed.

The inlet velocities were multiplied by the correction factor that was determined in Section 3.3.4.1 and the final calibration curve of the fan is illustrated in. The results indicate that the fan could deliver an inlet velocity of 19.5 m/s while operating at its highest setting and 2.1 m/s at its 10%

setting in the absence of particles. Thus, the fan could deliver the minimum and maximum requirements for this study.

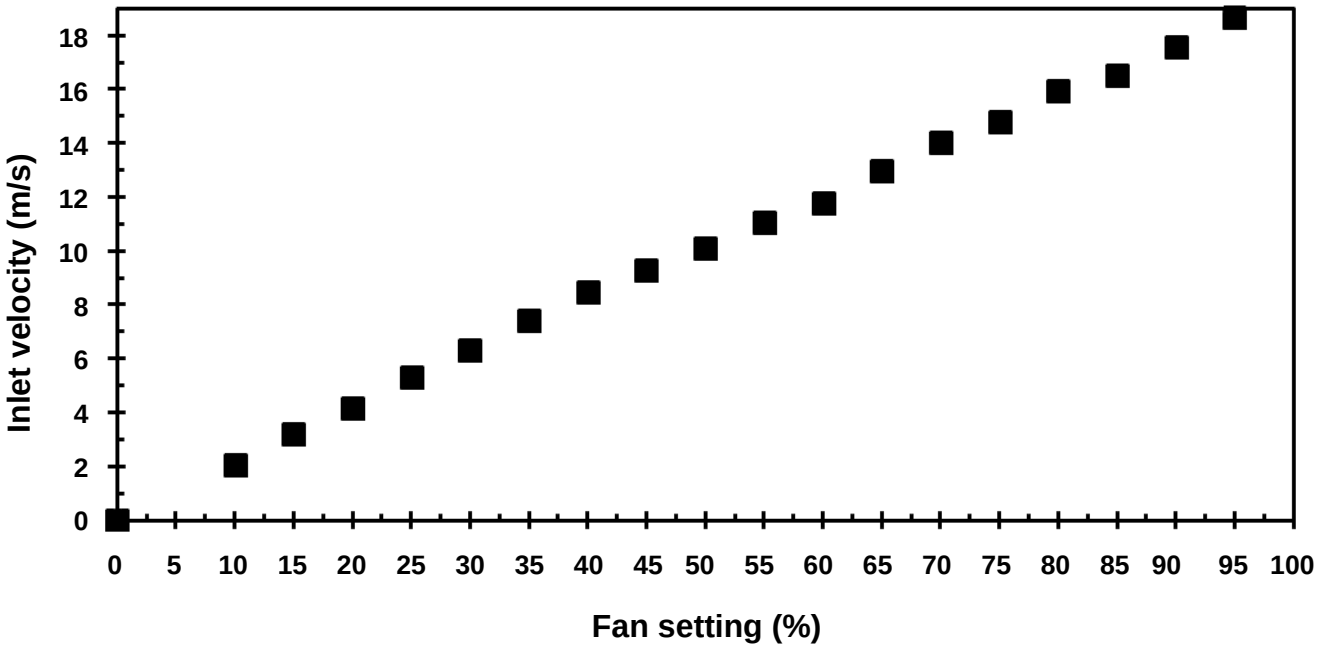

Figure E2: *Calibration curve of the fan*

Annexure F: Cyclone efficiency

The percentage solids that the cyclone removed from the suspension was determined through a material balance. The sorbent feeder was changed to its 20% setting and the hopper was loaded by a measured amount of sorbent. Once loaded, the riser was operated at an inlet air velocity of 6.1 m/s until the hopper was empty. The weight of the sorbent that was collected underneath the cyclone was recorded and this process was repeated two times. The results are provided in Table F1 and it can be seen that approximately 73.5 % of the particles that were present in the carrier gas were removed through the cyclone.

Table F1: *Material balance over the cyclone*

Sorbent loaded (kg)	Sorbent removed by cyclone (kg)	Percentage sorbent retained (%)
58.4	43.8	75.0
91.6	66.6	72.7
48.4	35.2	72.7
	Average	73.5

Annexure G: Sample preparation

G1. Mechanical riffler

The size of certain sorbent samples had to be reduced to smaller representative batches. Spin riffling is a more reliable method of powder sampling than cone and quartering and chute sampling, as it is less sensitive to the degree of homogeneity of the feed stock and creates a smaller opportunity for sampling errors due to operator bias[162]. For this reason the mechanical riffler as indicated in Figure G1 was used to reduce samples sizes from a starting batch of 5 kg or smaller.

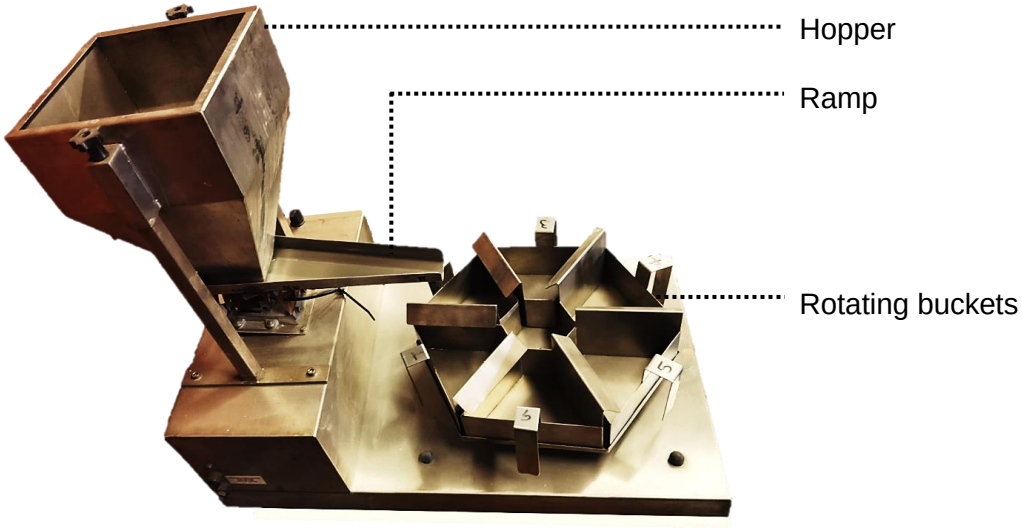

Figure G1: *Mechanical riffler that was used to decrease sample sizes*

Figure G2: *Hydrated lime in the first, third and fifth bucket*

The procedure to reduce a sample size was as follows:

1) The mechanical riffler was cleaned using a brush and a cloth to prevent contamination of the hydrated lime.

2) A 1 kg sample was added to the hopper and the vibration level was set to 50%. When the vibration level was increased beyond 50%, particles were lost over the edge of the ramp across which the material entered the rotating buckets.

3) The riffler was switched on and the material was divided into six batches that were representative of the original sample.

4) Once all of the material has been fed into the rotating buckets the riffler was switched off and the contents of the first, third and fifth bucket as illustrated in Figure G2, were returned to the hopper. Therefore, the weight of the contents inside the hopper was equal to one half of the material fed during the previous repetition. The material from the remaining buckets were placed in a storage container.

5) Steps 3) and 4) were repeated until the combined contents of the first, third and fifth bucket weighed approximately 8 g. The material from those three buckets were placed in an airtight storage container for particle density analysis, while the material from buckets two, four and six were returned to the hopper.

6) Steps 3) and 4) were repeated until the combined contents of the first, third and fifth bucket weighed approximately 1 g. The material from those buckets were stored in an airtight container for a PSD analysis.

7) The two samples were stored for analysis and the riffler was switched off and cleaned.

G2. <u>Cone and quartering</u>

When a sample batch weighed in excess of 5 kg, cone and quartering was performed until the sample size was small enough to use the mechanical riffler[163]. This was done by shovelling the hydrated lime powder into a cone that was then flattened. Following this, the heap was divided into four equal sections and two opposing corners of the quartered heap was removed. The remaining sorbent was mixed with the shovel during the process of creating a new cone. Finally, the whole process of flattening the cone, dividing it into four parts, removing two opposing corners from the heap and creating a new cone was repeated until a 5 kg sample remained. This process is illustrated by the flow diagram in Figure G3.

1. Create a well-mixed cone of sorbent.

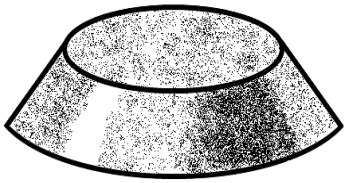

2. Flatten the cone using a shovel

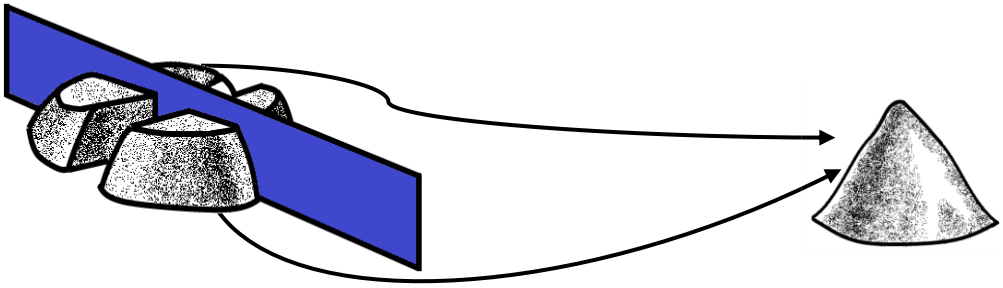

3. Divide the flattened heap into quarters.

4. Use two opposite corners to create a smaller well-mixed cone.

Figure G3: *The process of cone and quartering to reduce the size of large samples (Adapted from Michaud (2015))*[164]

Annexure H: PSD's & XRF trace elements

The difference between the D[3,2] and the D[4,3] lies within the property that is emphasised during its calculation. The D[3,2] indicates which particle size classes contribute the most to the available surface area of the bulk material, whereas the D[4,3] indicates which size classes contribute the most to the mass of the bulk material[165,166]. The formula that is used by the Malvern Mastersizer 3000 to compute the D[3,2] and the D[4,3] from the PSD is provided in Equation H-1[167]. Furthermore, the PSD's of the three additional supplied sorbents and the Sauter mean diameter and volume moment mean of each is provided by Figure H1 to Figure H3.

$$D[m,n] = \left[\frac{\sum V_i \cdot {d_i}^{m-3}}{\sum V_i \cdot {d_i}^{n-3}}\right]^{\frac{1}{m-n}} \qquad \textbf{H-1}$$

Where V_i represents the volume percentage of particles larger than size range i and d_i represents the geometric mean between size range i and $i+1$, i.e. $\left(\sqrt{d_i \times d_{i+1}}\right)$.

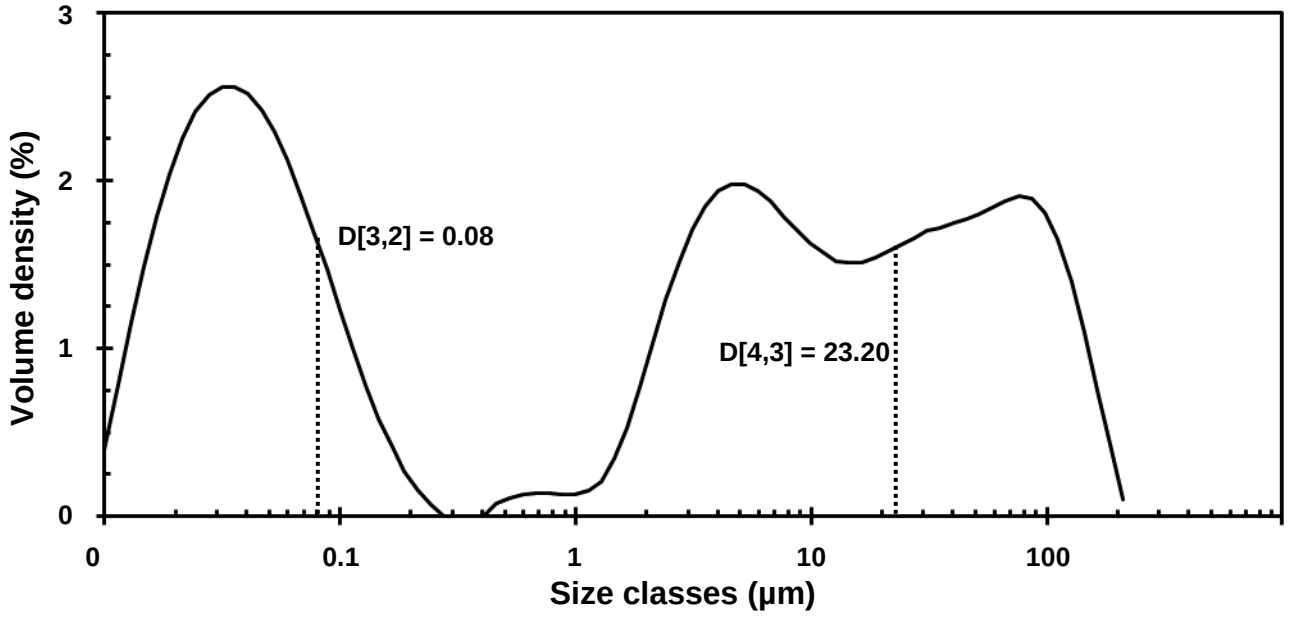

Figure H1: *The Sauter mean diameter (D[3,2]) and volume moment mean (D[4,3]) resulting from the PSD analysis of the hydrated lime sample from Idwala*

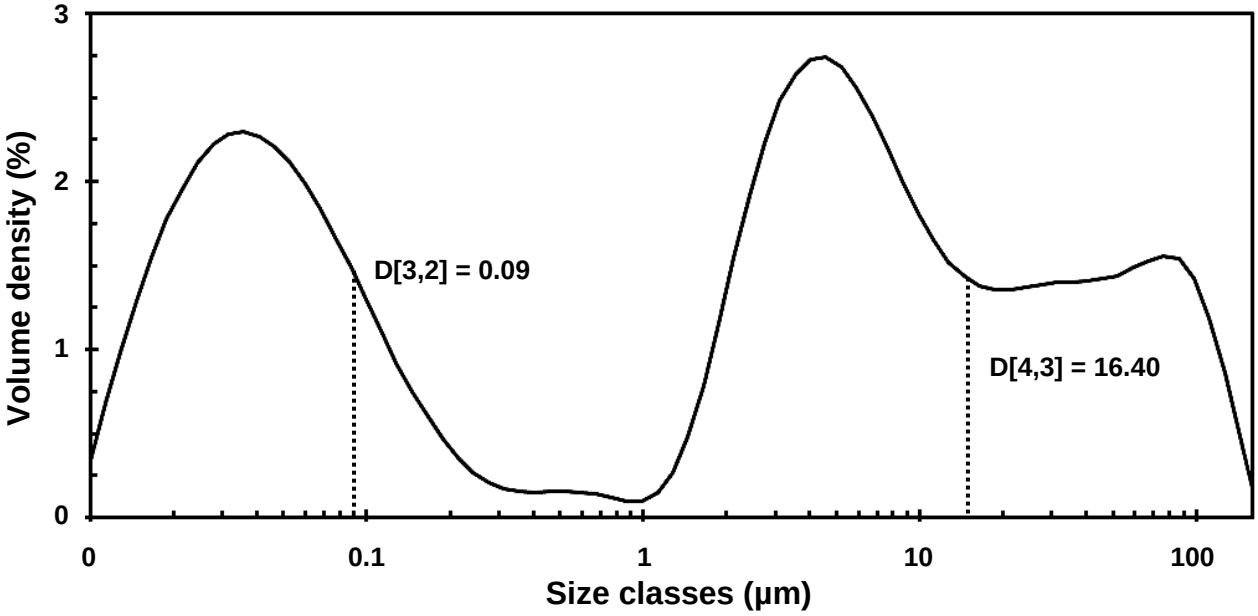

Figure H2: *The Sauter mean diameter (D[3,2]) and volume moment mean (D[4,3]) resulting from the PSD analysis of the hydrated lime sample from PPC*

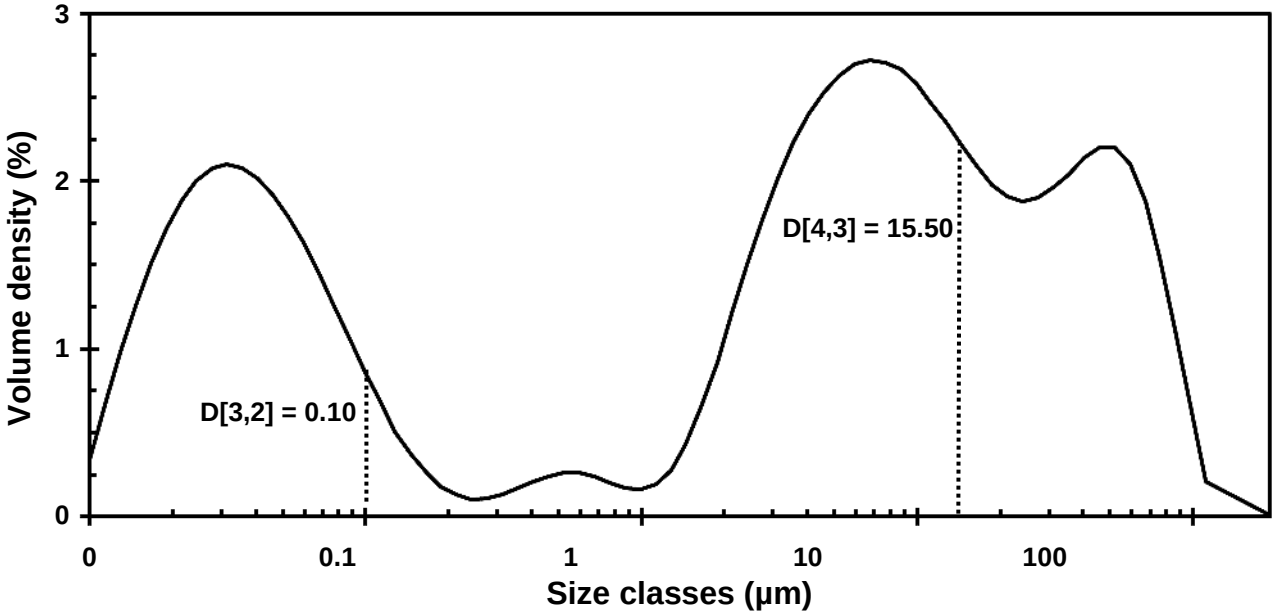

Figure H3: *The Sauter mean diameter (D[3,2]) and volume moment mean (D[4,3]) resulting from the PSD analysis of the hydrated lime sample from Tazchem*

From the XRF analysis it was determined that trace elements accounted for 1.8% of the total sorbent weight and they are listed in Table H1.

Table H1: *Minor elements present in the hydrated lime sorbent from Afri-lime as determined via an XRF analysis*

Element	Weight percentage (%)	Element	Weight percentage (%)
Ni	0.05	**Nd**	0.01
Zn	0.35	**Gd**	0.01
As	0.03	**Ho**	0.02
Sr	0.31	**Yb**	0.01
Zr	0.03	**Lu**	0.01
Ag	0.19	**Ta**	0.19
La	0.02	**Pb**	0.20
Ce	0.02	**Bi**	0.16
U	0.11	**Th**	0.06
V_2O_5	0.02	**Cr_2O_3**	0.01

Annexure I: regression analysis

I1. Linear Regression

The coefficients for the linear regression equation of any 2^3 factorial design can be determined from the fixed effects of the factors and their interactions. Suppose that the three factors are denoted by A, B and C respectively, then the experimental design matrix will have the form presented in Table I1. Once again, the -1 and 1 represent the low and high levels of the factors respectively. Example values for a theoretical response has been entered into the last column.

Table I1: *Example of a 2^3 full factorial design matrix*

A	B	C	AB	AC	BC	ABC	Response
-1	1	1	-1	-1	1	-1	0.6 = y_{122}
-1	-1	1	1	-1	-1	1	0.3 = y_{112}
-1	1	-1	-1	1	-1	1	0.5 = y_{121}
-1	-1	-1	1	1	1	-1	0.2 = y_{111}
1	1	1	1	1	1	1	1.0 = y_{222}
1	-1	1	-1	1	-1	-1	0.6 = y_{212}
1	1	-1	1	-1	-1	-1	0.9 = y_{221}
1	-1	-1	-1	-1	1	1	0.4 = y_{211}

If an “n” amount of replicates are performed at each factorial design point, the response is the sum of all replicates (i.e. if the top entry was found to be 0.6 and then 0.7, the column entry would be 1.3)[112]. The effect of the main factors are defined as the difference between the averaged result of the runs at the high level and the averaged result of the runs at the low level. This can be expressed mathematically by Equations I-1 - I-3[112].

$$A_{effect} = \bar{y}_{A+} - \bar{y}_{A-} = \frac{1}{2^{k-1}}(y_{222} + y_{212} + y_{221} + y_{211} - [y_{122} + y_{112} + y_{121} + y_{111}]) \quad \textbf{I-1}$$

$$B_{effect} = \bar{y}_{B+} - \bar{y}_{B-} = \frac{1}{2^{k-1}}(y_{122} + y_{121} + y_{222} + y_{221} - [y_{112} + y_{111} + y_{212} + y_{211}]) \quad \textbf{I-2}$$

$$C_{effect} = \bar{y}_{C+} - \bar{y}_{C-} = \frac{1}{2^{k-1}}(y_{122} + y_{223} + y_{222} + y_{212} - [y_{121} + y_{111} + y_{221} + y_{211}]) \quad \textbf{I-3}$$

Where k is the number of levels for each factor. In order to determine the two-way interaction effects, the difference between the average effect of factor one at a high level of factor two, and the average effect of factor one at a low level of factor two is computed[112]. Alternatively, the levels (-1 or 1) in the desired interaction column of Table I1 (for example AB) could be multiplied with the response corresponding to each level[104]. After this process has been completed, the resulting values should be added together and divided by 4n. The resulting mathematical expressions are provided in Equations I-4 - I-6[112,168].

$$AB_{effect} = \frac{1}{2^{k-1}}(-y_{122} + y_{112} - y_{121} + y_{111} + y_{222} - y_{212} + y_{221} - y_{211}) \quad \textbf{I-4}$$

$$AC_{effect} = \frac{1}{2^{k-1}}(-y_{122} - y_{112} + y_{121} + y_{111} + y_{222} + y_{212} - y_{221} - y_{211}) \quad \textbf{I-5}$$

$$BC_{effect} = \frac{1}{2^{k-1}}(+y_{122} - y_{112} - y_{121} + y_{111} + y_{222} - y_{212} - y_{221} + y_{211}) \quad \textbf{I-6}$$

Finally, the three-way interaction effect can be calculated using Equation I-7, following the same approach used to determine the two-way interaction effects[104].

$$ABC_{effect} = \frac{1}{2^{k-1}}(-y_{122} + y_{112} + y_{121} - y_{111} + y_{222} - y_{212} - y_{221} + y_{211}) \quad \textbf{I-7}$$

With all the main and interaction effects calculated, the coefficients in the linear regression model provided by Equation I-8 can be determined. With the exception of $\boldsymbol{\beta_0}$, the coefficients are exactly equal to a half of the interaction effects[112]. The constant $\boldsymbol{\beta_0}$, is the average value of the measured responses. Table I2 represents all of the coefficients required to complete the regression model.

$$y = \beta_0 + \beta_A A + \beta_B B + \beta_c C + \beta_{AB} AB + \beta_{BC} BC + \beta_{AC} AC + \beta_{ABC} ABC + \mathrm{E} \quad \textbf{I-8}$$

Table I2: *Determination of the various coefficients used in the linear regression model of a 2^3 full factorial design*[168]

$\beta_0 = \bar{y}$	$\beta_A = \frac{A_{effect}}{2}$	$\beta_B = \frac{B_{effect}}{2}$	$\beta_C = \frac{C_{effect}}{2}$
$\beta_{AB} = \frac{AB_{effect}}{2}$	$\beta_{AC} = \frac{AC_{effect}}{2}$	$\beta_{BC} = \frac{BC_{effect}}{2}$	$\beta_{ABC} = \frac{ABC_{effect}}{2}$

I2. Central composite design

The design matrix (denoted by X in Equation 3-6) of the central composite design with three factors used throughout this dissertation has 10 columns to calculate the regression coefficient of every term in the regression equation. The matrix is provided in Table I3, to illustrate the different combinations of the factors used. The first column consists of only 1's and is used to determine the constant in the regression equation. Clearly quadratic terms have been added to the calculation as can be seen in columns 5 – 7. Finally, the remaining three columns is used to determine the regression coefficients of the interaction terms.

Table I3: *Design matrix of a typical face centred central composite design*

1	A	B	C	$(A)^2$	$(B)^2$	$(C)^2$	(A) x (B)	(A) x (C)	(B) x (C)
1	-1	1	1	1	1	1	-1	-1	1
1	-1	0	0	1	0	0	0	0	0
1	1	1	-1	1	1	1	1	-1	-1
1	1	1	1	1	1	1	1	1	1
1	0	0	0	0	0	0	0	0	0
1	0	0	0	0	0	0	0	0	0
1	0	0	0	0	0	0	0	0	0
1	0	0	0	0	0	0	0	0	0
1	0	-1	0	0	1	0	0	0	0
1	0	1	0	0	1	0	0	0	0
1	0	0	0	0	0	0	0	0	0
1	1	0	0	1	0	0	0	0	0
1	-1	-1	1	1	1	1	1	-1	-1
1	-1	1	-1	1	1	1	-1	1	-1
1	0	0	-1	0	0	1	0	0	0
1	1	-1	-1	1	1	1	-1	-1	1
1	-1	-1	-1	1	1	1	1	1	1
1	1	-1	1	1	1	1	-1	1	-1
1	0	0	1	0	0	1	0	0	0
1	0	0	0	0	0	0	0	0	0

T-distributions

Following the discussion in Section 3.3.2.3 and Annexure R, the values of T at the relevant degrees of freedom for the different alpha values are provided in Table I4. The rest of the table can be found in Montgomery and Runger, 2014[105] although the table is available in most statistics handbooks. Should a T-value be identified that falls within two of the percentage points, interpolation may be used to find an approximate value of alpha – which can be used to find the P-value. The general formula for two point interpolation is given in Equation I-9[169].

Table I4: *Percentage points $t_{\alpha,v}$ of the t distribution at varying degrees of freedom (Taken from Montgomery and Runger, 2014)*[105]

DOF = 1		DOF = 2		DOF = 5		DOF = 10	
Percentage points	**α**	**Percentage points**	**α**	**Percentage points**	**α**	**Percentage points**	**α**
0.33	0.4000	0.29	0.4000	0.27	0.4000	0.26	0.4000
1.00	0.2500	0.82	0.2500	0.73	0.2500	0.70	0.2500
3.08	0.1000	1.89	0.1000	1.48	0.1000	1.37	0.1000
6.31	0.0500	2.92	0.0500	2.02	0.0500	1.81	0.0500
12.71	0.0250	4.30	0.0250	2.57	0.0250	2.23	0.0250
31.82	0.0100	6.97	0.0100	3.37	0.0100	2.76	0.0100
63.66	0.0050	9.93	0.0050	4.03	0.0050	3.17	0.0050
127.32	0.0025	14.09	0.0025	4.77	0.0025	3.58	0.0025
318.31	0.0010	23.33	0.0010	5.89	0.0010	4.14	0.0010
636.62	0.0005	31.60	0.0005	6.87	0.0005	4.59	0.0005

$$y = y_1 + \frac{x - x_1}{x_2 - x_1}(y_2 - y_1) \qquad \textbf{I-9}$$

Where y is the desired alpha value, y_1 and y_2 are the lower and upper limits corresponding to x_1 and x_2 respectively, x is the calculated t-statistic and x_1 and x_2 are the two percentage points that represents the upper and lower limits of the calculated the t-statistic.

Annexure J: Factorial design code

Two Microsoft Excel™ VBA codes were written to analyse the factorial design data. The first was a code for the full 2^3 factorial design whereas the second was for the face centred central composite design as discussed in Section 3.3.2. Initially, a sheet was created and given the name "Design matrix linear". In the sheet, the table that is presented in Figure J1 was constructed where cell "B2" contained the heading "Velocity". The columns of the table represented the three factors and factor combinations and the final column in contained the first entries from the experimental results. The entries were normalised such that the column contained values between zero and one. The remaining data was added in additional columns to the right of Figure J1.

Velocity	SFR	Height	Velocity x SFR	Velocity x Height	SFR x Height	Velocity x SFR x Height	ε, ave..BOT
-1	1	1	-1	-1	1	-1	0.12
-1	-1	1	1	-1	-1	1	0.49
-1	1	-1	-1	1	-1	1	1.00
-1	-1	-1	1	1	1	-1	0.70
1	1	1	1	1	1	1	0.22
1	-1	1	-1	1	-1	-1	0.00
1	1	-1	1	-1	-1	-1	0.20
0	0	0	0	0	0	0	0.24
0	0	0	0	0	0	0	0.23
1	-1	-1	-1	-1	1	1	0.11

Figure J1: *Excel table containing the linear design matrix and the relevant response data*

The low medium and high settings of the factors and their combinations were represented by a "-1", "0" or "1" respectively. These values are fixed characteristics of the 2^3 full factorial design. Two command buttons were added to sheet "Design matrix linear" as indicated in Figure J2. The top button contained the code which analysed the factorial design while the bottom button could be used to clear the sheet which would contain the results from the analysis. The code for the bottom button was as follows:

```
Private Sub CommandButton2_Click()
  Worksheets("Analysis Linear").Range("B25:R3000").Clear
End Sub
```

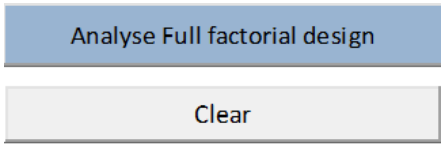

Figure J2*: Command buttons for the linear regression analysis*

The results from the top button in Figure J2, were printed in a separate excel sheet named “Analysis Linear” and in the initial formatting of the results sheet is provided in Figure J3.

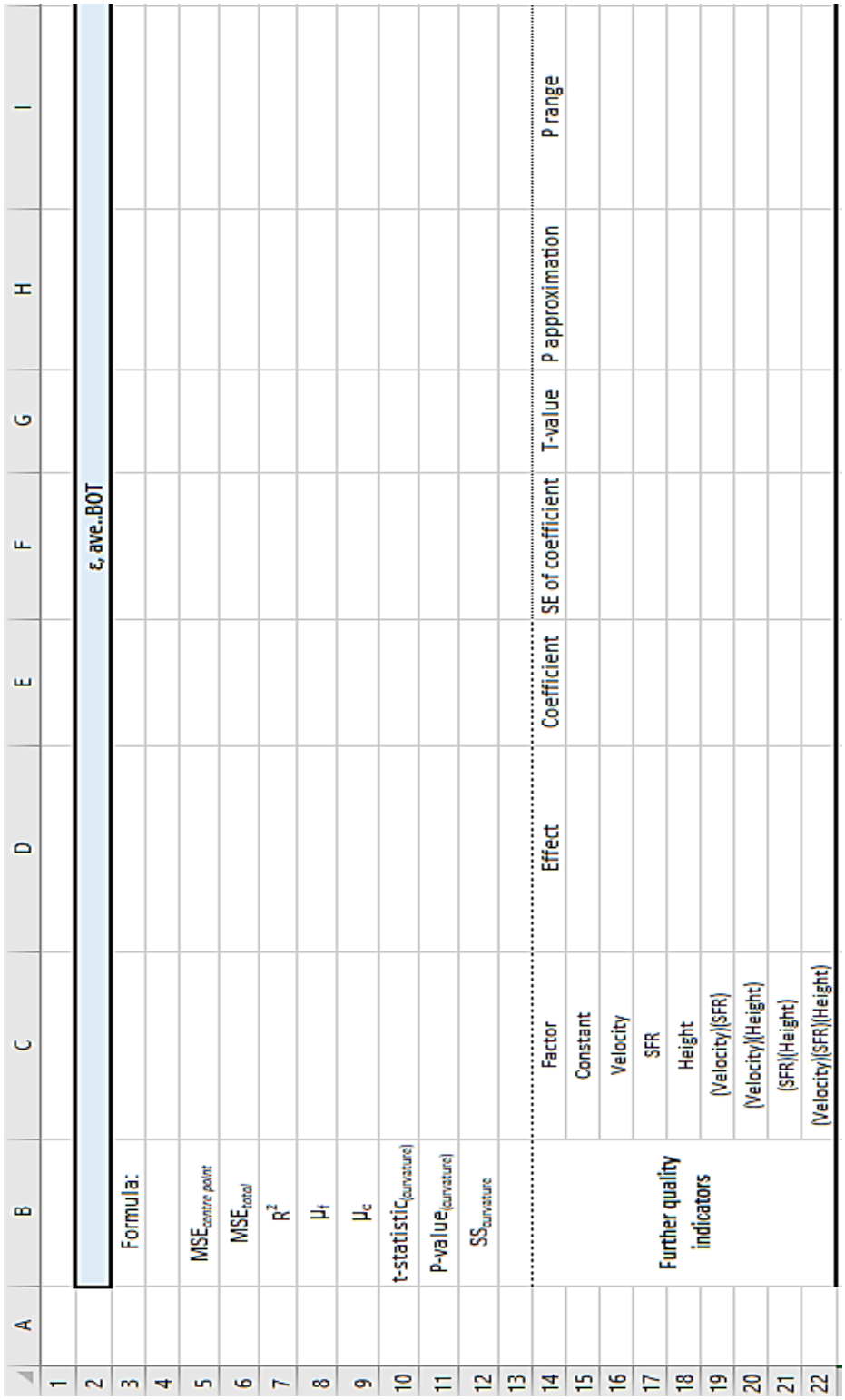

Figure J3: *Results sheet for the linear regression analysis*

The results from the VBA code included all the parameters discussed in Section 3.3.2. The P-values of the coefficients as well as the regression formulas were also discussed in-depth throughout this study. After the code has been activated, the empty spaces in Figure J3 were populated with data as illustrated in Figure J4. This process was repeated for each column of data that was entered into the table in the sheet “Design matrix Linear”.

	ε, ave..BOT						
Formula:	0.3309992392 + (-0.221)Velocity + (0.03)MFR + (-0.147)Height + (0.047)(Velocity)(MFR) + (0.125)(Velocity)(Height) + (-0.067)(MFR)(Height) + (0.102)(Velocity)(MFR)(Height)						
$MSE_{centre\ point}$	0.000110096						
MSE_{total}	1.14E-02						
R^2	97.34%						
μ_f	0.35						
μ_c	0.24						
$t\text{-statistic}_{(curvature)}$	14.34						
$P\text{-value}_{(curvature)}$	0.05	**0.020 < P(T > |t|) < 0.050**					
$SS_{curvature}$	2.264E-02						
Further quality indicators	Factor	Effect	Coefficient	SE of coefficient	T-value	P approximation	P range
	Constant		0.3309992	0.033726651	9.81417465	0.010	0.010 < P(T > |t|) < 0.020
	Velocity	-0.4413	-0.2206445	0.038	-5.8514695	0.033	0.020 < P(T > |t|) < 0.050
	SFR	0.0604	0.0301777	0.038	0.80030915	0.509	0.500 < P(T > |t|) < 0.800
	Height	-0.2944	-0.1472232	0.038	-3.9043425	0.064	0.050 < P(T > |t|) < 0.100
	(Velocity)(SFR)	0.0942	0.0470877	0.038	1.24876114	0.379	0.200 < P(T > |t|) < 0.500
	(Velocity)(Height)	0.2502	0.1250976	0.038	3.31757595	0.086	0.050 < P(T > |t|) < 0.100
	(SFR)(Height)	-0.1344	-0.0672003	0.038	-1.7821441	0.229	0.200 < P(T > |t|) < 0.500
	(Velocity)(SFR)(Height)	0.2039	0.1019546	0.038	2.70382575	0.121	0.100 < P(T > |t|) < 0.200

Figure J4: *Result population from the linear regression analysis*

The VBA code for the 2^3 full factorial design was as follows:

```
Private Sub CommandButton1_Click()
 Dim U, SFR, H, U_SFR, U_H, SFR_H, U_SFR_H, p, constant, zz As Variant
 Dim Tdist, Ue, SS, diff, diff2, SFRe, He, U_SFRe, U_He, SFR_He, totalf, U_SFR_He, calc, total, val, coef, y As
Variant
 Dim i, l, k, j, m, NC, NF, XX, XXX, gg, hh, A, B, T1, T2 As Integer
 Dim formula As String
 Dim muF, SSCURV, mu, MSESUM2, MSE, MSET As Double
 Dim MSESUM, subcalc1, tstat As Double


tests = 0
Save = 0

Z = 9
For tests = 0 To 30
If IsEmpty(Cells(3, Z)) Then
   tests = 30
Else
   tests = tests + 1
   Save = Save + 1
   Z = Z + 1
End If
Next

cc1 = 9
cc2 = 15
cc3 = 16
cc5 = 26
cc6 = 9
cc7 = 5
```

```
cc8 = 10
cc10 = 7
cc12 = 16
cc13 = 22
cc15 = 15
cc16 = 15
cc17 = 15
cc18 = 25
cc25 = 44
cc26 = 37
cc27 = 10
ccnew = 3


For parentLoop = 1 To Save


Worksheets("Analysis Linear").Range("B2:L22").Copy
Worksheets("Analysis Linear").Cells(cc18, 2).PasteSpecial Paste:=xlPasteFormats

Worksheets("Analysis Linear").Range("B3:B22").Copy
Worksheets("Analysis Linear").Range("B" & cc5, "B" & cc25).PasteSpecial Paste:=xlPasteAll

Worksheets("Analysis Linear").Range("C14:C22").Copy
Worksheets("Analysis Linear").Cells(cc26, 3).PasteSpecial Paste:=xlPasteAll

Worksheets("Analysis Linear").Range("D14:I14").Copy
Worksheets("Analysis Linear").Cells(cc26, 4).PasteSpecial Paste:=xlPasteAll

cc28 = cc1 + 1
Worksheets("Analysis Linear").Cells(cc18, 2) = Cells(2, cc28)

constant = WorksheetFunction.Average(Range(Cells(3, cc1), Cells(12, cc1)))
Worksheets("Analysis Linear").Cells(cc2, 5) = Round(constant, 10)



'effects and coefficients.....

val = 0
For i = 3 To 12
   calc = Cells(i, 2) * Cells(i, cc1)
   val = val + calc
Next

Ue = val

Worksheets("Analysis Linear").Cells(cc3, 4) = Ue / 4
Worksheets("Analysis Linear").Cells(cc3, 5) = Ue / 8

'.....

val = 0
For i = 3 To 12

   calc = Cells(i, 3) * Cells(i, cc1)
   val = val + calc
Next

SFRe = val
```

```
cc3 = cc3 + 1
Worksheets("Analysis Linear").Cells(cc3, 4) = SFRe / 4
Worksheets("Analysis Linear").Cells(cc3, 5) = SFRe / 8

'.....

val = 0
For i = 3 To 12

   calc = Cells(i, 4) * Cells(i, cc1)
   val = val + calc
Next

He = val
cc3 = cc3 + 1
Worksheets("Analysis Linear").Cells(cc3, 4) = He / 4
Worksheets("Analysis Linear").Cells(cc3, 5) = He / 8

'.....


val = 0
For i = 3 To 12

   calc = Cells(i, 5) * Cells(i, cc1)
   val = val + calc
Next

U_SFRe = val
cc3 = cc3 + 1
Worksheets("Analysis Linear").Cells(cc3, 4) = U_SFRe / 4
Worksheets("Analysis Linear").Cells(cc3, 5) = U_SFRe / 8

'.....

val = 0
For i = 3 To 12

   calc = Cells(i, 6) * Cells(i, cc1)
   val = val + calc
Next

U_He = val
cc3 = cc3 + 1
Worksheets("Analysis Linear").Cells(cc3, 4) = U_He / 4
Worksheets("Analysis Linear").Cells(cc3, 5) = U_He / 8

'.....

val = 0
For i = 3 To 12

   calc = Cells(i, 7) * (Cells(i, cc1))
   val = val + calc
Next

SFR_He = val
cc3 = cc3 + 1
Worksheets("Analysis Linear").Cells(cc3, 4) = SFR_He / 4
Worksheets("Analysis Linear").Cells(cc3, 5) = SFR_He / 8
```

```
'.....


val = 0
For i = 3 To 12

   calc = Cells(i, 8) * Cells(i, cc1)
   val = val + calc
Next

U_SFR_He = val
cc3 = cc3 + 1
Worksheets("Analysis Linear").Cells(cc3, 4) = U_SFR_He / 4
Worksheets("Analysis Linear").Cells(cc3, 5) = U_SFR_He / 8




'formula print.....

cc4 = cc2 + 7
coef = Worksheets("Analysis Linear").Range("E" & cc2, "E" & cc4)

formula = Round(coef(1, 1), 10) & " + (" & Round(coef(2, 1), 3) & ")Velocity + (" & Round(coef(3, 1), 3) &
")MFR + (" & Round(coef(4, 1), 3) & ")Height + (" & Round(coef(5, 1), 3) & ")(Velocity)(MFR) + (" &
Round(coef(6, 1), 3) & ")(Velocity)(Height) + (" & Round(coef(7, 1), 3) & ")(MFR)(Height) + (" &
Round(coef(8, 1), 3) & ")(Velocity)(MFR)(Height)"
Worksheets("Analysis Linear").Cells(ccnew, 3) = formula
'average factorial and cp runs.....

i = 3
j = 2
k = 3
l = 4

total = 0
totalf = 0

For i = 3 To 12
If Cells(i, j) = 0 And Cells(i, k) = 0 And Cells(i, l) = 0 Then
   total = total + Cells(i, cc1)

Else
   totalf = totalf + Cells(i, cc1)
End If
Next



muC = total * 0.5
Worksheets("Analysis Linear").Cells(cc6, 3) = muC

XXX = cc6 - 1
muF = totalf / 8
Worksheets("Analysis Linear").Cells(XXX, 3) = muF


'mse centre point.....
```

```
i = 3
j = 2
k = 3
l = 4
MSESUM2 = 0
MSESUM = 0

Do While i <= 12
If Cells(i, j) = 0 And Cells(i, k) = 0 And Cells(i, l) = 0 Then
   MSESUM = (Cells(i, cc1) - muC) ^ 2
   MSESUM2 = MSESUM + MSESUM2
End If
i = i + 1
Loop

Worksheets("Analysis Linear").Cells(cc7, 3) = MSESUM2


't and SS curvature.....
subcalc1 = Sqr(MSESUM2 * ((1 / 2) + (1 / 8)))
tstat = ((muF - muC) / (subcalc1))


Worksheets("Analysis Linear").Cells(cc8, 3) = tstat

cc9 = cc8 + 2
SSCURV = (2 * 8 * ((muF - muC) ^ 2)) / 10
Worksheets("Analysis Linear").Cells(cc9, 3) = SSCURV
A = 3
For A = 3 To 12
y = coef(1, 1) + (coef(2, 1) * Cells(A, 2)) + (coef(3, 1) * Cells(A, 3)) + (coef(4, 1) * Cells(A, 4)) + (coef(5, 1) *
Cells(A, 5)) + (coef(6, 1) * Cells(A, 6)) + (coef(7, 1) * Cells(A, 7)) + (coef(8, 1) * Cells(A, 8))
Cells(A, 1) = y
Next


'R square.....
A = 3
diff2 = 0
zz2 = 0
For A = 3 To 12
   diff = (Cells(A, cc1) - Cells(A, 1)) ^ 2
   zz = (Cells(A, cc1) - WorksheetFunction.Average(Range(Cells(3, cc1), Cells(12, cc1)))) ^ 2
   zz2 = zz2 + zz
   diff2 = diff2 + diff
Next

Rsqr = 1 - (diff2 / zz2)
Worksheets("Analysis Linear").Cells(cc10, 3) = FormatPercent(Rsqr, 2)
Range("A3:A12").Clear




MSET = diff2 / 2

cc11 = cc10 - 1
Worksheets("Analysis Linear").Cells(cc11, 3) = MSET
SS = Sqr(MSET) / Sqr(8)
```

```
Worksheets("Analysis Linear").Range("F" & cc12, "F" & cc13) = Round(SS, 10)

cc14 = cc12 - 1
Worksheets("Analysis Linear").Cells(cc14, 6) = Round(Sqr(MSET) / (Sqr(10)), 10)

i = 1
T1 = 1
For T1 = 1 To 8
Worksheets("Analysis Linear").Cells(cc15, 7) = Round(Worksheets("Analysis Linear").Cells(cc15, 5) /
Worksheets("Analysis Linear").Cells(cc15, 6), 10)
cc15 = cc15 + 1
Next

Tdist = Worksheets("Analysis Linear").Range("G" & cc16, "G" & cc13)


For k = 1 To 8
If Abs(Tdist(k, 1)) > Worksheets("T-distribution").Cells(13, "E") Then
   Worksheets("Analysis Linear").Cells(cc17, 8) = "± 0"
   Worksheets("Analysis Linear").Cells(cc17, 9) = "P(T > |t|) < 0.001"
ElseIf Abs(Tdist(k, 1)) < Worksheets("T-distribution").Cells(4, "E") Then
   Worksheets("Analysis Linear").Cells(cc17, 8) = "> 0.8"
   Worksheets("Analysis Linear").Cells(cc17, 9) = "P(T > |t|) > 0.8"
Else

   i = 4
   Do While i <= 13
   j = i + 1

    If Abs(Tdist(k, 1)) = Worksheets("T-distribution").Cells(i, "E") Then
      Worksheets("Analysis Linear").Cells(cc17, 8) = WorksheetFunction.RoundDown(2 * Worksheets("T-
distribution").Cells(i, "F"), 10)
      Worksheets("Analysis Linear").Cells(cc17, 9) = Worksheets("Analysis Linear").Cells(cc17, 8)
      i = 13
    End If

    If Worksheets("T-distribution").Cells(i, "B") < Abs(Tdist(k, 1)) And Abs(Tdist(k, 1)) < Worksheets("T-
distribution").Cells(j, "E") Then
      Worksheets("Analysis Linear").Cells(cc17, 8) = WorksheetFunction.RoundDown(2 * ((((Worksheets("T-
distribution").Cells(j, "F") - Worksheets("T-distribution").Cells(i, "F")) / (Worksheets("T-
distribution").Cells(j, "E") - Worksheets("T-distribution").Cells(i, "E"))) * (Abs(Tdist(k, 1)) - Worksheets("T-
distribution").Cells(i, "E"))) + Worksheets("T-distribution").Cells(i, "F")), 10)

      A = Round(2 * Worksheets("T-distribution").Cells(i, "F"), 10)
      B = Round(2 * Worksheets("T-distribution").Cells(j, "F"), 10)
      ranges = Format(B, "0.000") & "  < P(T > |t|) <  " & Format(A, "0.000")
      Worksheets("Analysis Linear").Cells(cc17, 9) = ranges
      i = 13
    End If

   i = i + 1

   Loop

End If
cc17 = cc17 + 1
Next


cc28 = cc27 + 1
```

```
If Abs(Worksheets("Analysis Linear").Cells(cc27, 3)) > Worksheets("T-distribution").Cells(13, "H") Then
   Worksheets("Analysis Linear").Cells(cc28, 3) = "± 0"
   Worksheets("Analysis Linear").Cells(cc28, 4) = "P(T > |t|) < 0.001"
   Worksheets("Analysis Linear").Cells(cc28, 4).Font.Size = 10
ElseIf Abs(Worksheets("Analysis Linear").Cells(cc27, 3)) < Worksheets("T-distribution").Cells(4, "H") Then
   Worksheets("Analysis Linear").Cells(cc28, 3) = "> 0.8"
   Worksheets("Analysis Linear").Cells(cc28, 4) = "P(T > |t|)> 0.8"
   Worksheets("Analysis Linear").Cells(cc28, 4).Font.Size = 10
Else

   i = 4
   Do While i <= 13
   j = i + 1

    If Abs(Worksheets("Analysis Linear").Cells(cc27, 3)) = Worksheets("T-distribution").Cells(i, "H") Then
      Worksheets("Analysis Linear").Cells(cc28, 3) = WorksheetFunction.RoundDown(2 * Worksheets("T-
distribution").Cells(i, "I"), 10)
      Worksheets("Analysis Linear").Cells(cc28, 4) = "P(T > |t|)= " & Worksheets("Analysis
Linear").Cells(cc28, 3)
      Worksheets("Analysis Linear").Cells(cc28, 4).Font.Size = 10
      i = 13
    End If

    If Worksheets("T-distribution").Cells(i, "H") < Abs(Worksheets("Analysis Linear").Cells(cc27, 3)) And
Abs(Worksheets("Analysis Linear").Cells(cc27, 3)) < Worksheets("T-distribution").Cells(j, "H") Then
      Worksheets("Analysis Linear").Cells(cc28, 3) = WorksheetFunction.RoundDown(2 * ((((Worksheets("T-
distribution").Cells(j, "I") - Worksheets("T-distribution").Cells(i, "I")) / (Worksheets("T-
distribution").Cells(j, "H") - Worksheets("T-distribution").Cells(i, "H"))) * (Abs(Worksheets("Analysis
Linear").Cells(cc27, 3)) - Worksheets("T-distribution").Cells(i, "H"))) + Worksheets("T-distribution").Cells(i,
"I")), 10)
      A = Round(2 * Worksheets("T-distribution").Cells(i, "I"), 10)
      B = Round(2 * Worksheets("T-distribution").Cells(j, "I"), 10)
      ranges = Format(B, "0.000") & "  < P(T > |t|) <  " & Format(A, "0.000")
      Worksheets("Analysis Linear").Cells(cc28, 4) = ranges
      Worksheets("Analysis Linear").Cells(cc28, 4).Font.Size = 10
      i = 13
    End If

   i = i + 1

   Loop

End If


cc1 = cc1 + 1
cc2 = cc2 + 23
cc3 = cc3 + 17
cc5 = cc5 + 23
cc6 = cc6 + 23
cc7 = cc7 + 23
cc8 = cc8 + 23
cc10 = cc10 + 23
cc12 = cc12 + 23
cc13 = cc13 + 23
cc15 = cc15 + 15
cc16 = cc16 + 23
cc17 = cc17 + 15
cc18 = cc18 + 23
cc25 = cc25 + 23
```

```
cc26 = cc26 + 23
cc27 = cc27 + 23
ccnew = ccnew + 23


Next

cc19 = cc7 - 3
Worksheets("Analysis Linear").Range("B" & cc19, "L" & cc13).Clear

End Sub
```

A face centred central composite design was also created for every response that was considered in the full factorial design analysis. A new sheet was created and named “Design matrix CCD” which contained the design matrix that is characteristic of a face centred CCD with three factors and three responses. This is illustrated in Figure J6. Once again, the final column of the table in Figure J6 contained the normalised experimental data and columns could be added or removed as required. The results from the CCD analysis were recorded in an additional sheet named “Analysis” and the initial formatting and population of the results table that was created is illustrated in Figure J7 and Figure J8. Once again all the necessary parameters as discussed in Section 3.3.2 were included. Two buttons were included in the sheet named “Design matrix CCD” and these are provided in Figure J5. The bottom button cleared the results sheet from the CCD analysis via the following code:

```
Private Sub CommandButton2_Click()
   Worksheets("Analysis").Range("B23:R3000").Clear

End Sub
```

The top button contained the VBA code which is provided in the remainder of this annexure.

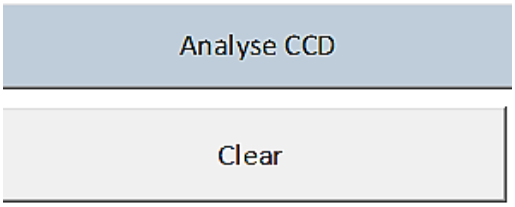

Figure J5: *Command buttons for the CCD analysis*

Constant	Velocity	SFR	Height	Velocity^2	SFR^2	Height^2	Velocity x SFR	Velocity x Height	SFR x Height	ε, ave..BOT
1	-1	1	1	1	1	1	-1	-1	1	0.16
1	-1	0	0	1	0	0	0	0	0	0.45
1	1	1	-1	1	1	1	1	-1	-1	0.23
1	1	1	1	1	1	1	1	1	1	0.26
1	0	0	0	0	0	0	0	0	0	0.28
1	0	0	0	0	0	0	0	0	0	0.26
1	0	0	0	0	0	0	0	0	0	0.32
1	0	0	0	0	0	0	0	0	0	0.14
1	0	-1	0	0	1	0	0	0	0	0.09
1	0	1	0	0	1	0	0	0	0	0.25
1	0	0	0	0	0	0	0	0	0	0.27
1	1	0	0	1	0	0	0	0	0	0.00
1	-1	-1	1	1	1	1	1	-1	-1	0.51
1	-1	1	-1	1	1	1	-1	1	-1	1.00
1	0	0	-1	0	0	1	0	0	0	0.32
1	1	-1	-1	1	1	1	-1	-1	1	0.15
1	-1	-1	-1	1	1	1	1	1	1	0.71
1	1	-1	1	1	1	1	-1	1	-1	0.04
1	0	0	1	0	0	1	0	0	0	0.10
1	0	0	0	0	0	0	0	0	0	0.24

Figure J6: *Excel table containing the CCD matrix and the relevant response data*

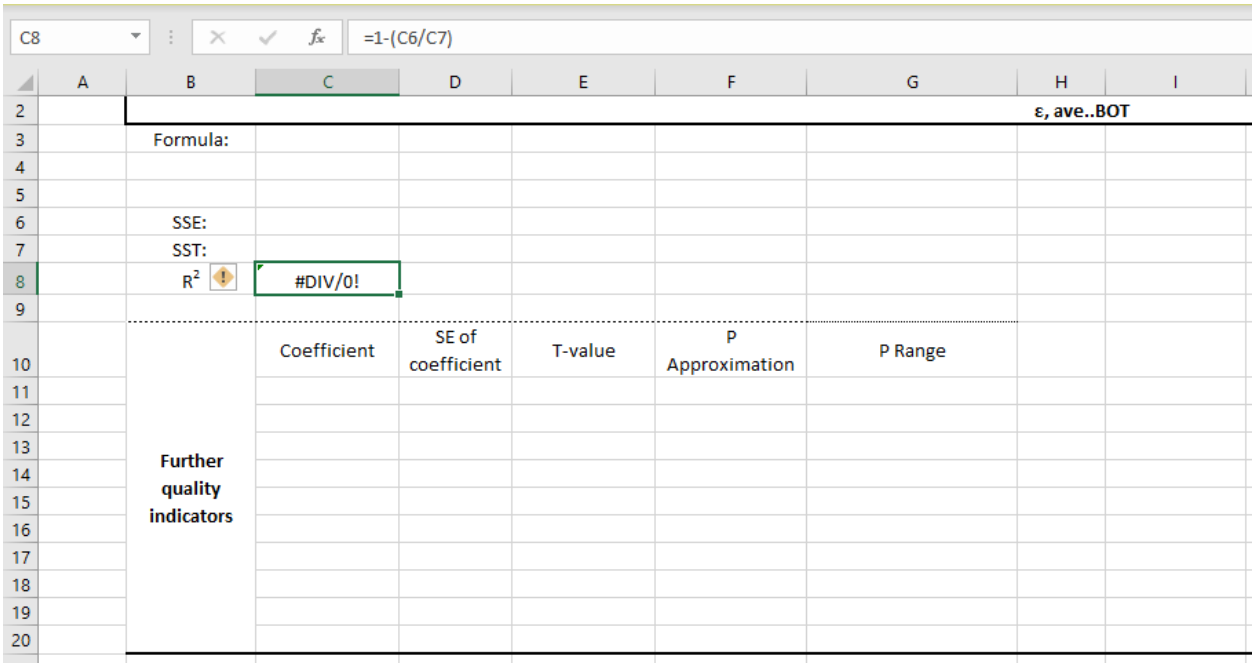

	A	B	C	D	E	F	G	H	I
2								ε, ave..BOT	
3		Formula:							
4									
5									
6		SSE:							
7		SST:							
8		R^2	#DIV/0!						
9									
10			Coefficient	SE of coefficient	T-value	P Approximation	P Range		
11									
12									
13									
14		Further quality indicators							
15									
16									
17									
18									
19									
20									

Figure J7: *Results sheet for the CCD regression analysis*

	ε, ave..BOT
Formula:	0.209 + (-0.214)Velocity + (0.039)MFR + (-0.134)Height + (0.078)Velocity^2 + (0.018)MFR^2 + (0.063)Height^2 + (0.045)(Velocity)(MFR) + (0.12)(Velocity)(Height) + (-0.064)(MFR)(Height)
	0
SSE:	0.134735267
SST:	1.048651867
R^2	87.15%

	Coefficient	SE of coefficient	T-value	P Approximation	P Range
Further quality indicators	0.209119	0.03990	5.241	0.00	< 0.001
	-0.213906	0.03671	-5.828	0.00	< 0.001
	0.039292	0.03671	1.070	0.33	0.200 < P(T > |t|) < 0.500
	-0.134426	0.03671	-3.662	0.00	0.002 < P(T > |t|) < 0.005
	0.078241	0.07000	1.118	0.31	0.200 < P(T > |t|) < 0.500
	0.018247	0.07000	0.261	0.70	0.500 < P(T > |t|) < 0.800
	0.062673	0.07000	0.895	0.41	0.200 < P(T > |t|) < 0.500
	0.044989	0.04104	1.096	0.32	0.200 < P(T > |t|) < 0.500
	0.119522	0.04104	2.912	0.02	0.010 < P(T > |t|) < 0.020
	-0.064205	0.04104	-1.564	0.16	0.100 < P(T > |t|) < 0.200

Figure J8: *Result population from the CCD regression analysis*

```
Private Sub CommandButton1_Click()
Worksheets("Design matrix CCD").Activate

Dim X, coef(), y, SSE, p(), value, SST, MSE, tcalc1(), SE(), PT(), temp As Variant
Dim formula, ranges As String
Dim i, j, k, DOF, tests, parentLoop, AP1, AP11, AP2, AP3 As Integer

'count columns.....
tests = 0
Save = 0

Z = 12
```

```
For tests = 0 To 30
If IsEmpty(Cells(3, Z)) Then
   tests = 30
Else
   tests = tests + 1
   Save = Save + 1
   Z = Z + 1
End If
Next

'paste formatting and headings.....
 AP1 = 11
 AP2 = 3
 AP3 = 12
 AP4 = 6
 AP5 = 7
 AP6 = 8
 ap7 = 23
 AP9 = 31

For parentLoop = 1 To Save
 H = parentLoop + 11


 AP8 = ap7 + 1

 Worksheets("Analysis").Range("B2:R20").Copy
 Worksheets("Analysis").Cells(ap7, 2).PasteSpecial Paste:=xlPasteFormats
 Worksheets("Analysis").Cells(8, 3).Copy
 Worksheets("Analysis").Cells(AP6, 3).PasteSpecial Paste:=xlPasteFormulas
 Worksheets("Analysis").Range("B3:B20").Copy
 Worksheets("Analysis").Cells(AP8, 2).PasteSpecial Paste:=xlPasteAll
 Worksheets("Analysis").Range("C10:G10").Copy
 Worksheets("Analysis").Cells(AP9, 3).PasteSpecial Paste:=xlPasteAll
 hh = H + 1
 Worksheets("Analysis").Cells(ap7, 2) = Worksheets("Design matrix CCD").Cells(2, hh)

X = Range("B3:K22")
y = Range(Cells(3, H), Cells(22, H))
coef() =
WorksheetFunction.MMult(WorksheetFunction.MInverse(WorksheetFunction.MMult(WorksheetFunction.Tr
anspose(X), X)), WorksheetFunction.MMult(WorksheetFunction.Transpose(X), y))


AP11 = AP1 + 9
Worksheets("Analysis").Range("c" & AP1, "c" & AP11) = coef()


formula = (Round(coef(1, 1), 3) & " + (" & Round(coef(2, 1), 3) & ")Velocity" & " + (" & Round(coef(3, 1), 3)
& ")MFR" & " + (" & Round(coef(4, 1), 3) & ")Height" & " + (" & Round(coef(5, 1), 3) & ")Velocity^2" & " + ("
& Round(coef(6, 1), 3) & ")MFR^2" & " + (" & Round(coef(7, 1), 3) & ")Height^2" & " + (" & Round(coef(8,
1), 3) & ")(Velocity)(MFR)" & " + (" & Round(coef(9, 1), 3) & ")(Velocity)(Height)" & " + (" &
Round(coef(10, 1), 3) & ")(MFR)(Height)")

Worksheets("Analysis").Cells(AP2, 3) = formula
AP2 = AP2 + 21
SSE = 0

Worksheets("Design matrix CCD").Activate
For i = 1 To 20
```

```
j = i + 2
Cells(j, 1) = coef(1, 1) + (coef(2, 1) * Cells(j, 3)) + (coef(3, 1) * Cells(j, 4)) + (coef(4, 1) * Cells(j, 5)) +
(coef(5, 1) * Cells(j, 6)) + (coef(6, 1) * Cells(j, 7)) + (coef(7, 1) * Cells(j, 8)) + (coef(8, 1) * Cells(j, 9)) +
(coef(9, 1) * Cells(j, 10)) + (coef(10, 1) * Cells(j, 11))
Next

p() = Range("A3", "A22")
Range("A3", "A22").Clear

i = 1
SSE = 0

For i = 1 To 20
   j = i + 2
   value = (Cells(j, AP3) - p(i, 1)) ^ 2
   SSE = SSE + value
Next


i = 1
SST = 0
For i = 1 To 20
   j = i + 2
   value = (Cells(j, AP3) - WorksheetFunction.Average(Range(Cells(3, AP3), Cells(22, AP3)))) ^ 2
   SST = SST + value
Next
AP3 = AP3 + 1


tcalc1() = WorksheetFunction.MInverse(WorksheetFunction.MMult(WorksheetFunction.Transpose(X), X))
DOF = 10
MSE = SSE / DOF

k = 1
For k = 1 To 10
   i = k + 2
   Cells(i, 1) = Sqr(tcalc1(k, k) * MSE)
Next


SE() = Range("A3:A12")
Worksheets("Analysis").Range("d" & AP1, "d" & AP11) = SE()


i = 1
AP111 = AP1
For i = 1 To 10
 Worksheets("Analysis").Cells(AP111, 5) = coef(i, 1) / SE(i, 1)
 AP111 = AP111 + 1
Next

Worksheets("Analysis").Cells(AP4, 3) = SSE
Worksheets("Analysis").Cells(AP5, 3) = SST


Dim T As Variant
Range("A3:A12").Clear
AP1111 = AP1 + 9
T = Worksheets("Analysis").Range("e" & AP1, "e" & AP1111)
```

```
k = 1
l = AP1

For k = 1 To 10
If Abs(T(k, 1)) > Worksheets("T-distribution").Cells(13, "B") Then
   Worksheets("Analysis").Cells(l, 6) = 0
   Worksheets("Analysis").Cells(l, 7) = "< 0.001"
ElseIf Abs(T(k, 1)) < Worksheets("T-distribution").Cells(4, "B") Then
   Worksheets("Analysis").Cells(l, 6) = 1
   Worksheets("Analysis").Cells(l, 7) = "> 0.8"
Else

   i = 4
   Do While i <= 12
   j = i + 1

    If Abs(T(k, 1)) = Worksheets("T-distribution").Cells(i, "B") Then
      Worksheets("Analysis").Cells(l, 6) = 2 * Worksheets("T-distribution").Cells(i, "C")
      Worksheets("Analysis").Cells(l, 7) = Worksheets("Analysis").Cells(l, 6)
      i = 13
    End If

    If Worksheets("T-distribution").Cells(i, "B") < Abs(T(k, 1)) And Abs(T(k, 1)) < Worksheets("T-
distribution").Cells(j, "B") Then
      Worksheets("Analysis").Cells(l, 6) = 2 * ((((Worksheets("T-distribution").Cells(j, "C") - Worksheets("T-
distribution").Cells(i, "C")) / (Worksheets("T-distribution").Cells(j, "B") - Worksheets("T-
distribution").Cells(i, "B"))) * (Abs(T(k, 1)) - Worksheets("T-distribution").Cells(i, "B"))) + Worksheets("T-
distribution").Cells(i, "C"))

      A = Round(2 * Worksheets("T-distribution").Cells(i, "C"), 3)
      B = Round(2 * Worksheets("T-distribution").Cells(j, "C"), 3)
      ranges = Format(B, "0.000") & "  < P(T > |t|) <  " & Format(A, "0.000")
      Worksheets("Analysis").Cells(l, 7) = ranges
      i = 13
    End If

   i = i + 1

   Loop

End If
l = l + 1
Next


 ap7 = ap7 + 21
 AP6 = AP6 + 21
 AP9 = AP9 + 21
 AP1 = AP1 + 21
 AP4 = AP4 + 21
 AP5 = AP5 + 21


Next
ap7 = ap7 - 21
AP10 = ap7 + 18
Worksheets("Analysis").Range("B" & ap7, "R" & AP10).Clear


End Sub
```

Throughout the VBA codes that were presented in this chapter, reference is made to a T-distribution and the applicable information was retrieved from a separate sheet named “T-distribution”. The information contained in the previously mentioned sheet is illustrated in Figure J9.

	A	B	C	D	E	F	G	H	I
1									
2		DOF = 10			DOF = 2			DOF = 1	
3		t	α		t	α		t	α
4		0.026	0.4000		0.289	0.4000		0.325	0.4000
5		0.700	0.2500		0.816	0.2500		1.000	0.2500
6		1.372	0.1000		1.886	0.1000		3.078	0.1000
7		1.812	0.0500		2.920	0.0500		6.314	0.0500
8		2.228	0.0250		4.303	0.0250		12.706	0.0250
9		2.764	0.0100		6.965	0.0100		31.821	0.0100
10		3.169	0.0050		9.925	0.0050		63.657	0.0050
11		3.581	0.0025		14.089	0.0025		127.320	0.0025
12		4.144	0.0010		23.326	0.0010		318.310	0.0010
13		4.587	0.0005		31.598	0.0005		636.620	0.0005

Figure J9: *T-distribution data*

Annexure K: Instrument details

K1. General information

The measurement ranges of the thermocouples, pressure transmitters and the anemometer as well as the operating ranges of the fan and feeder are provided in Table K1 along with additional information.

Table K1: *Measurement instrument and process unit information*

Description	***Range***	***Accuracy***	***Supplier***	***Model***
Variable speed screw feeder	0.03 – 0.34 kg/s	± 0.01 kg/s	ZEST Weg group	MBF with agitator
Variable speed fan motor	0.00 – 18.43 m/s	± (0.03 + (0.04 x U))	Trojan fans	BC10
Hot wire anemometer	0.0 – 50.0 m/s	± (0.03 + (0.04 x U))	Testo	Testo 440
Flush pressure transmitters	0.0 – 10.0 kPa	± 0.5 %	Wika	S-11
Resistance temperature detectors	0.0 – 300.0 °C	± 0.6 °C	Swift heat & control	PT-100

K2. Non-isokinetic sampling probe

(a)

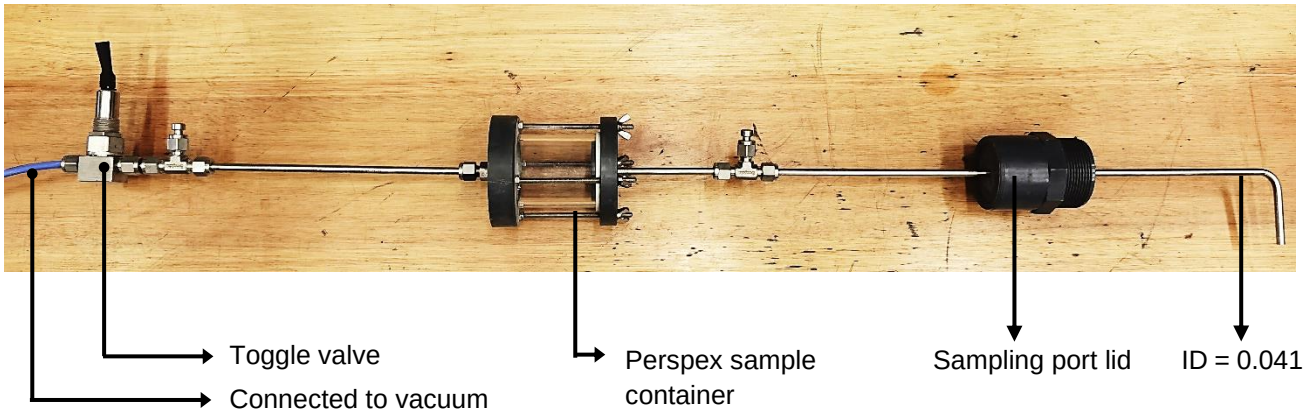

(b)

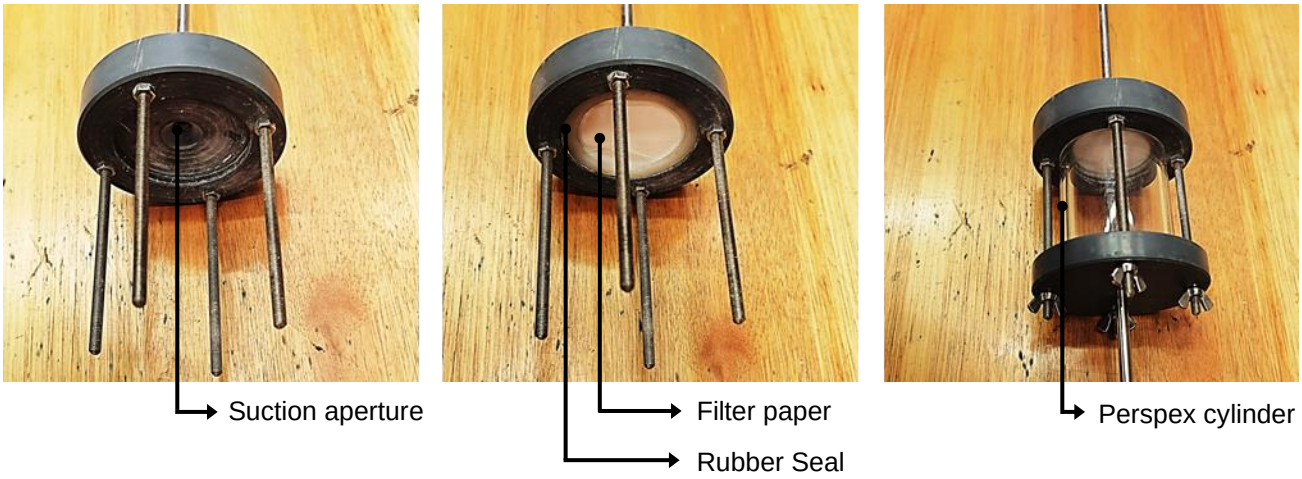

Figure K1: *(a) The sampling probe and (b) the sample containers' assembly*

The non-isokinetic sampling procedure was as follows:

1. The perspex container and a clean filter paper was weighed.
2. The filter paper was placed inside the sampling container and the sampler was assembled.
3. Both valves were opened and the suction velocity at the tip of the probe was measured using the Testo 440 hot wire anemometer.
4. The superficial gas velocity inside the riser was determined from the target inlet velocity of the given experiment.

5. The ball valve was adjusted until the average suction velocity at the probe tip over 60 seconds was close to the calculated superficial gas velocity.
6. The probe suction velocity thus had a value of 1.8 m/s, 2.7 m/s or 3.6 m/s when aiming for a target inlet velocity of 4.1 m/s, 6.1 m/s or 8.1 m/s respectively.
7. Once the desired suction velocity has been reached only the toggle valve was closed.
8. Once riser steady state has been reached the bottom port was opened and the sampler lid was fastened to the port.
9. The probe was placed at the first radial location as discussed in Section 3.3.4.3 with the tip facing downwards.
10. A stopwatch was started and the toggle valve was opened for 60 seconds after which it was closed.
11. The sampler was disassembled while the probe remained inside the riser.
12. The probe tip was rotated 180° to prevent excessive sample accumulation inside the line.
13. The sorbent, perspex container and filter paper was weighed and the difference in mass between the empty and full container was recorded.
14. The container was cleaned and weighed together with a clean filter paper.
15. The probe tip that was attached to the riser port was briefly cleaned with compressed air.
16. The filter paper was placed inside the sampling container and the sampler was reassembled.
17. The probe was positioned at the next radial location as discussed in Section 3.3.4.3 with the tip facing downwards.
18. Steps 10 – 17 were repeated at every radial sampling location.
19. The probe was removed and the port lid was secured.
20. The suction velocity was recalibrated according to steps 1 – 7.
21. The middle port was opened and the sampler lid was fastened to the port.
22. Steps 9 – 18 were followed at the middle port.
23. The probe was removed and the port lid was secured.
24. The suction velocity was recalibrated according to steps 1 – 7.
25. The top port was opened and the sampler lid was fastened to the port.
26. Steps 9 – 18 were followed at the middle port.
27. The probe was removed and the port lid was secured.

Annexure L: Transport velocity from Zhou *et al.,* (2011)

In order to determine the transport velocity for the FGD-CFB unit described by Zhou *et al.,* (2011) [64], the correlation from Bi and Grace was used. This is because the H/D ratio of the unit was equal to 5.4 while the Archimedes number had a value of 3.6. These factors made the correlation from Bi & Grace the only suitable correlation from the list of options that were provided in Table 2-1 of Section 2.2.1. The resulting transport velocity is provided in Table L1 together with the operating superficial gas velocity they reported. From Table L1 it can be seen that the condition where the superficial gas velocity should be equal to twice the transport velocity was exceeded.

Table L1: *Transport velocity of an industrial scale FGD-CFB unit*

Parameter	Value	Unit
U_{TR}	1.78	m/s
U_{riser}	4.43	m/s
$U_{TR} \times 2$	3.57	m/s

Annexure M: Setup photos

Figure M1: *Riser during its construction*

Figure M2: *Riser when only one cylindrical section was installed*

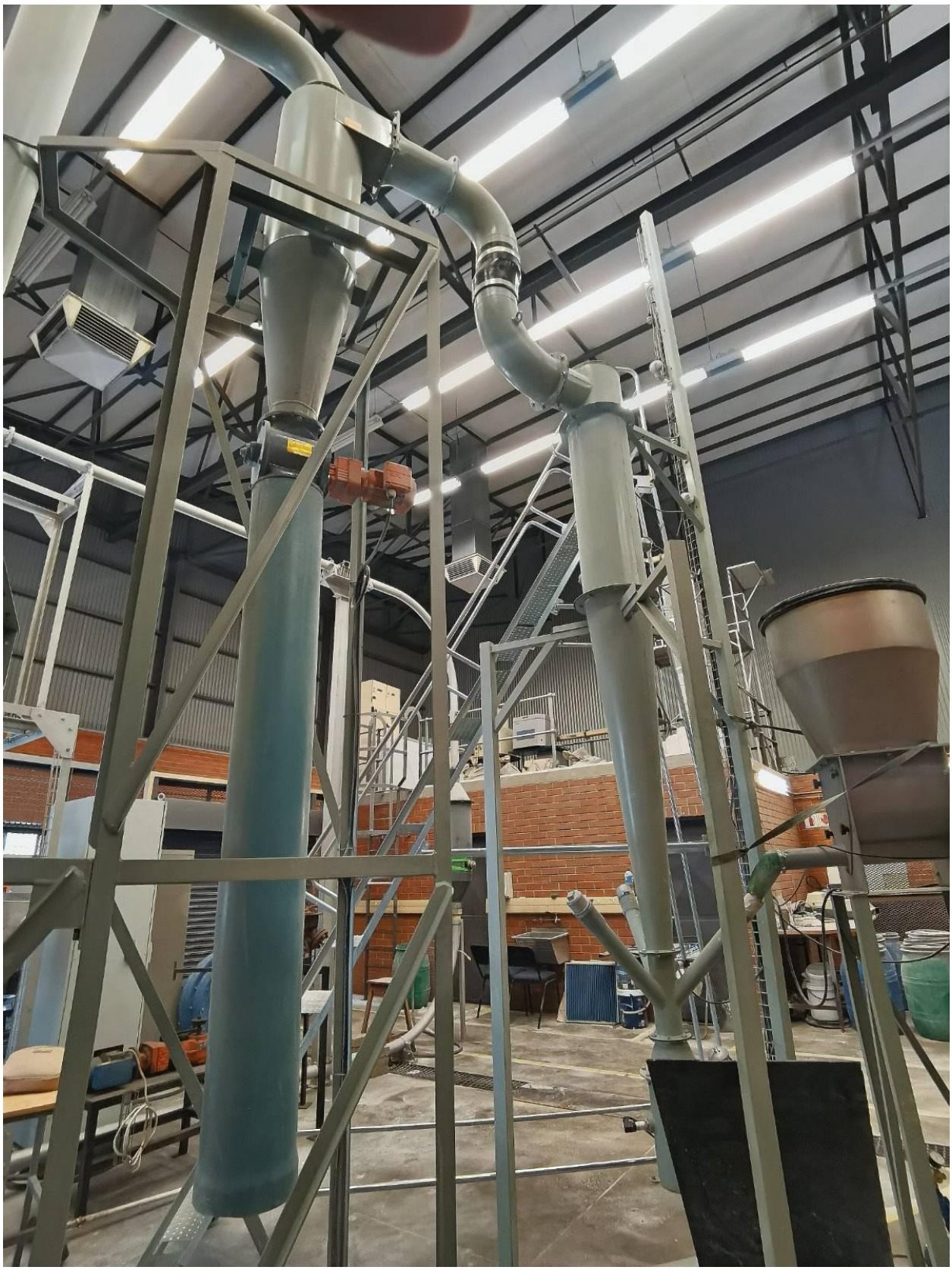

Figure M3: *The cyclone while it was attached to the bottom riser section*

Figure M4: *The scrubber*

Figure M5: *Different feeder assemblies that were tested*

Figure M6: *The sorbent mixer and screw feeder*

Figure M7: *The draught fan*

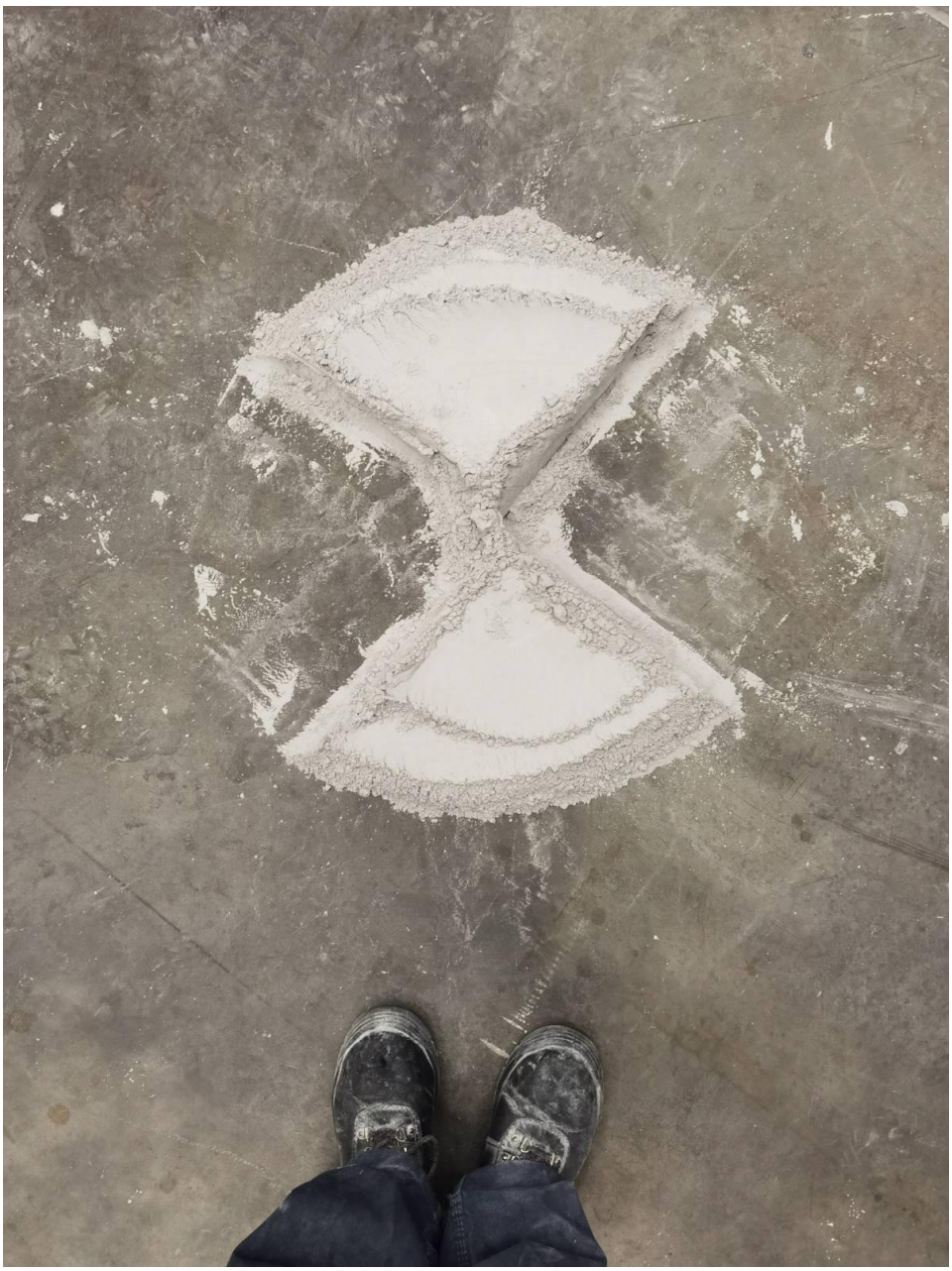

Figure M8: *An example of the sample during coning and quartering*

Figure M9: *Clogged feed pipe during operation*

CHAPTER 4

Annexure N: Calculation of the wall roughness height

The wall roughness height was approximated by applying friction factor correlations that were suggested by Nikuradse[60]. Depending on the tube properties, either the Reynolds number or the wall roughness will have the greatest effect on the friction factor. Equation N-1 is generally used to determine the friction factor in smooth tubes where the Reynolds number has the greatest influence. Alternatively, Equation N-2 is used to determine the friction factor in rough tubes where the roughness height has a more significant effect on the friction factor[60]. However, Equation N-1 may be applied to rough tubes below a certain threshold of Reynolds numbers even though it was originally defined for smooth tubes. The range of Reynolds numbers for which each correlation is applicable is limited by $Test_{ff}$, which is given by Equation N-3.

$$\frac{1}{\sqrt{f_f}} = 4 \times log_{10}\left(Re \times \sqrt{f_f}\right) - 0.4 \qquad Test_{ff} \gg 0.01 \qquad \textbf{N-1}$$

$$\frac{1}{\sqrt{f_f}} = 4 \times log_{10}\left(\frac{D}{e}\right) + 2.28 \qquad Test_{ff} < 0.01 \qquad \textbf{N-2}$$

$$Test_{ff} = \frac{\frac{D}{e}}{Re\sqrt{f_f}} \qquad \textbf{N-3}$$

Where f_f is the friction factor, Re is the Reynolds number, D is the riser diameter and e is the wall roughness height. The roughness height was approximated by using Equation N-1 under the assumption of smooth surfaces and Equation N-2 under the assumption of rough surfaces in order to determine the most suitable correlation. For Equation N-1, the Reynolds number was calculated from the highest superficial gas velocity setting used during the experiments. This was done to calculate the lowest possible value of $Test_{ff}$. With the Reynolds number known, the friction factor could be determined using Equation N-1 and the wall roughness could be approximated from Moody's friction factor plot as provided by Figure N1. The results are reported in Table N1 and indicate that the condition stipulated for Equation N-1 held true. Hence, the roughness height approximation of 0.02 mm could be applied.

For Equation N-2, Moody's diagram for friction factors in rough pipes as given in Figure N2 was used to determine the wall roughness height of commercial steel with a diameter of 0.3 m or 11.8 inches. With the roughness known, Equation N-2 could be used to calculate the friction factor and once again $Test_{ff}$ could be determined. From the results reported in Table N1, the $Test_{ff}$ condition for Equation N-2 was not satisfied. Consequently, the results from Equation N-1 was used in the simulation and it was determined that the Reynolds number made a greater contribution to the friction factor than the wall roughness height for this study.

Table N1: *Roughness height calculation results*

Variable	**Unit**	**Value**
D	m	0.30
U_0	m/s	3.6
ρ_f	kg/m^3	1.2
μ_f	$Pa \cdot s$	1.83×10^{-5}
Re	$(-)$	70463
Equation H-1, Valid when $Test_{ff}$>> *0.01*		
f_f	$(-)$	0.0048
e/D	$(-)$	5×10^{-5}
e	mm	0.02
$Test_{ff}$	$(-)$	4.1
Equation H-2, Valid when $Test_{ff}$ < *0.01*		
e/D	$(-)$	0.00016
f_f	$(-)$	0.00328
e	mm	0.05
$Test_{ff}$	$(-)$	1.6

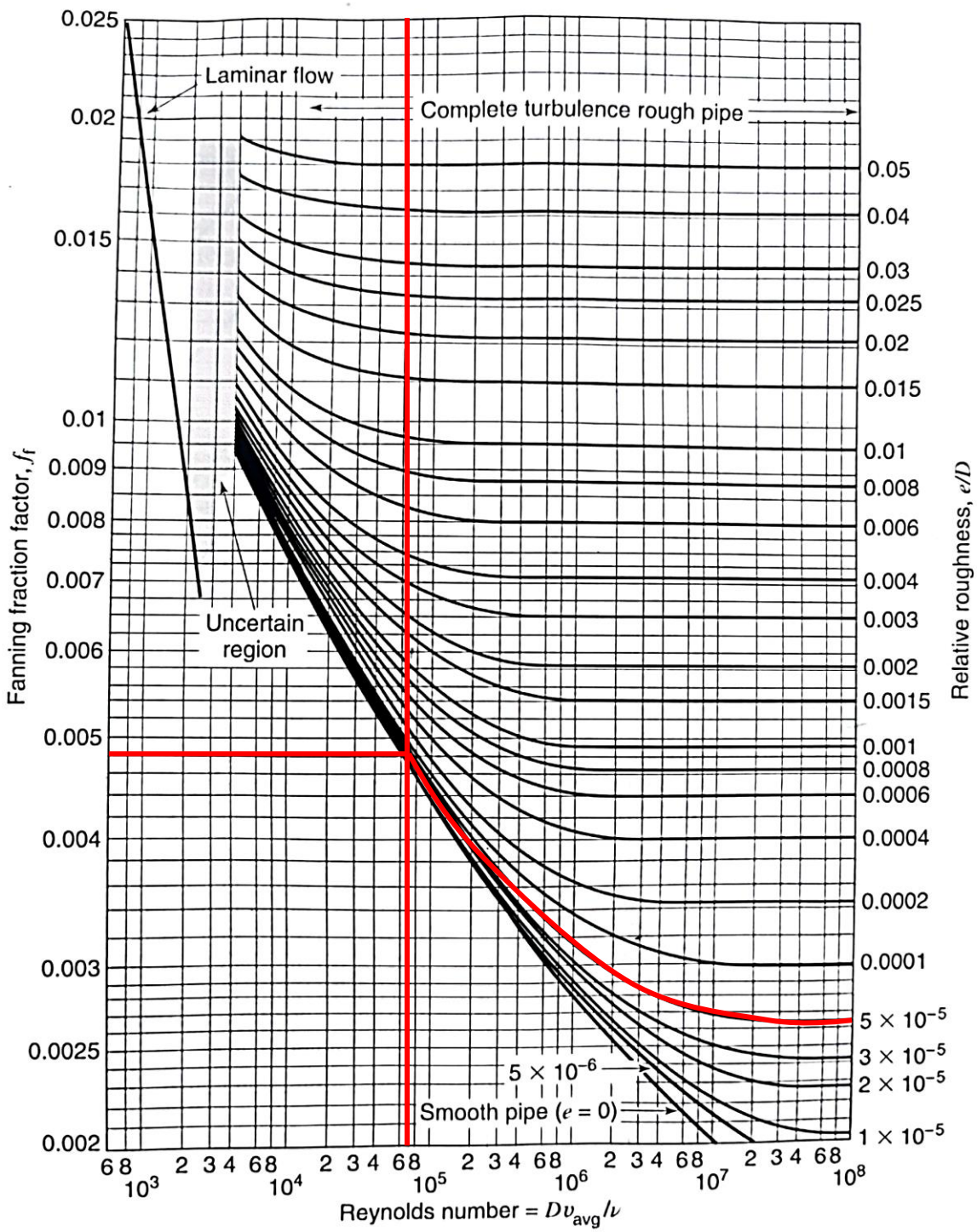

Figure N1: *Fanning friction factor as a function of the Reynolds number and relative roughness (Taken from Welty et al., 2013:185)*[60]

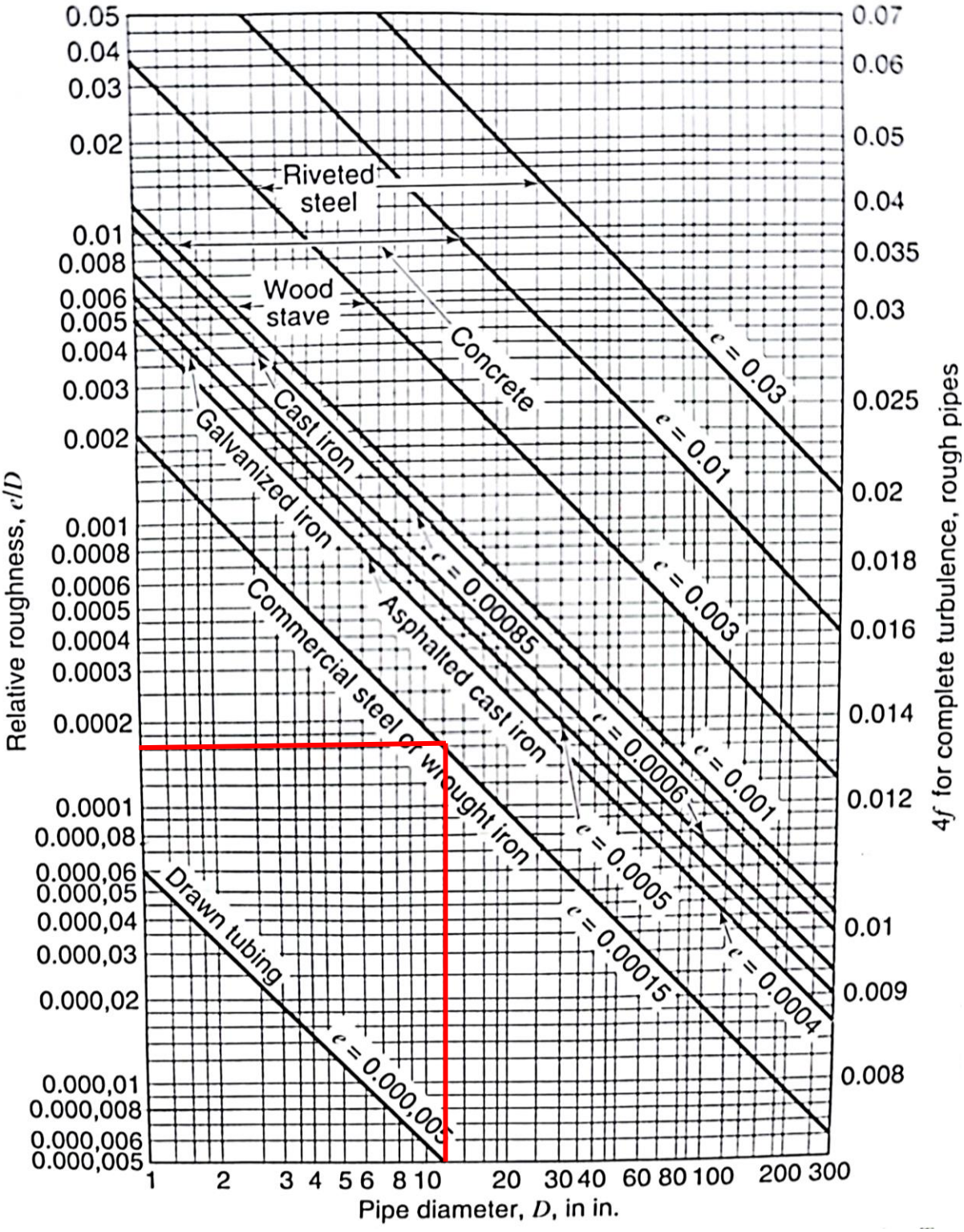

Figure N2: *Roughness parameters for tubes of different materials (Taken from Welty et al., 2013:186)*[60]

Annexure O: Calculation of the Schiller-Neumann limiting velocity

The particle Reynolds number may be determined from Equation O-1. In order for Equation O-1 to have a value of 800 in this study, the superficial gas velocity in the riser would have to exceed 520.63 m/s. The values of each variable that was used for the calculation is given in Table O1. Conversely, for a particle with an average diameter of 2 mm the superficial gas velocity limit would be equal to 6.15 m/s. Thus, the small diameter of the particles that were used within this study allowed for the use of the Schiller Neumann drag model as it ensured a low particle Reynolds number (<800) and in turn sufficiently dilute conditions.

$$Re_p = \frac{U_0 d_p \rho_f}{\mu_f} \qquad \textbf{O-1}$$

Table O1: *Values used to calculate the gas velocity at a particle Reynolds number of 800*

Variable	Value	Unit
$\boldsymbol{d_p}$	23.63	μm
$\boldsymbol{\rho_f}$	1.19	kg/m^3
$\boldsymbol{\mu_f}$	1.83×10^{-5}	$Pa \cdot s$

Annexure P: Scenes produced during the grid independence study

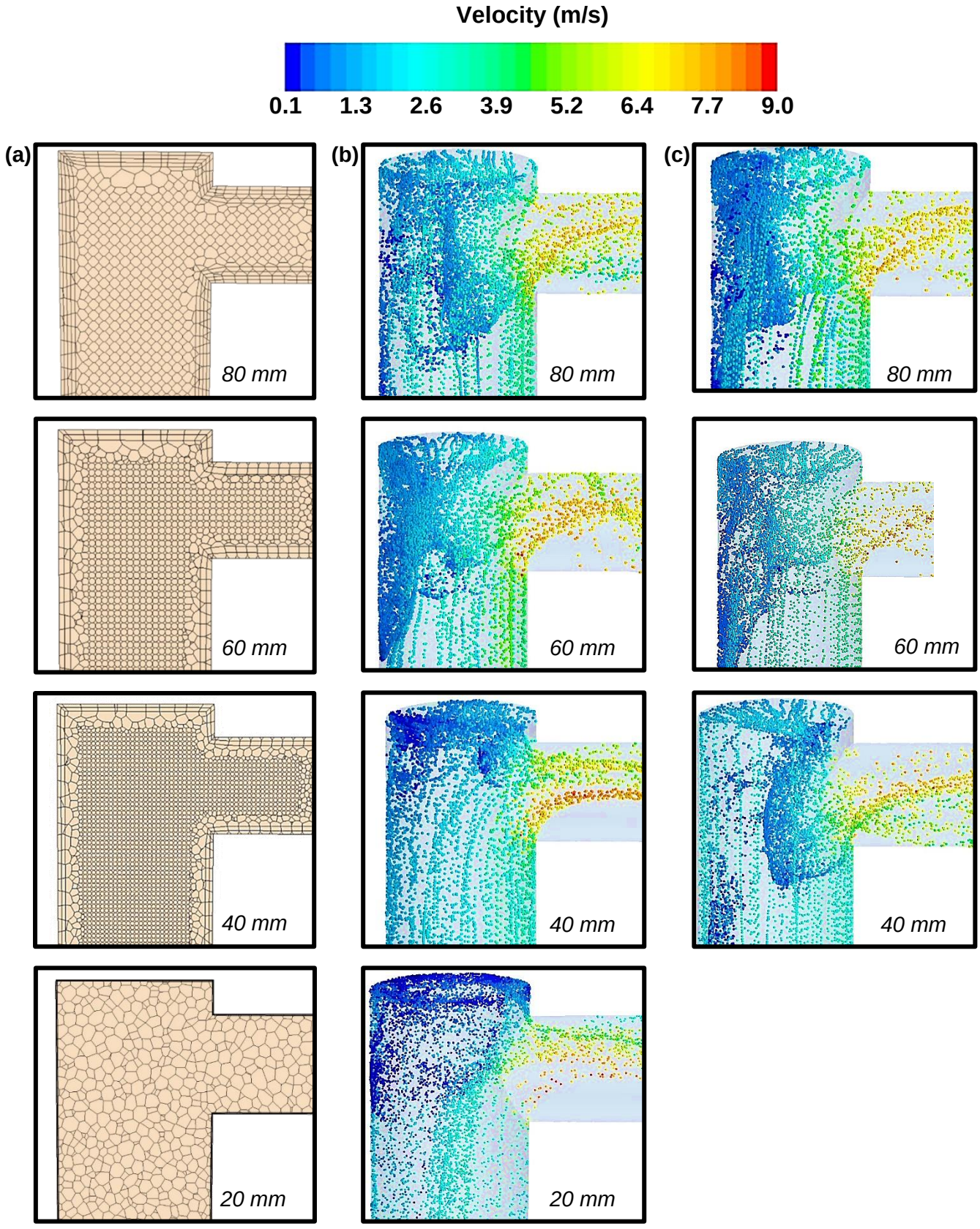

Figure P1: *(a) The finest mesh used for a given simulation and the particle velocity magnitude at the top of the riser (b) without local mesh refinement and (c) with local mesh refinement*

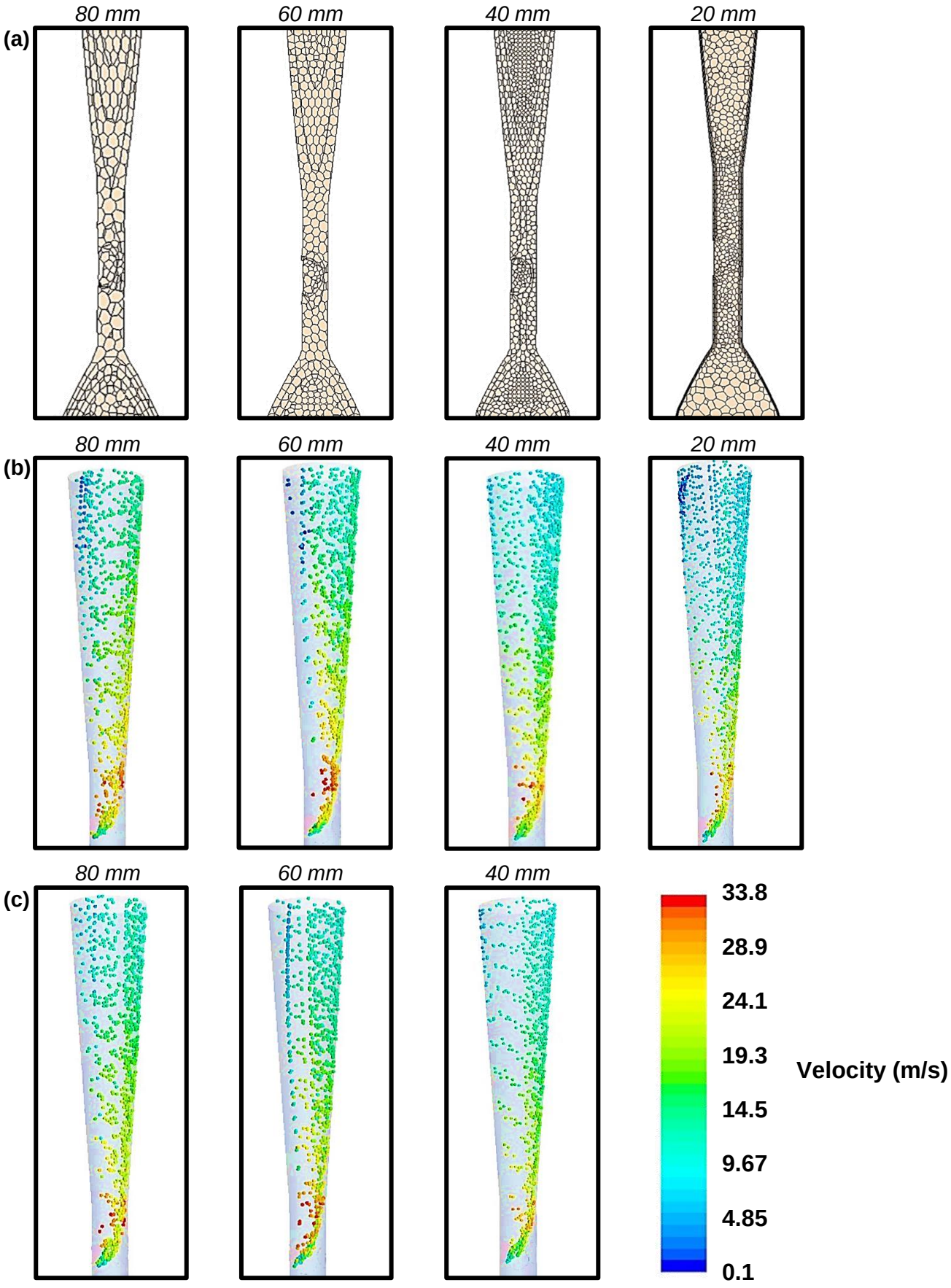

Figure P2: *a) The finest mesh used for a given simulation and the particle velocity magnitude at the bottom of the riser (b) without local mesh refinement and (c) with local mesh refinement*

CHAPTER 5

Annexure Q: Additional experimental results

In Figure Q1 - Figure Q4 the experimental radial solids holdup profiles at the three sampling ports are indicated. As discussed in Section 5.1.1, the following trends could be identified:

- An increase in the inlet air velocity or a decrease in the solids feed rate created flatter or more uniform radial solids holdup profiles by reducing clustering/phase interactions.
- Changes in the operating conditions had a greater effect on the particles near the wall when compared to those at the centre of the riser.
- When compared to the solids feed rate, the inlet air velocity had a stronger influence on the radial solids holdup profiles at all of the sampling ports.
- An increase in the riser height caused the maximum local solids holdup to shift to the left while also creating less uniform particle distributions in most cases.

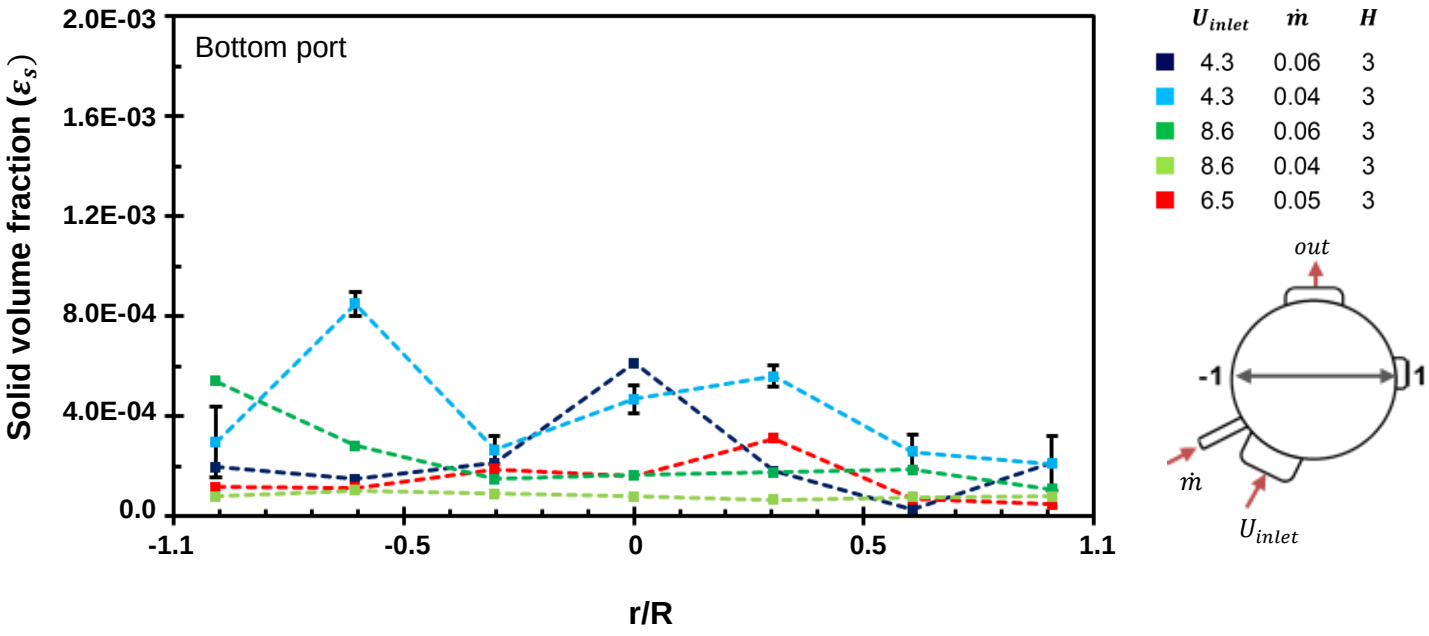

Figure Q1: *The radial solids holdup profile at the* ***bottom sampling port*** *under varying inlet velocity and solid feed rate settings*

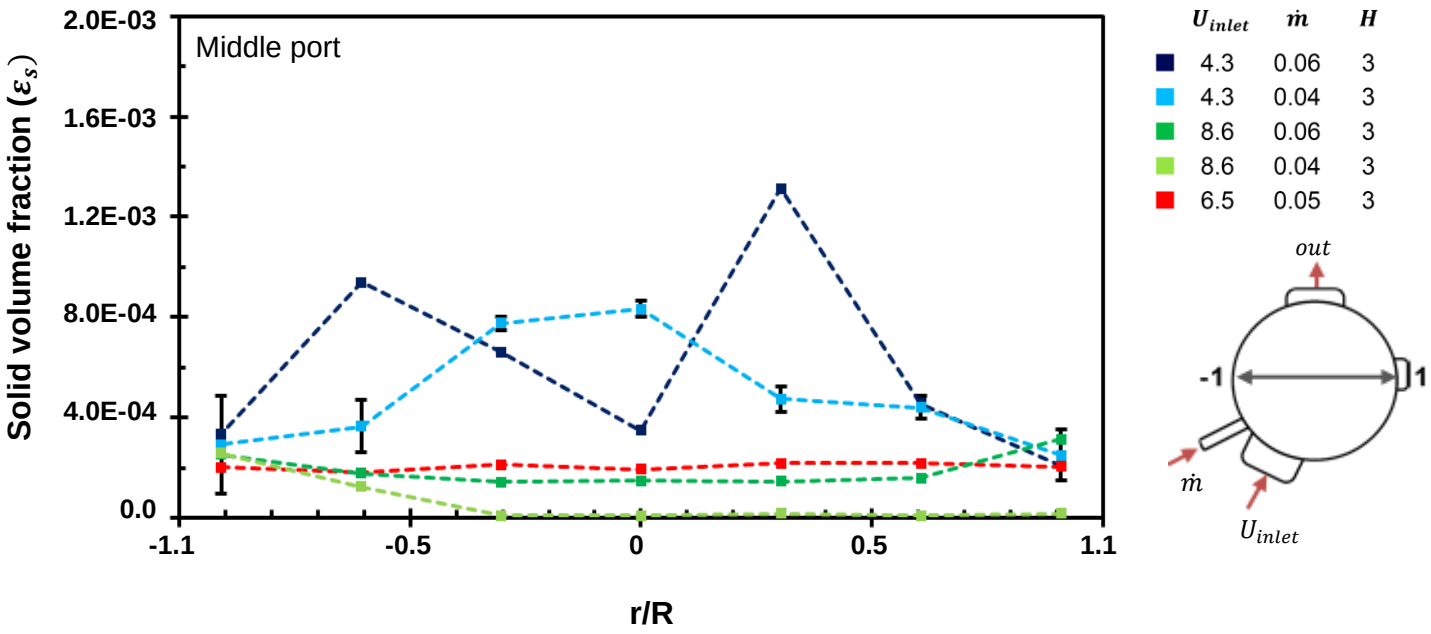

Figure Q2: *The radial solids holdup profile at the* ***middle sampling port*** *under varying inlet velocity and solid feed rate settings*

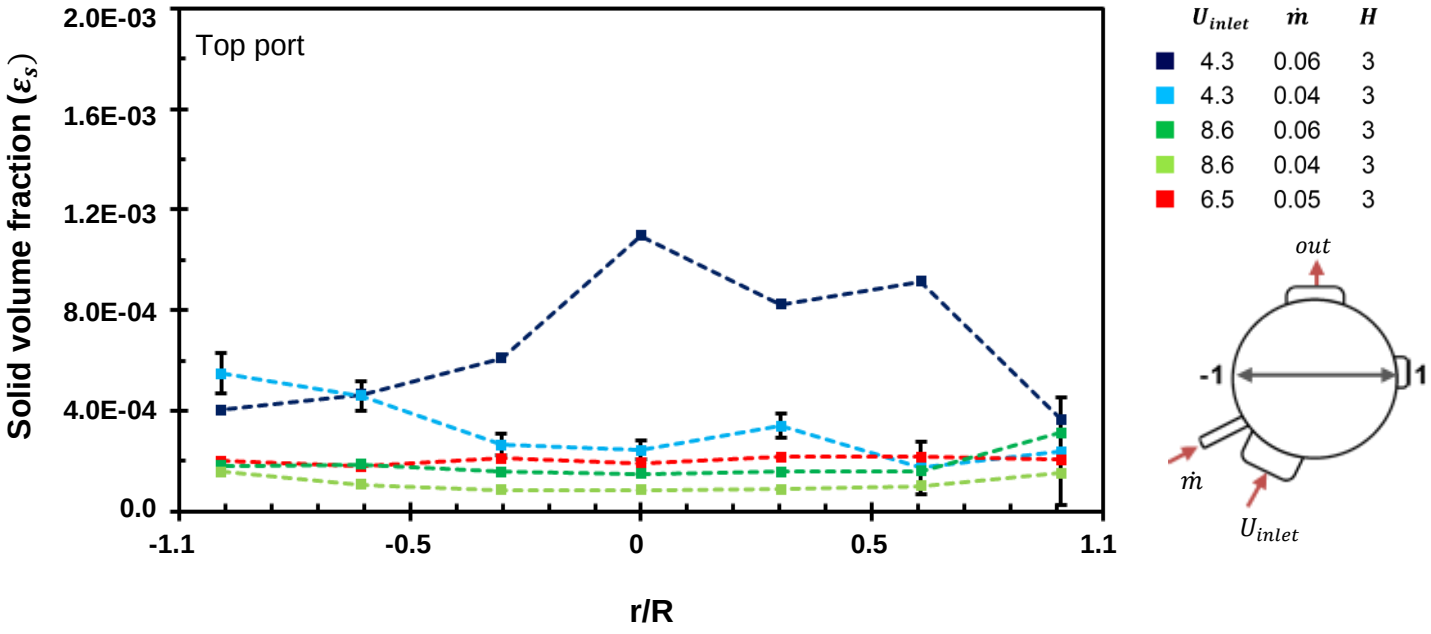

Figure Q3: *The radial solids holdup profile at the* ***top sampling port*** *under varying inlet velocity and solid feed rate settings*

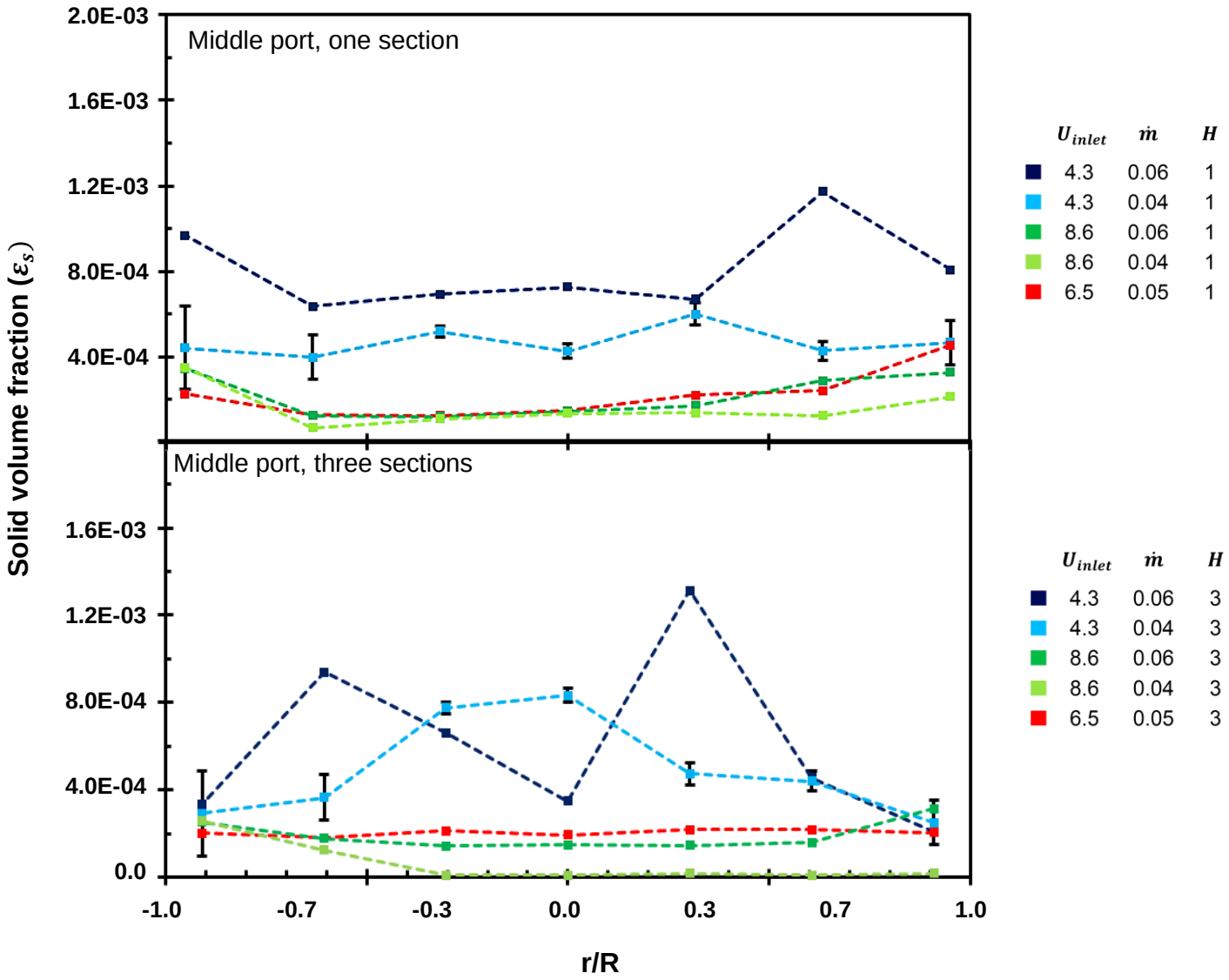

Figure Q4: *The influence of riser height on the radial solids holdup profiles at the middle sampling port*

Annexure R: Experimental confidence intervals

In order to assess the repeatability of the solid volume fraction measurements, confidence intervals were calculated. The collected data from the six repeated centre point runs were used (i.e. at the medium settings of the three independent variables). In Figure R1, the average solid volume fraction at every radial location at the bottom port is plotted. The 95% confidence intervals (CI) at each measurement location were included as error bars and were calculated using Equation R-1[105].

$$CI = \frac{t_{\alpha/2,n-1}(\hat{\sigma})}{\sqrt{n}} \qquad \textbf{R-1}$$

Where $t_{\alpha/2,n-1}$ is obtained from the t-distribution table in Annexure I, $\hat{\sigma}$ is the standard deviation and n refers to the number of experimental observations. The labels next to the data points in Figure R1, represent the standard deviations. The variation in the solid volume fraction estimates were less at the centre of the riser (-0.3 < r/R < 0.3) when compared to those near the riser walls in Figure R1. In Figure R2, the degree of confidence that is associated with each radial solid volume fraction measurement at the middle port is illustrated. Once again, larger confidence intervals were obtained at the walls of the riser as opposed to the centre region which indicates a greater degree of uncertainty near the wall regions. The same could be said about the solid volume fraction at the top port and this is illustrated in Figure R3

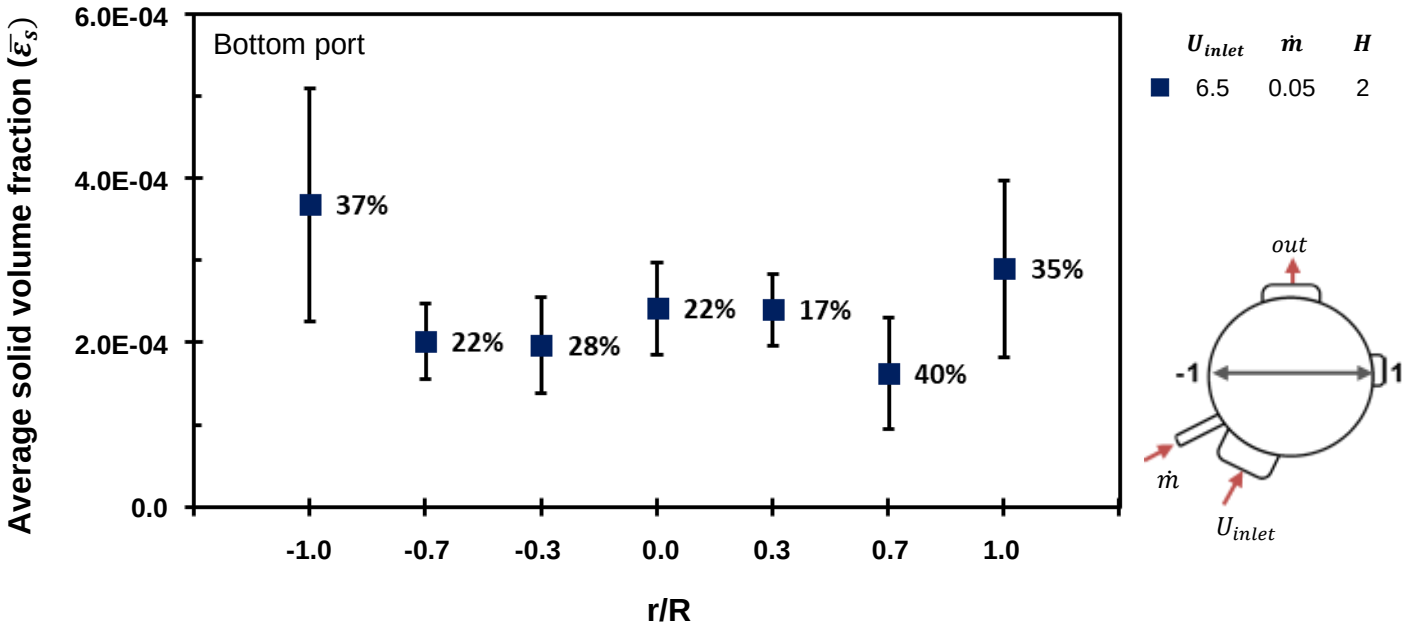

Figure R1: *Average solid volume fractions and associated confidence intervals along the diameter of the riser at the bottom port with data from six identical experiments.*

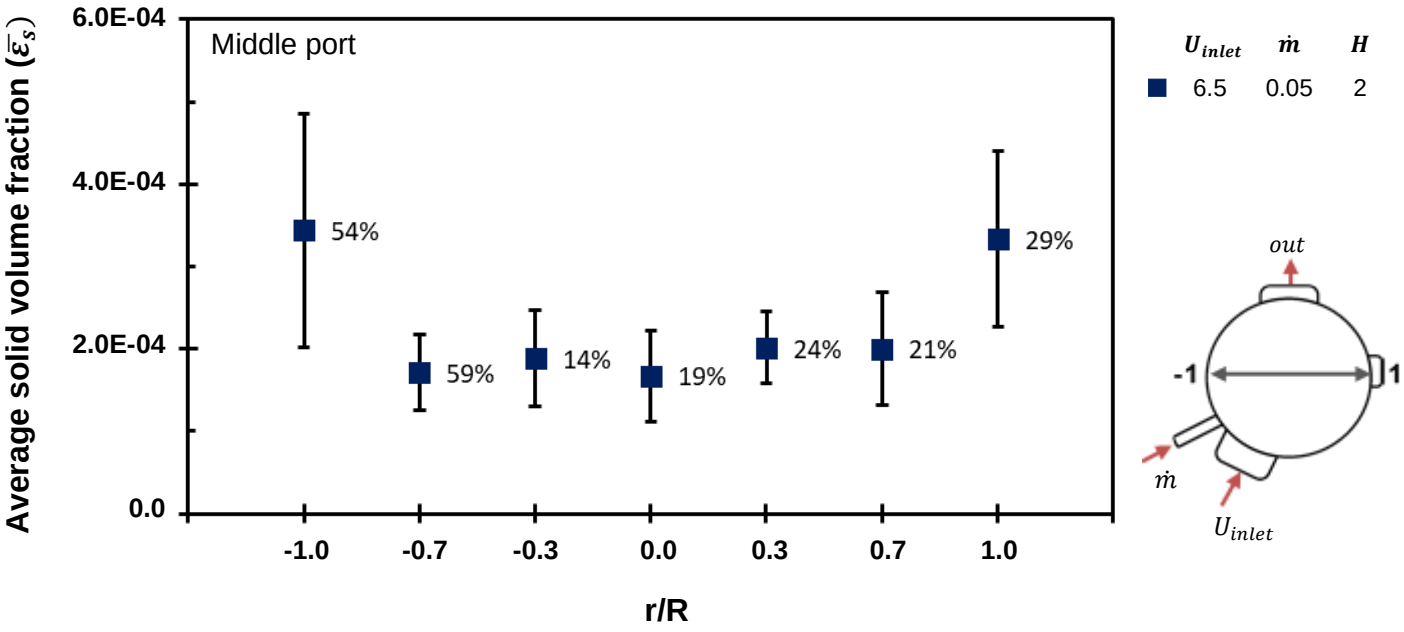

Figure R2: *Average solid volume fractions and associated confidence intervals along the diameter of the riser at the middle port with data from six identical experiments*

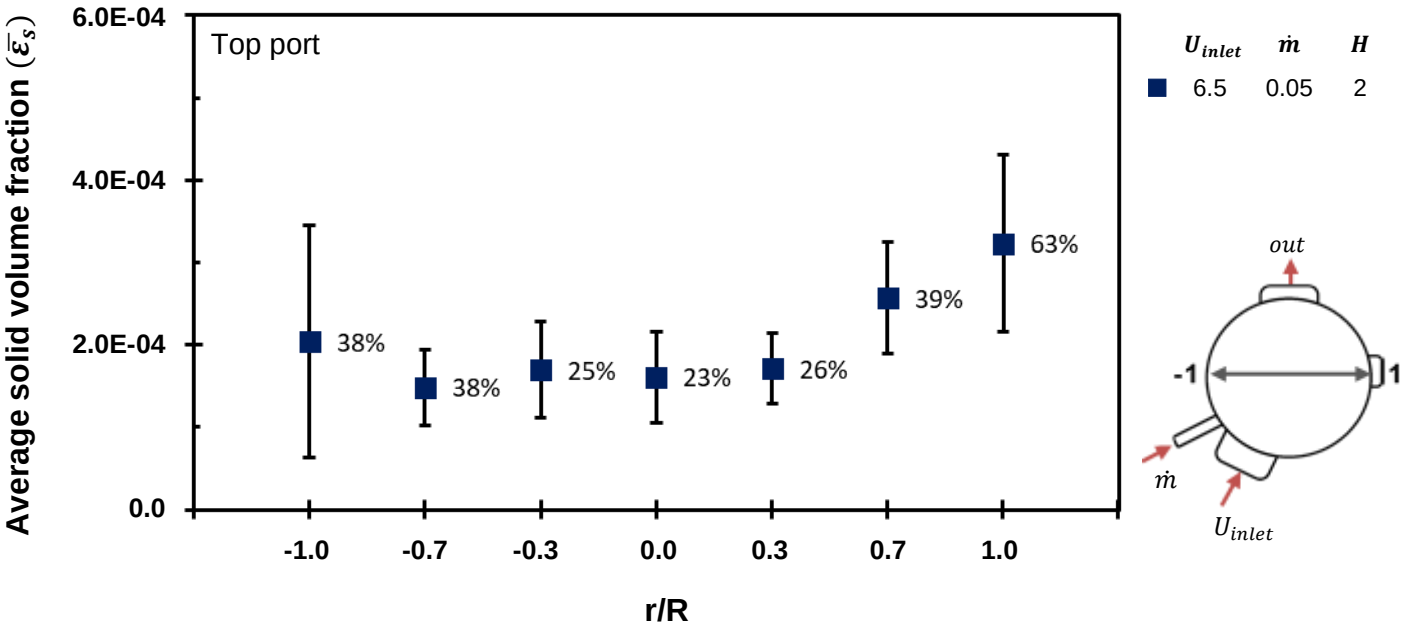

Figure R3: *Average solid volume fractions and associated confidence intervals along the diameter of the riser at the top port with data from six identical experiments*

The large variation in the solid volume fractions near the walls of the riser may be ascribed to the influence of wall friction and inter-particle interactions. As discussed in Chapter 5, these effects likely contributed to particle accumulation near the walls of the riser which increased the likelihood of particle clustering. According to Section 2.2.3.4, the ongoing formation and deformation of clusters could have influenced the drag forces, pressure drop, slip velocity, etc. In turn the variability in the solids holdup near the riser walls could have caused the increased standard deviations. It was also found that the standard deviation of the solid volume fractions near the centre of the riser and at the right riser wall were the lowest at the middle sampling port. Conversely, the standard deviation that was associated with the solids holdup near the left riser wall was the highest at the middle port. Nonetheless, the purpose of the experiments was to identify trends rather than exact ε_s values. Hence, the large standard deviations in Figure R1 to Figure R3 was not considered to be detrimental to the objectives of this study.

The confidence interval of the average solid volume fraction ($\bar{\varepsilon}_s$) at each sampling port was also determined and the result is illustrated in Figure R4. From Figure R4, it can be seen that a higher confidence interval was obtained at the top sampling port when compared to the middle and bottom sampling ports. This was likely due to internal recirculation at the top port due to the abrupt exit. Finally, the confidence intervals that were associated with the pressure drop across the riser and its installed sections are reported in Table R1. The standard deviation in the pressure differential measurements was equal to 5% which is sufficiently low for the aim of this study. Furthermore, the uncertainty was likely caused by the cluster formation and deformation in the riser and the occasional surging of particles through the system.

***Table R1**: Error that was associated with the pressure drop data*

$\boldsymbol{\Delta P_{riser}}$	$\boldsymbol{Pa}$	$[\boldsymbol{\Delta P_{riser}} = \boldsymbol{P_{(PT-09)}} - \boldsymbol{P_{(PT-01)}}]^*$	48
$\boldsymbol{\Delta P_{sections}}$	Pa	$\left[\Delta P_{riser} = P_{(PT-09)} - P_{(PT-03)}\right]$	3

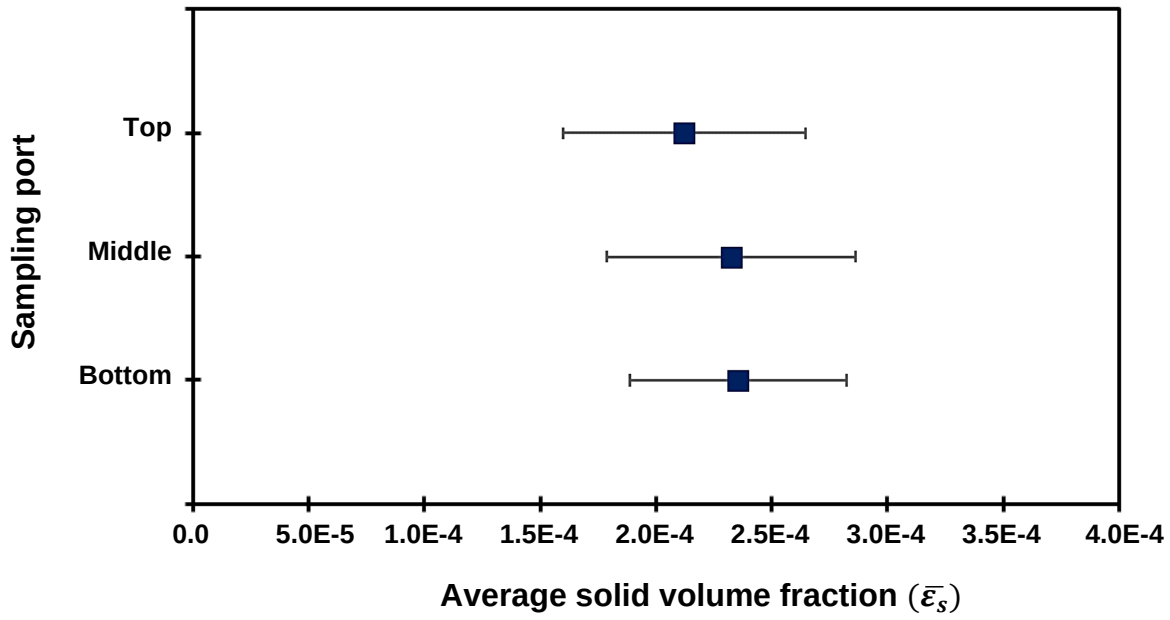

Figure R4: *Average solid volume fractions and associated confidence intervals along the height of the riser from six identical experiments*

Annexure S: Choice of $\bar{\varepsilon}_s$ calculation method

The two most popular methods for determining the average solid volume fraction in CFB risers have been provided in Section 2.2.3.1. The first method as represented by Equation 2-10 will be referred to as the integral method and the second method which is given by Equation 2-11 will be referred to as the pressure method. Both methods were used to determine the average solid volume fraction at the top sampling port as illustrated by the blue dot in Figure S1, while three cylindrical sections were installed. The pressure drop and height between PT-08 and PT-07 in Figure S1, was used for the pressure method while the sampled sorbent at the blue dot in Figure S1 was used for the integral method. The results are reported in Table S1 together with the arithmetic mean as determined from Equation S-1 for comparison.

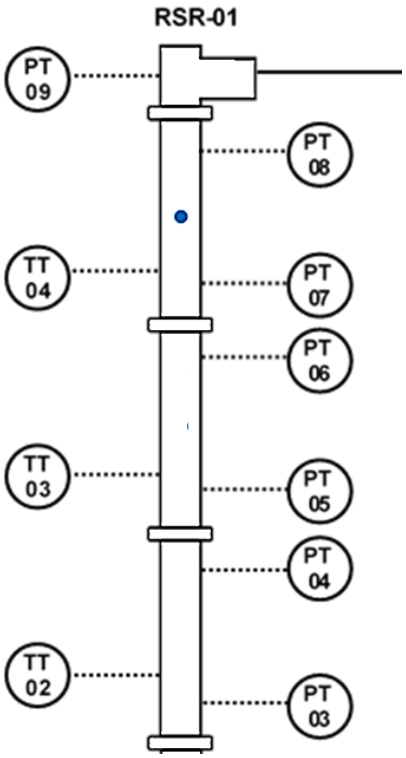

Figure S1: *The sampling port where the average solid volume fraction was determined in order to compare calculation methods*

$$\bar{\varepsilon}_s = \frac{1}{7} \times \sum_{i=1}^{7} \varepsilon_{s,i} \qquad \textbf{S- 1}$$

Where i indicates the radial measurement point along the riser diameter and ε_s indicates the solid volume fraction at the given point.

Table S1: *The average solid volume fraction at the top port resulting from two different calculation methods*

Operating conditions		**Method of $\bar{\varepsilon}_s$ calculation**		
Riser inlet velocity (m/s)	Solids feed rate (kg/s)	Integral ($\times 10^{-4}$)	Pressure differential ($\times 10^{-4}$)	Arithmetic mean ($\times 10^{-4}$)
4.3	0.04	3.3	39	3.2
4.3	0.06	6.2	47	6.7
8.6	0.06	1.9	37	1.9
8.6	0.04	1.2	42	1.1
6.5	0.05	2.0	44	2.0

By inspecting any given row in Table S1, it can be seen that the average solid volume fraction that was calculated via the pressure method was one order of magnitude larger than the values obtained via the integral method and the arithmetic mean. The over approximation occurred since the pressure method failed to account for the influence of phase interactions and frictional losses on the pressure drop as explained in Section 2.2.3.1. In addition, the distance between PT-08 and PT-07 may have been too large which further increased the error associated with the pressure method due to the wall friction and phase interactions. Given the uncertainty related to the pressure method and the availability of local solid volume fraction data, it was decided to use the integral method to calculate the average solid volume fractions in this study. Since data along the entire riser diameter was available, Equation 2-10 had to be applied twice and the average of the two values were used. This is because Equation 2-10 is defined along the radius of the riser instead of the entire diameter. From the seven local solids holdup values, the centre point was used twice – once in each calculation.

Annexure T: Additional CFD modelling results

T1. Radial solids distributions

The radial scenes from the CFD models that were not discussed in Section 5.2.1, are provided here. Figure T1 and Figure T2, represent the results at the bottom and top ports, respectively. As discussed in Section 5.2.1, an increase in the inlet air velocity or a decrease in the riser height improved the uniformity of the radial solids distributions. This trend was reflected regardless of whether the bottom, middle or top sampling points were used.

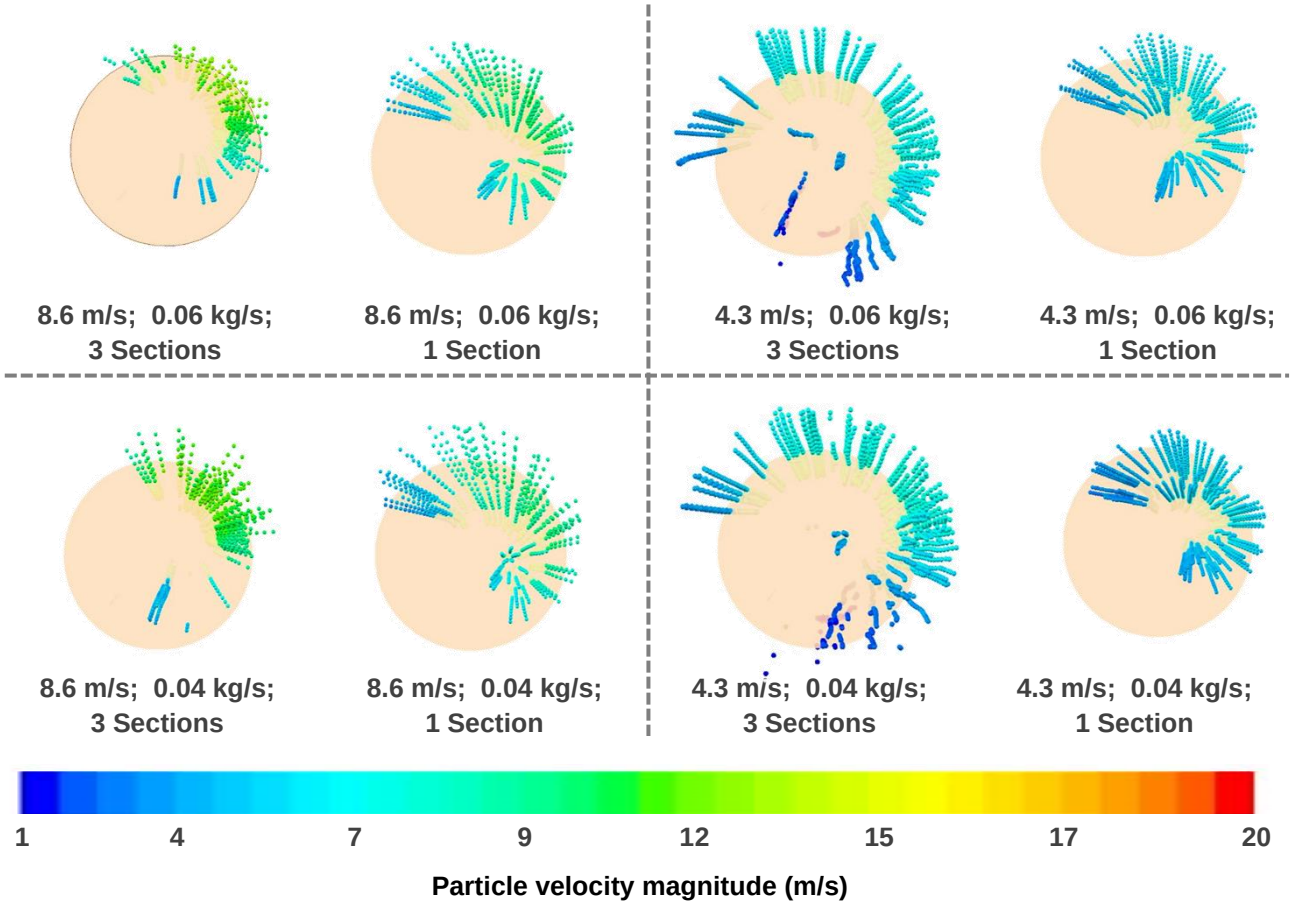

Figure T1: *The influence of varying operating and design parameters on the radial solids distribution at the bottom sampling port according to the CFD models*

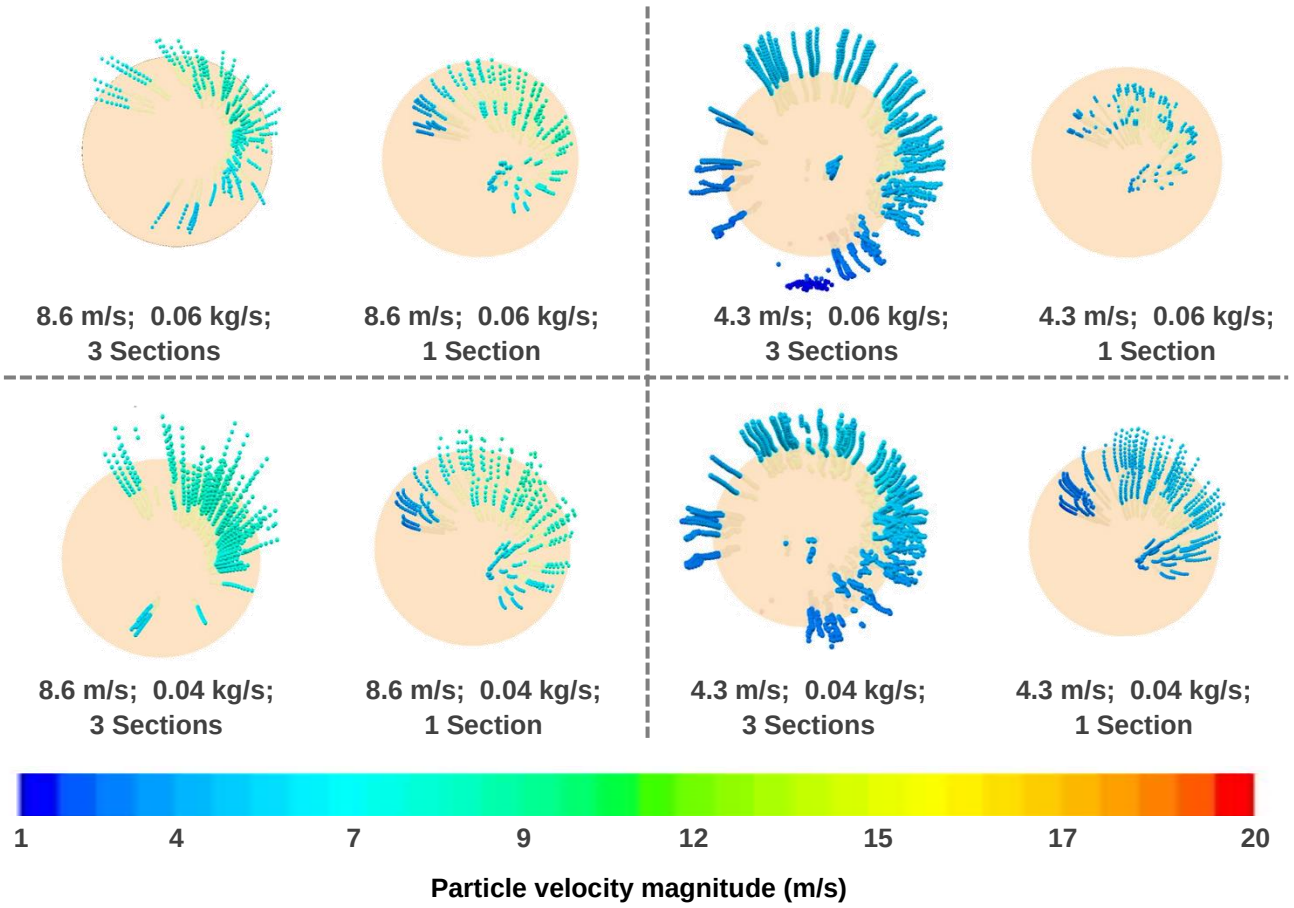

Figure T2: *The influence of varying operating and design parameters on the radial solids distribution at the top sampling port according to the CFD models*

T2. <u>Axial solids holdup profiles</u>

In Figure T3, the axial solids holdup profiles at within the tallest riser are provided. The same trends that were discussed in Section 5.2.3 can be seen from the profiles and may be summarised as follows:

- A decreased inlet air velocity enhanced the exit effect.
- A decreased inlet air velocity or an increased solids feed rate increased the overall solids holdup.

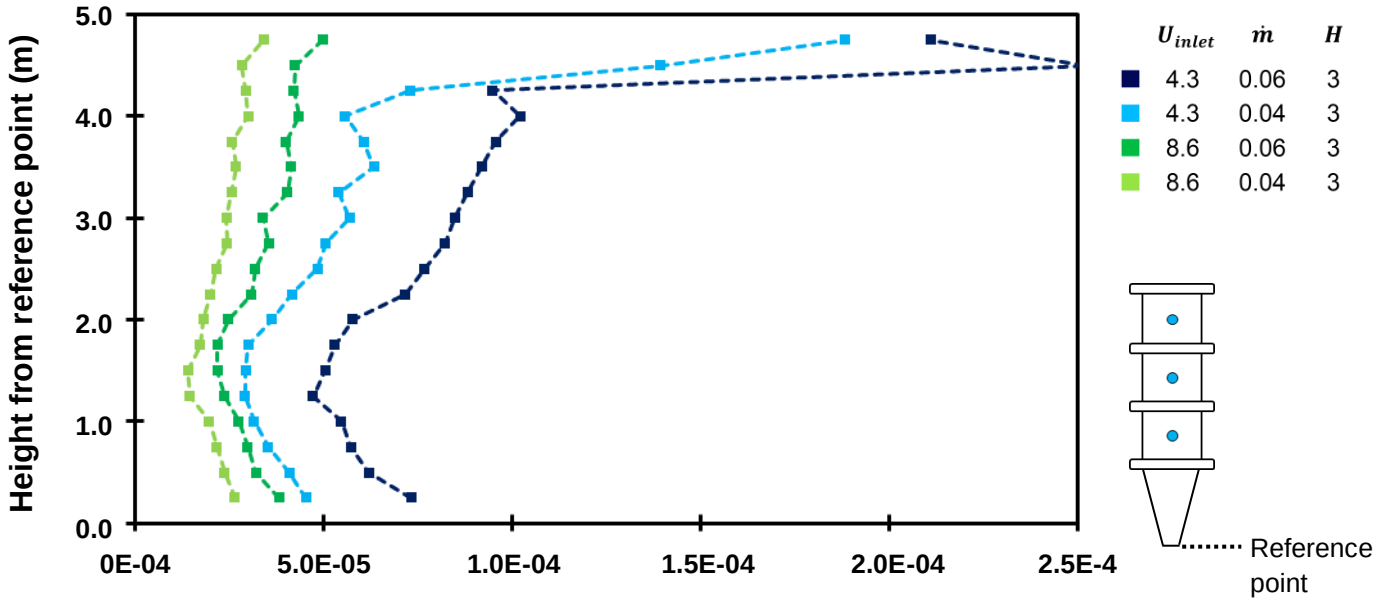

Figure T3: *Predicted axial solids holdup profiles under varying operating conditions at the maximum riser height setting*

Annexure U: Regression models

The final regression models that were used to discuss hydrodynamic parameters according to the factorial design analysis are provided in Table U1. A quadratic regression model rather than a linear regression model was used only for the following parameters:

- Radial non uniformity index at the top port ($RNI(\varepsilon_s)_{top}$).
- Average solid volume fraction at the top port ($\bar{\varepsilon}_{s_{top}}$).
- Pressure differential across the installed cylindrical riser sections ($\Delta P_{section}$).

Table U1: *Regression models for the hydrodynamic indicators that were discussed in Section 5.3*

Response	Regression model
$\boldsymbol{RNI(\varepsilon_s)_{bot}}$	0.688 + (-0.122)Velocity + (0.172)MFR + (-0.055)Height + (0.042)(Velocity)(MFR) + (-0.12)(Velocity)(Height) + (0.085)(MFR)(Height) + (0.107)(Velocity)(MFR)(Height)
$\boldsymbol{RNI(\varepsilon_s)_{mid}}$	0.438 + (0.135)Velocity + (-0.053)MFR + (0.147)Height + (-0.106)(Velocity)(MFR) + (-0.078)(Velocity)(Height) + (-0.112)(MFR)(Height) + (-0.098)(Velocity)(MFR)(Height)
$\boldsymbol{RNI(\varepsilon_s)_{top}}$	0.354 + (-0.079)Velocity + (0.024)MFR + (-0.026)Height + (0.367)Velocity^2 + (0.034)MFR^2 + (-0.313)Height^2 + (-0.042)(Velocity)(MFR) + (-0.085)(Velocity)(Height) + (0.016)(MFR)(Height)
$\boldsymbol{\bar{\varepsilon}_{s_{bot}}}$	0.331 + (-0.221)Velocity + (0.03)MFR + (-0.147)Height + (0.047)(Velocity)(MFR) + (0.125)(Velocity)(Height) + (-0.067)(MFR)(Height) + (0.102)(Velocity)(MFR)(Height)
$\boldsymbol{\bar{\varepsilon}_{s_{mid}}}$	0.354 + (-0.275)Velocity + (0.125)MFR + (-0.06)Height + (-0.063)(Velocity)(MFR) + (0.021)(Velocity)(Height) + (-0.023)(MFR)(Height) + (0.04)(Velocity)(MFR)(Height)
$\boldsymbol{\bar{\varepsilon}_{s_{top}}}$	0.234 + (-0.189)Velocity + (0.105)MFR + (-0.034)Height + (-0.088) Velocity^2 + (0.12)MFR^2 + (0.192)Height^2 + (-0.05)(Velocity)(MFR) + (-0.03)(Velocity)(Height) + (0.06)(MFR)(Height)
$\boldsymbol{\Delta P_{riser}}$	0.515 + (0.21)Velocity + (-0.06)MFR + (-0.16)Height + (-0.143)(Velocity)(MFR) + (-0.137)(Velocity)(Height) + (-0.083)(MFR)(Height) + (-0.101)(Velocity)(MFR)(Height)
$\boldsymbol{\Delta P_{section}}$	0.981 + (-0.013)Velocity + (0.009)MFR + (-0.412)Height + (-0.004)Velocity^2 + (-0.026)MFR^2 + (-0.498)Height^2 + (-0.005)(Velocity)(MFR) + (0.001)(Velocity)(Height) + (-0.021)(MFR)(Height)

Annexure V: Selected response surfaces

In Figure V1 and Figure V2 the two response surfaces that were mentioned in Section 5.3 are provided. In both figures the values of the selected independent variables were represented by a -1, 0 and 1 for the low medium and high settings respectively. In Figure V1, it can be seen that four of the blocks on the bottom plane were highlighted. These blocks represent the domain in which an increase in the riser height setting or a decrease in the inlet air velocity resulted in a lower non-uniformity at the middle sampling port. This region was highlighted it corresponds with the CFD findings in Section 5.2 as well as the literature findings from Sections 2.2.4.1 and 2.2.4.2.

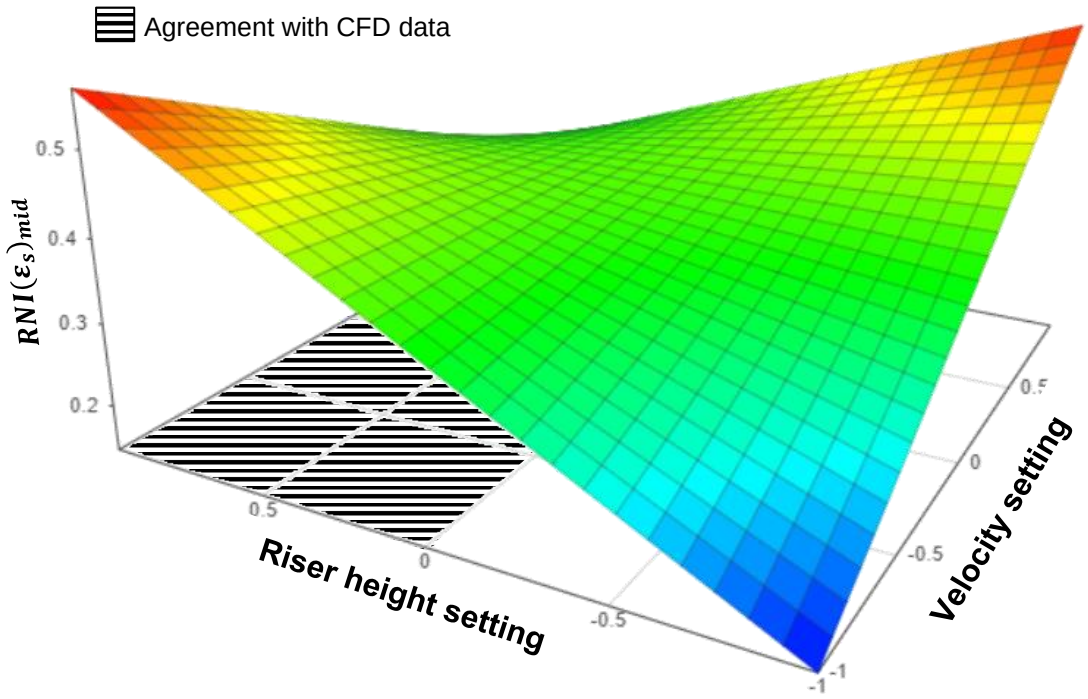

Figure V1: *Response surface of the $RNI(\varepsilon_s)_{mid}$ at a fixed solids feed rate of 0.06 kg/s*

In Figure V2, the response surface of the pressure differential across the installed cylindrical riser sections is provided. As discussed in Sections 5.1.3 and 5.3.3, the pressure differential across the installed sections was the greatest when the riser was at its medium height setting. However, from Figure V2, the pressure differential increases together with the riser height until a turning point is reached shortly after the medium riser height setting. After this point, the pressure differential started to decrease again according the quadratic regression model.

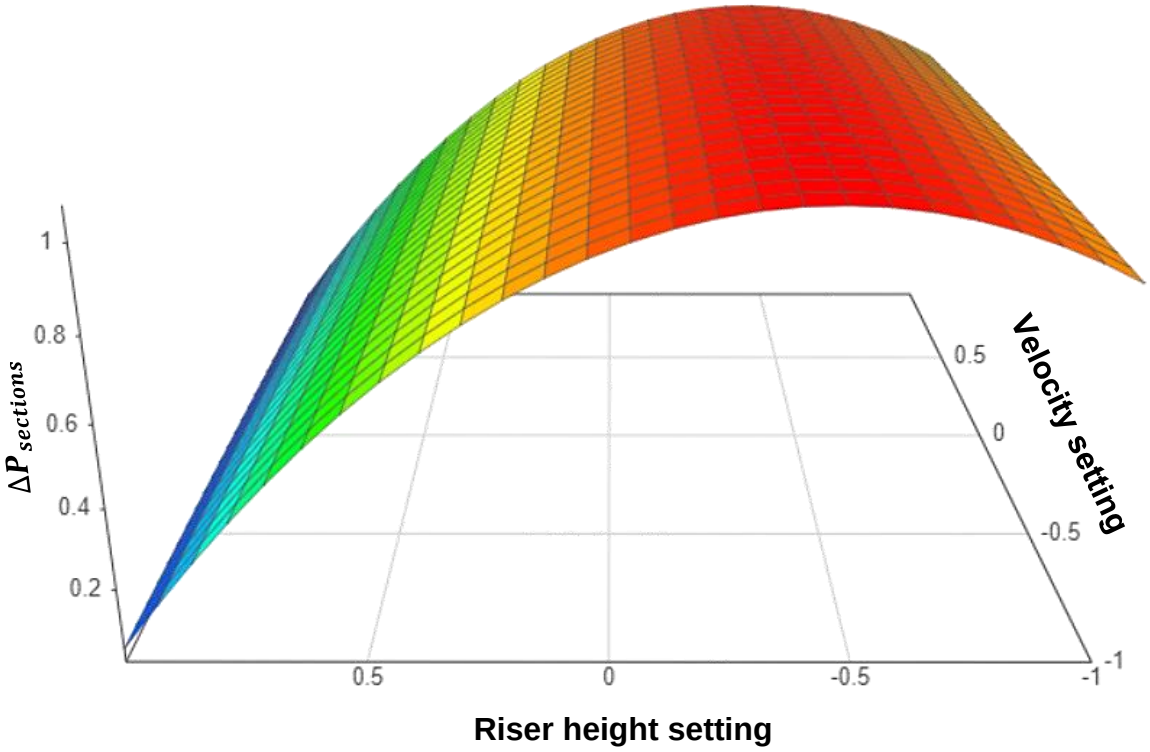

Figure V2: *Response surface of the $\Delta P_{sections}$ at a fixed solids feed rate of 0.06 kg/s*